

Award Number: W81XWH-10-1-0767

TITLE: A Partnership Training Program: Studying Targeted
Drug Delivery Using Nanoparticles In Breast Cancer Diagnosis
and Therapy

PRINCIPAL INVESTIGATOR: Paul C. Wang, Ph.D.

CONTRACTING ORGANIZATION: Howard University"
Washington, DC 20059

REPORT DATE: December 2015

TYPE OF REPORT: Annual Summary

PREPARED FOR: U.S. Army Medical Research and Materiel Command
Fort Detrick, Maryland 21702-5012

DISTRIBUTION STATEMENT:

X Approved for public release; distribution unlimited

The views, opinions and/or findings contained in this report are those of the author(s) and should not be construed as an official Department of the Army position, policy or decision unless so designated by other documentation.

REPORT DOCUMENTATION PAGE				Form Approved OMB No. 0704-0188	
Public reporting burden for this collection of information is estimated to average 1 hour per response, including the time for reviewing instructions, searching existing data sources, gathering and maintaining the data needed, and completing and reviewing this collection of information. Send comments regarding this burden estimate or any other aspect of this collection of information, including suggestions for reducing this burden to Department of Defense, Washington Headquarters Services, Directorate for Information Operations and Reports (0704-0188), 1215 Jefferson Davis Highway, Suite 1204, Arlington, VA 22202-4302. Respondents should be aware that notwithstanding any other provision of law, no person shall be subject to any penalty for failing to comply with a collection of information if it does not display a currently valid OMB control number. PLEASE DO NOT RETURN YOUR FORM TO THE ABOVE ADDRESS.					
1. REPORT DATE (DD-MM-YYYY) DECEMBER-2015		2. REPORT TYPE Annual Summary		3. DATES COVERED (From - To) 15 Sep 2010 to 14 Sep 2015	
4. TITLE AND SUBTITLE A Partnership Training Program: Studying Targeted Drug Delivery Using Nanoparticles In Breast Cancer Diagnosis and Therapy " "				5a. CONTRACT NUMBER	
				5b. GRANT NUMBER W81XWH-10-1-0767	
				5c. PROGRAM ELEMENT NUMBER	
6. AUTHOR(S) " Paul C. Wang, Ph.D. Email: pwang@howard.edu				5d. PROJECT NUMBER	
				5e. TASK NUMBER	
				5f. WORK UNIT NUMBER	
7. PERFORMING ORGANIZATION NAME(S) AND ADDRESS(ES) Howard University Washington, DC 20059				8. PERFORMING ORGANIZATION REPORT NUMBER	
9. SPONSORING / MONITORING AGENCY NAME(S) AND ADDRESS(ES) U.S. Army Medical Research and Materiel Command Fort Detrick, MD 21702-5012				10. SPONSOR/MONITOR'S ACRONYM(S)	
				11. SPONSOR/MONITOR'S REPORT NUMBER(S)	
12. DISTRIBUTION / AVAILABILITY STATEMENT Approved for public release; distribution unlimited					
13. SUPPLEMENTARY NOTES					
14. ABSTRACT Howard University (HU) Imaging Core has fully accomplished the goals of this training program. For five years, the Core was able to establish a Nanomedicine Core Lab that served as a ground for learning, training and professional development to 14 faculty, 14 non-HU scientists, 14 postdoctoral fellows, 21 graduate (2 of whom received Ph.D. degree) and 7 undergraduate students. Faculty trainees and postdocs of the program have submitted grants to various agencies and some received funding and invitation to submit a full proposal. The Core received various grants to not only further support the University Imaging Core but also enhance its ability to conduct imaging studies using large animals through the support received from a NIH supplement. The program offered more than 40 seminars, webinars, workshops and symposia in cancer, molecular imaging and nanomedicine. The Nanomedicine Core became a synergy center drawing multidisciplinary research collaborations using nanotechnology for targeted drug delivery and improving breast cancer diagnosis and therapy. Various peer-reviewed publications and presentations resulted from this training grant. The two research projects were successfully completed. Liposomes were generated with a narrow size distribution. A novel recombinant immunotoxin DT390-BiscFv806 that is highly promising for treatment of cancers arising from the brain, head and neck, lung, breast, and prostate were generated. Aside from these two research projects, several additional projects using computer modeling to study docking process between nanoparticles and their intended targets in cancer cells, using a convex analysis of mixtures algorithm to study compartmental modeling of MRI-DCE pattern of targeted delivery of nanoparticle containing MR contrast agent and the liposome use as drug delivery vehicle for cancer diagnosis.					
15. SUBJECT TERMS training, nanotechnology, breast cancer, diagnosis, therapy, imaging, drug delivery					
16. SECURITY CLASSIFICATION OF:			17. LIMITATION OF ABSTRACT	18. NUMBER OF PAGES	19a. NAME OF RESPONSIBLE PERSON
a. REPORT	b. ABSTRACT	c. THIS PAGE			USAMRMC
U	U	U	UU	13	19b. TELEPHONE NUMBER (include area code)

Table of Contents

	<u>Page</u>
Cover.....	1
SF 298.....	2
Table of Contents.....	3
Introduction.....	4
Body.....	4
Key Research Accomplishments.....	27
Reportable Outcomes.....	30
Conclusion.....	38
References.....	42
Appendices.....	44

A Partnership Training Program – Studying Targeted Drug Delivery Nanoparticles in Breast Cancer Diagnosis and Therapy

I. INTRODUCTION

In this program, we proposed to establish a Nanomedicine Core to train faculty and students at Howard University to pursue molecular imaging of breast cancer using nanoparticles as targeted drug delivery vehicles. This is a partnership with the Johns Hopkins University In Vivo Cellular Molecular Imaging Center and the Nanotechnology Characterization Lab at NCI-Frederick. At Howard University, this partnership involves a multidisciplinary consortium of four departments: Radiology, Radiation Oncology, Molecular Biology and Biochemistry, and Electrical Engineering. The program has two components, a research component and a broad training component. The Howard University trainees will obtain training through collaborative research and by participation in a broad based training program. Renowned experts in nanomedicine and molecular imaging will participate in the training through mentoring research, seminars, workshops, and by offering laboratory internships. This transfer of nanomedicine techniques will support ongoing, long-term breast cancer research at Howard University. The major goal is to provide faculty trainees and their students at Howard with updated nanomedicine techniques to apply to independent breast cancer research, thus enhancing their ability to educate the next generation of scientists. The program objectives are:

1. Train new researchers in breast cancer using modern nanomedicine techniques.
2. Offer lectures, seminars, workshops, and laboratory internships in nanotechnology and molecular imaging.
3. Conduct two proposed research projects.
4. Establish a Nanomedicine Core to support long-term sustainable research.
5. Research concept development and submission of competitive grants in breast cancer imaging.

II. BODY

Molecular imaging and functional MRI continue to provide new insights into the etiology, diagnosis, and treatment of breast cancer. In clinic, these methods have made a significant impact in breast cancer diagnosis and in monitoring response to therapy. As our understanding of breast cancer advances, we further recognized the complexities of this disease and the urgent need for individualized characterization and treatment. Recent exciting advances in the application of MR methods for breast cancer research have resulted from the development of contrast agents (CAs) that generate receptor-targeted or molecular-targeted contrast. Targeted CAs can be directed to cell surface receptors using antibodies or 'smart' agents activated by specific enzymes, or based on the expression of detectable reporters. These molecular imaging capabilities, in combination with the strong functional imaging capabilities of MR methods, allow molecular-functional characterization of cancer and the physiological microenvironment of tumors. Non-invasive MR can play an important role in the molecular-functional characterization of breast cancer for detection, drug delivery, development of therapeutics, and monitoring of treatment response. Lately, the development of nanotechnology has also had a dramatic impact on diagnosis and treatment. Among many possible applications of nanotechnology in medicine, the use of various nanomaterials as pharmaceutical delivery systems for drugs, DNA, and imaging agents has gained increasing attention. Many nanoparticle-based drug delivery and drug targeting systems have been approved by FDA or are under development. Their use aims to minimize drug degradation, prevent undesirable side effects, and increase drug bioavailability and the fraction of drug dosage delivered to the pathological area.

In order to achieve the goals of this training program, we proposed to conduct two research projects and to train researchers at Howard University in the field of the application of nanotechnology in targeted drug delivery through a broad-based training program. In conjunction with these activities, we also proposed establishing a University Nanomedicine Core to promote and facilitate campus-wide research and training. The following progress report is a summary of the accomplishments for the entire project period including the no cost extension year, in the following areas: (i) research, (ii) training, (iii) establishment of Nanomedicine Core, and (iv) alignment with the Statement of Work.

II.1. Research Projects

Project 1: Study the physicochemical characteristics of nanoparticles as MR contrast agent delivery system with the dynamic contrast enhancement pattern for clinical applications

Nanoparticles in the size range 10–150 nm — are emerging as a class of diagnostic and therapeutic agents for cancer. Early clinical results suggest that nanoparticle therapeutics can show enhanced efficacy, while simultaneously reducing side effects, owing to properties such as more targeted localization in tumors and active cellular uptake. Particles in the nanometer size range are of different sizes, shapes and material properties have many applications in biomedical imaging, clinical diagnostics and therapeutics. Commonly used nanoparticles include liposome (Lip), micelles; quantum dots (QDs), polymeric, gold, and magnetic nanoparticles. The unique physical and chemical properties of each nanoparticle significantly influence its interactions with tissues and cells. Its extraordinary properties such as flexible composition, large surface to volume ratio, various shape and small size, and optical properties, contribute to the novel applications in diagnostic imaging and therapy. Their use continues to grow rapidly, particularly in drug delivery applications and imaging. Better understanding of these interactions will greatly assist in the design of smart drugs and targeted CAs delivery, with great potential for molecular-based diagnostics and therapeutics.

Throughout the project period of 5 years, liposomes were created using sonication and/or extrusion methods. In this project, we focused on the physicochemical characteristic size of the nanoparticle. As the project progressed, we have recognized that we need to create liposomes with a narrower size distribution to better answer our research question.

To create liposomes, our lab utilized the method demonstrated by Dr. Langer's lab during a nanotechnology seminar at MIT. The method uses a microfluidic device for fabricating liposomes with an extremely narrow size distribution. A lipid tincture is hydrodynamically focused by aqueous buffer (Figure 1) in the microfluidic device. As the lipid and aqueous buffer interdiffuse, the lipid self-assembles into liposomes. By manipulating the flow ratios of the lipid and aqueous buffer, the size of the liposomes can be controlled. Prior studies have been able to accomplish extremely low polydispersity index (PDI) values (0.001 – 0.044).

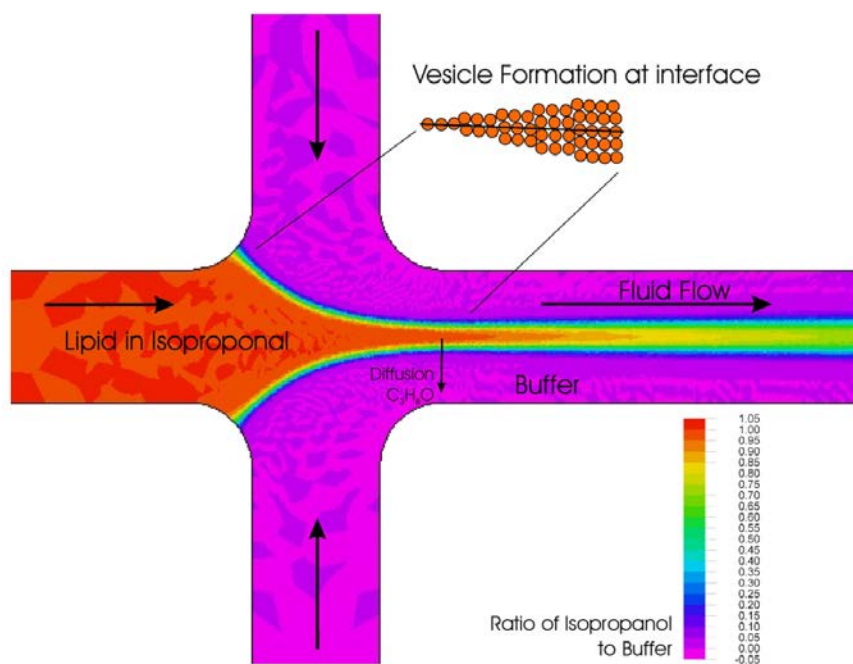


Figure 1: Schematic of liposome formation process in the microfluidic channel. Andreas Jahn. 2008.

Literature search performed on microfluidic devices revealed that aside from Dr. Langer's lab at MIT, two other labs, Dr. DeVoe at UMD, and Dr. Vreeland at NIST have the same systems set up. Dr. Vreeland accommodated two members of MIL, Jason Zhang and Stephen Lin to learn about their microfluidic setup. Dr. Abouzeid, a postdoc in Dr. Vreeland's lab, helped our members to learn and document set-up of their microfluidic device.

Materials and Methods

The microfluidic device consists of a polydimethylsiloxane block with microfluidic channels embossed on the surface and bonded to a glass slide. The first step in creating the device is designing the microfluidic channels. The design is created in a computer-aided design software (e.g. AutoCAD), which is then sent to a phototooling company to be laser plotted onto a photo-opaque material to create a photomask (Figure 2).

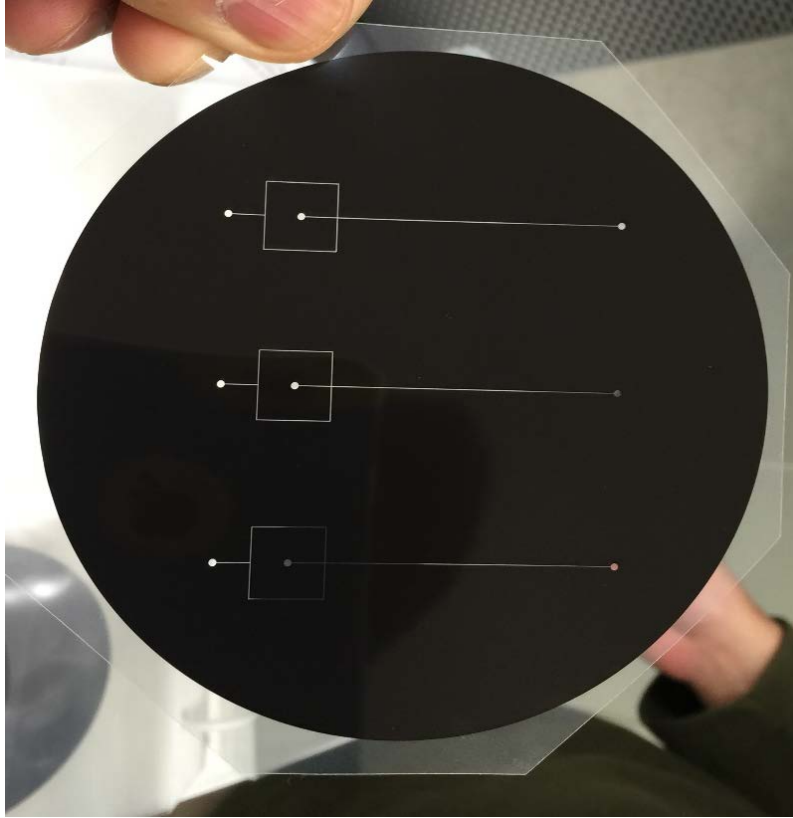


Figure 2: Photomask with microfluidic channel design

Blank molds are created by laminating layers of photoresist material at 110°C onto a clean glass slide. The desired depth of the microfluidic channel can be controlled by lamination of multiple layers of photoresist material (i.e., laminating two layers of 40µm thick photoresist will result in 80µm deep channels). The blank molds are then baked at 100°C on a hot plate for 20 minutes to allow the photoresist material to fully adhere to the glass slide. During this process, the photoresist material is covered with foil to protect the photoresist from light.

The blank mold is then photo-patterned with the microfluidic channel pattern using the photomask. The photomask is placed flush against the photoresist material on the blank mold. The mold is then exposed to ultraviolet (UV) light for 90 seconds, crosslinking the photoresist material not masked by the photomask (Figure 3). The mold is then developed by removing the unexposed photoresist material mechanically by scraping off excess material with a scalpel, and chemically with NaCO₂. The result is a positive relief mold (Figure 3).

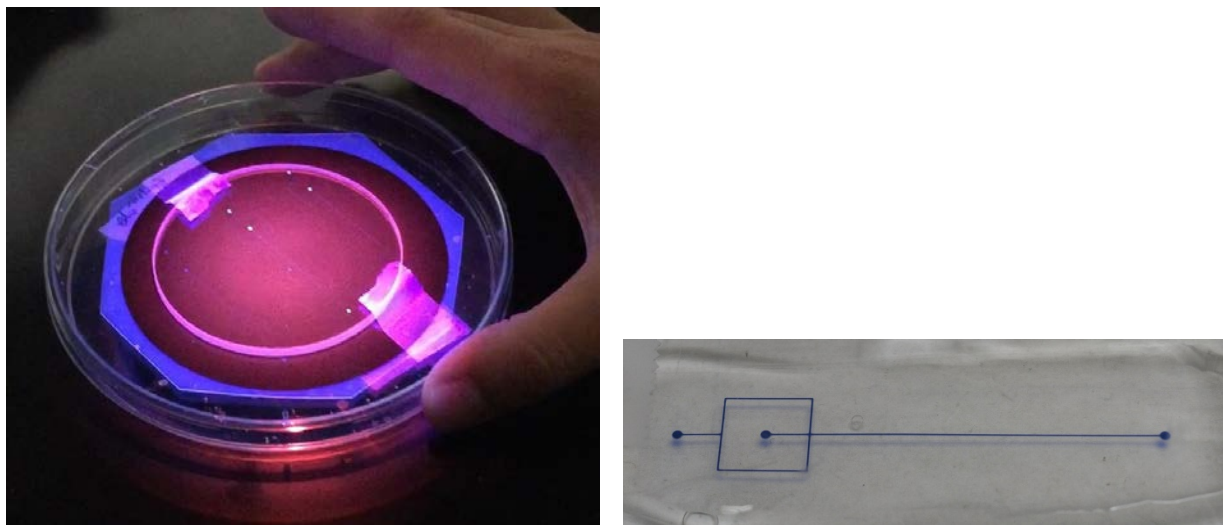


Figure 3: Blank mold exposed to UV light through photomask (left). Resulting mold after developing (right)

The mold can now be used to generate microfluidic devices. The mold is placed in a petri dish and PDMS is cast into the mold and allowed to cure. The PDMS is then cut with a scalpel to extract a device from the mold and the device is baked at 65°C to allow the device to cure. Using a biopsy punch, inlet and outlet holes are punched into the device and the device is plasma bonded onto a glass slide. Bent 23ga stainless steel tubing is inserted into the inlet and outlet holes and connected to syringes through Teflon tubing, completing the device (Figure 4).

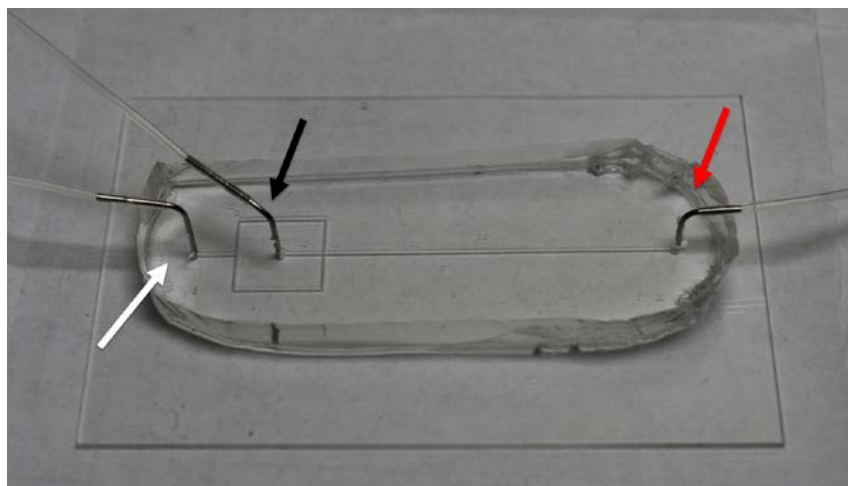


Figure 4: Completed microfluidic device with buffer (white arrow) and lipid (black arrow) inlet channels and outlet channel (red arrow)

Liposomes are generated with the device by flowing phosphate buffered saline (PBS) in the side channels and a lipid tincture through the central channel. The convergence of the PBS and lipid tincture is observed under light microscope to ensure stable, equal convergence and the complete mixture of the lipid tincture in the PBS (Figure 5).

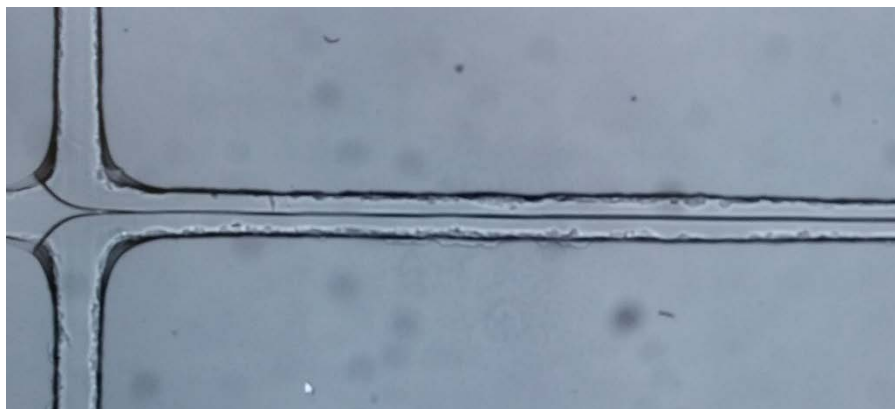


Figure 5: Light microscope image of the intersection of the microchannels, showing the hydrodynamic focusing of the lipid tincture by the buffer solution.

Results

Liposomes were generated using the device using a DPPC:Cholesterol:DSPE-PEG (5:4:1) lipid formulation. 10mM PBS with 0.05% azide and the lipid tincture was flowed through the device at a 1:10 and 1:20 ratios. Dynamic light scattering (DLS) (Nano ZS90, Malvern Instruments, Ltd.) was used to measure the size distribution of the liposomes giving a Z-average diameter of 139.9nm and 91.4nm, respectively and a PDI of 0.128 and 0.163. Liposomes were prepared with a mini-extruder device (Avanti Polar Lipids, Inc.) ranging from a Z-average size of 55nm to 200nm, which had a PDI ranging from 0.017 to 0.113.

Conclusion

The goal of the no cost extension funding to finish testing the nanoparticles in animal models was completed. The size distribution of the initial batch of liposomes generated with the microfluidic device was higher than expected, but was similar to the size distribution of the liposomes generated with well-established extrusion method. Further discussions with Dr. Vreeland suggested that the lipid was below the transition temperature of the lipid, which likely contributed to the poor size distribution. Running the device in a warmer environment, or changing the lipid formulation to one with a lower transition temperature would likely result in significantly improved size distributions. Additionally, in the second run, the lipid to aqueous buffer ratio was too high for the overall fluid flow, resulting in some lipid deposits in the channels in the device, which may have impeded the proper operation of the device for the third sample.

Despite these issues, we were still able to generate liposomes with a size distribution matching those created with the mini-extruder. It is expected that with some minor adjustments, the device will be able to significantly improve on the size distribution. The device proved to provide facile control of the liposome size by controlling the flow ratios of the lipid and aqueous buffer. Imaging contrast agents or therapeutic agents can then be added to either the buffer solution or the lipid tincture to utilize the liposome as a transport vehicle.

Project 2: Development of Multifunctional Nanoparticles for Breast Cancer Diagnosis and Treatment – Using Anti-VEGFR-2 Immunotoxin as Dual Purpose Ligand and Chemotherapeutics as Encapsulated payload

;"

"

"

Targeted imaging and therapy has long been recognized to be the most attractive strategy to make early diagnosis and reduce mortality of cancer. To achieve this goal, engineered antibody fragments and antibody fragment-based recombinant immunotoxins (RITs) represent one of the most promising modalities, while epidermal growth factor receptor (EGFR)/mutated EGFR variant III (EGFRvIII), and prostate-specific membrane antigen (PSMA) has been considered to be the optimal targets to develop antibody fragments and RITs.

EGFR is a transmembrane tyrosine kinase, belonging to the HER/erbB family. Activation of EGFR by its ligands resulted in homo- or heterodimerization of EGFR and autophosphorylation of tyrosine residues in its C-terminal domain, leading to cell proliferation and migration. Various types of human cancer including breast cancer have been shown to overexpress EGFR and possess the cancer-specific EGFRvIII in a high frequency. PSMA is a membrane-bound glycoprotein that possesses a large extracellular domain and is overexpressed in almost all prostate cancer with its highest expression level in the metastatic and hormone-refractory diseases. Interestingly, PSMA is also specifically expressed by the tumor-associated endothelial cells, but not by the endothelial cells in normal tissue. These unique features of EGFR/EGFRvIII and PSMA make them extremely attractive as targets for anti-cancer cell and anti-cancer vascular therapy in a wide variety of human cancer (Table 1).

Table 1: Expression of PSMA by tumor vasculature and EGFR and EGFRvIII by cancer cells in various types of cancer¹

Cancer type ²	PSMA	EGFR	EGFRvIII
Head neck cancer	75	90	0-42
Glioblastoma	100	60-90	60-70 ²
Breast cancers	74-100	16-48	4-62
Prostate cancer	17	39-47	N/A
Non-small cell lung carcinoma	100	40-80	16-39
Colorectal carcinomas	85-100	60-80	0-34
Ovarian cancer	75	61	73

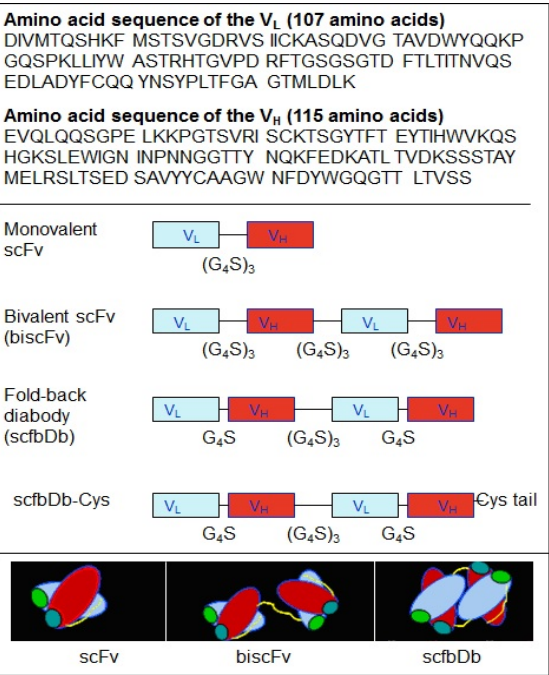
¹ The table lists only several representative types of cancer and the expression is expressed as frequency (%). ²EGFRvIII expression in glioblastomas with EGFR amplification.

In the past five years, we designed and generated various formats of antibody fragments and bivalent RITs targeting the EGFR/EGFRvIII and PSMA. The engineered antibody fragments showed high binding affinity with their targets and efficiently transferred the payload into the cancer cells and tumor xenografts. Correspondingly, the antibody fragment-derived, diphtheria toxin moiety-based RITs exhibited extremely high cytotoxicity against cancer cells and potent efficacy in inhibition of tumor xenograft growth. Below is a summary for the research rationale and experimental results regarding the engineered antibody fragments and EGFR/EGFRvIII/PSMA-targeted RITs.

1. Development of engineered antibody fragments as a platform for molecular imaging and therapy

Molecular imaging offers unique insights into the anatomy as well as the biological nature of a tumor. The high specificity of monoclonal antibodies (mAbs) along with the potential of imparting molecular specificity into existing imaging modalities makes them extremely attractive for molecular imaging. However, two major issues occurred as a critical barrier for their use in tumor imaging. One is the long circulation time (few days to weeks in blood), which requires at least 1-2 days after administration to reach a clear and specific tumor/background tissue contrast. Another is the poor tumor tissue penetration, imposed by the large molecular size of antibody, binding-site barrier, and high tumor interstitial pressure. As a result, the contrast enhancement is suboptimal, the same-day imaging is unachievable, and to date, only a small group of antibodies have been approved for clinical imaging.

To overcome these issues, engineered antibody fragments have been generated by fusing the variable regions of the antibody heavy (VH) and light chains (VL) with amino acid linker(s). The linker is usually ten to 15 amino acids in length and rich in Gly for flexibility and Ser or Thr for solubility. The smallest fragment that retains the original binding site of IgG antibody is the single-chain variable fragment (scFv, 25-30 kDa), which consists of one VH and one VL. The small size of scFv makes it efficient to penetrate into tumors, but also to be cleared too quickly from bloodstream ($t_{1/2}=0.5-2$ h). scFv also has a low binding affinity due to its monovalency. More desirable biological profiles have been achieved by the efforts in generating intermediate-sized bivalent scFv fragments (50-60 kDa, $t_{1/2}=3-7$ h). The optimal combination of rapid tumor penetration, high intratumor retention, and fast blood clearance sets the stage of bivalent scFv fragments for effective imaging. Larger fragments such as scFv-fusion proteins (80 kDa for minibody and 105 kDa for scFv-Fc) appear more suitable for tumor therapy than imaging because of the increased blood clearance time and decreased tissue penetration.

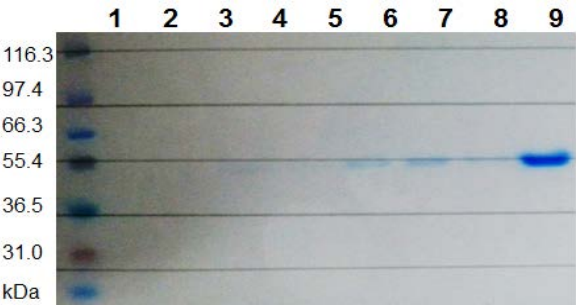


By leveraging the high specificity of the J591 antibody against the extracellular domain of PSMA, we first designed and generated different formats of antibody fragments, including scFv, bivalent tandem scFv (biscFv), and bivalent scFv fold-back diabody (scfbDb) (Fig. 1). The scFv contained one VL and one VH jointed by a 15 amino acid linker ((G4S)3), while the biscFv had two identical scFv. The long linker allows for proper folding and dimerization of the VL/VH within the same scFv to form the binding sites. Different from the scFv and biscFv, the scfbDb consisted of two scFv bridged by optimized lengths of GS linkers and presented in a fold-back structure.

Figure 1: The upper panel shows the VL/VH sequences. The middle panel shows the linear arrangement of VL/VH fragments, and the lowest panel presents the cartoon structures of the different formats.

We first characterized these fragments, especially the scfbDb, with HPLC and gel electrophoresis (Fig. 2). The size was ~27 kDa for scFv and ~54.6 kDa for biscFv and scfbDb. On the Superdex-200 size exclusion column, scfbDb gave a peak, corresponding to dimeric protein. Competition assay showed that the binding affinity of scfbDb was 7-fold and 2.5-fold higher than that of biscFv and scFv, respectively.

Figure 2: Non-reducing SDS-PAGE electrophoresis of the scfbDb as a representative of the fragments. Each lane represents the eluted scfbDb with different concentrations of NaCl from an anion exchange column. The scfbDb in lane 9 is the product used for studies.



The fold-back structure resulted in significantly increased binding affinity with PSMA and efficient drug delivery to tumor xenografts. The fold-back structure was formed by preventing dimer formation between the VL/VH within the same scFv by reducing the VL/VH linker to five residues (G4S), while permitting interactions between the distal and proximal VL/VH domains from different scFv by placing a longer linker ((G4S)3) between the two scFv. The enhanced rigidity and a close to 180° angle between the two binding sites may contribute to the improvement of binding affinity in closely packed tumors over the bisFcFv format. The interaction among the four variable domains from the two scFv may also provide extra-thermal stability for the fold-back structure and decrease the overall kinetic off-rate.

We then generated a recombinant immunotoxin using the scfbDb to test the delivery efficiency of the scfbDb and the anti-tumor efficacy of the immunotoxin. The immunotoxin comprised a deletion-mutated diphtheria toxin moiety (DT390) and the scfbDb with the scfbDb fused to the DT390 C-terminus. We confirmed that scfbDb could efficiently mediate the entry of the DT390 to the cytosol of PSMA-expressing LNCaP cells, but not to PSMA-absent PC-3 cells under confocal microscopy and with flow cytometry (Fig. 3).

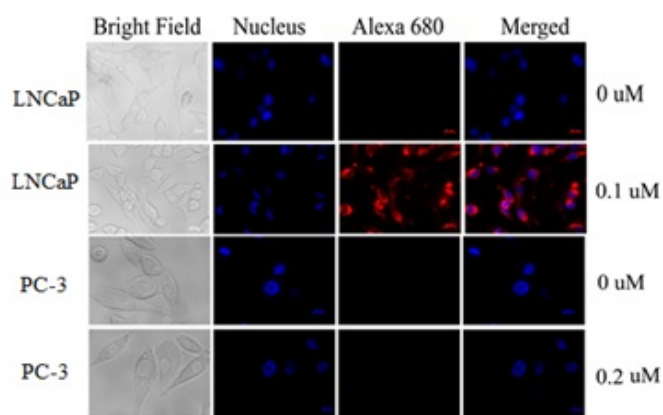


Figure 3: The scfbDb-mediated delivery of the toxin moiety to LNCaP cells, but not to PC-3 cells. The immunotoxin was labeled with dye AF680 and the cell nuclei were stained with DAPI.

The drug-delivery efficiency of scfbDb was also demonstrated with anti-tumor efficacy testing, showing that systemic administration of the scfbDb-based immunotoxin significantly inhibited the growth of LNCaP, but not the PC-3 tumor xenografts (refer to below). These results indicate that the engineered antibody fragments, especially the scfbDb, could serve as a springboard to develop PSMA-targeted imaging and therapeutic agents with high sensitivity and specificity against prostate cancer.

2. Development of a bivalent fold-back RIT for PSMA-targeted therapy

RITs refer to a group of protein-based therapeutics that are generated with recombinant DNA techniques by fusing one or more engineered scFv with a binding domain-deleted bacterial toxin fragment: the former allows the RITs to bind specifically to target cells, while the latter kills the cells upon cellular internalization. Development of RITs has been driven by their high specificity and extraordinary potency, and lack of drug resistance. Compared with mAbs and antibody-drug conjugates, RITs exhibit a better penetration capability because of smaller molecular size and a greater efficacy due to the enzymatic effect of the toxin moiety. The potency of RITs is estimated to be 7-10 orders of magnitude higher than that of traditional chemotherapeutics and one molecule RIT is sufficient to kill a cancer cell irrespective of cell cycle or cellular division.

Because of the higher binding affinity of scfbDb to PSMA, we generated a bivalent fold-back RIT, designated as A-dmDT390-scfbDb, by fusing the DT390 toxin moiety with the fold-back diabody. The diabody was placed in the DT390 C-terminus to minimize the influence on the DT390 activity. The A-dmDT390-scfbDb was produced with a DT-resistant *Pichia* expression system following the steps previously elucidated for producing other RITs. Purification was achieved following a four-step purification scheme: diafiltration, capture by hydrophobic chromatography, borate anion exchange chromatography, and anion exchange chromatography. The raw and purified yields were ~120 mg/L and ~90.8 mg/L, respectively, after a 163-hour induction period. By gel electrophoresis and Superdex 200 size-exclusion column analysis, the purified diabody and RIT exhibited a single band under non-reducing condition with the purity of estimated >95%. The size of A-dmDT390-scfbDb was estimated to be 97.1 kDa.

Confocal microscopy and flow cytometry demonstrated that the diabody efficiently mediated the entry of the truncated toxin to the cytosol of PSMA-positive LNCaP cells, but not to the PSMA-negative PC-3 cells (Fig. 4A and 4B). A-dmDT390-scfbDb exhibited a high cytotoxicity against LNCaP cells (IC_{50} , ~0.57 nM) after incubation for 48 h, but not against PC-3 cells even at concentration levels up to 100 nM (Fig. 4C). Flow cytometry and anti-annexin V immunostaining further revealed that A-dmDT390-scfbDb induced the cell cycle arrest and cell apoptosis in a dose-dependent manner.

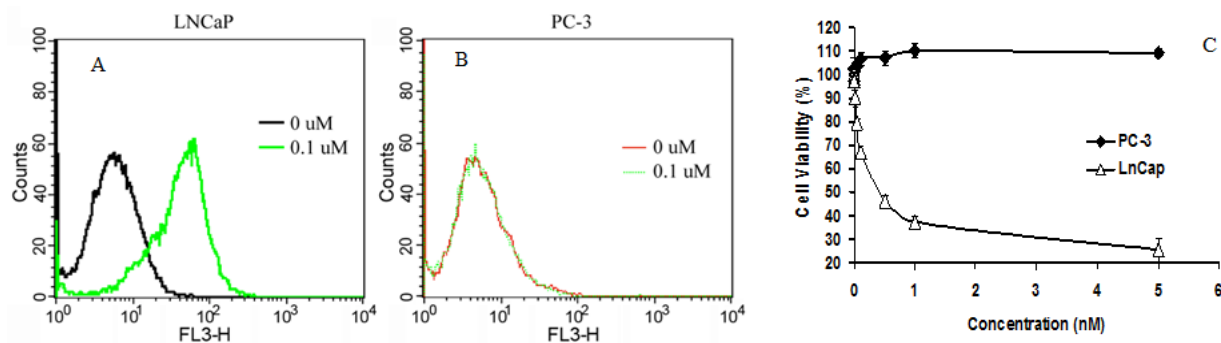


Figure 4: 4A and 4B demonstrate internalization and accumulation of the A-dmDT390-scfbDb in LNCaP cells (4A), but not in PC-3 cells (4B) with flow cytometry. 4C shows the extremely high cytotoxicity of the RIT to LNCaP cells but not to PC-3 cells with MTT assay.

We further tested the anti-tumor efficacy of the A-dmDT390-scfbDb in mice bearing LNCaP and PC-3 tumor xenografts. The RIT was given to mice intraperitoneally with a multiple dosing regimen of 200 μ g/kg, twice/day at a six-hour interval for six consecutive days. The growth of LNCaP xenografts was significantly inhibited but not the growth of PC-3 xenografts (Fig. 5). One month after treatment, the average weight of LNCaP xenografts was only 0.27 ± 0.09 g, which was significantly lower than the tumor weight in the control group (0.67 ± 0.11 g) ($P < 0.05$).

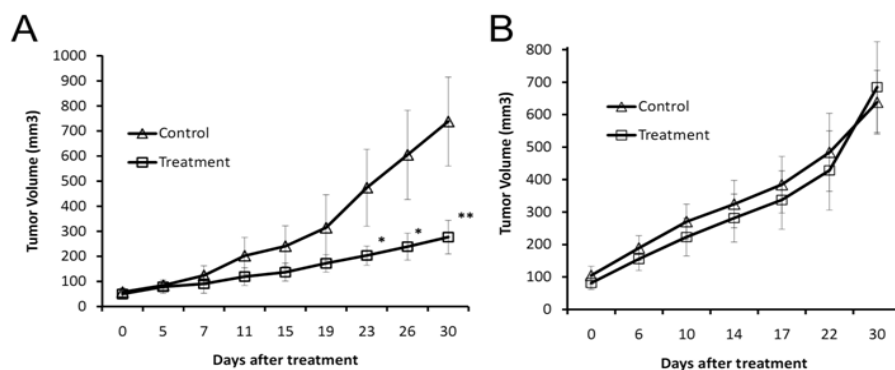


Figure 5: Growth inhibition of the A-dmDT390-scfbDb on LNCaP, but not on PC-3 tumor xenografts. A: LNCaP tumor volume vs. days; and B: PC-3 tumor volume vs. days after 30 days of treatment.

3. Development of a highly potent bivalent RIT for EGFR/EGFRvIII-targeted therapy

Taking advantage of the unique specificity and humanization-derived benefits of the mAb806, we generated a bivalent RIT, designated as DT390-BiscFv806, by fusing an engineered diphtheria toxin (DT) fragment (DT390) with the humanized mAb806-derived bivalent single-chain variable fragment (biscFv) via amino acid linkers. The full linear sequence of DT390-BiscFv806 was DT390-VL-(G4S)3-VH-(G4S)3-VL-(G4S)3-VH, which was confirmed by DNA sequencing.

The product was expressed with the DT-resistant *P. pastoris* system as described above. The purity of the final product was >95% as estimated under non-reducing condition, presenting a single band in the SDS-PAGE gel (Fig. 6A). The product shown in lane 1 of Fig. 6A was used for the present studies. Superdex 200 size-exclusion column analysis showed a major and a minor peak at the elution times of 28.323 min and 25.041 min, respectively (Fig. 6B). The major peak at 28.323 min represented the purified and the minor peak at 25.041 min might be the aggregated product. These results indicate that the final product of DT390-BiscFv806 was in a high purity with little aggregation.

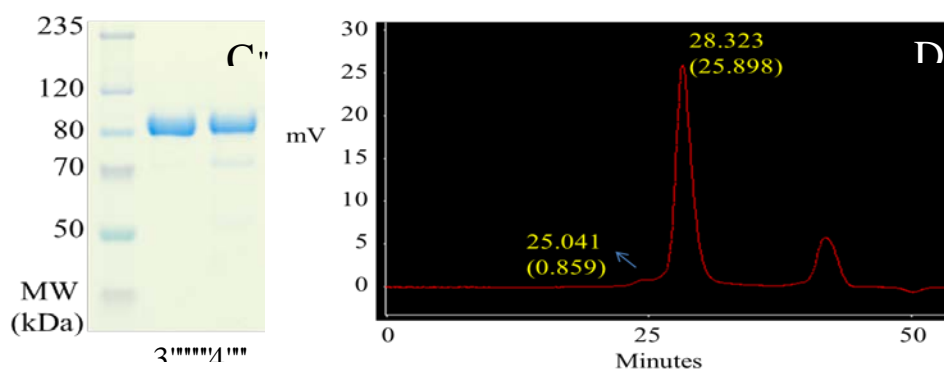


Figure 6: Characterization of the EGFR- and EGFRvIII-specific DT390-BiscFv806 with SDS-PAGE gel electrophoresis and HPLC analysis. The third peak appeared in the HPLC profile was used as a reference, which was confirmed to be due to the EDTA added in the sample buffer in our previous studies.

The cytotoxicity of DT390-BiscFv806 against the cultured cancer cells was determined after the cells were exposed to graded concentrations of DT390-BiscFv806. Fig. 7 shows the survival curves of different cancer cells plotted by the cell viability vs. the drug concentration, and the cell morphology

under different concentrations of DT390-BiscFv806. The IC₅₀ of DT390-BiscFv806 was measured to be 1.47 nM and 2.26 x 10⁻⁴ nM for U87 and U87-EGFRvIII cells, respectively. Notably, DT390-BiscFv806 had more than four orders of magnitude more potency against the U87-EGFRvIII cells than against the parental U87 cells. In morphology, cell death was obvious after exposure to DT390-BiscFv806.

We further analyzed the cytotoxicity of DT390-BiscFv806 against a group of six HNSCC cell lines. The cytotoxicity (IC₅₀) of DT390-BiscFv806 varied among the HNSCC cell lines with the highest against the JHU-13 (0.24 nM) and JHU-19 cells (0.89 nM), followed by JHU-29 (1.33 nM), JHU-6 (14.6 nM) and JHU-11 (21.7 nM), and the lowest against the JHU-22 cells (156 nM) (Fig. 7). To understand the EGFR expression status in the six HNSCC cell lines, we analyzed the presence of EGFRvIII using RT-PCR, the copy numbers of EGFR gene using real-time PCR, and the EGFR protein expression levels using Western blotting. In the analysis, U87-EGFRvIII cells were used as a positive control for the presence of EGFRvIII. Neither presence of EGFRvIII nor amplification of EGFR gene was detected in all of the six HNSCC cell lines (data not shown). Western blotting showed that the protein expression level of EGFR varied among the six cell lines with the highest in JHU-13 and the lowest in JHU-22 (Fig. 7). The cytotoxicity of DT390-BiscFv806 was consistent with the protein level of EGFR in HNSCC cell lines.

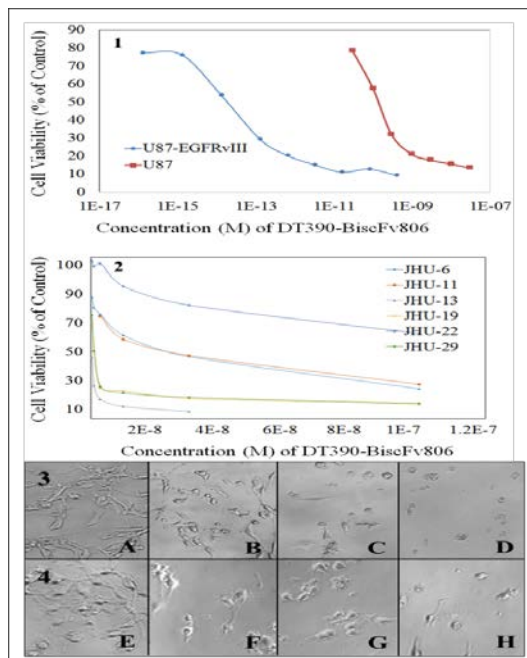


Figure 7: The high cytotoxicity of DT390-BiscFv806 against cancer cells. The panels 1 and 2 show the cell viability curves of glioblastoma cells and head and neck squamous cell carcinoma cells after exposure to graded concentrations of DT390-BiscFv806. The panels 3 and 4 show the representative morphology of the U87 (A to D) and U87-EGFRvIII (E to H) cells, respectively, following exposure of DT390-BiscFv806.

The anti-tumor efficacy of DT390-BiscFv806 was evaluated against the growth of established U87-EGFRvIII and U87 tumor xenografts. Because of the effect of enforced EGFRvIII expression, the growth patterns of U87 and U87-EGFRvIII tumor xenografts were significantly different. Therefore, different treatment regimens were designed to test the anti-tumor efficacy of DT390-BiscFv806 against the established U87 and U87-EGFRvIII tumor xenografts. Irrespective of the regimens, DT390-BiscFv806 significantly inhibited the growth of both U87-EGFRvIII and U87 tumor xenografts (Fig. 8).

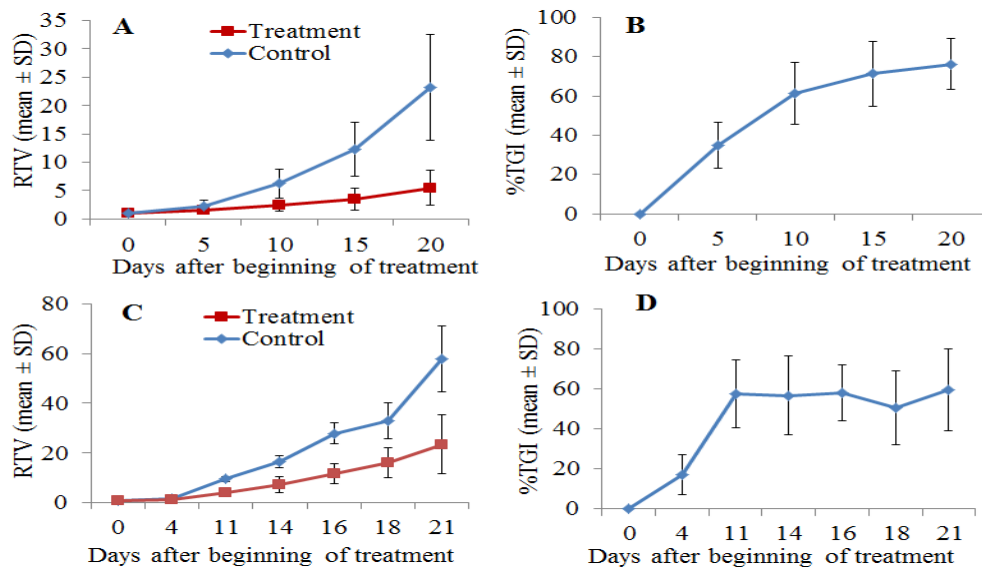


Figure 8: Growth inhibition of established tumor xenografts by DT390-BiscFv806.

Fig. 8A and 8B show the changes of mean RTV and %TGI for U77-EGFRvIII tumors after DT390-BiscFv806 administration. The RTV changes over the time were significantly different between the treatment and control groups ($n = 6$ mice/group). At the end point of experiment (day 18 after beginning of treatment), the RTV was 5.5 ± 3.0 vs. 23.1 ± 9.2 ; the tumor weight was 0.9 ± 0.6 g vs. 2.2 ± 0.9 g; and the tumor volume was 836.7 ± 555.7 mm³ vs. 2523.7 ± 1136.2 mm³ for the treatment vs. control groups (mean \pm SD, all $P < 0.05$). DT390-BiscFv806 led to a %TGI of 76.3% (ranging from 59.8%-96.2%) on the day 18, the last day after beginning of treatment. The cumulative %TGI increased over time, showing $34.7\% \pm 11.7$, $61.5\% \pm 15.9$, $71.3\% \pm 16.3$, and $76.3\% \pm 13.1$ on days 4, 10, 14, and 18, respectively (Fig. 8B).

Fig. 8C and 8D show the changes of mean RTV and %TGI over time for U87 tumors following DT390-BiscFv806 administration. Similarly, the RTV at each defined time point was also significantly different between the treatment and control groups ($n = 5$ mice/group). At the end point of experiment (day 21 after beginning of treatment), the RTV was 23.5 ± 11.8 vs. 57.9 ± 13.2 ($P < 0.05$) for the treatment vs. control groups and a %TGI of 59.4% (ranging from 31.5%-76.0%) was obtained. As shown in Fig. 8D, the cumulative %TGI was relatively stable from day 11 to day 21 after an initially rapid increase of tumor growth inhibition (day 4 to day 11) following treatment, showing $57.6\% \pm 17.1$, $56.7\% \pm 19.8$, $58.0\% \pm 13.9$, $50.6\% \pm 18.4$, and $59.4\% \pm 20.4$ on days 11, 14, 16, 18 and 21, respectively, which was different from that of the inhibitory growth of U87-EGFRvIII tumors; the latter showed an increased cumulative %TGI over time (Fig. 8B).

We comparatively analyzed the pathology between the RIT-treated and the control tumor xenografts. Under microscopy, both the RIT-treated and control tumors were composed of densely arranged tumor cells with heteromorphic and large nuclei. One striking change was the lower mitotic activity in the RIT-treated tumors than in the control tumors (Fig. 9). The mitotic figures were 5.23 ± 0.66 per HPF (400x) in the control group vs. 2.67 ± 0.86 per HPF in the RIT-treated group (two-tailed t-test, $P = 0.0002$) (Fig. 9B). Another striking change that was observed in all RIT-treated tumors was the presence of a large number of degenerative tumor cells. As shown in Fig. 9C and 9D, these degenerative cells had an empty cytoplasm and the outer boundary of nucleus with loss of the nuclear

details. These cells distributed throughout the entire tumors with more in the central region than in the peripheral region of tumors. These degenerative cells were rarely seen in the tumors of control group (Fig. 9E and 9F). The mechanism and significance for the presence of a large number of degenerative cells in the RIT-treated tumors remain to be studied.

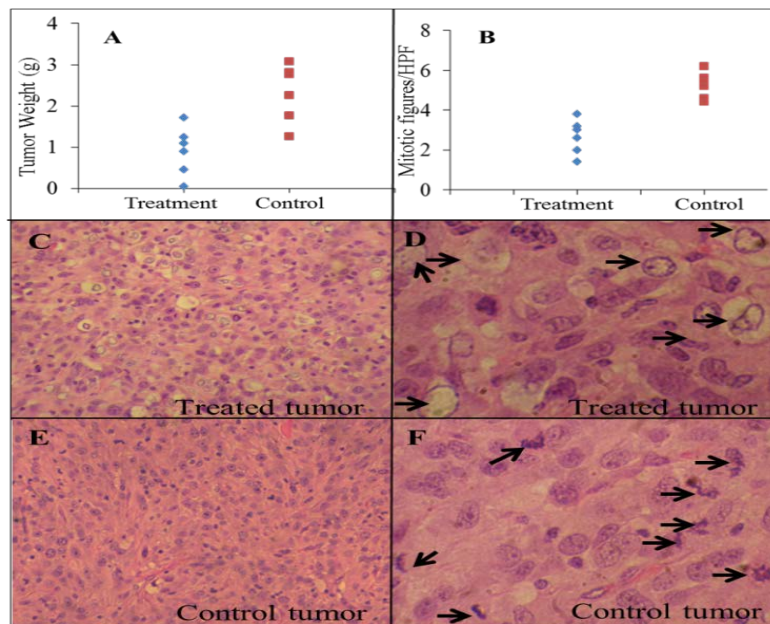


Figure 9: Comparative analysis between DT390-BiscFv806-treated U87-EGFRvIII tumors and control tumors.

Summary

In various types of human cancer, EGFR/EGFRvIII is overexpressed in cancer cells, while PSMA is specifically expressed in the tumor-associated blood vessels. EGFR/EGFRvIII and PSMA serve as an optimal target for anti-cancer and anti-angiogenic therapy, respectively. By taking advantage of the high specificity of mAb J591 against PSMA and mAb806 against EGFR/EGFRvIII, we designed and generated different formats of antibody fragments and further generated different bivalent RITs targeting PSMA and EGFR/EGFRvIII, respectively. In vitro, the antibody fragments showed high and specific binding affinity with the targets, while the RITs exhibited specific and potent cytotoxicity against cancer cells. System administration of the RITs significantly inhibited the growth of established tumor xenografts in mice. These results indicate that the engineered antibody fragments could serve as a springboard to develop targeted imaging and therapeutic agents, while the EGFR/EGFRvIII- and PSMA-targeted RITs are promising for therapy of various types of cancer by targeting tumors cells and targeting tumor blood vessels, respectively.

II.2. Broad Based Training Components

The Molecular Imaging Laboratory has experts who are dedicated in the development and application of physics and computer science for biological research. The laboratory serves as a ground for learning, training and professional development for graduate students, researchers and faculty members. The Molecular Imaging Lab offers regular biweekly group meetings, journal clubs, and

seminars. Some seminars have been arranged through webinars sponsored by imaging vendors, an opportunity for Howard University community to learn from experts from around the world. These sessions were followed by very productive and fruitful local discussions that engage participants in discussing the current status of research projects, analyzing any experimental issues of the current research, reviewing progress, and exchanging ideas, and have been the primary mode of interaction between Howard researchers and collaborating experts. Through participation in the Imaging Lab-sponsored seminars and workshops, and interaction with Imaging Core staff, a multidisciplinary imaging research community has continuously flourished and many fruitful exchanges of research ideas generated. Significant common synergies of interests have been identified, and much multidisciplinary research collaboration has developed. During the course of the funding period, the Imaging Lab has continued to provide didactic training for Howard researchers. The Imaging Lab has offered a series of NMR/MRI Lectures and Hands-on Training, and also has supported staff to attend a NIH FAES graduate nanomedicine course and a NIST workshop on standards for the advancement of optical medical imaging and special training on construction of microfluidic device

Dr. Yunkou Wu presented a MRI/PET mini course attended by 5 graduate and undergraduate students. Mr. Stephen Lin provided training for two Children's National Medical Center (CNMC) researchers including Dr. Jie Meng, a visiting scientist, in the operation of the IVIS Spectrum optical imaging system. The CNMC researchers were interested in using the optical imaging system to study a novel material for implants using fluorescent dye tracking. Dr. Meng used the optical imaging system to study fluorescently labeled targeted nanoparticles on tumor xenografts in mouse models.

Mr. Stephen Lin attended two training courses, "Paravision Operation & Applications Course" and "Paravision Programming Course", hosted by Bruker Biospin Inc., the manufacturer of our MRI machines. The "Paravision Operation and Applications" course is designed for user to learn software interface and it covers both low- and high-level imaging and spectroscopy techniques. The Paravision Programming course is dedicated to advanced users to develop experimental methods and covers both understanding low level spectrometer control and programming Paravision methods.

Last summer, Dr. Liang Shan mentored two graduate students (Ms. Christina Becco and Ms. Morgan Morrow) from the College of Dentistry. The students have learned the molecular biology skills and imaging techniques as well as how to design experiments and analyze experimental data.

This year, there were two new faculty members using the facility to conduct research in the nanomedicine field due to the establishment of the Nanomedicine Core through this funding support. In total, there were 14 faculty members from 7 departments and 14 scientists from the other institutions, including Children's National Medical Center, Johns Hopkins, Fu Jen University, and Angimmune, who used the core facility to conduct 28 research projects. Six postdoctoral fellows, 9 graduate students and 1 undergraduate student worked with principle investigators on various research projects. Two graduate students graduated this year and received PhD degrees. The faculty trainees and postdocs of the program have submitted grants to NIH, CDMRP, and NSF together with partnership leaders. We believe that trainees engaged in this training program have gained the interdisciplinary knowledge and skills they need to lead multidisciplinary research in the area of nanomedicine.

The seminars and workshops organized at Howard University, as well as at other institutions, during the entire project period are listed below:

Seminars and workshops

Year 1

1. Synthesis and Evaluation of Novel RGD peptide conjugates for Tumor Optical Imaging. Yunpeng Ye, PhD. September 29, 2010, Molecular Imaging Laboratory, Howard University Hospital Cancer Center.
2. Computational Biology & Bioinformatics, Biomedical Imaging and Proteomics. Drs. Paul C. Wang, William M. Southerland, Sergei Nekhai. RCMI. November 16, 2010, Howard University Symposium.
3. Imaging of Breast Cancer Metastasis Suppression by Naringenin. Fayun Zhang, PhD. December 17, 2010, Molecular Imaging Laboratory, Howard University Hospital Cancer Center.
4. Anti-PSMA bivalent single-chain Fv fold-back format immunotoxin for prostate cancer imaging and therapy. Fayun Zhang, PhD. January 14, 2011, Molecular Imaging Laboratory, Howard University Hospital Cancer Center.
5. Use of MRI/MRS to assess white matter development including injury, recovery, and maturation of white matter: DTI and Spectroscopy Analysis. Alexandru V. Korotcov, PhD. February 9, 2011. Molecular Imaging Laboratory, Howard University Hospital Cancer Center.
6. Formula for Grant Success. Anthony M. Coelho, Jr, PhD. February 22, 2011, Howard University Louis Stokes Library.
7. Integrin $\alpha\beta3$ -targeted Optical Imaging of Cancer by NIR Fluorescent cyclic RGD Peptides. Yunpeng Ye, PhD. March 29, 2011, Molecular Imaging Laboratory, Howard University Hospital Cancer Center.
8. Seminar: Synthesis of novel Quantum Dots for biomedical applications. Chung-Shieh Wu, Ph.D. May, 25, 2011, Howard University Hospital Cancer Center.
9. Manuscript Review. Thomas Heinbockel, PhD and Edward Cornwell III, MD. June 16, 2011, Howard University Blackburn Center.
10. Discovering Disease Mechanisms: Advancing Imaging in the Cell. Produced by the Science/AAAS and sponsored by PerkinElmer, June 28, 2011, webinar broadcasted in the Molecular Imaging Laboratory, Howard University Hospital Cancer Center.
11. New Signal-to-Noise Horizons in Preclinical and Molecular MRI – The MRI CryoProbe. Mat Brevard, PhD, Bruker BioSpin. June 28, 2011, Webinar broadcasted in the Molecular Imaging Laboratory, Howard University Hospital Cancer Center.
12. Super Resolution Microscopy: key tools and processes. Produced by BioOptics World. webcast and sponsored by Carl Zeiss Microimaging and Mad City Labs. July 13, 2011, broadcasted in the Molecular Imaging Laboratory, Howard University Hospital Cancer Center.
13. In Vivo Optical Imaging Probe Developments. Rajendra Singh, Ph.D, Director, Biology R&D, Caliper Life Sciences. July 21, 2011, Webinar broadcasted in the Molecular Imaging Laboratory, Howard University Hospital Cancer Center.
14. Introduction to Magnetic Resonance Imaging and Spectroscopy (theory and hands-on training). Alexandru V. Korotcov, PhD and Stephen Lin, M.Eng. July 25 - 26, 2011, Molecular Imaging Laboratory, Howard University Hospital Cancer Center.
15. Principles and Applications of Multiphoton Imaging. Drs. Simon C. Watkins, Tomasz Zal, and Janos Peti-Peterdi. Sponsored by Leica Microsystem. July 27, 2011, Webner broadcasted in the Molecular Imaging Laboratory, Howard University Hospital Cancer Center.
16. Light Scattering Technology: Theory and Applications Workshop. Physicochemical characterization of nanoparticles (theory and hands-on training). Stephen Kelly, Product Specialist, Malvern Instruments Inc. September 13, 2011, Howard University Hospital Cancer Center.

Seminars and workshops at John Hopkins University and other institutions

1. Combating Lung Cancer: Newer Targets and Delivery Systems. Mandip Singh Sachdeva, PhD. October 4, 2010, National Cancer Institute, Frederick, MD.
2. Molecular Imaging of the Tumor Microenvironment with PET and Bioluminescence Imaging. Carolyn Anderson, PhD November 10, 2010, Dept. of Radiology, John Hopkins University, Baltimore, MD.
3. Visualizing the Tumor Vasculature: Applications to Phenotyping, Systems Biology and Biomarkers. Arvind Pathak, PhD. March 16, 2011, Dept. of Radiology, John Hopkins University, Baltimore, MD.
4. Localized Hypoxia Results in Spatially Heterogeneous Metabolic Signatures in Breast Tumor Models. Lu Jiang, PhD. April 20, 2011, Dept. of Radiology, John Hopkins University, Baltimore, MD.
5. Multi-scale molecular imaging of the degradome in breast tumors. Kristine Glunde, PhD. May 4, 2011, Dept. of Radiology, John Hopkins University, Baltimore, MD.
6. 6th Annual Cancer Nanobiology Think Tank. Symposium. Organizers: Drs. Robert Blumenthal and Anu Puri. May 17, 2011, National Cancer Institute, Frederick, MD.
7. From Molecular Imaging to DCE-MRI: New Ideas and Developments. Dmitri Artemov, Ph.D. June 1, 2011, Dept. of Radiology, John Hopkins University, Baltimore, MD.
8. Translational MRI and MRS Methods to Study the Tumor and its Environment. Harish Poptani, PhD. August 31, 2011, Dept. of Radiology, John Hopkins University, Baltimore, MD.

Year 2

1. Writing for Biomedical Publication. Chris Papasian, Ph.D., September 26, 2011, Howard University Health Science Research Development Symposium.
2. Neurospectroscopy: the past, present, and future. Oluseyi Awodele, 3rd year medical student. October 4, 2011, Radiology Department, Howard University Hospital.
3. An Introduction to Flow Cytometry. Ina Schulte, Ph.D., Abcam Scientific, October 11, 2011, webinar broadcasted in the Molecular Imaging Laboratory, Howard University Hospital Cancer Center.
4. Mechanism and uses of a membrane peptide that target tumors and other acidic tissues in vivo. Chung-Shieh Wu, Ph.D., November 3, 2011, Howard University Hospital Cancer Center.
5. The Road to Research Advancement. Thomas A. Mellman, M.D., November 17, 2011, Howard University College of Medicine.
6. Determining the Impact of New Therapeutic Approaches: Advancing Imaging in Animals. Matthias Nahrendorf, M.D., Ph.D. and Patrick McConville, Ph.D. sponsored by PerkinElmer, December 7, 2011, webinar broadcasted in the Molecular Imaging Laboratory, Howard University Hospital Cancer Center.
7. Not Networking 101—Building Relationships for Success. Nick Oswald, Ph.D., December 14, 2011, webinar broadcasted in the Molecular Imaging Laboratory, Howard University Hospital Cancer Center.
8. Targeting Tumor Acidity. Yana Reshetnyak, Ph.D., January 24, 2012, Howard University Hospital Cancer Center.
9. Key Secrets of Spectroscopy for Life Sciences. Robert R. Alfano, Ph.D. and Stavros Demos, Ph.D. sponsored by BioOptics World, January 31, 2012, webinar broadcasted in the Molecular Imaging Laboratory, Howard University Hospital Cancer Center.
10. Computational Biology & Bioinformatics, Biomedical Imaging and Proteomics. Drs. Paul C. Wang, William M. Southerland, Sergei Nekhai, Core Laboratories RCMI workshop, January 31 & February 1, 2012, Howard University.
11. Two-photon microscopy: How, why and what. John M. Girkin, Ph.D. sponsored by BioOptics World,

February 7, 2012, webinar broadcasted in the Molecular Imaging Laboratory, Howard University Hospital Cancer Center.

12. A Ligand-Centric Approach for Function Prediction. Sona Vasudevan, Ph.D., March 8, 2012, Howard University College of Medicine.
13. Beyond the Diffraction Limit: Advances and Applications of Super-Resolution Imaging. Joerg Bewersdorf, Ph.D., Catherine Galbraith, Ph.D. & Markus Sauer, Ph.D. sponsored by Leica Microsystem, March 28, 2012, webinar broadcasted in the Molecular Imaging Laboratory, Howard University Hospital Cancer Center.
14. The Future of Molecular Imaging, Sam Gambhir, M.D., Ph.D. sponsored by VisualSonics, May 23, 2012, webinar broadcasted in the Molecular Imaging Laboratory, Howard University Hospital Cancer Center.
15. In vivo 3D fluorescence imaging. Brad Rice, Ph.D. sponsored by PerkinElmer, May 31, 2012, webinar broadcasted in the Molecular Imaging Laboratory, Howard University Hospital Cancer Center.
16. Assessment of MRI And FT-IR Studies of Cartilage Degradation Through Multivariate Analysis. Ping-Chang Lin, Ph.D., June 1, 2012, Howard University Hospital Cancer Center.
17. Optical Sectioning using Light Sheet Microscopy: In Vivo Imaging with Astounding Resolution. Ernst H. K. Stelzer, Ph.D., Pavel Tomancak, Ph.D. & Lars Hufnagel, Ph.D. sponsored by Science/AAAS, June 14, 2012, webinar broadcasted in the Molecular Imaging Laboratory, Howard University Hospital Cancer Center.
18. Nanoliposomes: Preparation and Analysis. Alexandru Korotcov, Ph.D., August 1, 2012, Molecular Imaging Laboratory, Howard University Hospital Cancer Center.
19. Quantification of In Vivo Imaging Pre-Clinical Models Using the ICON™ Compact, High-Performance MRI System. Mat Brevard, Ph.D & Tonya Coulthard, Ph.D. sponsored Bruker Biospin and Aspect Imaging, August 22, 2012, webinar broadcasted in the Molecular Imaging Laboratory, Howard University Hospital Cancer Center.

Seminars and workshops at John Hopkins University and other institutes

1. Imaging Metabolic Signatures of Cancer-Induced Cachexia. Marie-France Penet, Ph.D., October 5, 2011, Dept. of Radiology, John Hopkins University, Baltimore, MD.
2. Diffusion Weighted MRI - Where Are We in the Clinic? Nandita deSouza, M.D., Ph.D., October 14, 2011, Dept. of Radiology, John Hopkins University, Baltimore, MD.
3. Lipid-based Nanoparticles and Triggered Chemotherapy. Robert Blumenthal, Ph.D., November 8, 2011, National Institutes of Health, Bethesda, MD.
4. Molecular Cancer Imaging: New Optical Diagnostic Technologies and Beyond. Hisataka Kobayashi, M.D. Ph.D., February 15, 2012, Dept. of Radiology, John Hopkins University, Baltimore, MD.
5. Trials on Systemic Delivery of Cancer Therapeutics via Targeted Nanoparticles. Esther H. Chang, Ph.D., February 21, 2012, National Institutes of Health, Bethesda, MD.
6. Quantification of Tumor Vasculature Heterogeneity by DCE-MRI. Wenlian Zhu, Ph.D., February 29, 2012, Dept. of Radiology, John Hopkins University, Baltimore, MD.
7. Quantum Dots and Single Molecule Detection Enable Highly Sensitive Screening of Genetic Cancer Biomarkers. Jeff T.H. Wang, Ph.D., April 17, 2012, National Institutes of Health, Bethesda, MD.
8. Two-component Nanodelivery for Enhanced Internalization of Theranostics; Click Therapy on Her2/neu Overexpressing Breast Cancer. Sudath Hapuarachchige, Ph.D., May 2, 2012, Dept. of Radiology, John Hopkins University, Baltimore, MD.
9. Controllable Self-Assembly of Inorganic Nanocrystals for Biological Applications. Zhihong Nie, Ph.D., May 15, 2012, National Institutes of Health, Bethesda, MD.

10. Cutting-Edge Imaging Technologies and Strategies in Preclinical Small Animal Research. Carestream Molecular Imaging workshop. May 30, 2012, Hyatt Regency Bethesda, MD.

Year 3

1. Osteopontin Genotype as a Determinant of Muscle Remodeling: A Study of African American Young Adult Volunteers. Whitney Barfield, September 28, 2012
2. Nanoliposome: Preparation and Physical Properties Characterization. Alexandru Korotcov, October 12, 2012.
3. Workshop: Bruker 9.4 T MRI machine operation, October 16-17, 2012
4. MRI Dynamic Contrast Enhancement and Liposome, Alexandru Korotcov, December 18, 2012.
5. University Imaging Core Facility. Paul C. Wang, Ph.D., February 8, 2013, Joint Seminar with Children's National Medical Center.
6. Renal Oxygenation Levels Are Decreased in Peroxisome Proliferator Activated Receptor – α Knockout Mice during Angiotensin II Hypertension. Darah Wright (PhD student), April 1, 2013, Howard University Research Day.
7. Renal Oxygenation Levels Are Decreased in Peroxisome Proliferator Activated Receptor – α Knockout Mice during Angiotensin II Hypertension. Dexter Lee, Ph.D., April 3, 2013, Johnson Distinguished Lecture, Howard University.
8. Advantages of Multiple Modalities, Image Fusion and Data Analysis in Preclinical Small Animal Imaging. Sponsored by Bruker Corporation, May 20, 2013.
9. Applications of Nanotechnology in Medical Imaging and Targeted Drug Delivery. July 2, 2013, Fu Jen Catholic University/Catholic University of America Summer Program.
10. Discovering possible things that can be done and gaining background knowledge on bioinformatics. Joseph Arul, Ph. D., August 23, 2013.
11. An Anti-PSMA Bivalent Immunotoxin Exhibits Specificity and Efficacy for Prostate Cancer Imaging and Therapy. Fayun Zhang, Ph. D. September 8, 2013.
12. RCMI RTRN Webinar Research Resources Spotlight Series: Molecular Imaging Laboratory – Imaging Core facility. Paul Wang, PhD, September 26, 2013.

Year 4

1. RTRN Research Resources Spotlight Webinar Series - Howard University Imaging Core Facility: Molecular Imaging Laboratory. Paul Wang, September 26, 2013
2. Molecular Fluorescent Imaging Guided Cancer Resection – From Bench to Bedside. Sammel Achlefu, Johns Hopkins/Radiology, October 9, 2014
3. Measuring Renal Oxygenation in a Mouse Model of Volume-Dependent Hypertension using BOLD MRI. Darah Wright, November 20, 2013
4. Utilizing Multispectral Optoacoustic Tomography (MOST) for Imaging and Assessment of Tumor Growth, Angiogenesis and Therapeutic Intervention (webinar). Neal Burton, January 28, 2014
5. Understanding Underlying Mechanism of ICP-OES and ICP-MS (Thermo Scientific webinar). Anneorie Bogerts, January 29, 2014
6. Maglib Quantification by MRI. Zhenjiang Zhang, February 28, 2014
7. Glioblastoma Multiform – Building the Gap Diagnosis and Treatment (Bruker Biospin Corp webinar), March 18, 2014
8. Nanomedicine. NIH FAES Graduate course, weekly classes, March 24 – May 25, 2014
9. Targeting Vasculature in Inflammatory Bowel Disease (VisualSonics webinar), March 27, 2014
10. Multifunctional Nanoparticles: Applications in Cancer Therapy and Diagnostics. Mohammed

Shukoor, May 19, 2014

11. PMSA-Based Imaging and Therapy. Ying Chen, Johns Hopkins/Radiology, May 28, 2014
12. Water Exchange – Key Parameter for MRI Contrast Agent Design. Yunkou Wu, June 23, 2014
13. ICP-MS Techniques in Nanoparticle Analysis: Fundamentals, Challenges, and Prospectives (Spectroscopy Magazine webinar), Jorg Bettmer, June 25, 2014
14. Basic NMR Theory, PC Lin, July 23, 2014
15. Chemical Shifts and Coupling Constants, PC Lin, July 25, 2014
16. NMR Instrumentation, PC Lin, July 28, 2014
17. NMR Data Acquisition and Processing, PC Lin, July 31, 2014
18. NMR Dynamics, PC Lin, August 4, 2014
19. NMR Lab – Practice, Stephen Lin, August 7, 2014
20. Fourier Transform and MR Imaging Principles, PC Lin, August 11
21. Post-Imaging Processing Practice, PC Lin, August 14, 2014
22. MRI Imaging Lab Practice (I), P Wang, August 21, 2014
23. Advanced Imaging Techniques, P Wang, August 25, 2014
24. MRI Imaging Practice (II), P Wang, August 28, 2014
25. NIST Workshop on Standards for the Advancement of Optical Medical Imaging. NIST, Gaithersburg, August 26-26, 2014.

Year 5

1. Shan L, Lin S, Wang PC. Engineered Antibody Fragments for PSMA-targeted Imaging and Therapy of Prostate Cancer. World Molecular Imaging Conference 2015, Honolulu, HI, September 2-5, 2015.
2. Lin S, Zhang ZJ, Wang PC. Fabrication of a Microfluidic Device for Generating Liposomal Nanoparticles as Drug Delivery Vehicle. ChinaNANO 2015, Beijing, China, September 3-5, 2015.
3. Wang PC. Fabrication Microfluidic Device for Generating Liposome, Recombinant Immunotoxins (RITs) for Cancer Therapy, paraCEST MRI Agent for In Vivo pH Imaging. National Center for Nanoscience and Technology, Beijing, China, September 16, 2015
4. Wang PC. Introduction of Howard University Molecular Imaging Lab – Applications of Nanotechnology in Medical Imaging and Targeted Drug Delivery. Catholic University of America, Washington, DC, October 28, 2015.

II.3. Nanomedicine Core

It is essential for Howard University to establish a basic infrastructure that is capable of supporting a sustainable long-term research program in the field of molecular imaging of breast cancer and nanomedicine. In continuing to improve its infrastructure, the University Imaging Core has obtained a NIH Supplement grant, which has been used to pay for installation and moving costs associated with replacing an aging 4.7T MRI machine with a newer 7T MRI machine. In order to seek support beyond the current grant, the University Imaging Core, together with Computational Biology and Bioinformatics Core, and Proteomics Core, has applied for and received new funding from the NIH/RCMI (Research Centers for Minority Institutions) program. The Nanomedicine Core is part of the University Imaging Core facility. This funding will support a major portion of the operation costs and staff salary for the Imaging Core for the next 5 years. The Imaging Core's 4.7T system has aged to 26 years old and reached the end of its support lifecycle and was decommissioned in the fall of 2013. This year, the 4.7T system was replaced successfully with a Bruker 7T MRI machine from Children's National Medical Center. The Bruker 7T MRI machine has an AVIII console, PV5.1 software, and a Magnex 20 cm bore shielded magnet, which can accommodate animals bigger than a mouse. As of November 2015, the transfer of the

Bruker 7T MRI machine was a complete success. The magnet and electronic console have been installed in the Molecular Imaging Laboratory at Howard University. The machine's imaging function has been tested and yielded a high resolution with high contrast MR images. The Imaging Core is now capable to offer state-of-the-art MRI imaging for large animals using this new 7T MRI.

Howard University Health Sciences has implemented a Research Strategy Plan that sets the direction of the university biomedical research with emphasis on health disparities research. This plan embraces new research disciplines such as proteomics, computational biology, nanomedicine and genomics. The University's Research Strategy Plan and its commitment to nanomedicine research are fulfilled in the nearing completion of the construction of the new Interdisciplinary Research Building. A space for Nano biomedical imaging research has been designated. The lab space is for nanomaterial fabrication with ultrastructure imaging and analytical instrument for physicochemical characterization of nanoparticles, molecular biology labs with incubators and hoods for cell culture and flow cytometry, and imaging suites for confocal microscope. The University has also budgeted funds for purchasing a PET/SPECT/CT machine for small animal imaging research. These new lab space and facilities will further enhance nanomedicine and breast cancer research capabilities at Howard University.

While maintaining state-of-the-art infrastructure is critical to providing researchers with tools to perform the proposed researched projects, it is equally important to provide a broader research training experience for faculty and students. The Nanomedicine Core continues to offer training opportunities through seminar series, instrumentation workshops, and didactic lectures. The Nanomedicine Core staff has helped researchers in experimental design, conducting imaging experiments, and analyzing data. In the 5th year of this training program, we continued to expand the user base of the Nanomedicine Core to pursue multidisciplinary biomedical research. There are 28 research projects that have been supported by the Nanomedicine Core, including projects in the initial phase of research. A list of all the supported projects is listed in the Appendix.

II.4. Statement of Work Summary

The accomplishments aligned with the Statement-of-Work occurred in this reporting period is listed as following:

Research Component

- Task 1. To conduct Research Project 1 "Study the physicochemical characteristics of nanoparticles as MR contrast agent delivery system with the dynamic contrast enhancement pattern for clinical applications" (months 1-48).
- a. Purchase supplies for cell culture and materials for nanoparticles (months 1-2) (completed).
 - b. Construct liposome (Lip) nanoparticles with transferrin (Tf) as the ligand and encapsulated Gd-based MRI contrast agent (CA) inside as payload (months 3-9) (completed).
 - c. Characterize the physicochemical properties of nanoparticles, including size distribution, surface charge, encapsulation efficiency, and Tf linkage on the surface. Some of the measurements will be done at NCL, NCI-Frederick (months 6-12) (completed).
 - d. Study targeting efficiency of the liposome nanoparticle using MDA-MB-231 cells. Study the interactions of nanoparticles with breast cancer cells (months 13-24) (completed).

- e. Study the correlation of the dynamic contrast enhancement (DCE) pattern with the distribution of Tf-liposome nanoparticles in tumor xenografts. Both MR and optical imaging will be used (30 mice) (months 25-36) (completed).
 - f. Evaluate the potential clinical applications of the DCE pattern, focusing on the relationship between the DCE pattern and the tumor features of TfR expression level, permeability of neovasculatures, vascular density, tumor growth and necrosis (months 25-40) (completed).
 - g. Data analysis and preparation of manuscripts for publication (months 40-48) (completed).
- Task 2. To conduct Research Project 2 “Develop multifunctional nanoparticles for breast cancer diagnosis and treatment – using anti-VEGFR-2 immunotoxin as dual purpose ligand and chemotherapeutics as encapsulated payload” (months 1-48).
- a. Purchase supplies and prepare for the study (months 1-2) (completed).
 - b. Define the efficacy of the anti-murine anti-VEGFR-2 immunotoxin in endothelial cell killing and vascular permeability increase in animal models (months 3-18) (completed).
 - c. Construct and characterize the targeted anti-VEGFR-2 immunotoxin multifunctional nanoparticles. Some of the work will be done at NCL (months 13-18) (completed).
 - d. Determine the biodistribution, pharmacokinetics and toxicity of the nanoparticles in healthy mice (8) and mice bearing with tumor xenografts (22). Optical imaging will be used. Measurements of biodistribution will be done at NCL and HNF (months 19-40) (completed).
 - e. Define the synergistic effects of the targeted delivery, anti-angiogenics and chemotherapeutics in breast cancer animal models. Histological staining will be used to study the tumor vasculature (months 25-40) (completed).
 - f. Data analysis and preparation of manuscripts for publication (months 40-48) (completed).
- Task 3. Research concept development and submission of competitive grants in breast cancer targeted imaging and therapy (months 37-48) (completed).

Broad Training Component

- Task 4. Provide opportunities to the faculty trainees in Howard University to update knowledge of nanomedicine (months 1-48) (completed).
- a. Biweekly group meetings at the Molecular Imaging Lab (months 1-48) (completed).
 - b. Monthly Seminar series at Howard University Cancer Center to be presented by the mentors and invited speakers (months 1-48) (completed).
 - c. Johns Hopkins University ICMIC Seminar Series organized by Dr. Bhujwalla (months 1-48) (completed).
 - d. To attend the biweekly Nanobiology Program Seminar Series at NCI-Frederick organized by Dr. Blumenthal (months 1-48) (completed).
 - e. Annual scientific meetings with mentors and trainees (completed).
- Task 5. Train Howard faculty in advanced nanomedicine lab techniques (completed).
- a. Laboratory internships at the Johns Hopkins University and NCL, topics include molecular imaging and nano characterization techniques, 2-4 days each (months 1-36) (completed).
 - b. Workshop series. Topics include MR and optical imaging, SEM/TEM/AFM, optical

instrumentation, drug design and liposome (months 1-48) (completed).

Task 6. Administrative and communication affairs (coordinated by Drs. Wang and Bhujwalla) (Months 1-48) (completed).

- a. Status reports (quarterly and annual reports) (completed).
- b. Research progress review (quarterly) (completed).
- c. Administrative meetings (biannually meetings) (completed).
- d. Coordination of seminars, workshops, and laboratory internships (completed).

III. KEY RESEARCH ACCOMPLISHMENTS

Year 1

- Liposome nanoparticles of variable sizes were constructed. The liposomes were linked with transferrin as breast cancer cell targeting moiety on the surface. A Gd based MR contrast agent, Magnevist, was encapsulated inside the liposome for *in vitro* and *in vivo* imaging studies.
- The physicochemical properties of liposomal nanoparticles including size distribution, surface charges were characterized. The transferrin binding was confirmed by changes of particle size before and after conjugation.
- Transferrin protein nanospheres, silicon coated, doped rare earth oxide and rhodamine B isothiocyanate were constructed for enhancing MRI, CT and US contrast to provide both high resolution and high sensitivity of imaging at anatomical, functional and molecular level.
- To study the potential toxicity of nanoparticles, QDs coated with TOPO were constructed for breast cancer diagnosis. We have shown this commonly used TOPO coating is not stable under physiological conditions. It causes release of toxic cadmium ions in the body. For improvement, we have used a novel triblock copolymer for coating to reduce the potential toxicity of QDs.
- A fold-back of two single chain Fv fragments of anti-PSMA monoclonal antibody with diphtheria toxin (A-dmDT(390)-scfbDb(PSMA) has demonstrated the specific targeting and therapeutic efficacy towards PSMA positive LNCaP cells and solid tumor xenografts in mice.
- Bacterial magnetosomes synthesized by magnetotactic bacteria have recently been demonstrated as superior targeting nanoscale carriers for delivering antibodies, enzymes, nucleic acids, and chemotherapeutic drugs. We did a thorough literature review of the loading methods, strategies, and potential applications of the bacterial magnetosome as drug carrier.

Year 2

- Established a new, improved method of making well-controlled liposomes using a temperature controlled sonication followed by Tf covalent conjugation.
- The MDA-MB-231-luc cellular uptake of Tf-conjugated probe in vitro is more efficient compare with the uptake of dye or non-targeted liposomes. The uptake of Tf, Lip-CA, and Tf-Lip-CA was 1.8, 7.0 and 16 folds higher compared with untreated controls
- Studied the toxicity of nanoparticles using a NMR spectroscopy method to monitor the nanoparticles' stability. TOPO was shown to be cleaved from nanoparticles in the presence of a nucleophilic agent such as thiol, which is widely distributed in tissue and physiological fluids, degrading the nanoparticles in physiological systems and increasing risks of nanotoxicity.
- Investigated the delivery efficiency of tumor-seeking fluorescent nanoparticles by attaching more than one targeting moiety. Both cyp-GlcN and cyp-2GlcN NIRF probes exhibited good tumor-targeting properties in cancer cell cultures and live mice, but the cyp-2GlcN probe, with two targeting moieties, showed the highest uptake (almost double uptake) with good retention characteristics in vivo.
- Improved the efficacy of tumor-targeted delivery of liposomal nanoparticles with a pH-sensitive peptide. The pH-sensitive nanoprobe demonstrated good tumor-targeting properties in breast cancer xenografts in vivo and can be used for targeted drug delivery, detecting small tumors, performing diagnostic imaging, and treating acidic disease tissue.
- Optical imaging and MRI with the Alexa Fluor 680 labeled bivalent immunotoxin with a truncated diphtheria toxin [A-dmDT390-scfbDb(PSMA)] showed the specific targeting and

therapeutic efficacy of this immunotoxin towards solid tumor xenografts in athymic nude mice.

- Gadolinium metallofullerene nanoparticle has shown an antimetastatic effect in tumor bearing mouse model. The gadolinium metallofullerene nanoparticles inhibited the production of matrix metalloproteinase enzymes and further interfered with the invasiveness of cancer cells, thus showing an antimetastatic activity.

Year 3

- We have shown that the targeted nanocomplex, Tf-Lip-Mag significantly enhanced the MRI signals in MDA-MB-231 breast cancer xenograft tumors in mice. The image enhancement was superior to that obtained using the contrast agent alone. This superior enhancement capability of the nanocomplex can be used to increase the sensitivity of detecting small tumors.
- The tumor MRI dynamic contrast enhancement patterns are well correlated with histology, and could be used to evaluate tumor pathology in vivo and provide very useful timely information for patient's prognosis and response to treatment.
- Reviewed literature pertaining to the development, characterization and applications of nanoparticles in cancer imaging and therapy. Published one book chapter and two review articles.
- Analyzed the effect of single-walled carbon nanotubes (SWCNTs) on mitochondrial functions, including mitochondrial membrane potential, mitochondrial oxygen uptake and cytochrome c. We found that the mitochondrial membrane potential and oxygen uptake were greatly decreased and was accompanied by reduction of the cytochrome c.
- Studied the effect of the surface charge of nanoparticle on its cell penetration capability. We found that the negatively charged Au nanorod can penetrate deeper into the tumor spheroids and achieve a more significant thermal therapeutic benefit than positively charged Au nanorod.
- Generated a bivalent single-chain variable fragment (scFv) recombinant immunotoxin, AdmDT390-scFvDb(PSMA) utilizing the high specificity of the J591 antibody against the extracellular domain of PSMA.
- Characterized the novel immunotoxin A-dmDT390-scFvDb(PSMA) with PSMA-expressing and absent prostate cancer cells, and further established its anti-tumor efficacy in animal models. Our results suggested that this novel immunotoxin is a promising candidate for anti-cancer therapy, especially for cancers that overexpress PSMA, including breast cancer.
- Designed and initiated a new project to determine the antiangiogenic efficacy of the A-dmDT390-scFvDb(PSMA).

Year 4

- Constructed liposomes ranging in size from 50 to 170 nm using thin film hydration with polycarbonate membrane filters. The liposome size relative standard deviation was 20-30%.
- Implemented a new NMR method that utilizes a distinguished compartmental model to measure chemical exchange kinetics in a complex in vivo solid tumor environment.
- Generated a humanized bivalent scFv-derived, DT390-based recombinant immunotoxin, DT390-BiscFv806, capitalizing the unique specificity of antibody mAb806 against EGFR and EGFRvIII overexpressed in cancer but not the EGFR in normal tissue.
- Demonstrated that our novel recombinant immunotoxin DT390-BiscFv806 exhibited high cytotoxicity and anti-tumor efficacy against the cancer cells either with EGFR expression alone or with EGFR and EGFRvIII co-expression, indicating that DT390-BiscFv806 is highly promising for

treatment of cancers arising from the brain, head and neck, lung, breast, and prostate.

- Construct three formats of J591 antibody fragments: single-chain variable fragment (scFv), bivalent tandem scFv (biscFv), and bivalent scFv diabody (scFvDb) in fold-back structure for cancer imaging.
- Demonstrated that the fold-back structure of scFvDb has an increased efficiency of target binding and toxin delivery to target cells, compared with other formats.
- Designed a simple and highly sensitive sensing nanosystem for the detection of Hg²⁺ and Cu²⁺ based on fluorescence quenching of ultrasmall DNA–Ag NCs.
- Constructed small gold nanoparticles to study size-dependent penetration ability and the potential applications of for intranucleus delivery.
- Found that gold nanoparticles smaller than 10 nm can enter the nucleus, whereas larger ones (10 - 16 nm) can only be found in the cytoplasm.
- Reviewed the evolution of immunotoxin development, the challenges of immunotoxin therapy for human solid tumors, and the potential strategies to overcome these challenges in literature.
- Reviewed literature pertaining to the development, characterization and applications of nanoparticles in cancer imaging and therapy.
- Reviewed literature pertaining to mechanisms of membrane trafficking in drug-resistant cancer cells and the development of nanoparticles as drug delivery platforms to overcome drug resistance. Published a review article.

Year 5

- Acquired technical support from NIST to aid in improving the technique to construct liposomes with a narrow size distribution.
- Generated liposomes with a narrow size distribution similar to those created with the mini-extruder.
- The microfluidic device provided control of the flow ratios of the lipid and aqueous buffer, which significantly advanced the size distribution.
- Liposomes when added to either a buffer solution or a lipid tincture can be used as a transport vehicle for imaging contrast agents or therapeutic agents.
- The Imaging Core underwent significant infrastructure upgrade through the acquisition of a new magnet. The 7T MRI has been transferred to and the magnet and electronic console have been successfully installed in the Imaging Core. Importantly, the imaging function of this new MRI machine has been tested and high-quality images have been obtained successfully. With this new MRI machine, the Imaging core has regained its capability to offer state-of-the-art MRI imaging service for large animals.

IV. REPORTABLE OUTCOMES

Year 1

Publications

1. Wang TX, Sridhar R, Korotcov A, Ting AH, Francis K, Mitchell J, Wang PC. Synthesis of amphiphilic triblock copolymers as multidentate ligands for biocompatible coating of quantum dots. *Colloid and Surfaces A: Physicochem. Eng. Aspects*, 375(1-3)147-155, 2011.
2. McDonald MA, Wang PC, Siegel EL. Protein Nanospheres: Synergistic Nanoplatfrom-Based Probes for Multimodality Imaging. *Proc. of SPIE Vol. 7910*, 79101G1-14, 2011.
3. Sun JB, Li Y, Liang XJ, Wang PC. Bacterial Magnetosome: A Novel Biogenetic Magnetic Targeted Drug Carrier with Potential Multifunctions. *Journal of Nanomaterials*. Vol 2011, Article ID 469031. doi:10.1155/2011/469031.

Presentations

1. Korotcov AV, Ye Y, Chen Y, Zhang F, Huang S, Sridhar R, Achilefu S, Wang PC. Tumor Optical Imaging of Glucosamine Linked Fluorescent Probes in Mice. RCMI 12th International Symposium on Health Disparities, Nashville, TN, December 6-9, 2010.
2. Korotcov AV, Wang T, Chen Y, Sridhar R, Mitchell J, Wang PC. 31P NMR Study of the Interaction of TOPO-QDs with Mercaptoethanol. RCMI 12th International Symposium on Health Disparities. Nashville, TN, December 6-9, 2010.
3. Ye YP, Zhu L, Xu B, Wang PC, Achilefu S, Chen XY. Integrin targeting and tumor imaging: comparison of two RGD peptides. RCMI 12th International Symposium on Health Disparities, Nashville, TN, December 6-9, 2010.
4. Korotcov AV, Wang T, Chen Y, Sridhar R, Mitchell J, Wang PC. 31P NMR Study of Thiol Mediated Degradation of TOPO-Quantum Dots. Howard University College of Medicine Research Day 2010, Howard University, Washington, DC, April 15 2011.
5. Wang PC, Wang TX, Korotcov AV, Chen Y, Sridhar R, Mitchell JW. Monitoring Thiol-Mediated Degradation of TOPO-Quantum Dots by 31P Nuclear Magnetic Resonance Spectroscopy. *Proceedings of Era of Hope 2011*, Orlando, FL, August 2-5, 2011.
6. Wang PC, Liang XJ. Applications of Nanoparticles for In Vivo Imaging. *International Conference on Nanoscience & Technology, ChinaNANO 2011*, Beijing, China, September 7-9, 2011.
7. Korotcov AV, Wang TX, Chen Y, Sridhar R, Mitchell J, Wang PC. Study of TOPO-Quantum Dot Degradation by 31P NMR. *2011 World Molecular Imaging Congress*, San Diego, CA, September 7-10, 2011.

Grants

1. NIH M01RR010284-15 GHUCCTS 04/01/2011-03/31/2013 Verbalis J (Program PI), Mellman T (co-PI) Osteopontin Genotype As A Determinant Of Muscle Remodeling: A Study of African-American Young Adult Volunteers.

Year 2

Publications

1. Korotcov AV, Ye YP, Chen Y, Zhang FY, Huang S, Lin S, Sridhar R, Achilefu S, Wang PC. Glucosamine Linked Near-infrared Fluorescent Probes for Imaging of Solid Tumor Xenografts. *Mol. Imaging and Biology*. 14(4):443-51, 2012. PMID21971932, PMC3288187.
2. Meng H, Xing GM, Blanco E, Song Y, Zhao L, Sun BY, Li XD, Wang PC, Korotcov A, Li W, Liang XJ, Chen CY, Yuan H, Zhao F, Chen Z, Sun T, Chai ZF, Farrari M, Zhao YL. Gadolinium Metallofullerenol Nanoparticle Inhibits Cancer Metastasis through Matrix Metalloproteinase Inhibition: Imprisoning Instead of Poisoning Cancer Cells. *Nanomedicine: Nanotechnology, Biology and Medicine* 8(2):136-146, 2012. PMID 21930111.
3. Zhang FY, Shan L, Liu YY, NevilleD, Woo JH, Chen Y, Korotcov AV, Lin S, Huang S, Sridhar R, Liang W, Wang PC. An Anti-PSMA Bivalent Immunotoxin Exhibits Specificity and Efficacy for Prostate Cancer Imaging and Therapy. (Submitted to *Advanced Health Materials*, 09/2012)
4. Wang TX, Korotcov AV, Sridhar R, Chen Y, Mitchell JW, and Wang PC. A ³¹P NMR Study of TOPO Release from TOPO-coated Quantum Dots. (To be submitted to the *Journal of Colloid and Interface Science* 10/2012)

Presentations

1. Wang PC. Nanoparticles as Targeted Drug Delivery Vehicles for Molecular Imaging and Chemotherapy Applications. Hebei People's Hospital, Shijiazhuang, Hebei, China, Sep 13, 2011.
2. Wang PC. Nanoparticles as Targeted Drug Delivery Vehicles for Molecular Imaging and Chemotherapy Applications. Peking Union Medical College, Beijing, China, Sep 15, 2011.
3. Wang PC. Applications of Nanoparticles for In Vivo Imaging. Institute of Biophysics, Chinese Academy of Sciences, Beijing, China, Sep 16, 2011.
4. Wang PC. Nanoparticles as Targeted Drug Delivery Vehicles for Molecular Imaging and Chemotherapy Applications. Chinese National Center for Nanoscience and Nanotechnology, Beijing, China, Sep 16, 2011.
5. Wang PC. Nanoparticles as Targeted Drug Delivery Vehicles for Molecular Imaging and Chemotherapy Applications. University of Rhode Island, Kingston, RI, November 18, 2011.
6. Wu CS, Huang S, Korotcov AV, Lin S, Andreev OA, Reshetnyak YK, Wang PC. pH Sensitive Nanoprobe for Tumor Targeting. Howard University Health Sciences Research Day 2012, Howard University, Washington, DC, April 13 2012, p. 21.
7. Lin S, Korotcov A, Wu CS, Oh L, Wang PC. In vivo and ex vivo brain and spine magnetic resonance imaging in multiple sclerosis mouse model. Howard University College of Medicine, Research Day Symposium, April 13, 2012
8. Wang PC, Wang TX, Korotcov AV, Sridhar R, Chen Y, Mitchell J. Study of TOPO-Quantum Dot Degradation by ³¹P NM, The 6th International Conference on Nanotoxicology, Beijing, September 4-7, 2012.

Grants

1. NIH/NCI R21 07/12-06/14 Enhance mTOR-Targeting for Cancer Imaging and Therapy Yunpeng Ye (PI), Paul Wang (co-PI) (not funded)
2. NIH/NCI R03 07/12-06/14 Simultaneous inhibition of integrin $\alpha\beta3$ and mTOR for pancreatic cancer therapy Yunpeng Ye (PI), Paul Wang (co-PI) (not funded)

3. US Army Prostate Cancer Idea Development Award 09/12-08/14 Dual targeting of integrin $\alpha v \beta 3$ and mTOR for optical imaging and therapy of prostate cancer. Yunpeng Ye (PI), Paul Wang (co-PI) (not funded)
4. NSF/Biomaterials Program 07/01/2012 – 06/30/2015 Tumor-Targeted pH-Sensitive Nanoparticulate MRI Agent with Enhanced Contrast and Reduced Side Effect Tongxin Wang (PI), Alexandru Korotcov (co-PI), Ayele Gugssa (co-PI), and Laurence Chow (co-PI) (not funded)
5. NCCR/NIH/CTSA (part) GHUCCTS TTR 07/01/2012 – 06/30/2013 Dynamic contrast enhanced MRI of tumor using targeted nanoparticles Alexandru Korotcov (PI), Leroy Williams (PI) (not funded)
6. NIH 1UL1RR031975 (Verbalis & Mellman) 07/01/2012-06/30/2013 Georgetown-Howard Universities Center for Clinical and Translational Science (GHUCCTS) Pilot Project. A collaborative study using primary prostate cells and their reprogramming for the study of progression to castrate resistant prostate cancer Chris Albanese (PI), Alexandru Korotcov (co-PI) (not funded)

Year 3

Publications

1. Shan L, Gu XB, Wang PC. Design Principles of Nanoparticles as Contrast Agents for Magnetic Resonance Imaging. Nanopharmaceutics: The Potential Application of Nanomaterials. Chapter 11, Xing-Jie Liang (ed), World Scientific Publisher, 2012.
2. Wang PC, Shan L. Essential Elements to Consider for MRI Cell Tracking Studies with Iron Oxide based Labeling Agents. J Basic and Clinical Medicine 1(1)1-6, 2012.
3. Zhang RS, Zhou YF, Wang PC, Sridhar R. Evaluation of Tumor Cell Response to Hyperthermia with Bioluminescent Imaging. J Basic and Clinical Medicine 1(1)16-19, 2012.
4. Ma XW, Zhang LH, Wang LR, Xue X, Sun JH, Wu Y, Zou GZ, Wu X, Wang PC, Wamer WG, Yin JJ, Zheng KY, Liang XJ. Single-Walled Carbon Nanotubes Alter Cytochrome C Electron Transfer and Modulate Mitochondrial Function. ACS Nano 6(12)10486-96, 2012.
5. Jin SB, Ma XW, Ma HL, Zheng KY, Liu J, Hou SA, Meng J, Wang PC, Wu XC, Liang XL. Surface Chemistry-Mediated Penetration and Gold Nanorod Thermotherapy in Multicellular Tumor Spheroids. Nanoscale 5(1)143-6, 2012.
6. Hu XX, Hao XH, Wu Y, Zhang JC, Zhang XN, Wang PC, Zou GZ, Liang XJ. Multifunctional Hybrid Silica Nanoparticles for Controlled Doxorubicin Loading and release With Thermal and pH Dual Response. J Material Chem B (1)1109-1118, 2013. PMC3609667
7. Zhang FY, Shan L, Liu YY, Neville D, Woo JH, Chen Y, Korotcov A, Lin S, Huang S, Sridhar R, Liang W, Wang PC. An Anti-PSMA Bivalent Immunotoxin Exhibits Specificity and Efficacy for Prostate Cancer Imaging and Therapy. Adv. Healthcare Materials, 2(5)736-44, 2013, PMID 23184611.
8. Kumar A, Chen F, Mozhi A, Zhang X, Zhao YY, Xue XD, Hao YL, Zhang ZN, Wang PC, Liang XJ Innovative pharmaceutical development based on unique properties of nanoscale delivery formulation. Nanoscale (5)8307-25, 2103.

Presentations

1. Huang R, Gao RM, Drain CM, Wang PC, Gu XB, Imidazole-modified porphyrin ring (TIEBAP) for photodynamic therapy in cisplatin-resistant oral carcinoma cells in vitro and in vivo. 13th International RCMI Symposium on Health Disparity. San Juan, Puerto Rico, Dec 10-13, 2012.
2. Korotcov AV, Ishibashi N, Korotcova L, Chen Y, Lin S, Jonas RA, Wang PC. Cerebral white matter response to cardiopulmonary bypass in piglets. 13th International RCMI Symposium on Health Disparity. San Juan, Puerto Rico, Dec 10-13, 2012.

3. Lin S, Korotcov AV, Wu CS, Oh L, Wang PC. In vivo magnetic resonance imaging of multiple sclerosis mice. 13th International RCMI Symposium on Health Disparity. San Juan, Puerto Rico, Dec 10-13, 2012.
4. Wang PC. Introduction of Molecular Imaging laboratory at Howard University. 13th International RCMI Symposium on Health Disparity. San Juan, Puerto Rico, Dec 10-13, 2012.
5. Wright D, Lin S, Lin PC, Wu CS, Zhang D, Duerinckx A, Wang PC, Lee DL. Renal oxygenation levels are decreased in Peroxisome Proliferator Activated Receptor - α knockout mice during Angiotensin II hypertension. College of Medicine Research Day, Howard University, Washington DC, April 3, 2013.
6. Wright D, Lin S, Lin PC, Wu CS, Zhang D, Duerinckx A, Wang PC, Lee DL. Renal oxygenation levels are decreased in Peroxisome Proliferator Activated Receptor - α knockout mice during Angiotensin II hypertension. DB Johnson Distinguished Lecture, Howard University, Washington DC, April 3, 2013.
7. Zhang FY, Shan L, Liu YY, Neville D, Woo JH, Chen Y, Korotcov A, Lin S, Huang S, Sridhar R, Liang W, Wang PC. An Anti-PSMA Bivalent Immunotoxin Exhibits Specificity and Efficacy for Prostate Cancer Imaging and Therapy, ChinaNano 2013, Beijing, China, Sep 4-7, 2013.

Grants

1. NIH Mentored Clinical Scientist Development Award (K08)
Use of MRI/MRS to Assess for a Gamma-Glutamylcysteine Mediated in vivo Reduction in Hypoxic Stress-Induced Oxidative White Matter Injury in Mice
Dilip Nath (Children's Nat Med Centr, PI) Paul Wang (mentor) (09/17/2012 submitted, not funded)
2. NIH TR01
A Novel Non-invasive Device for Neuroregeneration in Dementia
Evaristus Nwulia (Psychiatry/Howard, PI), Paul Wang (co-PI) (09/22/2012 submitted, not funded)
3. NCCR/NIH/CTSA (part) GHUCCTS TTR
Development of An Anti-PSMA Fold-back Immunotoxin for Cancer Therapy
Liang Shan (8/3/2012 submitted, not funded)
4. NIH Exploratory/Developmental Research Grant Program (Parent R21)
Sheddable Bivalent Fold-back Format Immunotoxin for Prostate Cancer Therapy
Liang Shan (Radiology/Howard, PI) Paul Wang (co-PI) (06/03/2013 submitted, pending)
5. NSF
Howard University Center for Nanophotonics and Nanomaterials (NHCNN)
A Physics Frontiers for Study Interfacial Phenomena
Parbhar Misra (Physics/Howard, PI) Paul Wang (co-PI) (08/05/2013 submitted, pending)
6. DoD W81XWH-13-PCRP-IDA
An Anti-PSMA Bivalent Fold-back Format Immunotoxin for Prostate Cancer Therapy
Liang Shan (Radiology/Howard, PI) Paul Wang (co-PI) (10/01/2013 submitted, pending)

Year 4

Publications

1. Xue X, Hall HD, Zhang Q, Wang PC, Gottesman MM, Liang XJ. Nanoscale Drug Delivery Platforms Overcome Platinum-Based Resistance in Cancer Cells Due to Abnormal Membrane Protein Trafficking. ACS Nano vol.7 (12)10452-10464, 2013.
2. Shan L, Liu Y, Wang PC. Recombinant Immunotoxin Therapy of Solid Tumors: Challenges and Strategies. J. Basic Clin Med 2(2):1-6, 2013.
3. Lin PC, Lin S, Wang PC, Sridhar R. Techniques for Physicochemical Characterization of Nanomaterials. Biotechnol Adv. (4):711-726, 2014.
4. Li SL, Cao WP, Kumar A, Jin SB, Zhao YY, Zhang CQ, Zou GZ, Wang PC, Li F, Liang XJ. Highly Sensitive

Simultaneous Detection of Mercury and Copper Ions by Ultrasmall Fluorescent DNA–Ag Nanoclusters *New J. Chem* 38(4):1546-1550, 2014

5. Jin SB, Li SL, Wang CX, Liu J, Yang XL, Wang PC, Zhang X, Liang XJ. Biosafe Nanoscale Pharmaceutical Adjuvant Materials. *J Biomed Nanotechnology* (10)1-27, 2014
6. Huo S, Jin S, Ma X, Xue X, Yang K, Kumar A, Wang PC, Zhang J, Hu Z, Liang XJ. Ultrasmall Gold Nanoparticles as Carriers for Nucleus-Based Gene Therapy Due to Size-Dependent Nuclear Entry. *ACS Nano* 8(6):5852-5862, 2014.
7. Yang KN, Zhang CQ, Wang W, Wang PC, Zhou JP, Liang XJ. pH-Responsive Mesoporous Silica Nanoparticles Applied in Controlled Drug Delivery Systems for Cancer Treatment. *Cancer Biol Med.* 11(1):34-43, 2014.

Presentations

1. Wright D, Lin S, Lin PC, Wu CS, Zhang D, Duerinckx A, Wang PC, Lee DL. Measuring Renal Oxygenation in a Mouse Model of Volume-Dependent Hypertension using BOLD MRI. Radiological Society of Northern America, Chicago, IL, Dec 1-6, 2013.
2. Wang PC. Molecular Imaging and Nanoparticles as Drug Delivery Vehicles. Industrial Technology Research Institute, HsiChu, Taiwan, Dec.10. 2013.
3. Wang PC, Magnetic Resonance Imaging: Principles and Instrumentation. Fu Jen University Department of Electrical Engineering, Taipei, Taiwan, Dec. 11, 2013
4. Wang PC. Introduction of Howard University Molecular Imaging laboratory. Fu Jen University Medical School, Taipei, Taiwan, Dec 13, 2013.
5. Wang PC. Howard University Imaging Core Facility. The National Academies Committee on Review of Army Research Laboratory (ARL) Programs Support Historically Black Colleges and Universities and Minority Institutions (HBCUs/MIs), Washington, DC, Feb 24, 2014.
6. Zhang Z, Wang J, Nie X, Chen C, Wang PC. Near Infrared Laser Mediated Targeted Tumor Thermo-chemotherapy Using Thermosensitive Polymer Coated Gold Nanoparticles. Howard University Research Day 2014. Washington DC. April 4, 2014.
7. Shan L, Lin S, Lin PC, Zhang Z, Liu Y, Wang PC. Engineered Antibody Fragments and Immunotoxin for Targeted Imaging and Therapy of Prostate Cancer. Howard University Research Day 2014. Washington DC. April 4, 2014.
8. Lin S, Shan L, Lin PC, Zhang Z, Gu X, Wang PC. Construction of Transferrin Receptor–targeted Multi-modality Agents for Cancer Imaging. Howard University Research Day 2014. Washington DC. April 4, 2014.
9. Wang PC. Howard University Biomedical Core Facility. Howard University Research Day 2014. Washington DC. April 4, 2014
10. Zhang Z, Wang J, Nie X, Chen C, Wang PC. Near Infrared Laser Mediated Targeted Tumor Thermo-chemotherapy Using Thermosensitive Polymer Coated Gold Nanoparticles. Howard University Radiology Imaging Symposium. Washington DC. May 6, 2014.
11. Shan L, Lin S, Lin PC, Zhang Z, Liu Y, Wang PC. Engineered Antibody Fragments and Immunotoxin for Targeted Imaging and Therapy of Prostate Cancer. Howard University Radiology Imaging Symposium. Washington DC. May 6, 2014.
12. Lin S, Shan L, Lin PC, Zhang Z, Gu X, Wang PC. Construction of Transferrin Receptor–targeted Multi-modality Agents for Cancer Imaging. Howard University Radiology Imaging Symposium. Washington DC. May 6, 2014.
13. Wang PC. Molecular Imaging Laboratory. Howard University Radiology Imaging Symposium. Washington DC. May 6, 2014.

Grants

1. NIH/NCRR/RCMI/2 G12RR003048 03/01/14-05/31/19
Biomedical Infrastructure for Health Disparities Research Southerland (PI); Wang (co-PI)
Biomedical Imaging Care Facility (Role: Core Facility PI) \$ 2,009,920
2. NIH/NCRR/RCMI – Administrative Supplement 04/01/14-03/31/15
Biomedical Infrastructure for Health Disparities Research Southerland (PI); Wang (co-PI)
Request Support of Moving and Reinstallation Charges for a 7 T MRI Machine \$ 193,826
3. NIH/NIBIB Mentored Clinical Scientist Development Award (K08)
Prussian blue nanoconstructs for imaging and therapy of aggressive pediatric brain tumors
Rohan Fernandes (Children's Nat Med Centr, PI) Paul Wang (mentor) (10/01/13 submitted, not funded)
4. DoD University Research Instrumentation Program (DURIP)
Enhancement of STEM research and training through multiphoton confocal imaging
Eva Polston (PI, Howard/Physiology and Biophysics); Wang (co-PI) (10/20/13 submitted, not funded)
5. NSF
pH-Sensitive Nanoparticulate MRI Agent with Enhanced Contrast and Reduced Side Effects
Tongxin Wang (PI, Howard/School of Engineering), Paul Wang (co-PI) (10/21/13 submitted; not funded)
6. NIH
Novel Nanotechnology Platform for Breast Cancer Treatment
Emmanuel Akala (PI, Howard/Pharmaceutical Science). Paul Wang (co-PI) (1/14/14 submitted; not funded)
7. NIH
Engineered Antibody Fragments for PSMA-targeted Imaging and Therapy
Liang Shan (PI, Howard/Radiology), Paul Wang (co-PI) (02/15/14 submitted; not funded)
8. NIH
Howard University Blueprint Program for Enhancing Neuroscience Diversity through Undergraduate Research Education Experiences (HU BP-ENDURE)
Evaristus Nwulia (Howard/Psychiatry, PI), Paul Wang (co-PI) (05/23/14 submitted, not funded)
9. NSF
pH-Sensitive Nanoparticulate MRI Agent with Enhanced Contrast and Reduced Side Effects
Tongxin Wang (PI, Howard/ Engineering), Paul Wang (co-PI) (10/21/13 submitted; not funded)
10. DoD W81XWH-14-L
A humanized bivalent fold-back recombinant immunotoxin for prostate cancer therapy
Liang Shan (PI, Howard/Radiology), (09/15/21014 submitted, pending)

Degree Holders

1. Belinda Hauser (Nanomedicine Core predoctoral trainee) received a Ph.D. degree in Genetics. Thesis title: Epidermal Growth Factor Receptor (EGFR) Associated Head and Neck Squamous Cell Carcinoma (HNSCC) Tumorigenesis.
2. Whitney Barfield (Nanomedicine Core predoctoral trainee) received a Ph.D. degree in Microbiology. Thesis title: Osteopontin Genotype as a Determinant of Skeletal Muscle Remodeling – In vivo and in vitro studies show complex transcriptional regulation influencing muscle inflammation.

Year 5

Publications

1. Hauser B, Zhao Y, Pang X, Ling Z, Myers E, Wang P, Califano J, Gu X. Functions of MiRNA-128 on the

- regulation of head and neck squamous cell carcinoma growth and apoptosis. PLoS One 10(3):e0116321, 2015, PMID: 25764126
2. Gondre-Lewis MC, Gboluaje T, Reid SN, Lin S, Wang P, Green W, Diogo R, Fidelia-Lambert F, Herman MM. The Human Brain and Face: Mechanisms of Cranial, Neurological and Facial Development Revealed Through Malformations of Holoprosencephaly, Cyclopia and Aberrations in Chromosome 18. J Anat (227)255-267, 2015, PMID 26278930
 3. Meng J, Liu YY, Gao SY, Lin S, Gu XB, Pomper MG, Wang PC, Shan L. A Bivalent Recombinant Immunotoxin with High Potency against Tumors with EGFR and EGFRvIII Expression. Cancer Biol Ther. 2015 Oct 15:0. [Epub ahead of print], PMID 26467217.
 4. Zhang J, Li C, Zhang X, Huo S, Jin S, An FF, Wang X, Xue X, Okeke CL Duan G, Guo F, Zhang X, Hao J, Wang PC, Zhang J, Liang XJ. In vivo tumor-targeted dual-modal fluorescence/CT imaging using a nanoprobe co-loaded with an aggregation-induced emission dye and gold nanoparticles. Biomaterials 42:103-11. 2015, PMID 25542798
 5. Li SL, Zhang CQ, Cao WP, Ma BY, Ma XW, Jin SB, Zhang JC, Wang PC, Li F, Liang XJ. Anchoring Effects of Surface Chemistry on Gold Nanorods: Modulates Autophagy. J Mater Chem B Mater Biol Med 3(16):3324-3330, 2015, PMID 26301093
 6. Zhang J, Li S, An F, Liu J, Jin S, Zhang J, Wang PC, Zhang X, Lee C, Liang XJ, Self-carried Curcumin Nanoparticles for In vitro and In vivo Cancer Therapy with Real-time Monitoring of Drug Release. Nanoscale, 7(32):13503-10, 2015, PMID 26199064
 7. Zhao Y, Chen F, Pan Y, Li Z, Xue X, Okeke C, Wang Y, Li C, Peng L, Wang PC, Ma XW, Liang XJ. Nanodrug Formed by Coassembly of Dual Anticancer Drugs to Inhibit Cancer Cell Drug Resistance. ACS Appl Mater Interfaces. 7(34):19295-302, 2015, PMID 26270258
 8. Lin PC. Assessment of chemical exchange in tryptophan–albumin solution through 19F multicomponent transverse relaxation dispersion analysis. J Biomol NMR. 62(2)121-7, 2015. PMID 25900068.

Presentations

1. Wang PC. Introduction of Howard University Biomedical Imaging Core Facility. Children's National Medical Center, Washington, DC, February 12, 2015.
2. Lin S, Zhang ZJ, Wang PC. Fabrication of a Microfluidic Device for Generating Liposome Contrast Agent, Howard University Research Week, Washington, DC April 16, 2015.
3. Shan L, Meng J, Lin S, Gu XB, Wang PC. A Bivalent Recombinant Immunotoxin Exhibiting High Potency against Tumors with EGFR and EGFRvIII Expression. Howard University Research Week, Washington, DC, April 16, 2015.
4. Shan L, Meng J, Lin S, Gu, XB Wang PC. A Bivalent Recombinant Immunotoxin Exhibiting High Potency against Tumors with EGFR and EGFRvIII Expression, Howard University Imaging Conference, May 1, 2015
5. Wang PC. Howard University Imaging Core Facility. Nat TsingHwa Univ, HsinChu, Taiwan, May 4, 2015
6. Shan L, Lin S, Wang PC. Engineered Antibody Fragments for PSMA-targeted Imaging and Therapy of Prostate Cancer. World Molecular Imaging Conference 2015, Honolulu, HI, September 2-5, 2015.
7. Lin S, Zhang ZJ, Wang PC. Fabrication of a Microfluidic Device for Generating Liposomal Nanoparticles as Drug Delivery Vehicle. ChinaNANO 2015, Beijing, China, September 3-5, 2015.
8. Wang PC. Fabrication Microfluidic Device for Generating Liposome, Recombinant Immunotoxins (RITs) for Cancer Therapy, paraCEST MRI Agent for In Vivo pH Imaging. National Center for Nanoscience and Technology, Beijing, China, September 16, 2015
9. Wang PC. Introduction of Howard University Molecular Imaging Lab – Applications of Nanotechnology in Medical Imaging and Targeted Drug Delivery. Catholic University of America,

Washington, DC, October 28, 2015.

Grants

Active

1. NIH/NCRR/RCMI–Administrative Supplement (Dr. Southerland, PI; Wang, co-PI) 04/01/14 - 03/31/15, \$193,826
Title: Biomedical Infrastructure for Health Disparities Research: Request Support of Moving and Reinstallation Charges for a 7 T MRI Machine
2. USAMRMC W81XWH-10-1-0767 (Wang, PI) 09/15/10 – 09/14/15 \$1,479,958
Title: A Partnership Training Program – Studying Targeted Drug Delivery Using Nanoparticles In Breast Cancer Diagnosis and Therapy.
3. NIH 1R01HL104173-01 (Jonas, PI; Wang, co-PI) 08/15/10-04/30/15 \$212,163
Title: Protection of Developing White Matter During Cardiac Surgery.
4. NIDCR/NIH 1R15DE025138-01, (Shan, PI) 08/15/2015 – 07/31/2018 \$452,911
Title: EGFR and EGFRvIII-bispecific Bivalent Recombinant Immunotoxin for HNSCC Therapy
5. NIH/NCRR/RCMI/4, G12 RR003048, (Shan, PI) 11/01/2015 - 11/30/2017 \$100,000
Title: Development of a Multispecific Recombinant Immunotoxin for Cancer Therapy
6. U400067 Bridge Funds, Howard University College of Medicine (Shan, PI) 01/05/2015 - 01/04/2016, \$25,000
Title: An Anti-PSMA Bivalent Fold-back Format Immunotoxin for Prostate Cancer Therapy
7. NIDCR/NIH, 1R25DE025778-01, (Gu, PI; Shan, co-I) 01/01/2016 – 12/31/2020 \$261,955
Title: Howard University Summer Research Experience Program in Oral Health Disparity for Underrepresented Racial and Ethnic Students

Submitted/Pending Funding

1. NIH, Developing and Improving Institutional Animal Resources 07/28/2015
(Wang, co-Investigator)
2. NIH, Prenatal Treatment for White Matter Protection in Congenital Heart Disease (Dr. Ishibashi, PI) 07/01/2018 – 06/30/2021 (Wang, Subaward PI)
3. PRMP, Prenatal Treatment for Brain Protection in Congenital Heart Disease (Dr. Ishibashi, PI) 07/01/2017 – 06/30/2019 (Wang, subaward PI)
4. NIH, Olfactory Bulb Plasticity and Trauma Outcomes in Urban Dwelling HIV Populations in Washington DC (Nwulia, PI; Wang, Co-investigator) 05/06/2015
5. NIH, Novel Nanotechnology Platform for Breast Cancer Treatment (Dr. Akala, PI), 01/14/2105 (Wang, Co-investigator)
6. HEI/NIH, Multisensory Integration and Learning – Global Partnerships for the Training of Future Neuroscientists (Riesenhuber and Manaye, PI; Wang co-I), 04/21/2015
7. NIH Instrumentation Grant, Request for a PET-MR at JHU (Dr. Bhujwala, PI), 05/11/2015 (Wang, Subaward investigator)
8. DoD, Development of a PSMA-targeted Recombinant Immunotoxin for Prostate Cancer Therapy Submitted 09/24/15 (Shan, PI)

V. CONCLUSIONS

Research Component

There were two research projects that were started and completed throughout the five-year life of the grant. During the first two years, both research projects progressed well. Cationic liposomes encapsulated MRI contrast agents were constructed and characterized for improving the sensitivity and specificity of MRI in breast cancer imaging. Targeted delivery of MR contrast agents may potentially reduce the amount of Gd required to achieve high MR image contrast, which in turn reduces the toxicity of the Gd in particular to renal deficient patients. We studied the stability of nanoparticles in light of potential toxicity of nanoparticles used in humans. We have established a noninvasive method to monitor the dissociation of commonly used surfactant TOPO from quantum dots. We will use this method to test the stability of nanoparticles under harsh physiological conditions in live animals. We have also used AdmDT(390)-scfbDb(PSMA), a single chain Fv fragments of antibody with diphtheria toxin, to demonstrate that a nano sized immunotoxin can be used for targeted delivery of toxin to the cancer cells and at the same time it can be used as an imaging reporter of the cancer targeting efficiency. This immunotoxin has dual functions both as an imaging and as a therapeutic agent. To achieve better control on liposomal formation, we modified the liposome preparation method. The Tf in the new construct is attached by covalent bonding, improving the stability of liposomal nanoparticles. The Tf conjugated liposomal nanoparticles exhibited a significant increase in the in vitro cellular uptake compared to the uptake of dye or non-targeted liposomes. A toxicity study using NMR spectroscopy method showed that TOPO, a commonly used protective layer over quantum dots, can be cleaved from nanoparticles in the presence of physiological fluids, degrading the nanoparticles in physiological systems and increasing risks of nanotoxicity. In addition, we tested two different approaches of improving nanoparticle delivery efficacy. Doubling the number of targeting moieties increases the uptake of the probe in cells and in animal solid tumor model. Moreover, we showed that a pH sensitive peptide can be used as an effective ligand targeting acidic tumor environment, facilitating insertion of nanoparticle to the cancer cell membrane. We have completed a proof-of-principle study confirming the tumor targeting and therapeutic potentials of a bivalent immunotoxin generated by fusing a fold-back single-chain diabody derived from the Fv fragments of an anti-PSMA monoclonal antibody with a truncated diphtheria toxin containing the activity and translocation domains [A-dmDT390-scfbDb(PSMA)]. We have been working on anti-murine (VR16) and an anti-human (1121) anti-VEGFR-2 bivalent scFv (biscFv) fold-back immunotoxin synthesis. We have also shown anti-metastatic effect of gadolinium metallofullerene nanoparticles.

During the third year, we have shown that the targeted nanocomplex, Tf-Lip-Mag (~130 nm) significantly enhanced the MRI signals in MDA-MB-231 breast cancer xenograft tumors in mice. The image enhancement was superior to that obtained using the contrast agent alone. This superior enhancement capability of the nanocomplex can be used to increase the sensitivity of detecting small tumors. A much higher contrast in viable cells in the periphery of tumor was observed at the initial stage of the targeted DCE-MRI. The image intensity was persistently higher than the DCE-MRI of free CA and lasts for several hours. The nature of the elevated contrast level at the initial stage of targeted DCE-MRI in vivo may be due to receptor mediated endocytosis. The tumor enhancement patterns are well correlated with histology, and could be used to evaluate tumor pathology in vivo and provide very useful, timely information for the clinicians. In the future, specially formulated nanocomplex CA can be used to quantify the specific biomarkers expressed in tumors, which will be useful in determining the patient's prognosis and response to treatment. We also have reviewed literature pertaining to the development, characterization and applications of various nanoparticles in cancer imaging and therapy.

We have analyzed the effects of single-walled carbon nanotubes (SWCNTs) on mitochondrial function. We have synthesized gold nanorods (Au NRs) with three different polymer coatings, and further investigated the relationship between the surface chemistry and the penetration ability of Au NRs in a multicellular tumor spheroid model. We have designed and synthesized temperature and pH dual responsive PNiPAM/AA@SiO₂ core-shell particles loaded with doxorubicin for improving drug delivery efficiency for cancer treatment. We have established a bioluminescent imaging technique to evaluate tumor cell response to hyperthermia utilizing luciferase-expressing MDA-MB-231-luc human breast cancer cells. We have generated a bivalent single-chain variable fragment (scFv) recombinant immunotoxin, A-dmDT390-scFvDb(PSMA) with J591 antibody, against extracellular domain of PSMA in tumor epithelial cells in animal model. Our results suggested that this novel immunotoxin is a promising candidate for anti-cancer therapy.

Liposomes ranging in size from 50 to 170 nm using a thin film hydration combined with membrane filter method were created during the fourth project year. The relative standard deviation of liposome size was in the 20-30% range. We have used a microfluidic channel device to improve the liposome size distribution. A narrow size distribution is critical for studying the size dependence of targeted liposome uptake in solid tumors. For studying pharmacokinetics and targeting efficiency of liposome in solid tumor using DCE imaging data, we have implemented a distinguished compartmental model to measure ligand-target chemical exchange kinetics in a complex in vivo environment. By capitalizing on the unique specificity of antibody mAb806 against EGFR and EGFRvIII overexpressed in cancer but not the EGFR in normal tissue, and by further taking the mAb806 humanization-derived benefits, we generated a humanized bivalent scFv-derived, DT390-based recombinant immunotoxin, DT390-BiscFv806. This novel RIT exhibited high cytotoxicity and anti-tumor efficacy against the cancer cells either with EGFR expression alone or with EGFR and EGFRvIII co-expression. The results indicate that DT390-BiscFv806 is highly promising for treatment of cancers arising from the brain, head and neck, lung, breast, prostate, and others. To develop a PSMA-targeted platform of engineered antibody fragments for cancer imaging, we constructed three formats of antibody fragments including single-chain variable fragment (scFv), bivalent tandem scFv (biscFv), and bivalent scFv diabody (scFvDb) in fold-back structure, leveraging the high specificity of J591 antibody against the extracellular domain of PSMA. Initial studies showed that the fold-back structure of scFvDb resulted in an increased efficiency of target binding and toxin delivery to target cells, compared with other formats. The favorable properties of the fold-back diabody in pharmacology make it attractive as a springboard to develop imaging agents for cancer and cancer angiogenesis imaging. We have designed a simple and highly sensitive sensing nanosystem for the detection of Hg²⁺ and Cu²⁺ based on fluorescence quenching of ultrasmall DNA-Ag NCs. We have constructed small gold nanoparticles to study size-dependent penetration ability and the potential applications of for intranuclear delivery. We found gold nanoparticles smaller than 10 nm can enter the nucleus, whereas larger ones (10 - 16 nm) can only be found in the cytoplasm. We have reviewed literature and written an article on the development, characterization and applications of nanoparticles in cancer imaging and therapy. We have also written a review on the challenges of immunotoxin therapy for human solid tumors, and the potential strategies to overcome these challenges.

We have requested for a no-cost extension to complete the tasks we need to accomplish for the project that study the physicochemical characteristics of nanoparticles as MR contrast agent delivery system with the dynamic contrast enhancement pattern for clinical applications. For this period we were able to construct liposomes with a sufficiently narrow size distribution to properly study size dependence of targeted liposome uptake in solid tumors. The relative large size distribution currently generated leads to poor DCE data quality, which masks subtle differences in MR image enhancement

patterns resulting from liposome size difference. We completed testing of a new NMR method to study ligand binding process in vivo. We refined our liposome fabrication method to achieve a more narrow size distribution to improve the results from the DCE study in solid tumor model. We implemented the NMR T2 relaxation rate measurement to improve pharmacokinetic modeling to analyze the DCE image data.

Training Component

The Molecular Imaging Laboratory at Howard University has molecular imaging core and molecular biology core. Through the funding of this project, a Nanomedicine Core was established that augmented existing principles of multidisciplinary research and teaching activities in molecular imaging. The Imaging Core as a whole has experts who are dedicated in the development and application of physics and computer science for biological research. The Imaging Core serves as a ground for learning, training and professional development for graduate students, researchers and faculty members.

Throughout the 5 year project period, more than 40 seminars, webinars, workshops and symposia in cancer, molecular imaging and nanomedicine have been offered. Some seminars have been arranged through webinars sponsored by imaging vendors, an opportunity for Howard University community to learn from experts from around the world. These sessions were followed by very productive and fruitful local discussions that engage participants in discussing the current status of research projects, analyzing any experimental issues of the current research, reviewing progress, and exchanging ideas, and have been the primary mode of interaction between Howard researchers and collaborating experts. The discussion-based format of the meetings and seminars allowed for growth and generation of thought that led to a better understanding of nanomedicine and molecular imaging. Through these interactions, ideas are exchanged and shared, further support, guidance and multidisciplinary imaging collaborative relationships are enhanced.

The training activities have been coordinated by partnership leaders from Howard and John Hopkins Universities. Specifically, faculty members, and graduate and undergraduate students from different departments at Howard University have been trained in the use of nanoparticles as targeted drug delivery vehicles for cancer diagnosis and therapy. The Nanomedicine Core has supported more than 20 research projects including projects in the initial phase of research. There are 18 faculty members from 6 departments and 5 scientists from the neighboring institutions, including NIST, NIH and Georgetown University, who use the core facility to conduct these research projects. There are a total of 7 undergraduate students, 21 graduate students and 14 postdoctoral fellows working with principal investigators in these projects. Two graduate students received PhD degrees. The Nanomedicine Core has provided training and research opportunities for the faculty and students at Howard University to conduct breast cancer research using state-of-the-art nanotechnology. It has become a synergy center drawing multidisciplinary research collaborations using nanotechnology for targeted drug delivery and improving breast cancer diagnosis and therapy. We have initiated several additional projects using computer modeling to study the docking process between nanoparticles and their intended targets in cancer cells, using a convex analysis of mixtures algorithm to study compartmental modeling of MRI-DCE pattern of targeted delivery of nanoparticle containing MR contrast agent and the liposome use as drug delivery vehicle for head and neck cancer. Throughout the life of the grant, the Core received various grants to not only further support the University Imaging Core but enhance its ability to conduct imaging studies using large animals through the support received from a NIH supplement.

The main accomplishment for this project was the establishment of the Nanomedicine Core. It developed collaborative relationships through its consortium of the Nanomedicine Core and other core facilities on campus. Researchers who are conducting nanomedicine research can also have access to analytical and imaging instrumentation.

VI. REFERENCES

1. Pourtau L, Oliveira H, Thevenot J, Wan Y, Brisson AR, Sandre O, Miraux S, Thiaudiere E, Lecommandoux S. Antibody-Functionalized Magnetic Polymersomes: In vivo Targeting and Imaging of Bone Metastases using High Resolution MRI. *Advanced Healthcare Materials* 2013. Doi: 10.1002/adhm.201300061.
2. Gallo J, Long NJ, Aboagye EO. Magnetic nanoparticles as contrast agents in the diagnosis and treatment of cancer. *Chemical Society Reviews* 42(19): 7816-7833, 2013.
3. Gulaka PK, Yu JX, Liu L, Mason RP, Kodibagkar VD. Novel S-Gal analogs as ¹H MRI reporters for in vivo detection of β -galactosidase. *Magnetic Resonance Imaging* 31(6): 1006-1011, 2013.
4. Geninatti Crich S, Alberti D, Szabo I, Aime S, Djanashvili K. MRI visualization of melanoma cells by targeting overexpressed sialic acid with a Gd(III)-dota-en-pba imaging reporter. *Angewandte Chemie International Edition* 52(4): 1161-1164, 2013.
5. Penet MF, Glunde K, Jacobs MA, Pathak AP, Bhujwalla ZM. Molecular and functional MRI of the tumor microenvironment. *Journal of Nuclear Medicine* 49(5): 687-690, 2008.
6. Lammers T, Rizzo LY, Storm G, Kiessling F. Personalized nanomedicine. *Clinical Cancer Research* 18(18): 4889-4894, 2012.
7. Caruso F, Hyeon T, Rotello VM. Nanomedicine. *Chemical Society Reviews* 41(7): 2537-2538, 2012.
8. Lammers T, Aime S, Hennink WE, Storm G, Kiessling F. Theranostic nanomedicine. *Accounts of Chemical Research* 44(10): 1029-1038, 2011.
9. Kwon IK, Lee SC, Han B, Park K. Analysis on the current status of targeted drug delivery to tumors. *Journal of Controlled Release* 164(2): 108-114, 2012.
10. Sultana S, Khan MR, Kumar M, Kumar S, Ali M. Nanoparticles-mediated drug delivery approaches for cancer targeting: a review. *Journal of Drug Targeting* 21(2): 107-125, 2013.
11. Cheng Z, Al Zaki A, Hui JZ, Muzykantov VR, Tsourkas A. Multifunctional nanoparticles: cost versus benefit of adding targeting and imaging capabilities. *Science* 338(6109): 903-1020, 2012.
12. Laouini, A., Jaafar-Maalej, C., Limayem-Blouza, I., Sfar, S., Charcosset, C., & Fessi, H. (2012). Preparation, characterization and applications of liposomes: state of the art. *Journal of Colloid Science and Biotechnology*, 1(2), 147-168.
13. Immordino, M. L., Dosio, F., & Cattel, L. (2006). Stealth liposomes: review of the basic science, rationale, and clinical applications, existing and potential. *International journal of nanomedicine*, 1(3), 297-315.
14. Kato, H., et al. (2012). Accurate Size and Size-Distribution Determination of Polystyrene Latex Nanoparticles in Aqueous Medium Using Dynamic Light Scattering and Asymmetrical Flow Field Flow Fractionation with Multi-Angle Light Scattering. *Nanomaterials*, 2(1): 15-30.
15. Edwards, K. A., & Baeumner, A. J. (2006). Analysis of liposomes. *Talanta*, 68(5), 1432-1441.
16. Jahn, A., Vreeland, W. N., Gaitan, M., & Locascio, L. E. (2004). Controlled vesicle self-assembly in microfluidic channels with hydrodynamic focusing. *Journal of the American Chemical Society*, 126(9), 2674-2675.
17. Jahn, A., Stavis, S. M., Hong, J. S., Vreeland, W. N., DeVoe, D. L., & Gaitan, M. (2010). Microfluidic mixing and the formation of nanoscale lipid vesicles. *Acs Nano*, 4(4), 2077-2087.
18. Meng J, Liu Y, Gao Y, Lin S, Gu X, Pomper M, Wang PC, Shan L. A highly potent bispecific bivalent recombinant immunotoxin against tumors with EGFR and EGFRvIII expression. *Cancer Biol Therapy*, 2015, 2015, Oct 15:0. [Epub ahead of print]
19. Zhang F, Shan L, Liu Y, Neville D, Chen Y, Korotcov A, Lin S, Huang S, Sridhar R, Liang W, Wang PC. Diphtheria toxin-based anti-PSMA fold-back single-chain diabody immunotoxin exhibits specificity and efficacy for prostate cancer imaging and therapy. *Adv Healthc Mater*. 2(5):736-44, 2013

20. Shan L, Liu Y, Wang P. Recombinant immunotoxin therapy of solid tumors: challenges and strategies. J Basic Clin Med. 2(2):1-6, 2013

VII. APPENDICES

1. Dr. Yunkou Wu's CV
2. Research Projects Supported by the Nanomedicine Core
3. Personnel Who Received Pay for the Research
4. Students Who Participated in Nanomedicine Core Supported Research Projects
5. Reprints of Publication
6. Reprints of Abstracts

BIOGRAPHICAL SKETCH

Provide the following information for the Senior/key personnel and other significant contributors.
Follow this format for each person. DO NOT EXCEED FIVE PAGES.

NAME: Yunkou Wu

eRA COMMONS USER NAME (credential, e.g., agency login): YUNKOUWU

POSITION TITLE: Assistant Professor

EDUCATION/TRAINING (Begin with baccalaureate or other initial professional education, such as nursing, include postdoctoral training and residency training if applicable. Add/delete rows as necessary.)

INSTITUTION AND LOCATION	DEGREE (if applicable)	Completion Date MM/YYYY	FIELD OF STUDY
Jilin Institute of Chemical Technology, China Dalian University of Technology, China The University of Texas at Dallas	B.S. Ph.D. Postdoc.	1998-2002 2002-2007 2007-2010	Analytical Chemistry Applied Chemistry Inorganic Chemistry/ MRI and PET imaging probe synthesis

NOTE: The Biographical Sketch may not exceed five pages. Follow the formats and instructions below.

A. Personal Statement

Modern clinical cancer treatments rely heavily on the precise detection of malignancies with medical molecular imaging agents and technologies. My research interests are to develop MRI, PET and optical imaging agents for imaging of biological targets of interest such as pH and hypoxia. My work consists of two parts: 1) Develop new imaging agents; 2) Establish the methods for *in vivo* imaging of pH and hypoxia using the agents developed. I have a broad background in chemistry and molecular imaging science, with specific training and expertise in organic synthesis, cell culture, small animal handling, optical, MRI and PET imaging, and imaging data analysis, which were obtained from the diverse research projects during the last 13 years. I have motivation and enthusiasm necessary to successfully carry out the molecular imaging research projects.

Selected publications:

1. Fernando, W. Shirangi; Martins, André; Zhao, Piyu; Wu, Yunkou; Kiefer, Garry; Platas-Iglesias, Carlos; Sherry, A. Dean. "Breaking the barrier to slow water exchange rates for optimal magnetic resonance detection of paraCEST agents". *J. Am. Chem. Soc.*, **2015**, DOI: ja-2015-08897n.R1, in revision.
2. Yu, Jing; Martins, Andre F.; Preihs, Christian; Veronica, Clavijo Jordan; Zhao, Piyu; Wu, Yunkou; Nasr, Khaled; Kiefer, Garry E.; and Sherry, A. Dean. "Amplifying the Sensitivity of Zn(II)-responsive MRI Contrast Agents by Altering Water Exchange Rates". *J. Am. Chem. Soc.*, **2015**, DOI: 10.1021/jacs.5b09158, [Epub ahead of print].
3. Wu, Yunkou; Zhang, Shanrong; Soesbe, Todd C; Yu, Jing; Vinogradov, Elena; Lenkinski, Robert E. and Sherry, A Dean. "In Vivo pH Imaging of Mouse Kidneys using a paraCEST Agent" *Magn Reson Med.* **2015**, DOI 10.1002/mrm.25844, [Epub ahead of print].
4. Wu, Yunkou; Hao, Guiyang; Ramezani, Saleh; Sun, Xiankai; Saha, Debabrata; Zhao, Dawen and Sherry, A. Dean ⁶⁸Ga-HP-DO3A-Nitroimidazole: A Promising Agent for PET Detection of Tumor Hypoxia" *Contrast Media Mol. Imaging* **2015**, DOI: 10.1002/cmml.1649, [Epub ahead of print].
5. Wang, Xiaojing; Wu, Yunkou; Soesbe, Todd C.; Yu, Jing; Zhao, Piyu; Kiefer, Garry E. and Sherry, A. Dean. "A pH-Responsive MRI Agent that Can Be Activated Beyond the Tissue MT Window". *Angew. Chem. Int. Ed.*, **2015**, 127(30), 8786-8788.
6. Opina, Ana; Wu, Yunkou; Zhao, Piyu; Kiefer, Garry E.; Sherry, A. Dean. "The pH Sensitivity of -NH Exchange in LnDOTA-tetraamide Complexes Varies with Amide Substituent" *Contrast Media Mol. Imaging* **2011**, 6, 459-464.

7. Wu, Yunkou; Soesbe, Todd C.; Kiefer, Garry E.; Zhao, Piyu; Sherry, A. Dean. "A Responsive Europium(III) Chelate That Provides a Direct Readout of pH by MRI." *J. Am. Chem. Soc.* **2010**, 132(40), 14002-14003.
8. Wu, Yunkou; Zhou, Youfu; Ouari, Olivier; Woods, Mark; Zhao, Piyu; Soesbe, Todd C.; Kiefer, Garry E.; Sherry, A. Dean. Polymeric PARACEST Agents for Enhancing MRI Contrast Sensitivity. *J. Am. Chem. Soc.* **2008**, 130(42), 13854-13855.
9. Wu, Yunkou; Peng, Xiaojun; Fan, Jiangli; Gao, Shang; Tian, Maozhong; Zhao Jianzhang; Sun, Shiguo. "Fluorescence sensing of anions based on inhibition of excited-state intramolecular proton transfer" *J. Org. Chem.* **2007**, 72(1), 62-70.
10. Peng, Xiaojun; Du, Jianjun; Fan, Jiangli; Wang, Jingyun; Wu, Yunkou; Zhao Jianzhang; Sun, Shiguo; Xu, Tao. "A selective fluorescent sensor for imaging Cd²⁺ in living cells" *J. Am. Chem. Soc.* **2007**, 129(6), 1500-1501.

B. Positions and Honors

Positions and Employment

2010-2014	Assistant Instructor, Advanced Imaging Research Center, UT Southwestern Medical Center at Dallas
2014-2015	Instructor, Advanced Imaging Research Center & Department of Radiology, UT Southwestern Medical Center at Dallas
2015-Current	Assistant Professor, Department of Radiology, Howard University

Honors and Awards

2002	Houyufen Scholarship, Dalian University of Technology
2006	Wanhua Scholarship, Wanhua Chemical Group Co Ltd
2011	Achievement award for technology commercialization, The University of Texas at Dallas
2015	AACR MSI Faculty Scholar in Cancer Research Award, American Association for Cancer Research

Professional Societies

2010-2011	Member, American Chemical Society (ACS)
2012-2013	Member, World Molecular Imaging Society (WMIC)
2012-Current	Member, Society of Nuclear Medicine and Molecular Imaging (SNMMI)
2015-Current	Member, International Society for Magnetic Resonance in Medicine (ISMRM)

Editorial Activities

2013-Current	Editorial Board, Journal of Analytical & Molecular Techniques
2013-Current	Editorial Board, Frontiers in Inorganic Chemistry
2013-Current	Editorial Board, Cancer and Oncology Research

C. Contribution to Science

- 1) Develop new molecular imaging agents.

Molecular imaging differs from traditional medical imaging in that molecular imaging probes need to be utilized to image particular targets or pathways. Molecular imaging probes can be derived from small molecules, big nanoparticles, and chemical modification of peptides, aptamers, engineered proteins. Therefore, chemistry is the central part of molecular imaging research. Based on the different needs and design principles, the molecular imaging probe could be detected by different imaging modalities such as Positron Emission Tomography (PET), Single-Photon Emission Computed Tomography (SPECT), Computed Tomography (CT), Magnetic Resonance Imaging (MRI), Optical Imaging, and Ultrasound (US). As a principal researcher or co-investigator of the various imaging projects, I have developed (1) the fluorescence imaging probe for Cd²⁺ and Zn²⁺ detection; (2) the MR imaging probes for pH and Zn²⁺ detection; and (3) the PET tracer for tumor hypoxia detection during the last 13 years. Many of my research has been published in top journals and some of my research has been patented because the agents show great application potential. Given that my publications related to chemistry probe development project have been cited > **1300** times by researchers around the world, the impact of my research is clearly evident.

- 2) Establish the imaging methods for *in vivo* detection of pH and hypoxia.

Another central part of molecular imaging work is to establish the *in vivo* imaging methods or protocols. For example, based on Matlab, I have established the CEST MRI data processing method including B_0 correction and pixel-by-pixel fitting of the individual Z spectrum to Super-Lorentzian line shape. Meanwhile, I am developed on the hypoxia imaging protocols using imaging probes I developed. To further validate the hypoxia targeting capacity of the new agent, I am using BOLD fMRI and diffusion-weighted MRI to measure the pO_2 maps in tumor to find the correlation between the pO_2 maps and DCE-MRI maps.

Publications:

Patents

1. Lenkinski, Robert; Wu, Yunkou; Sherry, A. Dean. "An Ytterbium-based complex of HP-DO3A-Nitroimidazole as a Contrast Agent for Imaging Hypoxia Using CT" 2014 Initial disclosure
2. Sherry, A. Dean; Preihs, Christian; Yu, Jing; Wu, Yunkou; Zhao, Piyu; Nasr, Khaled "New gadolinium-based contrast agents for highly sensitive detection of Zn^{2+} with MRI" 2014 UTSD.P2780US.P1
3. Sherry, A. Dean; Wu, Yunkou; Kiefer, Garry E. "Agents and compounds for imaging and other applications, and methods of use and synthesis thereof" **2012** WO 2012006038.
4. Peng, Xiaojun; Fan, Jiangli; Du, Jianjun; Wang, Jingyun; Wu, Yunkou; Sun, Shiguo. "Boron dipyrromethene-based fluorescent probe for detection of intracellular cadmium ions" **2007** CN 101004422A.
5. Peng, Xiaojun; Wu, Yunkou; Guo, Binchen; Fan, Jiangli; Wang, Jingyun; Cui, Aijun; Tian, Maozhong. "Fluoroboric fluorescent probe for detecting zinc in cells" **2006** CN 1715919A.

Research Articles

6. Fernando, W. Shirangi; Martins, André; Zhao, Piyu; Wu, Yunkou; Kiefer, Garry; Platas-Iglesias, Carlos; Sherry, A. Dean. "Breaking the barrier to slow water exchange rates for optimal magnetic resonance detection of paraCEST agents". *J. Am. Chem. Soc.*, **2015**, DOI: ja-2015-08897n.R1, in revision.
7. Yu, Jing; Martins, Andre F.; Preihs, Christian; Veronica, Clavijo Jordan; Zhao, Piyu; Wu, Yunkou; Nasr, Khaled; Kiefer, Garry E.; and Sherry, A. Dean. "Amplifying the Sensitivity of Zn(II)-responsive MRI Contrast Agents by Altering Water Exchange Rates". *J. Am. Chem. Soc.*, **2015**, DOI: 10.1021/jacs.5b09158, [Epub ahead of print].
8. Wu, Yunkou; Zhang, Shanrong; Soesbe, Todd C; Yu, Jing; Vinogradov, Elena; Lenkinski, Robert E. and Sherry, A Dean. "In Vivo pH Imaging of Mouse Kidneys using a paraCEST Agent" *Magn Reson Med.* **2015**, DOI 10.1002/mrm.25844, [Epub ahead of print].
9. Wu, Yunkou; Hao, Guiyang; Ramezani, Saleh; Sun, Xiankai; Saha, Debabrata; Zhao, Dawen and Sherry, A. Dean " ^{68}Ga -HP-DO3A-Nitroimidazole: A Promising Agent for PET Detection of Tumor Hypoxia" *Contrast Media Mol. Imaging* **2015**, DOI: 10.1002/cmml.1649, [Epub ahead of print].
10. Wang, Xiaojing; Wu, Yunkou; Soesbe, Todd C.; Yu, Jing; Zhao, Piyu; Kiefer, Garry E. and Sherry, A. Dean. "A pH-Responsive MRI Agent that Can Be Activated Beyond the Tissue MT Window". *Angew. Chem. Int. Ed.*, **2015**, 127(30), 8786-8788.
11. Song, Bo; Wu, Yunkou; Yu, Mengxiao; Zhao, Piyu; Zhou, Chen; Kiefer, Garry E.; Sherry, A. Dean. "A Europium(III)-based PARACEST Agent for Sensing Singlet Oxygen by MRI" *Dalton Trans.* **2013**. 42(22), 8066-8069.
12. Opina, Ana; Wu, Yunkou; Zhao, Piyu; Kiefer, Garry E.; Sherry, A. Dean. "The pH Sensitivity of $-NH$ Exchange in LnDOTA-tetraamide Complexes Varies with Amide Substituent" *Contrast Media Mol. Imaging* **2011**, 6, 459–464.
13. Wu, Yunkou; Soesbe, Todd C.; Kiefer, Garry E.; Zhao, Piyu; Sherry, A. Dean. "A Responsive Europium(III) Chelate That Provides a Direct Readout of pH by MRI." *J. Am. Chem. Soc.* **2010**, 132(40), 14002-14003.
14. Wu, Yunkou; Carney, Christiane; Denton, Michael; Hart, Elaine; Zhao, Piyu; Streblow, Daniel N.; Sherry, A. Dean; Woods, Mark. "Polymeric PARACEST MRI contrast agents as potential reporters for gene therapy." *Org. Biomol. Chem.* **2010**, 8, 5333-5338.
15. Miller, Kyle J.; Saherwala, Ali A.; Webber, Benjamin C.; Wu, Yunkou; Sherry, A. Dean; Woods, Mark. "The Population of SAP and TSAP Isomers in Cyclen-Based Lanthanide(III) Chelates Is Substantially Affected by Solvent." *Inorg. Chem.* **2010**, 49(19), 8662-8664.

16. Wu, Yunkou; Zhao, Piyu; Kiefer, Garry E.; Sherry, A. Dean. "Multifunctional Polymeric Scaffolds for Enhancement of PARACEST Contrast Sensitivity and Performance: Effects of Random Copolymer Variations." *Macromolecules*. **2010**, 43(16), 6616-6624.
17. Wu, Yunkou; Zhou, Youfu; Ouari, Olivier; Woods, Mark; Zhao, Piyu; Soesbe, Todd C.; Kiefer, Garry E.; Sherry, A. Dean. Polymeric PARACEST Agents for Enhancing MRI Contrast Sensitivity. *J. Am. Chem. Soc.* **2008**, 130(42), 13854-13855.
18. Chen, Xiaoqiang; Peng, Xiaojun; Wang, Jingyun; Wang, Yan; Wu, Song; Zhang, Lizhu; Wu, Tong; Wu, Yunkou. "Efficient Increase of DNA Cleavage Activity of a Diiron(III) Complex by a Conjugating Acridine Group" *Eur. J. Inorg. Chem.* **2007**, 34, 5400-5407.
19. Wu, Yunkou; Peng, Xiaojun; Fan, Jiangli; Gao, Shang; Tian, Maozhong; Zhao Jianzhang; Sun, Shiguo. "Fluorescence sensing of anions based on inhibition of excited-state intramolecular proton transfer" *J. Org. Chem.* **2007**, 72(1), 62-70.
20. Peng, Xiaojun; Du, Jianjun; Fan, Jiangli; Wang, Jingyun; Wu, Yunkou; Zhao Jianzhang; Sun, Shiguo; Xu, Tao. "A selective fluorescent sensor for imaging Cd²⁺ in living cells" *J. Am. Chem. Soc.* **2007**, 129(6), 1500-1501.
21. Cui, Aijun; Peng, Xiaojun; Fan, Jiangli; Chen, Xiuying; Wu, Yunkou; Guo, Binchen. "Synthesis, spectral properties and photostability of novel boron-dipyrromethene dyes" *J. Photoch. Photobio. A: Chem.* **2007**, 186, 85-92.
22. Zhou, Lichuan; Zhao, Guangjiu; Liu, Jinfeng; Han, Keli; Wu, Yunkou; Peng, Xiaojun; Sun, Mengtao. "The charge transfer mechanism and spectral properties of a near-infrared heptamethine cyanine dye in alcoholic and aprotic solvents" *J. Photoch. Photobio. A: Chem.* **2007**, 187, 305-310.
23. Peng, Xiaojun; Xu, Yongqian; Sun, Shiguo; Wu, Yunkou; Fan, Jiangli. "A ratiometric fluorescent sensor for phosphates: Zn(II)-enhanced ICT and ligand competition" *Org. Biomol. Chem.* **2007**, 5, 226-228.
24. Guo, Binchen; Peng, Xiaojun; Cui, Aijun; Wu, Yunkou; Tian, Maozhong; Zhang, Lizhu; Chen, Xiaoqiang; Gao, Yunling. "Synthesis and spectral properties of new boron dipyrromethene dyes" *Dyes Pigments*. **2007**, 73(2), 206-210.
25. Han, Feng; Bao, Yuhui; Yang, Zhigang; Fyles, Thomas M.; Zhao Jianzhang; Peng, Xiaojun; Fan, Jiangli; Wu, Yunkou; Sun, Shiguo. "Simple bisthiocarbonohydrazones as sensitive, selective, colorimetric, and switch-on fluorescent chemosensors for fluoride anions" *Chem. Eur. J.* **2007**, 13, 2880-2892.
26. Wu, Yunkou; Peng, Xiaojun; Guo, Binchen, Fan, Jiangli; Zhang, Zhichao; Wang, Jingyun; Cui, Aijun; Gao, Yunling. "Boron dipyrromethene fluorophore based fluorescence sensor for the selective imaging of Zn(II) in living cells" *Org. Biomol. Chem.* **2005**, 3, 1387-1392.
27. Peng, Xiaojun; Wu, Yunkou; Fan, Jiangli; Tian, Maozhong; Han, Keli. "Colorimetric and ratiometric fluorescence sensing of fluoride: tuning selectivity in proton transfer" *J. Org. Chem.* **2005**, 70(25), 10524-10531.
28. Fan, Jiangli; Peng, Xiaojun; Wu, Yunkou; Lu, Erhu; Hou, Jun; Zhang, Hongbing; Zhang, Rong; Fu, Xinmei. "A new PET fluorescent sensor for Zn²⁺" *J. Lumin.* **2005**, 114(2), 125-130.
29. Fan, Jiangli; Wu, Yunkou; Peng, Xiaojun. "A naphthalimide fluorescent sensor for Zn²⁺ based on photo-induced electron transfer" *Chem. Lett.* **2004**, 33, 1392-1393.

Reviews and Book Chapters

30. Milne Mark; Wu, Yunkou; Sherry, A. Dean. "paraCEST agents: discovery, design & implementation" In *Chemical Exchange Saturation Transfer Imaging: Advances and Applications*, Edited by Michael McMahon, Pan Stanford Publishing, Singapore, **2014**.
31. Sherry, A. Dean; Wu, Yunkou. "The Importance of Water Exchange Rates in the Design of Responsive Agents for MRI" *Curr Opin Chem Biol.* **2013**, 17(2), 167-174.
32. Soesbe, Todd C.; Wu, Yunkou; Sherry, A. Dean. "Advantages of Paramagnetic Chemical Exchange Saturation Transfer (CEST) Complexes Having Slow to Intermediate Water Exchange Properties as Responsive MRI Agents." *NMR Biomed.* **2013**, 26(7), 829-38.
33. Wu, Yunkou; Sun, Xiankai; Sherry, A. Dean. "Molecular Imaging and Cancer Management: PET and MR Agents for Molecular Imaging of Cancer Metabolism" In *Principles of Molecular Diagnostics and Personalized Cancer Medicine*, Edited by Dongfeng Tan, MD, and Henry Lynch, MD, Lippincott, Williams & Wilkins, Philadelphia, **2012**, Chapter 20, pp. 233-246.

34. Wu, Yunkou; Evbuomwan, Mary; Melendez, Milleo; Opina, Ana; Sherry, A. Dean. Advantages of macromolecular to nanosized chemical-exchange saturation transfer agents for MRI applications. *Future Medicinal Chemistry*. **2010**, 2(3), 351-366.

D. Research Support

Ongoing Research Support

N/A

Completed Research Support (The following research supports were terminated after moving to Howard University on April-6th-2015)

Title: PARACEST Agents for Molecular Imaging of Cancer by MRI (5 R01 CA115531-07; PI: Sherry)

Supporting agency: NIH

Performance period: 03/01/11 - 01/31/16

Level of funding: \$168,539 annual direct cost

Role: Co-investigator

Goals: The major goal is to develop applications of paramagnetic chemical exchange saturation transfer imaging agents when bound to macromolecules and as small molecule sensors of hypoxia.

Title: Southwestern NMR Center for *In Vivo* Metabolism – Project 1 (5 P41 EB015908-25; PI: Malloy)

Supporting agency: NIH

Performance period: 09/01/11- 07/31/16

Level of funding: \$151,327 annual direct cost

Role: Co-investigator

Goals: The goal of this project is to develop CEST imaging techniques to image liver glycogen *in vivo*, to map tissue pH, and to image the distribution of extracellular glucose in tissues *in vivo*.

Title: Using T2-exchange from Ln3+DOTA-based Chelates for Contrast-Enhanced Molecular Imaging of

Prostate Cancer with MRI (PC121497; W81XWH-12-PCR-P-EHDA; PI: Soesbe)

Supporting agency: NIH

Performance period: 09/01/13 - 08/31/14

Level of funding: \$75,000

Role: Co-investigator

Goals: To develop a new class of highly sensitive MRI contrast agents for the early detection applications, diagnosis and therapy in cancer.

Appendix 2 Research Projects Supported by the Nanomedicine Core

1. Physicochemical Characteristics of Nanoparticles as MR Contrast Agent Delivery System with the Dynamic Contrast Enhancement Pattern for Clinical Applications (Wang PC, Ping-Chang Lin/Radiology; Sridhar R/ Radiation Oncology; Bhujwala Z/Radiology/Johns Hopkins)
2. Develop multifunctional nanoparticles for breast cancer diagnosis and treatment – using anti-VEGFR-2 immunotoxin as dual purpose ligand and chemotherapeutics as encapsulated payload (Shan L/Radiology; Liu YY, Naville D/ NIH and Angimmune LLC).
3. Relativity simulation vs. 2D HSQC measurements of multiple fluorine compounds mixture (Ping-Chang Lin/Radiology)
4. Design of Multifunctional Polymeric Nanoparticles for Breast Cancer Diagnosis and Treatment (Akala E/Pharmacy)
5. Use of MRI/MRS to Assess for a Gamma-Glutamylcysteine Mediated in vivo Reduction in Hypoxic Stress-Induced Oxidative White Matter Injury in Mice (Costello J, Nath D, Jonas R/Children's National Medical Center)
6. Use of MRI in Mouse brain tumor model and drug delivery (Nazarian J/Children's National Medical Center)
7. A Fluorescence Imaging Approach to Visualizing peripherally inserted central catheters (Shekhar, Raj/Children's National Medical Center)
8. SPIOs with modified polymer-pHLIP peptide surface as an effective MRI-contrast agent for diagnosis of pancreatic tumor (Qibing Zhou/ Huazhong University of Science and Technology, Shan L/Radiology)
9. Neural Mechanisms of Age-Related Decline in Olfaction and Associated Cognitive Abilities (Nwulia E/Psychiatry, Obisesan T/Medicine/Howard, Casella N/Psychiatry/Johns Hopkins)
10. Efficiency of Brain Delivery of Novel Therapeutics Through the Olfactory Neuroepithelium (Nwulia E/Psychiatry)
11. Parallel computing in bioinformatics (Yayin Fan/Biochemistry, Joseph Arul/Fu Jen University)
12. Renal Oxygenation levels are Decreased in Peroxisome Proliferator Activated Receptor – α Knockout Mice during Angiotensin II Hypertension (Darah Wright, Dexter Lee/Physiology, Biophysics; Ping-Chang Lin, Stephen Lin/Radiology)
13. Anti-PSMA Diphtheria Immunotoxin for Prostate Cancer Imaging and Therapy (Shan L, /Radiology; Liu YY/ Angimmune LLC)
14. Osteopontin Genotype as a Determinant of Muscle Remodeling: A Study of African-American Young Adult Volunteers (Barfield W, Bond V/ Health and Human Performance, Wang PC, Williams L/Radiology, Hoffman EP/Children's National Medical Center)
15. Liposomal Formulation of BTZQ for Head and Neck Cancer (YL Lin/Fu Jen University)
16. Using Permanent Magnet to Guide Diffusion of Magnetic Nanoparticles in Brain Tissue Samples (Partam Manalai/Psychiatry and Behavioral Sciences)
17. Correlation of recruitment of osteogenic stem cells by stem cell derive factor 1(SDF-1) in
18. damaged muscle (Zijun Zhang/Medstar Health Research Institute)
19. Tissue-Specific Compartmental Analysis for Dynamic Contrast-Enhancement MR Imaging of
20. Complex Tumors (Wang Y/Virginia Polytechnic Institute and State University, Bhujwala Z/JohnsHopkins, Wang PC/Howard)
21. Monitoring Thiol Mediated Degradation of TOPO-Quantum Dots by ^{31}P NMR Spectroscopy (Wang TX/Chemical Engineering, Korotcov A/Radiology; Sridhar R/Radiation Oncology/Howard University).

22. Tumor Optical Imaging of Glucosamine Linked Fluorescent Probes in Mice (Korotcov A, Ye Y, Wang PC/Radiology; Achilefu S/Radiology/Washington University at St. Louis)
23. Integrin $\alpha v \beta 3$ -targeted Prostate Cancer Imaging by Near-Infrared Fluorescent Mono- and Divalent RGD Compounds (Ye Y, Korotcov A/ Radiology/ Howard University).
24. Evaluation of Novel Disulfide-containing Cyclic RGD Compounds for Prostate Cancer Optical Imaging (Yunpeng Ye, Wang PC/Radiology/Howard University)
25. Protein Nanospheres: Synergistic Nanoplatfrom-Based Probes for Multimodality Imaging (McDonald MA/ Material Measurement Laboratory/NIST, Wang PC/Radiology/Howard, Siegel EL/Radiology/University of Maryland)
26. Circumvention of Cisplatin-Resistance in Prostate Cancer (Canada R/Physiology and Biophysics)
27. Immunoliposome Based Nanotherapy of Brain Tumor (Chang E /Oncology/ Georgetown U)
28. Tumor-Targeted pH-Sensitive Nanoparticulate MRI Agent with Enhanced Contrast and Reduced Side Effect (Wang TX/Chemical Engineering, Korotcov A/Radiology)

Appendix 3 Personnel Receiving Pay in This Research Effort

Year 2

- Paul C. Wang, Ph.D (PI)
- Alexandru V. Korotcov, PhD.
- Yunpeng Ye, Ph.D.
- Rajgopalan Sridhar, Ph.D.
- Yue Chen, B.S.
- Sophia Huang, B.S.

Year 3

- Paul C. Wang, Ph.D (PI)
- Alexandru V. Korotcov, PhD.
- Ping-Chang, Lin, Ph.D. (new)
- Chung-Shieh Wu, Ph.D.
- Yue Chen, B.S.

Year 4

- Paul C. Wang, Ph.D (PI)
- Ping-Chang, Lin, Ph.D.
- Liang Shan, Ph.D.
- Zhenjiang Zhang, Ph.D.

Year 5

- Paul C. Wang, Ph.D (PI)
- Liang Shan, Ph.D.

Appendix 4 Students Who Participated in Nanomedicine Core Supported Research Projects

Postdoctoral Fellows		
Year 1, 2, 3	Chung-Shieh Wu	Chemistry/Radiology
Year 2	Hong Wang	Anatomy
	Progya Saha	Anatomy
	Yukti Sharma	Physiology & Biophysics
	Mingfe Wu	Anatomy
	David Wu	Cancer Center
Year 2, 3	Bin Zhi	Anatomy
Year 3	Fayun Zhang	Radiology
Year 3, 4	Javad Nazarian	Children's National Medical Center
	Rohan Fernandes	Children's National Medical Center
Year 4	Jie Meng	Chinese Academy of Medical Sciences
	Shimelis Hailu	Chemistry
	Shuang Shi	Dentistry
	Zhenjiang Zhang	Chemistry/Radiology
Predoctoral M.D./Ph.D./Dental Students		
Year 1	Stephen Greene	Dentistry
	Patrick Christophe	Dentistry
	David Abdelmalak	Dentistry
	Patrice Smith-Rios	Dentistry
	Stephen Hayes	Dentistry
Year 1, 2, 3, 4	Belinda Hauser	Genetics (received Ph.D. degree)
Year 1, 2	Oluseyi Awodele	Medicine
Year 2	Chunxiao Cai	Dental School
	Yuan Zhao	Dental School
Year 3	Xixue Hu	China Nat Nano Center
	Shubin Jin	China Nat Nano Center
	Xiao Ma	China Nat Nano Center
	Anil Kumar	Radiology
Year 3, 4	Whitney Barfield	Microbiology (received Ph.D. degree)
	Darah White	Physiology and Biophysics
	Philippe Auguste	Medicine
Year 4	Kenisha Ford	Physics
	Eyob Hulu	Pharmaceutical Sciences
	Ermias Tilahun	Pharmaceutical Sciences
	Brian Wu	Medicine
	Jie Xia	Pharmaceutical Sciences
Undergraduate Students		
Year 1, 2, 3	Akeem Moore -	Biology
	Sophia Huang	Pre-med
Year 2	Sulman Rahmat	Anatomy
	Kristopher Beckwith	Biology

	Subhas Mukherjee	Biology
Year 2, 3	Kacey Davis	Anatomy
Year 4	Taylor Williams	Biology

Appendix 5 Reprints of Publications (Year 5)

1. Zhang J, Li C, Zhang X, Huo S, Jin S, An FF, Wang X, Xue X, Okeke CL Duan G, Guo F, Zhang X, Hao J, Wang PC, Zhang J, Linag XJ. In vivo tumor-targeted dual-modal fluorescence/CT imaging using a nanoprobe co-loaded with an aggregation-induced emission dye and gold nanoparticles. *Biomaterials* 42:103-11. 2015, PMID 25542798
2. Li SL, Zhang CQ, Cao WP, Ma BY, Ma XW, Jin SB, Zhang JC, Wang PC, Li F, Liang XJ. Anchoring Effects of Surface Chemistry on Gold Nanorods: Modulates Autophagy. *J Mater Chem B Mater Biol Med*. 2015 Apr 28;3(16):3324-3330, PMID 26301093
3. Zhang J, Li S, An F, Liu J, Jin S, Zhang J, Wang PC, Zhang X, Lee C, Liang XJ, Self-carried Curcumin Nanoparticles for In vitro and In vivo Cancer Therapy with Real-time Monitoring of Drug Release. *Nanoscale*, 7(32):13503-10, 2015, PMID 26199064
4. Meng J, Liu YY, Gao SY, Lin S, Gu XB, Pomper MG, Wang PC, Shan L. A Bivalent Recombinant Immunotoxin with High Potency against Tumors with EGFR and EGFRvIII Expression. *Cancer Biol Ther*. 2015 Oct 15:0. [Epub ahead of print] PubMed PMID 26467217.
5. Lin PC. Assessment of chemical exchange in tryptophan–albumin solution through ¹⁹F multicomponent transverse relaxation dispersion analysis. *Journal of biomolecular NMR*. 2015 Apr 22:1-7.
6. Heier CR, Guerron AD, Korotcov A, Lin S, Gordish-Dressman H, Fricke S, Sze RW, Hoffman EP, Wang P, Nagaraju K. Non-invasive MRI and spectroscopy of mdx mice reveal temporal changes in dystrophic muscle imaging and in energy deficits. *PLoS One*. 2014 Nov 12;9(11):e112477. doi: 10.1371/journal.pone.0112477. eCollection 2014. PubMed PMID: 25390038; PubMed Central PMCID: PMC4229202.



In vivo tumor-targeted dual-modal fluorescence/CT imaging using a nanoprobe co-loaded with an aggregation-induced emission dye and gold nanoparticles

Jimei Zhang^{a, b, 1}, Chan Li^{b, 1}, Xu Zhang^b, Shuaidong Huo^b, Shubin Jin^b, Fei-Fei An^{b, ***}, Xiaodan Wang^a, Xiangdong Xue^b, C.I. Okeke^b, Guiyun Duan^a, Fengguang Guo^a, Xiaohong Zhang^c, Jifu Hao^{a, **}, Paul C. Wang^d, Jinchao Zhang^e, Xing-Jie Liang^{b, *}

^a College of Pharmacy, Taishan Medical University, Taian 271016, PR China

^b Chinese Academy of Sciences (CAS), Key Laboratory for Biological Effects of Nanomaterials and Nanosafety, National Center for Nanoscience and Technology, No. 11, First North Road, Zhongguancun, Beijing 100190, PR China

^c Nano-organic Photoelectronic Laboratory and Key Laboratory of Photochemical Conversion and Optoelectronic Materials, Technical Institute of Physics and Chemistry, Chinese Academy of Sciences, Beijing 100190, PR China

^d Laboratory of Molecular Imaging, Department of Radiology, Howard University, Washington, DC 20060, USA

^e College of Chemistry and Environmental Science, Chemical Biology Key Laboratory of Hebei Province, Hebei University, Baoding 071002, PR China

ARTICLE INFO

Article history:

Received 11 September 2014

Accepted 25 November 2014

Available online 15 December 2014

Keywords:

Dual-modal imaging

AIE dye

Gold nanoparticles

Tumor-targeting

Non-invasive fluorescence imaging

X-ray computed tomography

ABSTRACT

As an intensely studied computed tomography (CT) contrast agent, gold nanoparticle has been suggested to be combined with fluorescence imaging modality to offset the low sensitivity of CT. However, the strong quenching of gold nanoparticle on fluorescent dyes requires complicated design and shielding to overcome. Herein, we report a unique nanoprobe (M-NPAPF-Au) co-loading an aggregation-induced emission (AIE) red dye and gold nanoparticles into DSPE-PEG₂₀₀₀ micelles for dual-modal fluorescence/CT imaging. The nanoprobe was prepared based on a facile method of "one-pot ultrasonic emulsification". Surprisingly, in the micelles system, fluorescence dye (NPAPF) efficiently overcame the strong fluorescence quenching of shielding-free gold nanoparticles and retained the crucial AIE feature. *In vivo* studies demonstrated the nanoprobe had superior tumor-targeting ability, excellent fluorescence and CT imaging effects. The totality of present studies clearly indicates the significant potential application of M-NPAPF-Au as a dual-modal non-invasive fluorescence/X-ray CT nanoprobe for *in vivo* tumor-targeted imaging and diagnosis.

© 2014 Elsevier Ltd. All rights reserved.

1. Introduction

The past decade has witnessed the rapid development of imaging nanoprobes, which are able to provide physiological and pathological information with high sensitivity and specificity for disease diagnosis [1–5]. However, single imaging techniques are only able to supply limited information, which is sometimes insufficient for accurate imaging diagnosis [6–9]. Due to this

drawback, dual-modal nanoprobes, which combine the advantages of each imaging modality, have attracted great attention in recent years [10–12].

As a clinically approved imaging modality, X-ray computed tomography (CT) possesses the incomparable advantages of high spatial resolution and unlimited penetration depth [13,14]. Among various CT contrast agents, gold nanoparticle owns an extremely high X-ray absorption coefficient, regardless its preparation method, shape, diameter, etc. [15]. However, CT imaging modality shows an inherent disadvantage of low sensitivity [13]. Hence, in order to develop a complementary dual-modal imaging probe, some imaging modalities with high sensitivity need to be combined with CT.

Among all other imaging modalities, red to near-infrared (Red-NIR, 600–900 nm) fluorescence imaging is highly attractive for early

* Corresponding author. Tel.: +86 010 82545569; fax: +86 010 62656765.

** Corresponding author. Tel./fax: +86 0538 6229751.

*** Corresponding author. Tel.: +86 010 82545615; fax: +86 010 62656765.

E-mail addresses: ff_an@aliyun.com (F.-F. An), haojifu@163.com (J. Hao), liangxj@nanoctr.cn (X.-J. Liang).

¹ Authors contributed equally to this work.

non-invasive detection of cancers because it has lots of excellent advantages such as high sensitivity, low consumption and facile operation [16,17]. Fluorescence probes with long wavelength emission are highly desirable for detection, because biological tissues show relatively low absorption and autofluorescence in this region [18,19]. Therefore, it is advisable to fabricate sensitive fluorescence nanoprobes using Red-NIR dyes. However, fluorescence imaging suffers from its own shortcomings, including low spatial resolution and limited penetration depth even at Red-NIR wavelengths [7].

Based on the analysis above, it would be ideal to combine CT and fluorescence imaging together to develop a complementary imaging method with high spatial resolution and high sensitivity. However, conventional fluorescence dyes always suffer from low brightness due to a notorious phenomenon known as aggregation caused quenching (ACQ) [20]. In addition, gold nanoparticles (Au NPs), an intensely explored CT contrast agent, are well known as a strong quencher of fluorescence dyes [21]. Thus, the fabrication of fluorescence/CT dual-modal nanoprobes has been a great challenge [22,23]. In 2001, Tang et al. unveiled a fluorescent molecule which emitted strong fluorescence when aggregated and thus presented an early example of aggregation-induced emission (AIE) [16]. These unique AIE fluorescent molecules are resistant to self-quenching and provide a promising solution for fabricating new imaging probes with superior performance both *in vitro* and *in vivo*. Furthermore, if the size of a nanoprobe is appropriate, it is ideal for tumor-targeted imaging because of the enhanced permeation and retention (EPR) effect [24]. To date, however, there is rare report in the literature of whether the AIE dyes could overcome the quenching effect of gold nanoparticles to fabricate highly efficient dual-modal fluorescence/CT nanoprobes.

Herein, we fabricated a unique nanoprobe by co-loading the AIE red dye (NPAPF) and gold nanoparticles into the well-known FDA-approved material 1,2-distearoyl-sn-glycero-3-phosphoethanolamine-*N*-[methoxy(polyethylene glycol)-2000] (DSPE-PEG₂₀₀₀) micelles. The nanoprobe was prepared by a facile method of “one-pot ultrasonic emulsification”. Unexpectedly, the utilized AIE dye (NPAPF) showed relatively enhanced emission in the as-prepared micelles system despite the existence of gold nanoparticles, which guaranteed its efficient fluorescence imaging effect. *In vitro* and *in vivo* results demonstrate the nanoprobe has good biocompatibility, long blood circulation half-life, superior tumor-targeting ability, and excellent fluorescence and CT imaging effects. To our knowledge, this is the rarely reported fluorescence/CT dual-modal micelles system in which red fluorescence dye (NPAPF) reserves its AIE feature in the presence of shielding-free gold nanoparticles.

2. Materials and methods

2.1. Materials and instruments

1,2-Distearoyl-sn-glycero-3-phosphoethanolamine-*N*-[methoxy(polyethylene glycol)-2000] (DSPE-PEG₂₀₀₀) was purchased from Avanti Polar Lipids (Alabaster, AL). Bis(4-(*N*-(2-naphthyl) phenylamino) phenyl)-fumarodinitrile (NPAPF) was synthesized according to a previous report [25]. 4-bromophenylacetone, *N*-phenyl-substituted amine, Pd(OAc)₂, Cs₂CO₃ and P(*t*-Bu)₃ were purchased from J&K Scientific Ltd. Diethyl ether, sodium, dichloromethane, petroleum, methanol, toluene, chloroform, metal-oxide-semiconductor (MOS) grade nitric acid, hydrochloric acid and hydrogen peroxide were purchased from the Beijing Chemical Reagents Institute (Beijing, China). Au NPs were prepared according to the literature [26]. Gold chloride trihydrate (99.9%, HAuCl₄·3H₂O) and oleylamine (70%) were purchased from Energy-Chemical (Beijing, China). Au standard solution (1000 µg/mL) was obtained from the National Analysis Center for Iron and Steel (Beijing, China). All of the glasswares used for the preparation and storage of Au NPs were pre-cleaned with aqua regia (HCl:HNO₃ = 3:1, v/v). All of the chemicals were used without further purification, and Milli-Q water (18.2 MΩ) was used throughout this study.

The micelles were prepared on a KQ-100DE ultrasonic cleaner (Kunshan, China). Particle size was determined by dynamic light scattering (DLS) using a Malvern Zeta sizer ZS90 instrument (Worcestershire, U.K.). TEM images of all micelles were obtained through a FEI Tecnai G2 F20 S-Twin TEM (Hillsboro, OR). Emission spectra

were characterized by a Fluoromax4 spectrometer (Horiba Jobin Yvon, Edison, NJ). UV–Vis–NIR spectra were obtained by a LAMBDA 950 UV/Vis/NIR spectrometer (PerkinElmer, U.S.A.). Cellular uptake was characterized with a Zeiss LSM510 confocal laser microscope (Carl Zeiss Shanghai Co. Ltd, Shanghai, China) and an Attune® acoustic focusing cytometer (Applied Biosystems, Life Technologies, Carlsbad, CA). The biodistribution of Au in tumor tissues and organs was determined by NexION 300× inductively coupled plasma mass spectrometry (ICP-MS), (PerkinElmer, U.S.A.). *In vitro* and *in vivo* fluorescence images were collected by a Maestro 2 multi-spectral imaging system (Cambridge Research & Instrumentation, U.S.A.). *In vitro* and *in vivo* CT images were obtained by SPECT/CT scanning system (Triumph X-SPECT/X-O CT, GMI Company, U.S.A.).

2.2. Preparation and characterization of M-NPAPF-Au

Micelles loaded with NPAPF, or Au NPs, or NPAPF and Au NPs together (shortened as M-NPAPF, M-Au, M-NPAPF-Au, respectively) were prepared by “one-pot ultrasonic emulsification”. Briefly, DSPE-PEG₂₀₀₀ (8 mg) powder was placed into a round-bottom flask, and then Au NPs in chloroform (2 mg/L, 0.5 mL) and NPAPF in chloroform (1 mg/mL, 1 mL) were added into the flask and mixed thoroughly until the DSPE-PEG₂₀₀₀ was completely dissolved. After that, 10 mL Milli-Q water (18.2 MΩ) was added into the mixture, then the flask was placed in an ultrasonic bath cleaner for about 10 min ultrasonic emulsification at 100 W power. The organic solvent was then removed by evaporation while stirring in a fume hood overnight at room temperature. Following similar procedures, M-NPAPF was prepared without using Au NPs and M-Au was prepared without using NPAPF.

The morphology of M-NPAPF, M-Au and M-NPAPF-Au was examined using a Tecnai G2 20 STWIN transmission electron microscope with a 200 kV acceleration voltage. The distribution of hydrodynamic particle size was measured by a Malvern Zeta sizer ZS90.

2.3. Analysis of AIE properties and quantum yield determination

The absorption spectra of M-NPAPF, M-Au and M-NPAPF-Au were determined using a UV/Vis spectrometer and the photoluminescence (PL) spectrum was measured with a luminescence spectrometer. The concentration of CH₃CN in the CH₃CN/H₂O mixture ranged from 0% to 99.9%. Fluorescence quantum yields (QY) were determined according to the published reports in the literature [27]. Rhodamine B was chosen as a standard molecule. All UV–Vis absorption values were measured at a wavelength of 500 nm, and all PL spectra data were obtained with an excitation wavelength of 500 nm. QY values were calculated according to the following equation [28]:

$$\phi_u = \phi_s \cdot (F_u/F_s) \cdot (A_s/A_u) \quad (1)$$

(ϕ_u : quantum yield of test substance; ϕ_s : quantum yield of standard substance; F_u : integrated fluorescence intensity of test substance; F_s : integrated fluorescence intensity of standard substance; A_u : UV absorption of test substance; A_s : UV absorption of standard substance.)

2.4. Cytotoxicity studies

The cytotoxicity of M-NPAPF-Au was evaluated by MTT assay. BALB/c mice colon adenocarcinoma cells (CT26) were incubated in RPMI 1640 medium, human hepatocellular carcinoma cells (HepG2) and normal human liver cells (L02) were incubated in DMEM medium, which were all supplemented with 10% FBS, 100 U/mL penicillin, and 100 U/mL streptomycin. The cells were seeded at 5×10^3 per well into a 96-well plate overnight, respectively, then incubated with 100 µL medium containing various concentrations of M-NPAPF-Au ranging from 37.5 to 600 µg/mL for 24 h. After that, the medium was replaced with medium containing MTT (0.5 mg/mL, 100 µL) for 4 h, and then the MTT medium was replaced with 100 µL DMSO. The absorbance was measured at 570 nm with a reference wavelength of 630 nm using an Infinite M200 microplate reader (Tecan, Durham, U.S.A.). Untreated cells were used as control. All experiments were carried out with five replicates.

2.5. Flow cytometric analysis

CT26 cells were seeded at 1×10^5 cells per well into 6-well plates, then incubated with 2 mL M-NPAPF-Au (200 µg/mL). Cells were harvested at 6, 12, 24 h, and then analyzed using an Attune® acoustic focusing cytometer.

2.6. Confocal laser scanning microscopy (CLSM) imaging

CT26 cells were seeded with a density of 5×10^4 per dish in 35 mm glass microscopy dishes and incubated overnight at 37 °C. After washing with PBS, cells were incubated with 1 mL M-Au, M-NPAPF or M-NPAPF-Au (in each case the concentration of micelles was 200 µg/mL) for 24 h. Excess micelles were removed by washing three times with PBS, then cells were stained with 200 µL DAPI (20 µg/mL) for 1 min, washed three times with PBS (100 µL) and observed by confocal laser scanning microscopy (CLSM) with laser excitation at 488 nm. Fluorescence was collected at wavelengths from 660 nm to 750 nm.

2.7. Measurement of the Hounsfield units of M-NPAPF-Au

The CT numbers (called Hounsfield units, HU) of M-NPAPF-Au at different concentrations (50, 100, 200, 400, 800 $\mu\text{g/mL}$) were determined using a SPECT/CT scanning system (Triumph X-SPECT/X-O CT, GMI Company, U.S.A.). The measurement parameters were set as follows: effective pixel size, 50 μm ; 80 kVp, 500 μA ; field of view, 91.07 mm \times 91.07 mm \times 91.07 mm; fly, 360; binning, 2. Hounsfield units were acquired and analyzed using SPECT/CT scanning system workplace software.

2.8. In vivo fluorescence imaging, biodistribution and semi-quantitative pharmacokinetics studies

Female BALB/c mice aged 4–6 weeks were purchased from Vital River Company. All protocols for this animal study conformed to the Guide for the Care and Use of Laboratory Animals. All animal experiments were performed in accordance with guidelines approved by the ethics committee of Peking University. Tumor-bearing mice models were established by subcutaneous injection of 2×10^7 CT26 cells into each mouse. Two weeks later, CT26 tumor-bearing mice were intravenously injected with 200 μL of M-NPAPF-Au (1 mg/mL) and imaged using the Maestro *in vivo* spectrum imaging system. The peak excitation wavelength was 488 nm and multi-spectral imaging was from 600 to 850 nm (in 10 nm steps). The exposure time was 1000 ms for all fluorescence images and 200 ms for all bright field images.

CT26 tumor-bearing mice injected with M-NPAPF-Au were sacrificed by cervical dislocation at 6, 12 and 24 h after injection. The tumor tissues and organs including brain, heart, liver, spleen, lung, kidney and intestine were collected and imaged immediately after sacrifice. Semi-quantitative biodistribution analysis of the average ($n = 3$) fluorescence intensity of each tissue and organ was calculated using Maestro 2 software.

For semi-quantitative pharmacokinetic studies, free NPAPF (in DMSO) and M-NPAPF-Au solution were intravenously injected into different groups of BALB/c mice [29]. About 10–20 μL blood samples were drawn from the tail vein at 5, 15 and 30 min and 1, 2, 4, 6, 8, 12 and 24 h after intravenous injection. The blood samples were then solubilized with lysis buffer (RIPA) and analyzed for NPAPF with a fluorescence spectrometer at 640 nm ($\lambda_{\text{ex}} = 488 \text{ nm}$). The fluorescence of NPAPF was calculated by deducting the blank control blood sample.

2.9. In vivo CT imaging and biodistribution

For CT imaging of animals treated by direct injection into tumors, CT26 tumor-bearing mice were intratumorally injected with M-NPAPF-Au (30 μL , 70 mg/mL), then anesthetized and imaged using a SPECT/CT scanning system 15 min post-injection.

For CT imaging of animals treated by injection into the bloodstream, CT26 tumor-bearing mice were intravenously injected with M-NPAPF-Au (200 μL , 70 mg/mL), anesthetized by chloral hydrate (3.5%, w/v, 100 $\mu\text{L}/10 \text{ g}$ body weight), then imaged using a SPECT/CT scanning system at 6, 12 and 24 h after injection.

The CT imaging parameters were set as follows: effective pixel size, 50 μm ; 80 kVp, 500 μA ; field of view, 91.07 mm \times 91.07 mm \times 91.07 mm; fly, 360; binning, 2. Images were acquired and analyzed using the SPECT/CT scanning system workplace software. For biodistribution evaluation of intravenously injected M-NPAPF-Au, tumor tissue and organs including brain, heart, liver, spleen, lung, kidney and intestine were collected and digested by aqua regia, and then the Au concentration was determined by ICP-MS measurement according to a previously published method [30].

3. Results and discussion

3.1. Synthesis and characterization of M-NPAPF-Au

NPAPF, with a hydrophobic molecular structure (Fig. 1a), was synthesized according to a previous report [25]. Hydrophobic Au NPs with diameters of $\sim 9 \text{ nm}$ were prepared in oil phase [26]. TEM confirmed the particle size and morphology of the obtained Au NPs (Fig. S1). Due to the hydrophobic properties of NPAPF and Au NPs, they could both be encapsulated inside the hydrophobic core of DSPE-PEG₂₀₀₀ micelles (Fig. 1a). Micelles loaded with NPAPF or Au NPs, or co-loaded with NPAPF and Au NPs (called M-NPAPF, M-Au, M-NPAPF-Au, respectively) were prepared based on a “one-pot ultrasonic emulsification” method. A schematic diagram of the preparation procedure of M-NPAPF-Au is shown in Fig. 1b. The concise optimization were conducted and shown in Table S1. The 1:1:8 ratio of Au/NPAPF/DSPE-PEG₂₀₀₀ (w/w/w) was chosen to prepare the micelles.

The size and morphology of M-NPAPF-Au, M-NPAPF and M-Au were characterized through TEM and dynamic light scattering

(DLS) (Fig. 1c and S2). The average diameter of M-NPAPF-Au is $\sim 65 \text{ nm}$. DLS studies showed that the micelles had good mono-dispersity with an average diameter of $\sim 120 \text{ nm}$ (Fig. 1d), PDI = 0.200. It is known that particles with sizes between 30 and 150 nm are particularly favorable for tumor-targeted *in vivo* imaging due to the EPR effect [24].

3.2. AIE properties of M-NPAPF-Au

The photophysical properties of M-NPAPF-Au were studied. Firstly, NPAPF was dissolved in CH_3CN , and water was added subsequently. It was obvious that the fluorescence emission intensity of NPAPF was weak in pure CH_3CN , but surprisingly it increased when the water fraction (f_w) in the CH_3CN /water mixture was higher than 50%. At $f_w > 50\%$, the fluorescence emission intensity continuously increased as more water was added. This phenomenon is called aggregation-induced emission (AIE) (Fig. S3). It is attributed to the aggregation-induced restriction of intramolecular rotation and consequential suppression of non-radiative pathways. At a water fraction of approximately 100%, the fluorescence emission intensity is ~ 750 times higher than that in pure CH_3CN . As Au NPs can easily quench the fluorescence emission of dyes, it is crucial to verify whether the fluorescence of NPAPF is quenched when Au NPs are co-loaded into the micelles. The fluorescence emission intensity of a mixture of DSPE-PEG₂₀₀₀, NPAPF and Au NPs in pure CH_3CN is extremely low (Fig. S4a). When f_w in the CH_3CN /water mixture was less than 50%, the fluorescence of M-NPAPF-Au was extremely weak, but as f_w rose above 50%, the fluorescence was gradually enhanced. M-NPAPF-Au became highly emissive in pure aqueous solution, a phenomenon that is typical of AIE (Fig. S4a and Fig. S4b). This means that the AIE property of NPAPF is reserved in M-NPAPF-Au. UV-induced fluorescence photographs (Fig. S5) also showed that the fluorescence intensity of M-NPAPF-Au in water was obviously stronger than NPAPF in pure organic solvent (CH_3CN). This indicated that NPAPF retained its AIE properties in M-NPAPF-Au, and overcame the fluorescence quenching caused by Au nanoparticles [21]. As presented in Table S2, the fluorescence quantum yield of NPAPF in the micelles in the presence of Au NPs (QY = 8%) is much higher than that in pure CH_3CN (QY = 0.024%), suggesting that the as-prepared M-NPAPF-Au might be suitable for *in vivo* fluorescence imaging. The UV–Vis spectrum showed no impurity peak (Fig. 2a), indicating that the micelles did not aggregate. Therefore, we could affirm that the preparation method was very successful. The optimum emission of NPAPF is at $\sim 640 \text{ nm}$ (Fig. 2b), which is beneficial for non-invasive imaging because longer wavelength light (600–900 nm) has deeper penetration through biological tissues and weaker autofluorescence [17]. In addition, the Stokes shift of the as-prepared M-NPAPF-Au is as large as $\sim 120 \text{ nm}$, which will help to reduce the optical interference from the excitation light source. M-NPAPF-Au combines the advanced properties of strong Red-NIR fluorescence, large Stokes shift and appropriate size, and might therefore be applicable for *in vivo* non-invasive and tumor-targeted fluorescence imaging.

3.3. Cytotoxicity assay

Before M-NPAPF-Au can be applied as a dual-modal fluorescence/CT imaging nanoprobe, it is crucial to investigate its biocompatibility *in vitro*. After CT26, HepG2, L02 cells were incubated with M-NPAPF-Au at different concentrations (from 37.5 to 600 $\mu\text{g/mL}$) for 24 h, an MTT colorimetric assay was performed to assess cell viability (Fig. 3). Compared with the group treated with PBS, cells treated with M-NPAPF-Au were highly viable ($> 80\%$) even

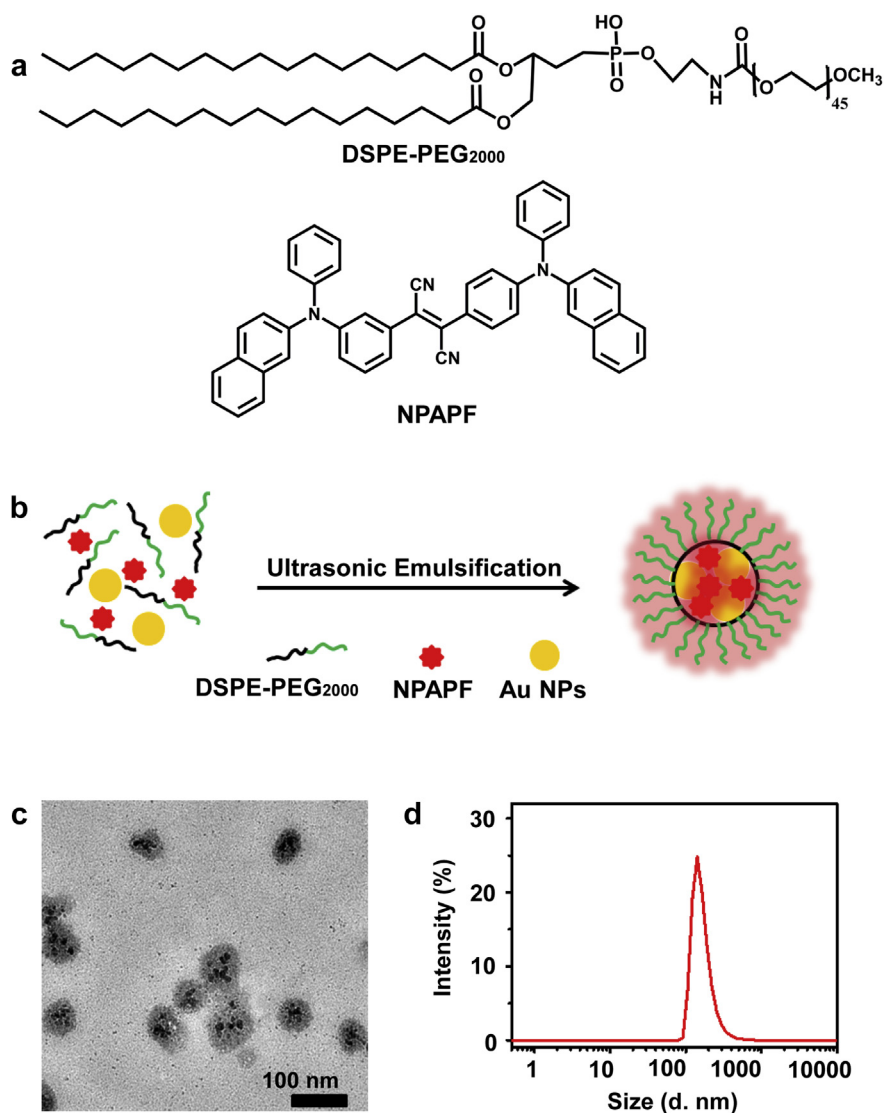


Fig. 1. (a) Molecular structures of DSPE-PEG₂₀₀₀ and NPAPF. (b) Scheme for preparation of M-NPAPF-Au. (c) TEM image of M-NPAPF-Au. (d) Size distribution of M-NPAPF-Au.

at M-NPAPF-Au concentrations up to 600 $\mu\text{g/mL}$. Our results indicate that the as-prepared M-NPAPF-Au has superior biocompatibility with both tumor cells and normal cells. In the subsequent cell studies, the M-NPAPF-Au concentration was kept under 600 $\mu\text{g/mL}$, within the safe concentration range.

3.4. Fluorescence properties *in vitro*

The *in vitro* fluorescence imaging performance of M-NPAPF-Au was next examined. As shown in Fig. 4a, higher nanoprobe concentrations resulted in stronger fluorescence intensity.

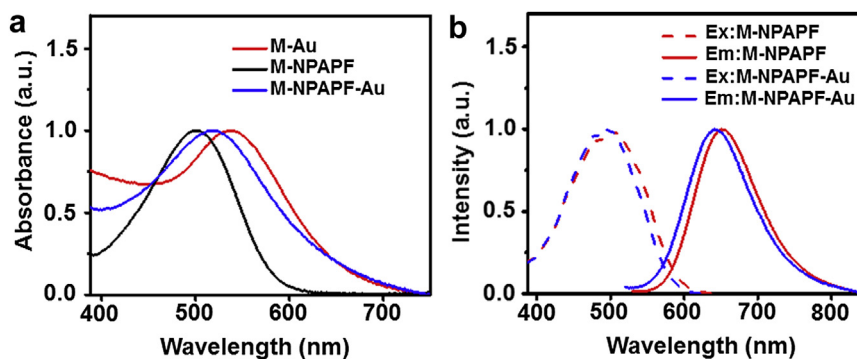


Fig. 2. (a) Normalized UV-Vis absorption spectra of M-Au, M-NPAPF and M-NPAPF-Au. (b) Normalized excitation and emission spectra of M-NPAPF and M-NPAPF-Au.

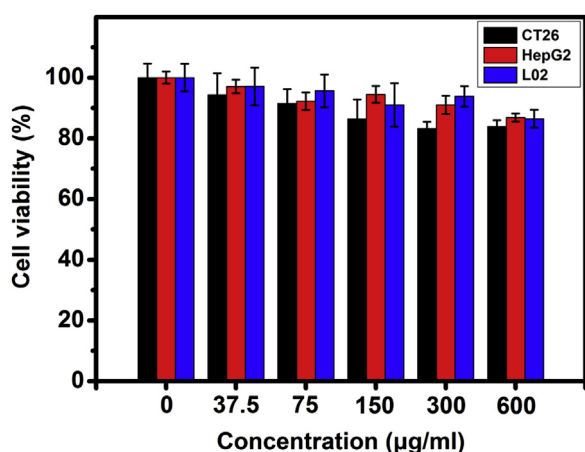


Fig. 3. Viability of CT26, HepG2, L02 cells incubated with different concentrations of M-NPAPF-Au for 24 h.

Subsequently, we quantified the cellular uptake of M-NPAPF-Au by flow cytometry. The intracellular fluorescence intensity of NPAPF gradually increased when the incubation time was extended from 6 h to 24 h (Fig. 4b), which indicated that M-NPAPF-Au (200 µg/mL) was gradually taken up by CT26 cells in a time-dependent manner (within 24 h). The intracellular imaging performance of M-NPAPF-Au was then examined. CT26 cells were incubated for 24 h with M-Au, M-NPAPF and M-NPAPF-Au (micelle concentrations were 200 µg/mL in each case), and then cells were stained with DAPI prior to CLSM imaging. As shown in Fig. 4c, blue and red regions represented DAPI (which labels nuclei) and NPAPF, respectively. For CT26 cells incubated with M-NPAPF-Au and M-NPAPF, strong red fluorescence could be observed, while no signal could be detected from cells treated with M-Au, which demonstrated that the red fluorescence came from NPAPF. In addition, the fluorescence of NPAPF in M-NPAPF-Au was not strongly quenched by Au NPs. In summary, M-NPAPF-Au has excellent fluorescence emission properties and superior biocompatibility, and therefore shows great promise for use in *in vivo* fluorescence imaging studies.

3.5. X-ray attenuation property *in vitro*

Theoretically, a good CT contrast agent must have a high X-ray attenuation coefficient [13]. Traditional CT imaging agents have

high X-ray absorption coefficients but also have several inherent shortcomings such as rapid clearance by the kidney (preventing long-term imaging), and serious renal toxicity [31,32]. Recently, some nanoparticles containing Au NPs have been actively used for CT imaging, and have given beautiful results [33,34], attributable to the higher X-ray absorption coefficient and superior biocompatibility of Au NPs. In our study, the Hounsfield units (HU) of M-NPAPF-Au at different concentrations (50, 100, 200, 400 and 800 µg/mL) were evaluated using a SPECT/CT scanning system. As demonstrated in Fig. 5a, samples of higher concentration had a deeper color and were more radiodense than more dilute samples, which corresponded with previously reported results that higher concentration led to a stronger X-ray CT attenuation intensity [35]. The HU of M-NPAPF-Au was evaluated using a SPECT/CT scanning system, and was described by the following equation:

$$HU = 0.2242 \cdot X + 3.2139 \quad (2)$$

(HU: CT numbers; X: concentration of M-NPAPF-Au, µg/mL).

Further, there is a well-correlated linear relationship ($R^2 = 0.9983$) between M-NPAPF-Au concentration and HU (Fig. 5b). These results suggest that M-NPAPF-Au is an ideal candidate for a positive CT imaging nanoprobe.

3.6. *In vivo* fluorescence imaging, biodistribution and semi-quantitative pharmacokinetics studies

Before evaluating the *in vivo* imaging, we used hemolysis analysis to study the blood compatibility of M-NPAPF-Au. As shown in Fig. S6, no visible hemolytic effects were seen even at the highest M-NPAPF-Au concentration of 10 mg/mL, indicating that M-NPAPF-Au had good hemocompatibility (<3.5%) [36].

The performance of M-NPAPF-Au in *in vivo* tumor-targeted and non-invasive fluorescence imaging was examined in CT26 tumor-bearing mice. After intravenous injection of M-NPAPF-Au (200 µL, 1 mg/mL), the mice were scanned with a multi-spectral imaging system at different time points (up to 24 h). Fig. 6a showed how the *in vivo* tumor-targeted fluorescence imaging effects changed over time. There were basal fluorescence signals from the skin and hair before injection. After intravenous injection of M-NPAPF-Au solution, the signal at the tumor site gradually became more intense and could be distinguished more readily from the autofluorescence of the mice as the time increased. At 24 h post-injection, the tumor site was much brighter than any other body part. This was

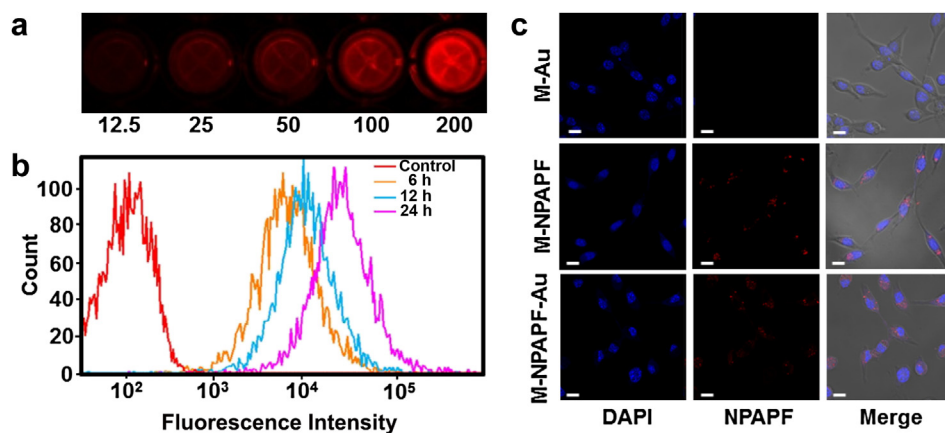


Fig. 4. (a) Change in the fluorescence intensity of M-NPAPF-Au with increasing concentration (µg/mL). (b) Quantitative analysis of M-NPAPF-Au uptake by flow cytometry. (c) Confocal images of CT26 cells after incubation with M-Au, M-NPAPF and M-NPAPF-Au for 24 h at micelle concentrations of 200 µg/mL. The images were recorded under excitation at 488 nm with 660–750 nm bandpass filters. Scale bars are 10 µm.

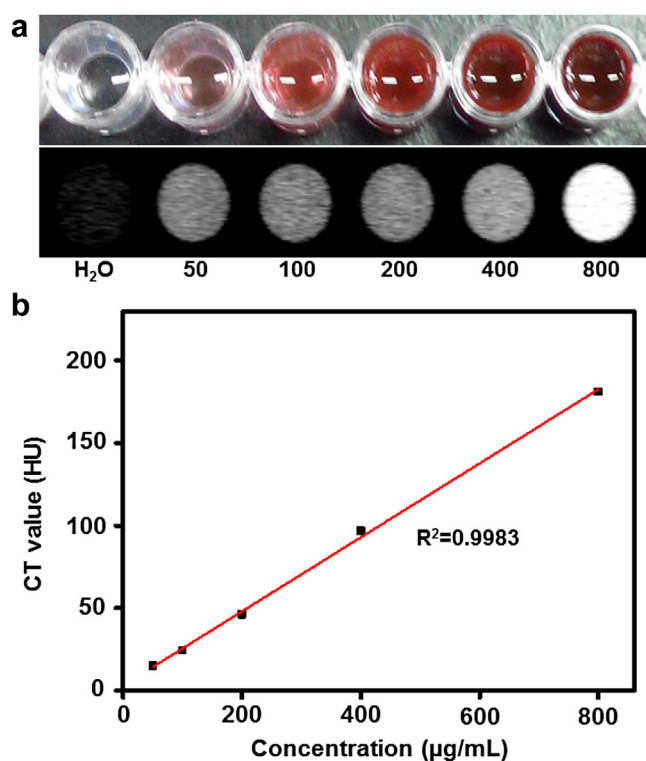


Fig. 5. (a) Digital photos (top) and corresponding CT images (bottom) of M-NPAPF-Au samples of increasing concentration (µg/mL). (b) Standard curve of CT values (Hounsfield units, HU) of M-NPAPF-Au at different concentrations.

attributed to passive enrichment of the as-prepared nanoprobe at the tumor site by the EPR effect [18].

Next, semi-quantitative biodistribution analysis was performed. A series of dissected organs and tumor tissues of mice ($n = 3$) were freshly collected at various time points (6, 12 and 24 h) post-injection, and fluorescence images were immediately taken with the multi-spectral imaging system. The fluorescence intensity of each image was subsequently calculated to give average intensity values as well as standard errors. Background autofluorescence values, obtained from tumors and organs from a control mouse without M-NPAPF-Au treatment, were subtracted. Fig. 6b showed that the as-prepared M-NPAPF-Au accumulated at higher levels in the tumor than any other organ except the liver, which was in agreement with the images of the dissected tumors and organs. The accumulation level of nanoprobe in liver was higher than that of other organs, this was consistent with other reports [31,37], which suggested that nanoparticles tended to accumulate in the reticuloendothelial system (RES). Hence, the high intensity of nanoprobe in liver is due to the uptake nature of liver.

In order to study the pharmacokinetics profile, free NPAPF (in DMSO) and M-NPAPF-Au solution were intravenously injected in two different groups of BALB/c mice [29]. 10–20 µL blood was drawn from the tail vein at different time points after injection and solubilized in lysis buffer, and then the NPAPF concentration was determined by measuring the fluorescence intensity of NPAPF and subtracting the blank blood sample from an untreated control mouse. As shown in Fig. 6c, the blood circulation half-life of free NPAPF and M-NPAPF-Au was 0.5 h and 8 h, respectively. The greatly prolonged half-life of M-NPAPF-Au was largely attributed to the perfect stability of the carrier material DSPE-PEG₂₀₀₀ [38,39]. The long half-life explains why the M-NPAPF-Au nanoparticles gradually accumulated at the tumor site throughout the test period (24 h).

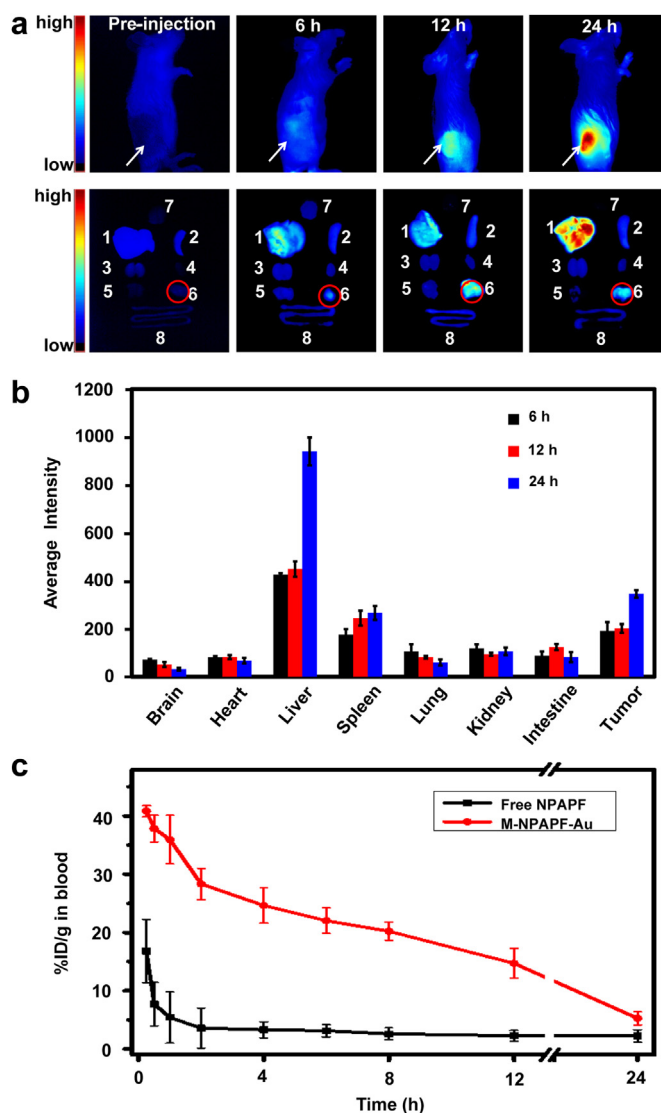


Fig. 6. (a) Non-invasive fluorescence images of CT26 tumor-bearing mice and their dissected tumors and organs 6, 12 and 24 h after intravenous injection. The white arrows indicate tumor sites and the red circles indicate dissected tumors. 1 – Liver, 2 – Spleen, 3 – Kidney, 4 – Heart, 5 – Lung, 6 – Tumor, 7 – Brain, 8 – Intestine. (b) Semi-quantitative biodistribution of M-NPAPF-Au in mice determined by the averaged fluorescence intensity of each tumor and organ (after subtraction of the fluorescence intensity before injection). Error bars are based on three mice per group. (c) Blood circulation curves of free NPAPF (black) and M-NPAPF-Au (red) determined by measuring the fluorescence intensity of NPAPF in the blood at different time points post-injection. The y-axis shows the percentage of injected dose per gram tissue (%ID/g). (For interpretation of the references to color in this figure legend, the reader is referred to the web version of this article.)

Overall, these results clearly indicate that the M-NPAPF-Au has significant potential for *in vivo* tumor-targeted fluorescence imaging.

3.7. *In vivo* CT imaging and biodistribution

Computed tomography is one of the most useful clinical diagnostic tools, and has been widely explored for its potential in tumor detection [13,14]. The distinguished *in vitro* performance of M-NPAPF-Au as a potential CT contrast agent encouraged us to test its applicability to *in vivo* CT imaging by two different methods. Initially, one group of CT26 tumor-bearing mice ($n = 3$) were

intratumorally injected with M-NPAPF-Au (20 μ L, 70 mg/mL). Pre-injection mice were used as reference (Movie. S1) and the average HU of the tumor site was estimated to be 65. After intratumoral injected for 15 min (Movie. S2), the average HU of the tumor site increased to 201. It was clear that after 15 min, the tumor region injected with M-NPAPF-Au showed an obvious enhancement of CT signal compared with the pre-injection reference (Fig. S7), indicating that the nanoprobe is suitable for *in vivo* CT imaging. Secondly, another group of CT26 tumor-bearing mice ($n = 3$) were intravenously injected with M-NPAPF-Au (200 μ L, 70 mg/mL). The average pre-injection and post-injection (6, 12, 24 h) HU values were 73 and 94, 110, 149, respectively (Fig. 7a, Movie S3–S6). We concluded that as the post-injection time increased, the nanoprobe diffused into tumor regions and gradually accumulated there via the EPR effect [24]. These results corresponded well with the multi-spectral fluorescence imaging data. Together, the results clearly demonstrate that M-NPAPF-Au has tumor-targeting properties and can be suitably used as a CT imaging agent.

Supplementary video related to this article can be found at <http://dx.doi.org/10.1016/j.biomaterials.2014.11.053>

In addition, we also analyzed the biodistribution of M-NPAPF-Au after intravenous injection. Elemental Au accumulation in the major organs including brain, heart, liver, spleen, lung, kidney, intestine and tumor was examined by ICP-MS (Fig. 7b). It was clear

that at 6, 12 and 24 h post-injection, tumor, liver and spleen had a gradually increased Au uptake. Comparing to the biodistribution analyzed by semi-quantitative fluorescent analysis, the general biodistribution data consisted with each other, in spite of minor difference. This may be contributed by the intrinsic different characteristics of organic molecule and inorganic nanoparticle, as well as the distinction of detecting techniques.

It is well known that surface PEGylation can increase the blood circulation time of nanoparticles, reduce their clearance by the reticuloendothelial system (RES) and facilitate their accumulation at the tumor site. With the prolonged circulation time resulting from DSPE-PEG₂₀₀₀ encapsulation, M-NPAPF-Au gradually accumulated at tumor sites, while in other organs except liver and spleen, Au NPs uptake was quite low.

In order to evaluate the *in vivo* toxicity of M-NPAPF-Au, especially toward the liver and spleen, we investigated body weight variation and histology analysis of mice injected with M-NPAPF-Au (200 μ L, 70 mg/mL). No obvious body weight variation was observed from the micelles injection group (Fig. S8) compared to the control group. 8 days post-injection, the mice were sacrificed, livers and spleens were sectioned and stained by hematoxylin and eosin (H&E) for histology analysis (Fig. S9). In spite of relatively high uptake of M-NPAPF-Au in liver and spleen, no apparent histopathological abnormalities were observed in comparison with

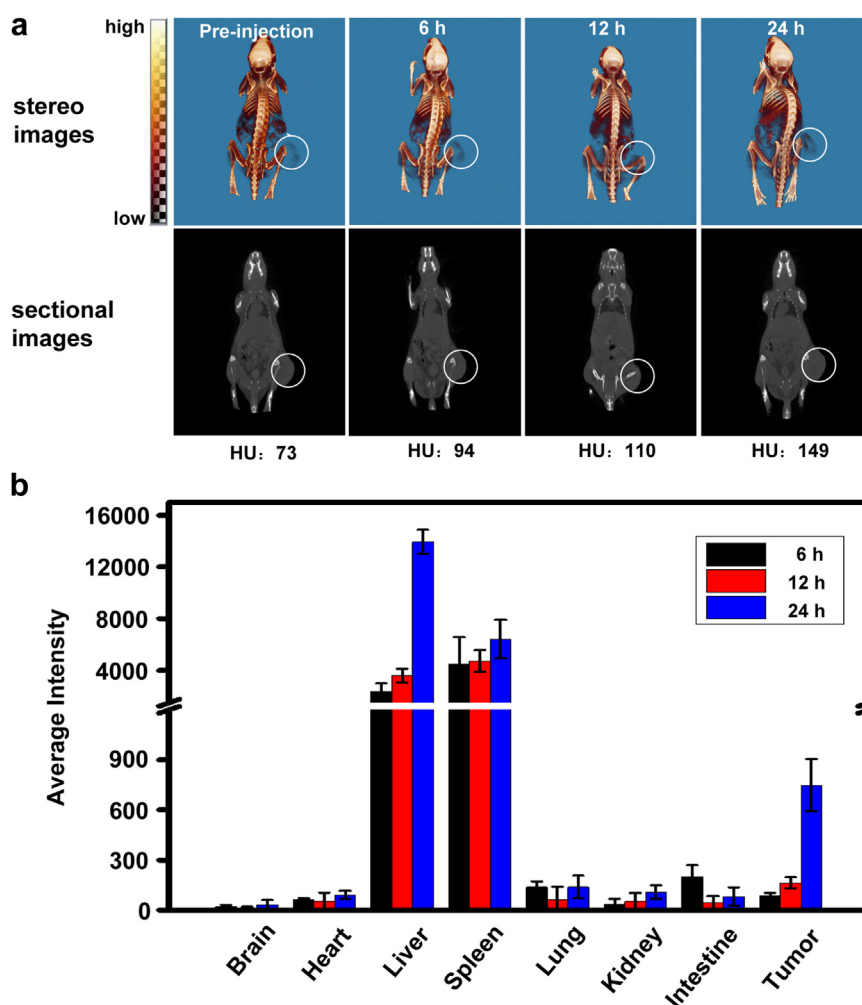


Fig. 7. (a) CT images of mice bearing transplanted CT26 tumors before (pre-injection) and after (6, 12 and 24 h) intravenous injection of M-NPAPF-Au. The white circles indicate tumor regions. The top row shows stereo images; the bottom row shows sectional images. (b) Biodistribution of Au by ICP-MS in tumor tissues and major organs including brain, heart, liver, spleen, lung, kidney, and intestine.

the control mice. These demonstrated that M-NPAPF-Au had un conspicuous *in vivo* toxicity at the concentration we used.

Above all, these results indicate that the as-prepared M-NPAPF-Au might be a unique and promising nanoprobe for potential *in vivo* tumor-targeted CT imaging. Notably, the signal intensity and nanoprobe accumulation in the tumor 24 h post intravenous injection are much higher than at the other time points. This is beneficial for future clinical applications because the contrast agents can be administered to patients during the daytime and the imaging procedure can be carried out at the same time the next day.

4. Conclusions

In summary, we have successfully developed a unique and promising dual-modal fluorescence/CT nanoprobe for tumor-targeted imaging. The nanoprobe was facile to be fabricated, via “one-pot ultrasonic emulsification”. Most important of all, the utilized AIE dye (NPAPF) showed relatively enhanced emission and retained the crucial AIE feature in the as-prepared micelles system despite the existence of gold nanoparticles, which guaranteed its efficient fluorescence imaging capacity. *In vitro* and *in vivo* results demonstrate that the nanoprobe has good cytocompatibility and hemocompatibility, long blood circulation half-life, superior tumor-targeting ability, un conspicuous *in vivo* toxicity, and excellent fluorescence and CT imaging effects. To our knowledge, this is the rarely reported fluorescence/CT dual-modal micelles system in which red fluorescence dye (NPAPF) reserves its AIE feature in the presence of shielding-free gold nanoparticles. Overall, the studies assuredly indicate the significant potential application of M-NPAPF-Au as a dual-modal non-invasive fluorescence/X-ray CT nanoprobe for *in vivo* tumor-targeted imaging and diagnosis.

Acknowledgments

This work was supported by the Chinese Natural Science Foundation project (81171455), National Distinguished Young Scholars grant (31225009) from the National Natural Science Foundation of China, Chinese Academy of Sciences (CAS) “Hundred Talents Program” (07165111ZX), CAS Knowledge Innovation Program (2012AA020804) and State High-Tech Development Plan (SS2014AA020708). The authors also appreciate the support by the “Strategic Priority Research Program” of the Chinese Academy of Sciences, Grant No. XDA09030301 and the external cooperation program of BIC, Chinese Academy of Science, Grant No. 121D11KYSB20130006. This work was also supported by grants obtained from the National Nature Science Foundation of China (No. 81102820, 81373896), Natural Science Foundation of Shandong Province (No. ZR2011HL052, J13LM51). This work was also supported in part by NIH/NCRR 3 G12 RR003048, NIH/NIMHD 8 G12 MD007597, and USAMRMC W81XWH-10-1-0767 grants. We thank Shizhu Chen for the help on the hemolytic test and histology analysis.

Appendix A. Supplementary data

Supplementary data related to this article can be found at <http://dx.doi.org/10.1016/j.biomaterials.2014.11.053>.

References

- [1] Ling D, Hackett MJ, Hyeon T. Cancer imaging: lighting up tumours. *Nat Mater* 2014;13:122–4.
- [2] Cormode DP, Jarzyna PA, Mulder WJ, Fayad ZA. Modified natural nanoparticles as contrast agents for medical imaging. *Adv Drug Deliv Rev* 2010;62:329–38.
- [3] Kobayashi H, Ogawa M, Alford R, Choyke PL, Urano Y. New strategies for fluorescent probe design in medical diagnostic imaging. *Chem Rev* 2009;110:2620–40.
- [4] Wyszocki LM, Lavis LD. Advances in the chemistry of small molecule fluorescent probes. *Curr Opin Chem Biol* 2011;15:752–9.
- [5] Baker M. Whole-animal imaging: the whole picture. *Nature* 2010;463:977–80.
- [6] Sailor MJ, Park JH. Hybrid nanoparticles for detection and treatment of cancer. *Adv Mater* 2012;24:3779–802.
- [7] Lee DE, Koo H, Sun IC, Ryu JH, Kim K, Kwon IC. Multifunctional nanoparticles for multimodal imaging and theragnosis. *Chem Soc Rev* 2012;41:2656–72.
- [8] Cutler CS, Hennkens HM, Sisay N, Huclier-Markai S, Jurisson SS. Radiometals for combined imaging and therapy. *Chem Rev* 2013;113:858–83.
- [9] Ma X, Zhao Y, Liang X-J. Theranostic nanoparticles engineered for clinic and pharmaceuticals. *Acc Chem Res* 2011;44:1114–22.
- [10] Lehman S, Stiehl DP, Honer M, Dominietto M, Keist R, Kotevic I, et al. Longitudinal and multimodal *in vivo* imaging of tumor hypoxia and its downstream molecular events. *Proc Natl Acad Sci USA* 2009;106:14004–9.
- [11] Cheng Z, Al Zaki A, Hui JZ, Muzykantor VR, Tsourkas A. Multifunctional nanoparticles: cost versus benefit of adding targeting and imaging capabilities. *Science* 2012;338:903–10.
- [12] Kim J, Piao Y, Hyeon T. Multifunctional nanostructured materials for multimodal imaging, and simultaneous imaging and therapy. *Chem Soc Rev* 2009;38:372–90.
- [13] Lee N, Choi SH, Hyeon T. Nano-sized CT contrast agents. *Adv Mater* 2013;25:2641–60.
- [14] Lusic H, Grinstaff MW. X-ray-computed tomography contrast agents. *Chem Rev* 2012;113:1641–66.
- [15] Jing LJ, Liang X, Deng ZJ, Feng SS, Li XD, Huang MM, et al. Prussian blue coated gold nanoparticles for simultaneous photoacoustic/CT bimodal imaging and photothermal ablation of cancer. *Biomaterials* 2014;35:5814–21.
- [16] Hong Y, Lam JWY, Tang BZ. Aggregation-induced emission. *Chem Soc Rev* 2011;40:5361–88.
- [17] Qin W, Ding D, Liu JZ, Yuan WZ, Hu Y, Liu B, et al. Biocompatible nanoparticles with aggregation-induced emission characteristics as far-red/near-infrared fluorescent bioprobes for *in vitro* and *in vivo* imaging applications. *Adv Funct Mater* 2012;22:771–9.
- [18] Jiang W, Singhal A, Zheng J, Wang C, Chan WC. Optimizing the synthesis of red-to near-IR-emitting CdSe-capped CdTe_xSe_{1-x} alloyed quantum dots for biomedical imaging. *Chem Mater* 2006;18:4845–54.
- [19] Byrne WL, DeLille A, Kuo C, de Jong JS, van Dam GM, Francis KP, et al. Use of optical imaging to progress novel therapeutics to the clinic. *J Control Release* 2013;172:523–34.
- [20] Ding D, Li K, Liu B, Tang BZ. Bioprobes based on AIE fluorogens. *Acc Chem Res* 2013;46:2441–53.
- [21] Li F, Pei H, Wang LH, Lu JX, Gao JM, Jiang BW, et al. Nanomaterial-based fluorescent DNA analysis: a comparative study of the quenching effects of graphene oxide, carbon nanotubes, and gold nanoparticles. *Adv Funct Mater* 2013;23:4140–8.
- [22] Hayashi K, Nakamura M, Miki H, Ozaki S, Abe M, Matsumoto T, et al. Gold nanoparticle cluster-plasmon-enhanced fluorescent silica core-shell nanoparticles for X-ray computed tomography-fluorescence dual-mode imaging of tumors. *Chem Commun* 2013;49:5334–6.
- [23] Sun IC, Eun DK, Koo H, Ko CY, Kim HS, Yi DK, et al. Tumor-targeting gold particles for dual computed tomography/optical cancer imaging. *Angew Chem Int Ed* 2011;123:9520–3.
- [24] Kunjachan S, Pola R, Gremse F, Theek B, Ehling J, Moeckel D, et al. Passive versus active tumor targeting using RGD- and NGR-modified polymeric nanomedicines. *Nano Lett* 2014;14:972–81.
- [25] Yang YL, An FF, Liu Z, Zhang XJ, Zhou MJ, Zhou MJ, et al. Ultrabright and ultrastable near-infrared dye nanoparticles for *in vitro* and *in vivo* bioimaging. *Biomaterials* 2012;33:7803–9.
- [26] Ojea-Jiménez I, García-Fernández L, Lorenzo J, Puentes VF. Facile preparation of cationic gold nanoparticle-bioconjugates for cell penetration and nuclear targeting. *ACS Nano* 2012;6:7692–702.
- [27] Dong Y, Pang H, Yang HB, Guo C, Shao J, Chi Y, et al. Carbon-based dots co-doped with nitrogen and sulfur for high quantum yield and excitation-independent emission. *Angew Chem Int Ed* 2013;52:7800–4.
- [28] Wu DQ, Li ZY, Li C, Fan JJ, Lu B, Chang C, et al. Porphyrin and galactosyl conjugated micelles for targeting photodynamic therapy. *Pharm Res* 2010;27:187–99.
- [29] Shan G, Weissleder R, Hilderbrand SA. Upconverting organic dye doped core-shell nano-composites for dual-modality NIR imaging and photo-thermal therapy. *Theranostics* 2013;3:267–74.
- [30] Chithrani BD, Ghazani AA, Chan WC. Determining the size and shape dependence of gold nanoparticle uptake into mammalian cells. *Nano Lett* 2006;6:662–8.
- [31] Wei T, Liu J, Ma HL, Cheng Q, Huang YY, Zhao J, et al. Functionalized nanoscale micelles improve drug delivery for cancer therapy *in vitro* and *in vivo*. *Nano Lett* 2013;13:2528–34.
- [32] Rabin O, Perez JM, Grimm J, Wojtkiewicz G, Weissleder R. An X-ray computed tomography imaging agent based on long-circulating bismuth sulphide nanoparticles. *Nat Mater* 2006;5:118–22.
- [33] Patra CR, Bhattacharya R, Mukhopadhyay D, Mukherjee P. Fabrication of gold nanoparticles for targeted therapy in pancreatic cancer. *Adv Drug Deliv Rev* 2010;62:346–61.

- [34] Popovtzer R, Agrawal A, Kotov NA, Popovtzer A, Balter J, Thomas E, et al. Targeted gold nanoparticles enable molecular CT imaging of cancer. *Nano Lett* 2008;8:4593–6.
- [35] Xiao QF, Bu WB, Ren QG, Zhang SJ, Xing HY, Chen F, et al. Radiopaque fluorescence-transparent TaO_x decorated upconversion nanophosphors for in vivo CT/MR/UCL trimodal imaging. *Biomaterials* 2012;33:7530–9.
- [36] Zhao YN, Sun XX, Zhang GN, Trewyn Brian G, Slowing Igor I, Lin Victor S-Y. Interaction of mesoporous silica nanoparticles with human red blood cell membranes: size and surface effects. *ACS Nano* 2011;5:1366–75.
- [37] Johnstone TC, Kulak N, Pridgen EM, Farokhzad OC, Langer R, Lippard SJ. Nanoparticle encapsulation of mitaplatin and the effect thereof on in vivo properties. *ACS Nano* 2013;7:5675–83.
- [38] Kastantin M, Ananthanarayanan B, Karmali P, Ruoslahti E, Tirrell M. Effect of the lipid chain melting transition on the stability of DSPE-PEG(2000) micelles. *Langmuir* 2009;25:7279–86.
- [39] Torchilin Vladimir P. PEG-based micelles as carriers of contrast agents for different imaging modalities. *Adv Drug Deliv Rev* 2010;62:329–38.

PAPER



Cite this: *J. Mater. Chem. B*, 2015, **3**, 3324

Anchoring effects of surface chemistry on gold nanorods: modulating autophagy†

Shengliang Li,^{*ab} Chunqiu Zhang,^{*a} Weipeng Cao,^a Benyu Ma,^c Xiaowei Ma,^a Shubin Jin,^a Jinchao Zhang,^d Paul C. Wang,^{ef} Feng Li^{‡b} and Xing-Jie Liang^{‡a}

Gold nanorods (Au NRs) have been receiving extensive attention owing to their extremely attractive properties which make them suitable for various biomedical applications. Au NRs could induce nano-toxicity, but this problem could be turned into therapeutic potential through tuning autophagy. However, the autophagy-inducing activity and mechanism of Au NRs is still unclear. Here we showed that surface chemical modification can tune the autophagy-inducing activity of Au NRs in human lung adenocarcinoma A549 cells. CTAB-coated Au NRs induce remarkable levels of autophagy activity as evidenced by LC3-II conversion and p62 degradation, while PSS- and PDDAC-coated Au NRs barely induce autophagy. More importantly, we also demonstrated that the AKT-mTOR signaling pathway was responsible for CTAB-coated Au NRs-induced autophagy. We further showed that CTAB-coated Au NRs also induce autophagy in human fetal lung fibroblast MRC-5 cells in a time-dependent manner. This study unveils a previously unknown function for Au NRs in autophagy induction, and provides a new insight for designing surface modifications of Au NRs for biomedical applications.

Received 13th January 2015,
Accepted 13th March 2015

DOI: 10.1039/c5tb00076a

www.rsc.org/MaterialsB

Introduction

Owing to their unique properties, which depend on their shape, size, and aspect ratio, nanomaterials have attracted intense interest from scientists as therapeutic and diagnostic agents.^{1–3} Gold nanorods (Au NRs) are one of most promising nanomaterials because their size, aspect ratio (ratio of length to diameter) and coating can all be easily controlled. Their applications in the biomedical field include cell and animal imaging, drug and gene delivery, and therapy and diagnosis in many diseases.^{4–8} The most convenient synthesis method for Au NRs is the seed-mediated method using cetyltrimethylammonium bromide (CTAB),

and CTAB is a well-known toxic cationic surfactant. Consequently the CTAB-Au NRs should be further coated by negatively charged PSS, positively charged PDDAC and PEG for biomedical applications. Recent studies have reported preliminary research into the intracellular localization, uptake and cytotoxicity of Au NRs in cells and whole animals. Qiu *et al.* showed that the aspect ratio and surface chemistry mediated the cellular uptake and cytotoxicity of Au NRs.⁹ In addition, Wang *et al.* demonstrated that Au NRs can be selectively targeted to mitochondria and induce cell death for cancer therapy.¹⁰ Our previous studies also indicated that the penetration and thermotherapy efficacy of Au NRs were determined by surface chemistry in multicellular tumor spheroids.¹¹ However, the mechanism of cell death induced by Au NRs is still unclear, and further study of the cell death mechanism is urgently needed before Au NRs are widely used in clinical studies.

Autophagy is a lysosome-based degradation process by which eukaryotic cells self-digest long-lived proteins and dysfunctional organelles, and thereby maintain intracellular homeostasis. Autophagy also plays an essential role in a variety of human diseases, including cancer, neurodegenerative disorders and infectious diseases.^{12–14} In general, autophagy is regarded as a prosurvival mechanism. However, increasing evidence demonstrates that autophagy plays a key role in cell death.^{15–17} Nanomaterials have been suggested to play different roles in autophagy and cell death due to their specific properties.^{18,19} Recently, several studies have demonstrated that autophagy can be induced by a variety of nanomaterials, including quantum dots (QDs), polyamidoamine (PAMAM), single-walled carbon

^a Chinese Academy of Sciences Key Lab for Biological Effects of Nanomaterials and Nanosafety, National Center for Nanoscience and Technology, No. 11, First North Road, Zhongguancun, 100190 Beijing, P. R. China. E-mail: liangxj@nanoctr.cn

^b Department of Neurobiology and Anatomy, Zhongshan School of Medicine, Sun Yat-sen University, Guangzhou, China. E-mail: lifeng@mail.sysu.edu.cn

^c The State Key Laboratory of Biomembrane and Membrane Biotechnology, Tsinghua-Peking Center for Life Sciences, School of Life Sciences, Tsinghua University, Beijing 100084, China

^d College of Chemistry & Environmental Science, Chemical Biology Key Laboratory of Hebei Province, Hebei University, Baoding, P. R. China

^e Laboratory of Molecular Imaging, Department of Radiology, Howard University, Washington, D.C. 20060, USA

^f Fu Jen Catholic University, Taipei 24205, Taiwan

† Electronic supplementary information (ESI) available. See DOI: 10.1039/c5tb00076a

‡ These authors contributed equally to this work.

nanotubes (SWNTs) and lanthanide-based nanocrystals.^{20–25} Our previous results show that gold nanoparticles can block autophagy in a size-dependent manner by increasing the lysosomal pH. In this work, we investigated the effect of Au NRs with different surface coatings on autophagy activity, and analyzed the underlying mechanisms and signaling pathway involved in Au NRs-induced autophagy.

Results and discussion

Synthesis and characterization of Au NRs

In order to investigate the surface chemistry-dependent induction of autophagy activity by Au NRs, we synthesized Au NRs with three different polymer coatings: cetyltrimethylammonium bromide (CTAB), polystyrene sulfonate (PSS) and poly(diallyldimethylammonium chloride) (PDDAC) as described in the Experimental section. CTAB, PSS and PDDAC are frequently used as model polymer coatings in Au NRs. As shown in Fig. 1a, the morphology and size of the Au NRs were measured and statistically analyzed based on TEM images. The aspect ratio of all Au NRs was 4, and the mean size of the Au NRs was 55 nm × 14 nm (length × diameter). The UV-Vis-NIR absorption spectra showed that the maximum absorption peaks were close to 808 nm, and the visible absorption spectrum was correlated with the shape, size, monodispersion and surface stabilization of the Au NRs (Fig. 1b). Zeta potential is usually used to predict the surface charge and stability of nanomaterials in solution. We measured the zeta potentials and found that the CTAB-coated Au NRs and the PDDAC-coated Au NRs were positively charged, whereas the PSS-coated Au NRs were negatively charged (Fig. 1c–e). This result is consistent with previous studies on coated Au NRs under the same conditions. It has been previously reported that the size and zeta potential of Au NRs are critical for the nonspecific adsorption of serum proteins onto the surface, and the presence of these proteins on the surface of the nanoparticles is related to the cellular uptake and cytotoxicity.⁹ We further examined the zeta potential of the surface-coated Au NRs after incubating them with DMEM containing 10% fetal bovine serum for 2 hours.

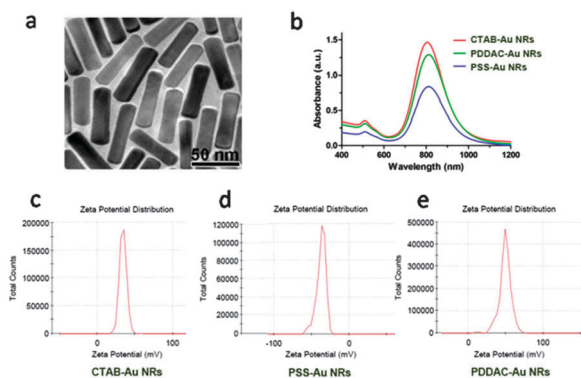


Fig. 1 Characterization of Au NRs. (a) TEM image of the CTAB-coated Au NRs. (b) Representative UV-Vis-NIR absorption spectra of CTAB-coated Au NRs, PSS-coated Au NRs and PDDAC-coated Au NRs. (c–e) Zeta potential distribution of Au NRs coated with CTAB (c), PSS (d) and PDDAC (e).

The surface charges of all the Au NRs immediately became negative, as we expected (Fig. S1 in ESI†). Thus the results of the following autophagy studies most likely depend on the surface coating of the Au NRs instead of their zeta potential.

Autophagic cell death induced by CTAB-coated Au NRs

In order to understand the mechanism of cell death induced by Au NRs, we first examined the cytotoxicity of CTAB-, PSS- and PDDAC-coated Au NRs using the autophagy inhibitor 3-methyladenine (3-MA). Starvation, the most widely used inducer of autophagy, was employed as a positive control. The results showed that 70 pM Au NRs exhibited coating-dependent toxicity to human lung adenocarcinoma A549 cells (Fig. 2a). The CTAB-coated Au NRs have notable cytotoxicity, but when further coated with PSS and PDDAC, the cytotoxicity of the Au NRs decreased greatly to negligible levels. Interestingly, we observed that the cytotoxicity induced by CTAB-coated Au NRs could be rescued by treatment with 3-MA, suggesting that CTAB-coated Au NRs likely induced cell death *via* autophagy.

To further confirm our hypothesis that CTAB-coated Au NRs induced cell death through autophagy, we used TEM to examine the formation of autophagosomes, which are key intermediate vesicles in the autophagy pathway. TEM imaging revealed that treatment with CTAB-coated Au NRs significantly increased autophagosome formation in A549 cells (Fig. 2b), compared to those treated with PSS- and PDDAC-coated Au NRs. We next examined the conversion of the autophagy-related protein

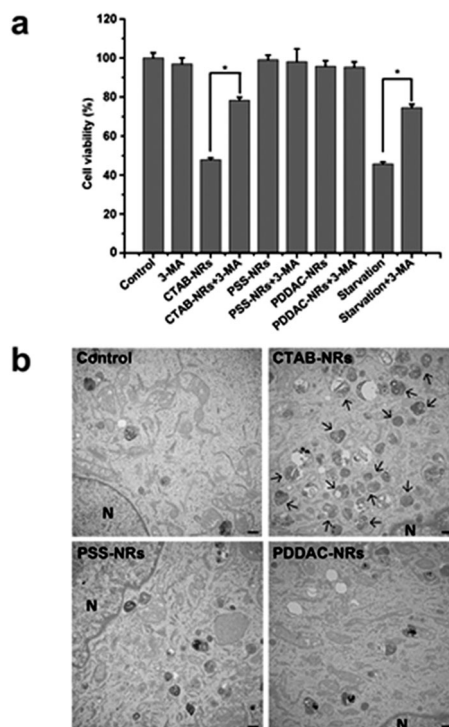


Fig. 2 Autophagic features induced by Au NRs. (a) Cell death detection after treatment with Au NRs alone, or Au NRs plus the autophagy inhibitor 3-MA. (b) TEM images of autophagosomes in A549 cells treated with Au NRs for 4 hours. Black arrows, autophagosomes. Scale bar, 500 nm.

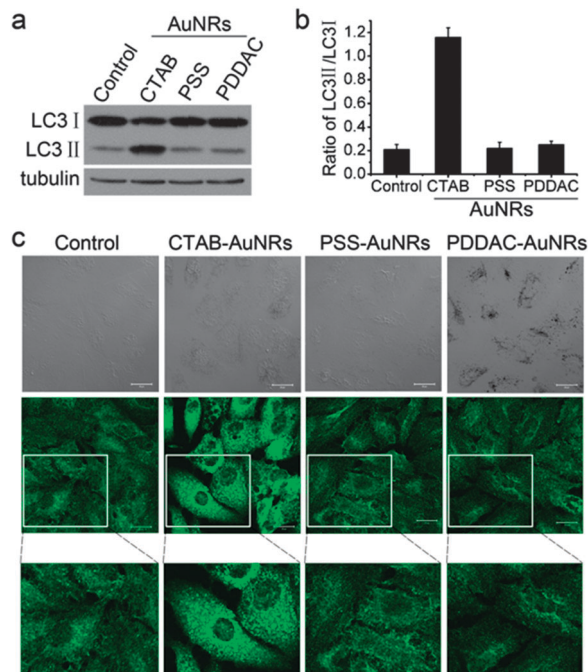


Fig. 3 Changes in LC3 distribution induced by Au NR treatment. (a) Western blotting of LC3 in A549 cells that were untreated (control) or treated with Au NRs for 4 h. (b) Statistical analysis of the LC3-II band intensity relative to that of LC3-I in (a). (c) Confocal microscopy images of the formation of endogenous LC3-positive dots in A549 cells treated with different surface-coated Au NRs for 4 h. Scale bar, 20 μ m.

microtubule-associated protein 1 light chain 3 (LC3).²⁶ LC3 has two isoforms, LC3-I, which is cytosolic, and LC3-II, which associates with autophagosomal membranes. Autophagy is characterized by an increase in LC3-II protein and LC3-positive puncta. We analyzed the expression of LC3 by western blotting and found that CTAB-coated Au NRs induced a remarkable increase in LC3-II expression compared to the control, while PSS- and PDDAC-coated Au NRs did not change the LC3-II/LC3-I ratio (Fig. 3a and b). Consistently, CTAB-coated Au NRs but not PSS- and PDDAC-coated Au NRs increased LC3 puncta formation (Fig. 3c). Moreover, we also observed that the number of PDDAC-coated Au NRs in cells was much greater than that of CTAB- or PSS-coated Au NRs. These results indicated that the level of Au NR uptake was not related to the level of autophagy induction. In addition, CTAB-coated Au NRs also induce accumulation of LC3-II in a HeLa cell line which stably expresses GFP-tagged LC3 (Fig. S2, ESI†). To confirm these results, human fetal lung fibroblast (MRC-5) cells, a normal cell line, was chose to analyze LC3-II conversion after treatment with CTAB-coated Au NRs (Fig. S3, ESI†). CTAB-coated Au NRs also induce autophagy in MRC-5 cells in a time-dependent manner. Taken together, these data demonstrate that CTAB-coated Au NRs can influence the autophagy process.

Au NRs have no effect on the function of lysosomes

Autophagosome accumulation and the enhancement of the LC3-II/LC3-I ratio may be due to inhibition or induction of autophagy.²⁷ It is well known that lysosome function, especially the internal pH, plays vital roles in maintaining cellular processes,

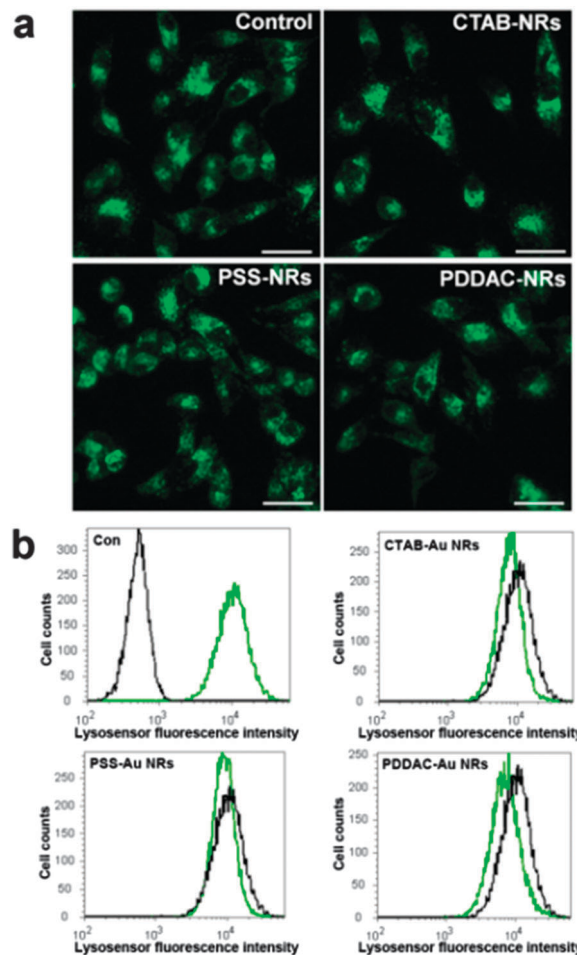


Fig. 4 Effect of different surface-coated Au NRs on lysosome pH. (a) Representative fluorescence images of A549 cells treated with different surface-coated Au NRs for 4 h, then exposed for 30 min to 1 μ M LysoSensor Green DND-189 (scale bar, 50 μ m). (b) FACS analysis of cells stained with LysoSensor Green DND-189.

including autophagy. LysoSensor Green DND-189 shows an acidification-dependent increase in fluorescence intensity, which allows us to monitor pH changes in lysosomes.^{28,29} Our previous study showed that gold nanoparticles decreased the alkalization of lysosomes and therefore inhibited autophagy in a size-dependent manner.³⁰ In order to examine whether Au NRs can affect lysosome pH, A549 cells were labeled with LysoSensor Green DND-189 dye after treatment with different Au NRs. Confocal microscopy analysis demonstrated that lysosome pH was unaffected in Au NR-treated cells (Fig. 4a). Flow cytometry analysis also confirmed this result (Fig. 4b and Fig. S4, ESI†). These results indicate that CTAB-, PSS- and PDDAC-coated Au NRs have no effect on lysosome pH and do not influence the autophagy process by this mechanism.

The AKT-mTOR signaling pathway is involved in CTAB-coated Au NR-induced autophagy

To further distinguish whether the main effect of CTAB-coated Au NRs is on autophagy induction or the blockage of autophagic flux, the ratio of LC3-II/LC3-I was checked in the presence and

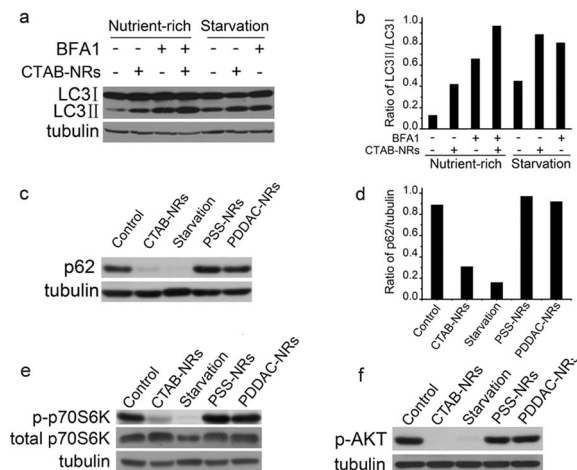


Fig. 5 Au NRs induce autophagy through the AKT-mTOR signaling pathway. (a) Western blotting of LC3 in A549 cells that were treated with CTAB-Au NRs under nutrient-rich or starvation conditions for 4 h with or without BFA1. (b) Statistical analysis of the LC3-II/LC3-I band density ratio in (a). (c) The degradation of p62 was detected by Western blotting. (d) Statistical analysis of the p62/tubulin band density ratio in (c). (e) Effect of Au NRs on the level of phospho-p70S6 kinase (p-p70S6K). Cells starved or treated with Au NRs for 4 h were analyzed with anti-p70S6K and anti-phospho-p70S6K antibodies. (f) Western blotting analysis of Au NR-treated and untreated control cells probed with anti-phospho-AKT antibody.

absence of a lysosome degradation inhibitor, bafilomycin A1 (BFA1). It was found that BFA1 further increased the CTAB-coated Au NR-induced conversion of LC3-II (Fig. 5a and b). This result indicates that the CTAB-coated Au NRs themselves actually induced autophagy. p62 (also known as SQSTM1/sequestome1), a substrate that is preferentially degraded by autophagy, was also monitored by western blotting analysis.³¹ As shown in Fig. 5c and d, starvation induced rapid down-regulation of p62. CTAB-coated Au NRs also caused marked down-regulation of p62, while PSS- and PDDAC-coated Au NRs had no effect on p62 protein level. These data suggest that CTAB-coated Au NRs promote autophagy to accelerate p62 turnover through blocking autophagic flux. In mammalian cells, autophagy is regulated by several classical signaling pathways, most of which involve the inhibition of a serine/threonine protein kinase, mammalian target of rapamycin (mTOR).^{32,33} The mTOR protein exists in a phosphorylated form and suppresses autophagy under normal conditions, but when the level of phosphorylated mTOR is down-regulated, such as during starvation, autophagy is up-regulated. To test whether CTAB-coated Au NRs induced-autophagy occurred *via* inhibition of mTOR activity, the level of phosphorylated p70 S6 kinase (p-p70S6K), an indicator for mTOR activity, was examined by western blotting analysis. It was found that both CTAB-coated Au NRs and starvation significantly decreased the level of (p-p70S6K), while PSS- and PDDAC-coated Au NRs had no effect on the expression of p-p70S6K (Fig. 5e). This demonstrated that CTAB-coated Au NRs induced autophagy through down-regulation of mTOR activity. Previous studies have shown that the effect of mTOR on autophagy can be regulated by the PI3K-AKT-TSC1/2 pathway.³⁴ To further understand the signaling pathway involved in

CTAB-coated Au NR-induced autophagy, we examined phosphorylated AKT, a vital marker upstream of the mTOR pathway.³⁵ As shown in Fig. 5f, the phosphorylated AKT level was significantly decreased when cells were incubated with CTAB-coated Au NRs, and starvation caused similar reductions. PSS- and PDDAC-coated Au NRs were analyzed under the same conditions, and had no effect on the levels of phosphorylated AKT, as we expected. Together, these results revealed that CTAB-coated Au NRs induced autophagy through the AKT-mTOR signaling pathway, while other surface coatings did not induce autophagy.

Conclusions

Accumulating evidence shows that Au NRs cause cell death for cancer therapy, however, the molecular mechanism to trigger cytotoxicity is poorly understood. As illustrated in Fig. 6, we have provided compelling evidence that CTAB-coated Au NRs promote autophagy while other surface-modifying polymers did not cause an obvious autophagy process, indicating that the autophagy-inducing activity of Au NRs is tuned by surface chemistry. Meanwhile, CTAB-coated Au NRs also induce autophagy in human fetal lung fibroblast MRC-5 cells in a time-dependent manner. Furthermore, we demonstrated that the AKT-mTOR signaling pathway is involved in the induction of autophagy by CTAB-coated Au NRs. Herein, this study unveils a previously unknown function for CTAB-coated Au NRs in autophagy induction and provides guidance for the rational design of surface coatings for nanoparticles in biomedical applications and pharmaceutical therapy.

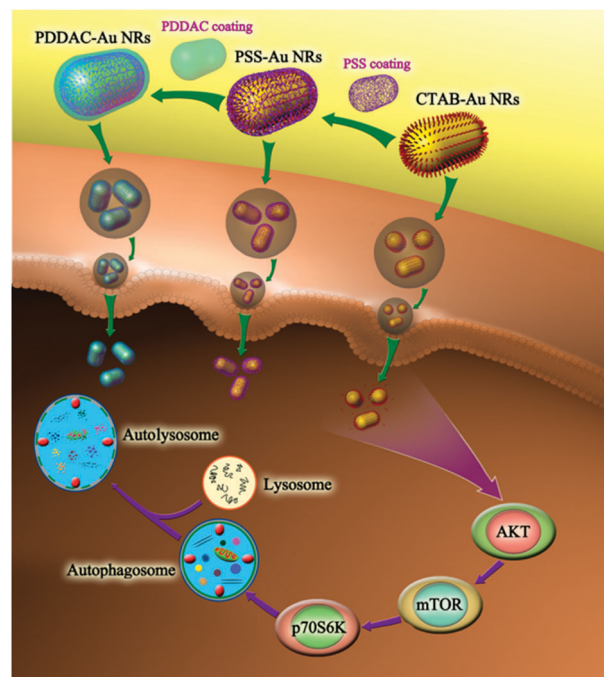


Fig. 6 Schematic illustration of the mechanism and signaling pathways in autophagy induced by CTAB-Au NRs.

Experimental section

Materials and antibodies

Dulbecco's Modified Eagle's Medium (DMEM) and fetal bovine serum (FBS) were obtained from Hyclone (Logan, UT, USA). Cetyltrimethylammonium bromide (CTAB), hydrogen tetrachloroaurate(III) trihydrate ($\text{HAuCl}_4 \cdot 3\text{H}_2\text{O}$), silver nitrate (AgNO_3), L-ascorbic acid, and sodium borohydride (NaBH_4) were purchased from Alfa Aesar. Poly(sodium-*p*-styrenesulfate) (PSS, molecular weight: 70 000) and poly (diallyldimethyl ammonium chloride) (PDDAC, 20%) were obtained from Aldrich. Lysosensor green DND-189 (L-7535) was purchased from Invitrogen. The polyclonal anti-LC3 antibody (NB100-2220) was obtained from MBL. The anti-p62 antibody was purchased from MBL. The monoclonal anti-p70S6K (#2708) and anti-phospho-p70S6K antibodies (#9206) were obtained from Cell Signaling Technology. Deionized water ($18.2 \text{ M}\Omega \text{ cm}^{-1}$) produced by a Milli-Q system (Millipore Co., USA) was used in all the experiments. Unless specified, all of the commercial products were used without further purification.

CTAB-coated Au NRs

As described previously, the CTAB-coated Au NRs were synthesized by seed-mediated growth.^{36,37} First, the CTAB-capped Au seeds were obtained by chemical reduction of HAuCl_4 with NaBH_4 : 7.5 ml CTAB (0.1 M) was mixed with 100 μl HAuCl_4 (24 mM) and diluted with water to 9.4 ml. Then, 0.6 ml ice-cold NaBH_4 (0.01 M) was freshly prepared and added while stirring magnetically. After 2 min of vigorous stirring, the seed solution was kept at room temperature (25 °C) and used within 2–5 h. Second, the Au NR growth solution, consisting of 100 ml CTAB (0.1 M), 2 ml HAuCl_4 (24 mM), 2 ml H_2SO_4 (0.5 M), a certain amount of AgNO_3 (10 mM), and 800 μl ascorbic acid (0.1 M) was prepared. The amount of Ag ions added was used to control the aspect ratio of the Au NRs. Afterwards, 240 μl of seed solution was added to the above growth solution to initiate the growth of the Au NRs. The reaction was stopped after 12 h and the outcome was centrifuged at 8000 rpm for 10 min. The precipitates were collected and re-suspended in deionized water. Au NRs with an aspect ratio of 4 were obtained.

Polyelectrolyte-coated Au NRs

The preparation of multilayer polyelectrolyte-coated Au NRs was performed *via* a layer-by-layer approach according to previous references.^{38,39} The multilayer polyelectrolyte-coated Au NRs were synthesized by sequentially coating negatively charged PSS and positively charged PDDAC onto the as-synthesized CTAB-coated Au NRs. For PSS coating, 12 ml Au NRs were centrifuged at 12 000 rpm for 10 min, and the precipitate was dispersed in 12 ml of 2 mg ml^{-1} PSS aqueous solution (containing 6 mM NaCl). The solution was stirred magnetically for 3 h. Afterwards, this solution was centrifuged at 12 000 rpm for 10 min, and the precipitate was redispersed in water. For further coating with PDDAC, a similar procedure was applied to the PSS-coated Au NRs.

Characterization of Au NRs

UV-Vis-NIR absorbance, transmission electron microscopy (TEM) and dynamic light scattering (DLS) were used for characterization of the optical properties, size and zeta potential of the particles. The UV-Vis-NIR absorption spectra were measured with a Lambda 950 UV/Vis/NIR spectrophotometer (Perkin-Elmer, USA). The size and morphology of the Au NRs was determined using a Tecnai G220 STWIN transmission electron microscope (FEI Company, Philips, Netherlands) with 200 kV acceleration voltage. The zeta-potential distribution of the Au NRs was measured by a Zetasizer Nano ZS (Malvern, England), at 25 °C.

CCK-8 assay

The human lung adenocarcinoma A549 cell line was purchased from ATCC, and cultured in DMEM supplemented with 10% FBS and 100 U ml^{-1} penicillin/streptomycin at 37 °C in a 5% CO_2 incubator at 95% humidity. A549 cells were seeded at a density of 5×10^3 cells per well in 96-well plates in culture medium and incubated overnight. The cells were then pre-treated with or without 3-MA for 4 h and the medium was then replaced with 100 μl of 70 pM Au NRs, Au NRs plus 3-MA or 3-MA. After a further incubation period of 24 h, cytotoxicity assays were performed using CCK-8 Kits (Dojindo Molecular Technologies, Tokyo, Japan). Absorbance was detected at 450 nm with a TECAN Infinite M200 microplate reader (Tecan, Durham, USA). All experiments were conducted in triplicate.

Transmission electron microscopy analysis

3×10^5 A549 cells were seeded in 33 mm dishes overnight, then incubated with 70 pM Au NRs for 4 h. The cells were fixed in 2.5% glutaraldehyde in 0.01 M PBS (pH 7.4) for 10 min at room temperature. The fixed cells were then embedded, sectioned and double stained with uranyl acetate and lead citrate for observation under the transmission electron microscope (H-7650B).

Evaluation of lysosomal acidity

A549 cells were collected from growth media after treating with 70 pM Au NRs for 4 h and washed three times with 0.01 M PBS. The cells were incubated for 30 min under growth conditions with 500 μl of prewarmed medium containing $2 \mu\text{mol L}^{-1}$ LysoSensor Green DND-189 dye (Invitrogen). After washing, the cells were resuspended in 0.01 M PBS and immediately analyzed by an Attune[®] acoustic focusing cytometer (Applied Biosystems, Life Technologies, Carlsbad, CA). The cytometer was purchased jointly with the Nanotechnology lab for bioapplications, and was installed by Life Technologies Corp. in the National Center for Nanoscience and Technology, China. The green fluorescence was collected within 1 min from a population of 20 000 cells.

Immunofluorescence analysis

Immunofluorescence analysis was performed as described previously.⁴⁰ Cells were grown in six-well plates on glass coverslips and treated with 70 pM Au NRs for 4 h. Before incubation with antibodies, cells were fixed for 30 min with 4% paraformaldehyde at room temperature, permeabilized for 10 min with

0.2% Triton X-100 (Sigma) and blocked for 2 h in 10% horse serum albumin. Incubation overnight at 4 °C with the primary antibody was followed by the secondary antibody for 3 h at room temperature. Endogenous LC3 was detected with anti-LC3 antibodies. Confocal laser scanning was done on a Zeiss LSM 710 Laser Scanning Microscope.

Western blotting

After incubating with 70 pM Au NRs for 4 h, A549 cells were lysed in lysis buffer, denatured at 100 °C for 10 min and then the proteins were separated by SDS-PAGE before transferring to PVDF membranes. Membranes were blocked for 1 h with 0.01 M PBS/0.05% Tween/5% milk. The PVDF membranes were incubated with the primary antibody at 4 °C overnight, washed in TBST, and detected by a horseradish peroxidase-conjugated secondary antibody at room temperature for 1 hour followed by treatment with the ECL detection system. Quantitative analysis was calculated using AlphaEaseFC software.

Statistical analysis

All data are presented as the mean \pm standard deviation (SD). Differences between groups were analyzed by a one-way analysis of variance (ANOVA) and *t*-test using the SPSS software package. In all statistical analyses, *p* < 0.05 was regarded as statistically significant.

Acknowledgements

This work was supported by the Chinese Natural Science Foundation project (No. 30970784, 81171455 and 81271476), a National Distinguished Young Scholars grant (31225009) from the National Natural Science Foundation of China, the National Key Basic Research Program of China (2009CB930200), the Chinese Academy of Sciences (CAS) “Hundred Talents Program” (07165111ZX), the CAS Knowledge Innovation Program and the State High-Tech Development Plan (2012AA020804). This work was also supported in part by NIH/NIMHD 8 G12 MD007597, and USAMRMC W81XWH-10-1-0767 grants. The authors also appreciate the support by the “Strategic Priority Research Program” of the Chinese Academy of Sciences, Grant No. XDA09030301 and support by the external cooperation program of BIC, Chinese Academy of Science, Grant No. 121D11KYSB20130006.

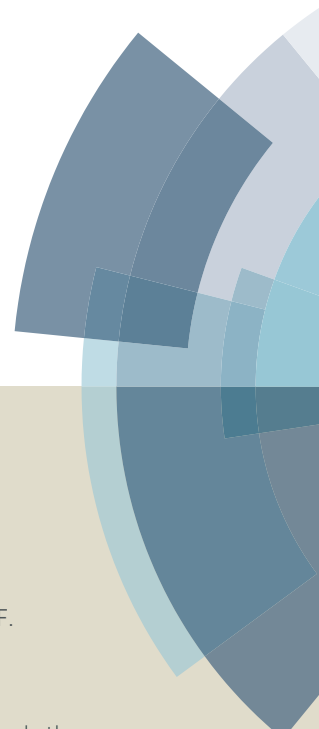
Notes and references

- 1 Y. Xia, Nanomaterials at work in biomedical research, *Nat. Mater.*, 2008, 7, 758.
- 2 E. Lavik and H. von Recum, The role of nanomaterials in translational medicine, *ACS Nano*, 2011, 5, 3419.
- 3 M. Srikanth and J. A. Kessler, Nanotechnology-novel therapeutics for CNS disorders, *Nat. Rev. Neurol.*, 2012, 8, 307.
- 4 D. P. Yang and D. X. Cui, Advances and prospects of gold nanorods, *Chem. – Asian J.*, 2008, 3, 2010.
- 5 W. I. Choi, A. Sahu, Y. H. Kim and G. Tae, Photothermal cancer therapy and imaging based on gold nanorods, *Ann. Biomed. Eng.*, 2012, 40, 534.
- 6 X. Huang, I. H. El-Sayed, W. Qian and M. A. El-Sayed, Cancer cell imaging and photothermal therapy in the near-infrared region by using gold nanorods, *J. Am. Chem. Soc.*, 2006, 128, 2115.
- 7 A. K. Salem, P. C. Searson and K. W. Leong, Multifunctional nanorods for gene delivery, *Nat. Mater.*, 2003, 2, 668.
- 8 X. H. Huang, S. Neretina and M. A. El-Sayed, Gold Nanorods: From Synthesis and Properties to Biological and Biomedical Applications, *Adv. Mater.*, 2009, 21, 4880.
- 9 Y. Qiu, Y. Liu, L. Wang, L. Xu, R. Bai, Y. Ji, X. Wu, Y. Zhao, Y. Li and C. Chen, Surface chemistry and aspect ratio mediated cellular uptake of Au nanorods, *Biomaterials*, 2010, 31, 7606.
- 10 L. Wang, Y. Liu, W. Li, X. Jiang, Y. Ji, X. Wu, L. Xu, Y. Qiu, K. Zhao, T. Wei, Y. Li, Y. Zhao and C. Chen, Selective targeting of gold nanorods at the mitochondria of cancer cells: implications for cancer therapy, *Nano Lett.*, 2011, 11, 772.
- 11 S. Jin, X. Ma, H. Ma, K. Zheng, J. Liu, S. Hou, J. Meng, P. C. Wang, X. Wu and X. J. Liang, Surface chemistry-mediated penetration and gold nanorod thermotherapy in multicellular tumor spheroids, *Nanoscale*, 2012, 5, 143.
- 12 N. Mizushima, B. Levine, A. M. Cuervo and D. J. Klionsky, Autophagy fights disease through cellular self-digestion, *Nature*, 2008, 451, 1069.
- 13 B. Levine, N. Mizushima and H. W. Virgin, Autophagy in immunity and inflammation, *Nature*, 2011, 469, 323.
- 14 D. C. Rubinsztein, P. Codogno and B. Levine, Autophagy modulation as a potential therapeutic target for diverse diseases, *Nat. Rev. Drug Discovery*, 2012, 11, 709.
- 15 Y. Tsujimoto and S. Shimizu, Another way to die: autophagic programmed cell death, *Cell Death Differ.*, 2005, 12, 1528.
- 16 D. Denton, S. Nicolson and S. Kumar, Cell death by autophagy: facts and apparent artefacts, *Cell Death Differ.*, 2012, 19, 875.
- 17 G. Kroemer and B. Levine, Autophagic cell death: the story of a misnomer, *Nat. Rev. Mol. Cell Biol.*, 2008, 9, 1004.
- 18 F. Wang, M. G. Bexiga, S. Anguissola, P. Boya, J. C. Simpson, A. Salvati and K. A. Dawson, *Nanoscale*, 2013, 5, 10868.
- 19 J. A. Kim, C. Åberg, G. de Cárcer, M. Malumbres, A. Salvati and K. A. Dawson, *ACS Nano*, 2013, 7, 7483.
- 20 O. Seleverstov, O. Zabinnyk, M. Zscharnack, L. Bulavina, M. Nowicki, J. M. Heinrich, M. Yezhelyev, F. Emmrich, R. O'Regan and A. Bader, Quantum dots for human mesenchymal stem cells labeling. A size-dependent autophagy activation, *Nano Lett.*, 2006, 6, 2826.
- 21 C. Li, H. Liu, Y. Sun, H. Wang, F. Guo, S. Rao, J. Deng, Y. Zhang, Y. Miao, C. Guo, J. Meng, X. Chen, L. Li, D. Li, H. Xu, H. Wang, B. Li and C. Jiang, PAMAM nanoparticles promote acute lung injury by inducing autophagic cell death through the Akt-TSC2-mTOR signaling pathway, *J. Mol. Cell Biol.*, 2009, 1, 37.
- 22 H. L. Liu, Y. L. Zhang, N. Yang, Y. X. Zhang, X. Q. Liu, C. G. Li, Y. Zhao, Y. G. Wang, G. G. Zhang, P. Yang, F. Guo,

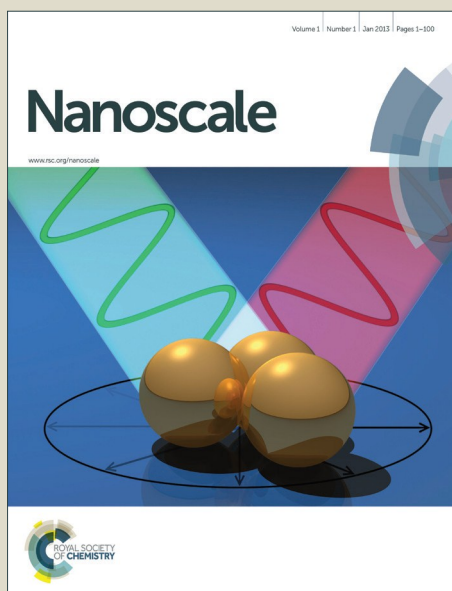
- Y. Sun and C. Y. Jiang, A functionalized single-walled carbon nanotube-induced autophagic cell death in human lung cells through Akt-TSC2-mTOR signaling, *Cell Death Dis.*, 2011, **2**, e159.
- 23 Y. Zhang, F. Zheng, T. Yang, W. Zhou, Y. Liu, N. Man, L. Zhang, N. Jin, Q. Dou, Y. Zhang, Z. Li and L. P. Wen, Tuning the autophagy-inducing activity of lanthanide-based nanocrystals through specific surface-coating peptides, *Nat. Mater.*, 2012, **11**, 817.
- 24 J. J. Li, D. Hartono, C. N. Ong, B. H. Bay and L. Y. Yung, Autophagy and oxidative stress associated with gold nanoparticles, *Biomaterials*, 2010, **31**, 5996.
- 25 S. Hussain, F. Al-Nsour, A. B. Rice, J. Marshburn, B. Yingling, Z. Ji, J. I. Zink, N. J. Walker and S. Garantzotis, Cerium dioxide nanoparticles induce apoptosis and autophagy in human peripheral blood monocytes, *ACS Nano*, 2012, **6**, 5820.
- 26 Y. Kabeya, N. Mizushima, T. Ueno, A. Yamamoto, T. Kirisako, T. Noda, E. Kominami, Y. Ohsumi and T. Yoshimori, LC3, a mammalian homologue of yeast Apg8p, is localized in autophagosome membranes after processing, *EMBO J.*, 2000, **19**, 5720.
- 27 A. Kuma, M. Matsui and N. Mizushima, LC3, an autophagosome marker, can be incorporated into protein aggregates independent of autophagy: caution in the interpretation of LC3 localization, *Autophagy*, 2007, **3**, 323.
- 28 J. Han and K. Burgess, Fluorescent indicators for intracellular pH, *Chem. Rev.*, 2010, **110**, 2709.
- 29 B. Poole and S. Ohkuma, Effect of weak bases on the intralysosomal pH in mouse peritoneal macrophages, *J. Cell Biol.*, 1981, **90**, 665.
- 30 X. Ma, Y. Wu, S. Jin, Y. Tian, X. Zhang, Y. Zhao, L. Yu and X. J. Liang, Gold nanoparticles induce autophagosome accumulation through size-dependent nanoparticle uptake and lysosome impairment, *ACS Nano*, 2011, **5**, 8629.
- 31 G. Bjørkøy, T. Lamark, A. Brech, H. Outzen, M. Perander, A. Overvatn, H. Stenmark and T. Johansen, p62/SQSTM1 forms protein aggregates degraded by autophagy and has a protective effect on huntingtin-induced cell death, *J. Cell Biol.*, 2005, **171**, 603.
- 32 L. Yu, C. K. McPhee, L. Zheng, G. A. Mardones, Y. Rong, J. Peng, N. Mi, Y. Zhao, Z. Liu, F. Wan, D. W. Hailey, V. Oorschot, J. Klumperman, E. H. Baehrecke and M. J. Lenardo, Termination of autophagy and reformation of lysosomes regulated by mTOR, *Nature*, 2010, **465**, 942.
- 33 C. H. Jung, S. H. Ro, J. Cao, N. M. Otto and D. H. Kim, mTOR regulation of autophagy, *FEBS Lett.*, 2010, **584**, 1287.
- 34 Y. P. Yang, Z. Q. Liang, Z. L. Gu and Z. H. Qin, Molecular mechanism and regulation of autophagy, *Acta Pharmacol. Sin.*, 2005, **26**, 1421.
- 35 C. Mammucari, S. Schiaffino and M. Sandri, Downstream of Akt: FoxO3 and mTOR in the regulation of autophagy in skeletal muscle, *Autophagy*, 2008, **4**, 524.
- 36 M. Liu and P. Guyot-Sionnest, Mechanism of silver(I)-assisted growth of gold nanorods and bipyramids, *J. Phys. Chem. B*, 2005, **109**, 22192.
- 37 T. K. Sau and C. J. Murphy, Seeded high yield synthesis of short Au nanorods in aqueous solution, *Langmuir*, 2004, **20**, 6414.
- 38 H. Ding, K. T. Yong, I. Roy, H. E. Pudavar, W. C. Law, E. J. Bergey and P. N. Prasad, Gold nanorods coated with multilayer polyelectrolyte as contrast agents for multimodal imaging, *J. Phys. Chem. C*, 2007, **111**, 12552.
- 39 A. M. Gole and C. J. Murphy, Polyelectrolyte-coated gold nanorods: synthesis, characterization and immobilization, *Chem. Mater.*, 2005, **17**, 1325.
- 40 J. S. Guan, Z. Z. Xu, H. Gao, S. Q. He, G. Q. Ma, T. Sun, L. H. Wang, Z. N. Zhang, I. Lena, I. Kitchen, R. Elde, A. Zimmer, C. He, G. Pei, L. Bao and X. Zhang, Interaction with vesicle luminal protachykinin regulates surface expression of delta-opioid receptors and opioid analgesia, *Cell*, 2005, **122**, 619.

Nanoscale

Accepted Manuscript



This article can be cited before page numbers have been issued, to do this please use: J. Zhang, S. Li, F. An, J. Liu, S. Jin, J. Zhang, P. C. Wang, X. Zhang, C. Lee and X. Liang, *Nanoscale*, 2015, DOI: 10.1039/C5NR03259H.



This is an *Accepted Manuscript*, which has been through the Royal Society of Chemistry peer review process and has been accepted for publication.

Accepted Manuscripts are published online shortly after acceptance, before technical editing, formatting and proof reading. Using this free service, authors can make their results available to the community, in citable form, before we publish the edited article. We will replace this *Accepted Manuscript* with the edited and formatted *Advance Article* as soon as it is available.

You can find more information about *Accepted Manuscripts* in the [Information for Authors](#).

Please note that technical editing may introduce minor changes to the text and/or graphics, which may alter content. The journal's standard [Terms & Conditions](#) and the [Ethical guidelines](#) still apply. In no event shall the Royal Society of Chemistry be held responsible for any errors or omissions in this *Accepted Manuscript* or any consequences arising from the use of any information it contains.

ARTICLE

Self-carried Curcumin Nanoparticles for *In vitro* and *In vivo* Cancer Therapy with Real-time Monitoring of Drug Release

Cite this: DOI: 10.1039/x0xx00000x

Received xxxx 2015,
Accepted xxxx 2015

DOI: 10.1039/x0xx00000x

www.rsc.org/Nanoscale

Jinfeng Zhang^{a,d†}, Shengliang Li^{b†}, Fei-Fei An^a, Juan Liu^b, Shubin Jin^b, Jin-Chao Zhang^c, Paul C. Wang^f, Xiaohong Zhang^{a,c*}, Chun-Sing Lee^{d*}, and Xing-Jie Liang^{b*}

The use of different nanocarriers for delivering hydrophobic pharmaceutical agents to tumor sites has garnered major attention. Despite the merits of these nanocarriers, further studies are needed for improving their drug loading capacities (typically less than 10%) and reducing their potential systemic toxicity. So development of alternative self-carried nanodrug delivery strategies without using any inert carriers is highly desirable. In this study, we developed a self-carried curcumin (Cur) nanodrug for highly effective cancer therapy *in vitro* and *in vivo* with real-time monitoring of drug release. With a biocompatible C₁₈PMH-PEG functionalization, the Cur nanoparticles (NPs) showed excellent dispersibility and outstanding stability in physiological environment, with drug loading capacity higher than 78 wt.%. Both confocal microscopy and flow cytometry confirmed the cellular fluorescent “OFF-ON” activation and real-time monitoring of Cur molecule release. *In vitro* and *in vivo* experiments clearly show that therapeutic efficacy of the PEGylated Cur NPs is much better than that of free Cur. This self-carried strategy with real-time monitoring of drug release may open a new way for simultaneous cancer therapy and monitoring.

1. Introduction

Cancer challenges the survival of people in the world and accounts for several millions of deaths every year.^{1,2} Among various treatments against cancer, chemotherapy is a dominant modality for its high efficiency comparing with other treatments. Unfortunately, most conventional anticancer drugs are hydrophobic and have no specific selectivity; these thus lead to various problems including poor bioavailability, rapid blood/renal clearance, low accumulation in tumors, and adverse side effects for healthy tissues.³⁻⁹ To overcome these drawbacks, much current attention has been drawn to the use of nanostructured carriers for encapsulating active drug molecules. This approach can effectively deliver hydrophobic anticancer drugs to tumor sites with improved therapeutic activity and reduced side effects.¹⁰⁻¹⁶ However, as most nanocarriers reported are inert in human body and have no therapeutic efficacy by themselves, their applications raises concerns regarding their possible toxicities and the biodegradation. Furthermore, drug loading capacity of such nanocarrier-based drug delivery system (DDS) is comparatively low (typically less than 10%) and this would reduce the effective tumor accumulation and therapeutic efficacy of the anticancer drugs.¹⁷⁻²⁰ Therefore, development of alternative self-carried nanodrug delivery strategies without using any inert carriers is highly desirable.²¹⁻²⁶ In 2012, Kasai *et al.* modified the drug-solvent interactions by jointing two drug molecules into a dimer

which enable them to form self-carried pure nanodrugs of 30-50 nm sizes via reprecipitation method.²² Recently, our group has developed an AAO-template-assisted approach for preparing 20 to 100 nm sized self-carried nanodrugs with good size and morphological controls.²⁶ However, so far most reported self-carried nanodrugs give no or weak fluorescence and thus do not provide signal for tracking their releases.

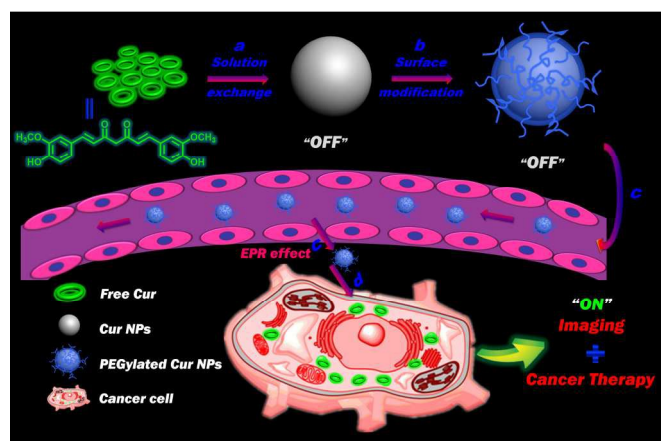
On the other hand, activatable theranostic agents that combines fluorescent and cytotoxic modalities allowing real-time monitoring of drug release in physiological systems has recently gained considerable attention.²⁷⁻³³ As most antitumor drugs give no or weak fluorescence, the most prevalent strategy for getting such theranostic agents is to load drugs into inert fluorescent NPs or trap drugs and fluorescent dyes into non-fluorescent NPs (e.g. coumarin, silicon, carbon etc.).^{12,14,30,34} However, these inert fluorescent NPs or fluorescent dyes lack therapeutic modality which leads to the mentioned issues of low drug loading capacities and potential long-term toxicities of carrier-based DDS. Furthermore, the design and synthesis of such multi-component DDS are usually time-consuming and involve complicated procedures. To address these problems, self-carried nanodrugs have been developed and demonstrate to have superior performance.²¹⁻²⁶ However, so far most reports on self-carried nanodrugs involve only *in vitro* cancer therapy; and there are few reports on their *in vivo* application.^{20,35} While it is thus highly desirable to develop self-carried nanodrug without any redundant fluorophor for *in vitro* and *in vivo* cancer therapy

with real-time monitoring capacity, this is so far not achieved to the best of our knowledge.

Herein, we choose curcumin (Cur), a hydrophobic polyphenol derived from the rhizome of the herb *Curcuma longa*, as a model hydrophobic drug to demonstrate the merits of the strategy. Cur exhibits a wide range of pharmacological effects including anti-inflammatory, anti-cancer, and anti-angiogenic properties to many tumor cell lines.^{36,37} Despite Cur's remarkable anticancer characteristics, its extremely low water solubility and poor bioavailability are impeding its wide clinical use. To address this issue, in previous works, Cur has been loaded into various inert carriers such as mesoporous silica nanoparticles,^{38,39} gold nanoparticles⁴⁰ and polymeric nanoparticles.^{41,42} However, besides their low Cur-loading capacities, the large amount of inert carriers used could lead to other concerns including their metabolisms and potential long-term toxicities.¹⁷⁻²⁰ Another reason for choosing Cur in this study is Cur's different fluorescent characteristics in its solid and molecular forms. While isolated Cur molecule gives strong green fluorescence (ON state), Cur solid shows no emission (OFF state) because of intermolecular aggregation. This two emission states is exploited in this study for monitoring the release of Cur molecules (ON) from drug nanoparticles (OFF) upon cell internalization. In this paper, Cur NPs are first prepared by reprecipitation method and then followed by surface functionalization with poly(maleic anhydride-alt-1-octadecene)-polyethylene glycol (C₁₈PMH-PEG) through hydrophobic interaction to achieve better biocompatibility, which exhibit significantly enhanced drug efficacy to colon carcinoma cells (CT-26 cells) with real-time monitoring of drug release and display improved tumor inhibition in CT-26 cell bearing mice comparing to free Cur drugs.

2. Results and Discussion

2.1 Preparation, characterization and surface functionalization of Self-carried Cur NPs



Scheme 1. Schematic illustration of functionalized self-carried Cur NPs from nanoparticle formation, PEGylation to delivery. (a) Preparation of pure Cur NPs with no fluorescence (OFF) via solution exchange method. Upper-left: the chemical structure of Cur. (b) Surface modification of the pure Cur NPs with C₁₈PMH-PEG through hydrophobic interaction. (c) Passive tumor targeting is achieved via the EPR effect, which facilitates the PEGylated Cur NPs to access tumors by way of their leaky

vasculature. (d) The PEGylated Cur NPs entered tumor cells by endocytosis and released the Cur molecules which recover their strong green fluorescence (ON).

Our proposed strategy for preparing self-carried pure Cur NPs for cancer therapy with real-time monitoring of drug release is illustrated in Scheme 1. The self-carried Cur NPs were prepared by reprecipitation method in which Cur dissolved in tetrahydrofuran (THF) solution was rapidly injected into deionized water under vigorous stirring. Due to the sudden change in solvent environment, Cur molecules will aggregate and precipitate out to form NPs. We choose the well documented reprecipitation approach here is because the technique is very simple but versatile, it is widely employed in many biomedical researches including many recent works.⁴³⁻⁴⁷ Fig. 1a and Fig. S1a show respectively an SEM and a TEM images of the Cur NPs in the form of well-defined and monodispersed nanospheres of 80-90 nm in diameter. Dynamic light scattering measurement (DLS, see Fig. 1b) presents a hydrodynamic diameter of 83.2 nm and a polydispersity index (PDI) value of 0.18.

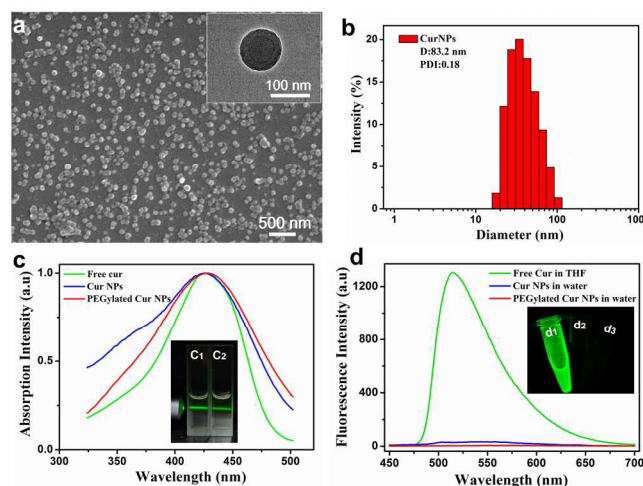


Fig. 1. Characterization and photo-physical properties of Cur NPs. a) an SEM image of the as-prepared Cur NPs (Inset is a corresponding TEM image). b) DLS and PDI measurements of the as-prepared Cur NPs in deionized water. c) Absorption and d) fluorescence spectra of free Cur dissolved in THF, the as-prepared Cur NPs and the PEGylated Cur NPs dispersed in deionized water. Inset in (c) displays that a beam of green laser shines through the samples showing scattering from the NPs via the Tyndall effect (c1: as-prepared Cur NP; c2: the PEGylated Cur NP). Inset in (d) shows photograph of the fluorescence from the three samples (d1: free Cur; d2: as-prepared Cur NP; d3: the PEGylated Cur NP).

To enhance their biocompatibility for facilitating further *in vivo* application, surface modification of the as-prepared Cur NPs is essential. Previous researchers have demonstrated that PEG is an effective biocompatible building block that has been widely applied to biomaterials for reducing nonspecific adsorption of biological substances and provide excellent long-term *in vivo* stability.⁴⁸⁻⁵¹ Here, C₁₈PMH-PEG was anchored to the surface of the as-prepared Cur NPs by ultrasonication (the product hereafter referred as PEGylated Cur NPs). Fig. S1b show a TEM image and a DLS measurement (inset) of the PEGylated Cur NPs with sizes around 100 nm. We also measured zeta potentials of the Cur NPs and the PEGylated Cur

NPs which both displays negative charge (Fig. S2). Fig. S3 presents the digital photographs of different samples including free Cur in THF, free Cur, Cur NPs and PEGylated Cur NPs dispersed in water respectively, which show a good dispersibility and better stability of NP than that of free drug in water. We also observed that while the PEGylated Cur NPs exhibit high stability in water and physiological saline even over 5 days, the as-prepared Cur NPs show fast agglomeration into larger particles (Fig. S4). Thus, it demonstrates that surface functionalization of Cur NPs was successfully achieved with excellent water stability, thus making the PEGylated Cur NPs *in vivo* drug delivery possible.

An obvious advantage of self-carried pure nanodrug delivery systems is their high drug loading capacities. Owing to no addition of any inert excipients, the average Cur loading efficiency and encapsulation efficiency here are estimated to be 78.5% and 95.8% respectively by using standard absorbance technique (Fig. S5). This loading capacity is much higher than those achieved with carrier-based DDS (typically less than 10%) and is the highest value reported among all reported Cur-based nanomedicine (Table S1).

To further investigate photo-physical properties of the Cur NPs, we measured absorption and fluorescence spectra of free Cur dissolved in THF, the as-prepared Cur NPs and the PEGylated Cur NPs dispersed in deionized water. As exhibited in Figure 1c, the three samples show similar absorption spectra with the same Cur characteristic absorption peak at about 428 nm suggesting that the Cur molecular structure remains unchanged in preparation process. As expected, the free Cur solution shows strong green fluorescence (ON), while the two Cur NP dispersions show no fluorescence (OFF) (Fig. 1d) because of aggregation-caused quenching effect. When Cur NPs enter tumor cells, Cur molecule will be released and recovering its green fluorescence again (ON). Subsequent cell imaging experiments will further confirm the successful implementation of this fluorescent "OFF-ON" system which enables self-monitoring of Cur drug release.

2.2 Cumulative drug release profiles

The drug release profile is of great importance for practical drug delivery applications of the proposed DDS. Concentrations of released Cur were determined via absorption measurement (Fig. S5). As depicted in Fig. 2, in the first 32 hours, the as-prepared Cur NPs reached approximately 46 wt% drug release and the PEGylated Cur NPs exhibited about 36 wt% drug release. Due to dissolution of the exterior PEG layer, the PEGylated Cur NPs show a slower release comparing to the as-prepared Cur NPs. Both of these two as-prepared NPs show no initial burst release, but a sustained release feature with over 60%, and Cur being released for as long as 300 hours. The slow and steady release without burst discharge of the Cur NPs is essential for their *in vivo* applications for improved long-term blood circulation and more efficient delivery to tumors with reduced drug leakage on their ways.

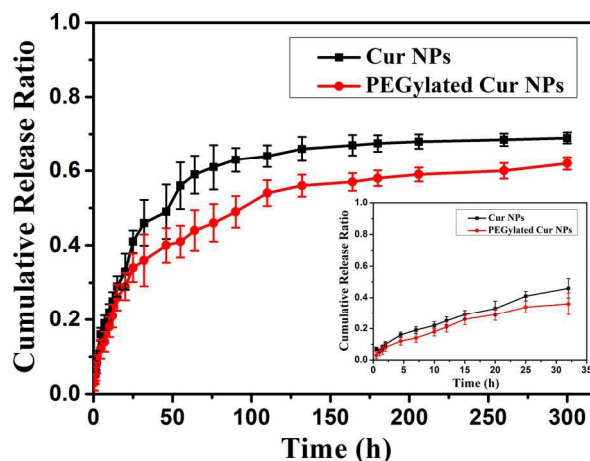


Fig. 2. Cumulative drug releases from the as-prepared Cur NPs and the PEGylated Cur NPs as a function of release time in PBS medium over 300 hours. Inset is the results for the first 32 hours.

2.3 Cellular uptake and imaging of PEGylated Cur NPs

To investigate the cellular uptake and intracellular distribution of the released Cur molecules, the CT-26 cells were incubated with PEGylated Cur NPs at 37 °C for 4 h. Fluorescence images of the incubated cells were taken with a confocal laser scanning microscope, where 4, 6-diamidino-2-phenylindole (DAPI) was used as a nucleus located dye. LysoTracker Red or MitoTracker Red was also used for staining the lysosomes and the mitochondria respectively. As shown in Fig. 3, the intense homogeneous cytoplasmic green fluorescences around the nuclei confirm Cur molecules have been released in the cells. Besides labeling the lysosomal vesicles, the Cur molecules are also able to stain almost everywhere else in the cytoplasm, providing insights into the sub-cellular distribution of the Cur NPs.

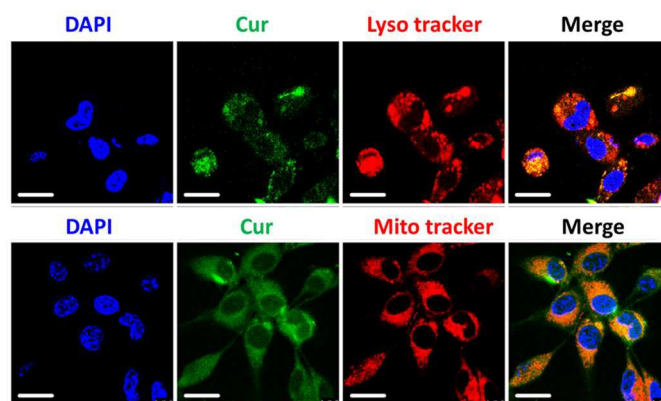


Fig. 3. Confocal microscopic images of colocalized experiment in CT-26 cells. Cell nuclei is stained with DAPI (blue signal) and lysosome and mitochondria are stained with LysoTracker Red (red signal) and Mitotracker Red (red signal) respectively. The upper and lower roles of micrographs show that the Cur molecules have been released into lysosome and mitochondria respectively. Scale bar is 20 μm .

We next studied the cellular fluorescent "OFF-ON" and real-time monitoring of Cur molecule release. The CT-26 cells were cultured with PEGylated Cur NPs for different durations (0,

ARTICLE

0.5, 1 and 4 h), and fluorescence from the cells was then analyzed with both confocal microscopy and flow cytometry. As mentioned above, the fluorescence of Cur are quenched (OFF) in the form of NPs, but recovered (ON) upon cell internalization as free molecules. As expected, Fig. 4 and Fig. S6 show that after 30 min or longer incubation duration, green Cur molecular fluorescence (ON) can be detected; whereas no signal (OFF) can be observed at the beginning of incubation since Cur is still in the state of NP. This demonstrates that the present Cur NPs are promising for monitoring drug release with a cellular fluorescent “OFF-ON” action. To further confirm the real-time monitoring capacity of the NPs, flow cytometric analyses of the CT-26 cells after incubation with PEGylated Cur NPs for different durations was shown in Figure S7. Enhanced green fluorescence in the cell was observed after 1 and 4 h of incubations, which could be attributed to Cur molecules gradually released from the NPs in a cellular environment. These results indicated that PEGylated Cur NPs possessed a time-dependent cellular release ability.

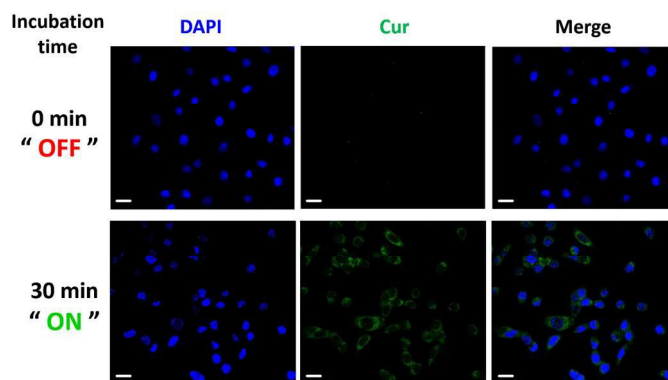


Fig. 4. Confocal microscopic images of the CT-26 cells treated with the PEGylated Cur NPs. The images were taken immediately (upper roll) and 30 min (lower roll) after adding 5 μM of the Cur NPs to the cells. Scale bar is 20 μm .

2.4 *In vitro* cytotoxic activity

We next studied cytotoxicity profiles of the PEGylated Cur NPs to the CT-26 cells compared with free Cur with a MTT assay. As depicted in Fig. 5 and Fig. S8, PEGylated Cur NPs show considerably higher cytotoxicity than the free Cur in all doses. The MTT data reveal that the Cur NPs can obviously inhibit the proliferation of the CT-26 cells, as shown by a 8-fold decrease in the half-maximal inhibitory concentration (IC_{50}) values from the free Cur ($\text{IC}_{50} = 33.4 \mu\text{M}$) to the PEGylated Cur NPs ($\text{IC}_{50} = 4.2 \mu\text{M}$) at 24 h. The improved drug efficiency may be due to the more efficient internalization of the functionalized NPs compared with that of free molecules. To check that the observed cytotoxicity is not caused by the PEG coating, MTT assay was carried out for the C_{18}PMH -PEG surfactant. The results as presented in Fig. S9 confirm that the surfactant has no cytotoxicity. Moreover, bright field microscopic images of the CT-26 cells were collected to monitor cell viability directly (Fig. S10). Significant damage to the impregnated CT-26 cells could be clearly observed with the least live cells in the PEGylated Cur NPs incubated group while the control and C_{18}PMH -PEG group show no cytotoxicity, which agree well with the MTT experiments. These results show that the self-carried functionalized Cur NPs have improved inhibiting effect on CT-26 cell growth.

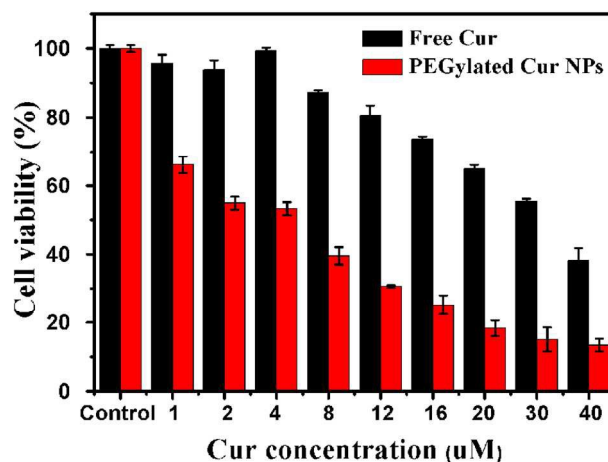


Fig. 5. Cell viability of free Cur and PEGylated Cur NPs in CT-26 cell line after 24 hours of incubation.

2.5 *In vivo* cytotoxic activity

Before intravenous injection, hemolysis assay was performed to confirm the biocompatibility of the PEGylated Cur NPs (Fig. S11). The hemolysis percentages of mice erythrocytes incubated for 3 h at 37 $^{\circ}\text{C}$ with the NPs of different concentrations were determined to be insignificant. This confirms that the PEGylated Cur NPs do not cause erythrocytes rupture. To evaluate whether the PEGylated Cur NPs do have better therapeutic efficacy *in vivo*, CT-26 tumor-bearing nude mice were intravenously injected with free Cur and the PEGylated Cur NPs respectively. For comparison, physiological saline was used as a control for the intravenous injection. Tumor volume and body weight of the tumor-bearing mice were monitored for 21 days. At the end of the experiments, the tumor volumes (Fig. 6a) in mice treated with PEGylated Cur NPs were much smaller than those treated with saline and free Cur. After treatment for 21 days, the tumor volumes in the PEGylated Cur NPs group and the free Cur group are only 32% and 87% respectively of that in the saline group. This shows that the PEGylated Cur NPs do have predominant tumor growth inhibitory efficacy comparing to saline and free Cur. These observations are in accordance with the results of *in vitro* evaluations. In addition, no significant weight loss was observed in the tumor-bearing mice treated with various formulations, indicating negligible side effect of Cur NPs for tumor therapy at the employed dose (10 mg kg^{-1} Cur-equivalent) (Fig. 6b). After treatment for 21 days, the mice were sacrificed and the tumors were dissected and photographed (Fig. 6c). The tumor inhibitory rate (TIR) was calculated from tumor weights (Fig. 6c). Comparing with that of the saline group, TIR of the PEGylated Cur NPs reaches up to 45%, which is significantly higher than that of free Cur (5%) (Fig. 7d). All these results confirm that therapeutic efficacy of the PEGylated Cur NPs is much better than that of the free Cur both *in vitro* and *in vivo*.

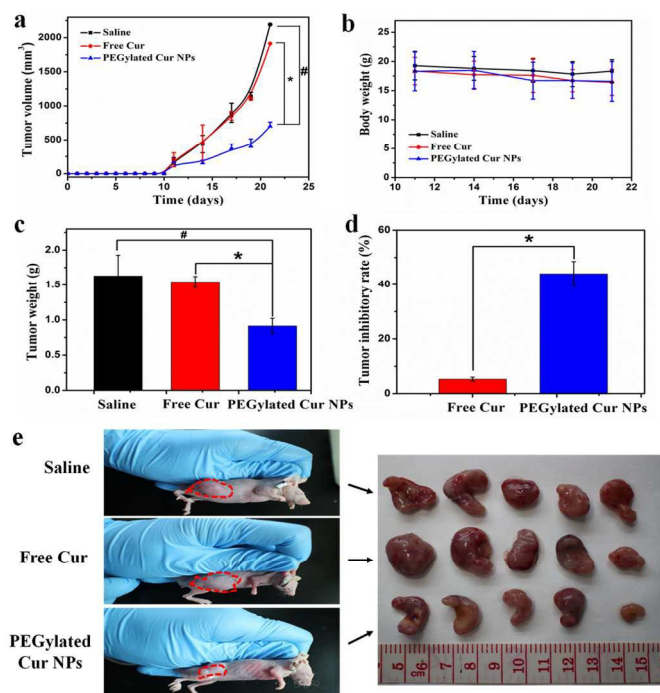


Fig. 6. *In vivo* anticancer activity. a) Tumor volume after intravenous injection of saline, free Cur and PEGylated Cur NPs in CT-26 tumor-bearing nude mice. b) Body weights of CT-26 tumor-bearing mice after treatment with saline, free Cur and PEGylated Cur NPs. c) Mean weight of tumors separated from mice after different treatments. d) The tumor inhibitory rate (TIR) after treatment with free Cur and PEGylated Cur NPs in CT-26 tumor-bearing nude mice. The TIR is calculated using the following equation: $TIR(\%) = 100 \times (\text{mean tumor weight of control group} - \text{mean tumor weight of experimental group}) / \text{mean tumor weight of control group}$. Data are represented as average \pm standard deviation ($n = 5$). Statistical significance: * $P < 0.005$; # $P < 0.001$. (e) The tumor size is real-time monitored during the 21-day evaluation period (Left) and representative tumors separated from animals after intravenous injection of saline, free Cur and PEGylated Cur NPs (Right).

2.6 *In vivo* systematic toxicity

The potential *in vivo* toxicity has always been a great concern in the development of nanomedicines. Besides measuring body weights of mice in each cohort (Fig. 6b), immunohistochemical analysis was also adopted to assess the *in vivo* systematic toxicity of the treatments. Age-matched healthy mice were used as a control group. Standard heart function markers including creatine kinase (CK), aspartate aminotransferase (AST) and lactic dehydrogenase (LDH), liver function markers including alanine aminotransferase (ALT), albumin/globulin ratio (A/G) and total protein (TP), kidney function marker including creatinine (Cr), blood urea nitrogen (BUN) and uric acid (UA) were detected and compared to control (Fig. 7a). No observable toxicity was noted, suggesting no obvious heart, liver and kidney dysfunction of mice induced by the PEGylated Cur NPs treatment. In addition to the blood tests, we collected the main organs of the mice from the control and treated groups and sliced them for hematoxylin and eosin (H&E) staining (Fig. 7b). Neither noticeable organ damage nor inflammation lesion was observed compared with the control group. All these

results evidenced that the PEGylated Cur NPs based *in vivo* cancer treatment induced no significant side effect to the treated mice.

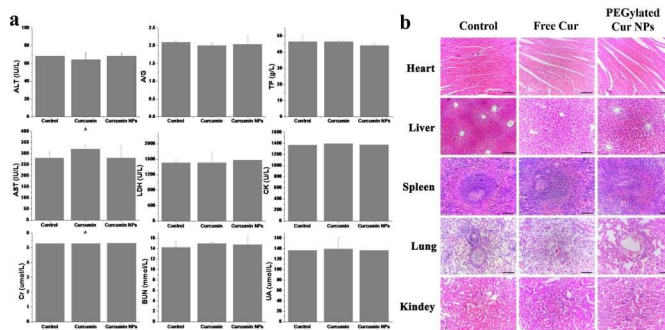


Fig. 7. *In vivo* toxicology study and serum biochemistry results obtained from CT-26-bearing nude mice after intravenous injection with free Cur and PEGylated Cur NPs. a) Blood analysis data of the CT-26-bearing nude mice treated with different formulations after 21 days. Age-matched healthy mice were used as the control group. Data are the mean \pm standard deviation from five separate experiments. b) Hematoxylin and eosin (H&E) stained organ slices from the CT-26-bearing nude mice treated with different formulations after 21 days. Age-matched healthy mice were used as the control group.

3. Conclusions

In summary, we prepared self-carried Cur nanodrugs for highly effective cancer therapy *in vitro* and *in vivo* with real-time monitoring of drug release. With a biocompatible C_{18} PMH-PEG functionalization, the Cur NPs show excellent dispersibility and outstanding stability in physiological environment, with high drug loading capacity higher than 78%. Furthermore, the cellular fluorescent “OFF-ON” activation and real-time monitoring of Cur molecule release were confirmed by both confocal microscopy and flow cytometry, indicating the potential for cancer diagnosis. Finally, both *in vitro* and *in vivo* data clearly show that therapeutic efficacy of the PEGylated Cur NPs is much better than that of free Cur. Above all, the NPs show no observable systematic toxicity *in vivo*. We believe that this self-carried strategy with real-time monitoring of drug release may open a new way for simultaneous cancer therapy and diagnosis.

4. Experimental

4.1 Materials

Curcumin (Cur), poly(maleic anhydride-alt-1-octadecene) (C_{18} PMH), poly(ethylene glycol)-amine (mPEG-NH₂, 5k) and 1-Ethyl-3-(3-dimethylaminopropyl)-carbodiimide (EDC) were purchased from Sigma Aldrich. 3-(4,5-Dimethylthiazol-2-yl)-2,5-diphenyl tetrazolium bromide (MTT) was obtained from Sigma-Aldrich and used after drying in vacuo for 24 h. RPMI 1640 culture medium, fetal bovine serum (FBS), Dulbecco's phosphate buffered saline (PBS), trypsin-EDTA (0.5% trypsin, 5.3mM EDTA tetra-sodium), and the antibiotic agents penicillin-streptomycin (100 U/ml) were from Invitrogen (USA). High-purity water with a resistivity greater than 18.4 M Ω -cm was collected from an in-line Millipore RiOs/Origin water purification system. Unless otherwise noted, all

chemicals were used without further purification. C₁₈PMH-PEG was synthesized following the literature procedure.^{52,53} Briefly, 10 mg (1 eq) of C₁₈PMH and 143 mg (1 eq) of mPEG-NH₂ were dissolved in 5 mL of dichloromethane, 6 μ L triethylamine and 10 mg of EDC. After 24 h of stirring, the solvents were evaporated by blowing with dry N₂. The leftover solid was dissolved in water, forming a transparent clear solution, which was dialyzed against distilled water for 3 days in a dialysis bag with molecular weight cut-off of 14000 Da to remove unreacted mPEG-NH₂. After lyophilization, the final product in a white solid was stored at 4 °C for future use.

4.2 Preparation and functionalization of self-carried Cur NPs

In a typical run, 1.5 mM of Cur was first dissolved in tetrahydrofuran (THF). 200 μ L of the solution was then quickly injected into 5 mL of high-purity water under vigorous stirring at room temperature. For functionalization of the Cur NPs, 300 μ L of C₁₈PMH-PEG (0.9 mg) aqueous solution was added to 5 mL of the Cur NPs suspensions, and sonicated for 5 min. Through this process, C₁₈PMH-PEG would attach to the surface of the Cur NPs by noncovalent hydrophobic interaction.

Drug loading capacity (DLC) and drug loading efficiency (DLE) were calculated according to the following formulae: $\text{DLC (wt. \%)} = (\text{weight of loaded drug} / \text{weight of PEGylated Cur NPs}) \times 100\%$; $\text{DLE (\%)} = (\text{weight of loaded drug} / \text{weight of drug in feed}) \times 100\%$. The weight of loaded drug and weight of drug in feed was determined with the UV-Vis absorption spectra at 428 nm and calculated by using standard absorbance technique (Fig. S5). The weight of PEGylated Cur NPs was calculated by electronic balance after freeze-drying.

4.3 Characterization of Cur and PEGylated Cur NPs

Sizes and morphologies of the Cur and the PEGylated Cur NPs were examined with SEM (HITACHI S-4300) and TEM (JEM-2100). SEM samples were prepared by drying the nanoparticles onto a Si substrate followed by a 2 nm layer of Au coating. Hydrodynamic sizes of the NPs were measured in aqueous solutions using a DLS instrument (Malvern Zetasizer Nano ZS). Ultraviolet-visible (UV-vis) and fluorescence spectra were respectively recorded with a Hitachi U-3900 and a Hitachi F-4600 systems.

4.3 *In vitro* drug-release

Firstly, Cur NPs, PEGylated Cur NPs were diluted by PBS at pH 7.4. Secondly, five milliliters of each suspension were added into a dialysis bag (3500 molecular weight cut-off, Fisherbrand®, Pittsburgh, PA, USA) followed by immersion in 200 mL of PBS at 37 °C with constant shaking. Thirdly, aliquots of 2 mL were collected from the solution at certain time points. During the dialysis, the solution volume was maintained constant by topping up 2 mL of PBS after each sampling. The amount of the released Cur was measured by UV-Vis absorbance. The assay was performed 3 times for each sample.

4.4 Cell culture

CT-26 cells were cultured with RPMI 1640 (Invitrogen, USA) supplemented with 10 % FBS (Hyclone Company, South Logan, UT), penicillin (100 μ g/mL), and streptomycin (100 μ g/mL; Gibco, Grand Island, NY, USA) in 5% CO₂ at 37 °C in a humidified incubator.

4.5 Confocal laser scanning microscopy

Imaging of cells was performed using a Leica laser scanning confocal microscope. CT-26 cells were seeded in a 24-well cell-culture plate for 24 h (37 °C, 5% CO₂). Then PEGylated Cur NPs were added to the wells. The cells were then incubated for 30 min, 1 h and 4 h (37 °C, 5% CO₂). Before observation, the cells were washed three times with PBS and then fixed with 4% paraformaldehyde. Imaging was performed under 488 nm laser excitation and the emission was collected within the range of 515–550 nm. The control group was the cells without incubation with the NPs.

4.6 *In vitro* cytotoxicity

Cell cytotoxicity was determined through a standard MTT assay. CT-26 cells were seeded into a 96-well cell-culture plate with 100 μ L (5000 cells) per well and then incubated for 24 h at 37 °C under 5% CO₂. Then the cells were incubated with free Cur, PEGylated Cur NPs of different concentrations for 24 h and 48 h respectively before the MTT assay.

4.7 *In vivo* antitumor efficacy

Female BALB/c nude mice of 18–20 g were purchased from Vital River Company (Beijing, China) and raised under standard pathogen-free conditions. All animal experiments were performed in accordance with the principles of care and use of laboratory animals. The tumor xenografts were implanted in the BALB/c nude mice by injecting 3×10^6 CT-26 cells into the right flank of each mouse. The xenografted mice were randomly divided into 3 groups (five mice per group) when the tumor volume reached about 100 mm³. Saline, free Cur, PEGylated Cur NPs were administered by intravenous (i.v.) injection at a Cur-equivalent dose of 10 mg/kg every 3 days. Tumor progression in the mice was then monitored every three days. The mice were sacrificed and their tumors were immediately removed and weighed. Meanwhile, plasma was collected for biochemical studies, including assays for respectively heart, liver and renal functions. Haematoxylin/eosin (H&E) staining of the tumor sections were carried out for tissues studies.

4.8 Statistical Analysis

All data are presented as means \pm standard deviation (S.D.). The significant differences between groups were evaluated with the Tukey's method after analysis of variance (ANOVA). In all statistical analyses, $p < 0.05$ was considered to be statistically significant.

Acknowledgements

This work was supported by the Chinese Natural Science Foundation general project (81171455) and key project (31430031), National Distinguished Young Scholars grant (31225009) from the National Natural Science Foundation of China, National Key Basic Research Program of China (2009CB930200), Chinese Academy of Sciences (CAS) "Hundred Talents Program" (07165111ZX), CAS Knowledge Innovation Program and State High-Tech Development Plan (2012AA020804 and SS2014AA020708), and the Key Basic Research Special Foundation of Science Technology Ministry of Hebei Province (Grant No. 14961302D). This work was also supported in part by NIH/NIMHD 8 G12 MD007597, and

USAMRMC W81XWH-10-1-0767 grants. The authors also appreciate the support by the "Strategic Priority Research Program" of the Chinese Academy of Sciences, Grant No. XDA09030301 and support by the external cooperation program of BIC, Chinese Academy of Science, Grant No. 121D11KYSB20130006.

Notes and references

a Nano-organic Photoelectronic Laboratory, Technical Institute of Physics and Chemistry, Chinese Academy of Sciences, 100190 Beijing, P. R. China.

b Chinese Academy of Sciences (CAS) Key Laboratory for Biological Effects of Nanomaterials and Nanosafety, National Center for Nanoscience and Technology, Beijing, P. R. China.

c Functional Nano & Soft Materials Laboratory (FUNSOM) and Jiangsu Key Laboratory for Carbon-Based Functional Materials & Devices, Soochow University, Suzhou, P. R. China.

d Center of Super-Diamond and Advanced Films (COSDAF) & Department of Physics and Materials Science, City University of Hong Kong, Hong Kong SAR, P. R. China.

e College of Chemistry & Environmental Science, Chemical Biology Key Laboratory of Hebei Province, Hebei University, Baoding, P. R. China.

f Molecular Imaging Laboratory, Department of Radiology, Howard University, Washington D.C., USA.

† These authors contributed equally to this work.

* Corresponding author.

E-mail: xiaohong_zhang@suda.edu.cn

E-mail: apcslee@cityu.edu.hk

E-mail: liangxj@nanoctr.cn

Electronic Supplementary Information (ESI) available: [details of any supplementary information available should be included here]. See DOI: 10.1039/b000000x/

- 1 D. Peer, J. M. Karp, S. Hong, O. C. Farokhzad, R. Margalit, R. Langer, *Nat. Nanotechnol.* 2007, **2**, 751.
- 2 R. Siegel, D. Naishadham, A. Jemal, *CA Cancer J. Clin.* 2013, **63**, 11.
- 3 J. H. Atkins, L. J. Gershell, *Nat. Rev. Cancer* 2002, **2**, 645.
- 4 B. A. Chabner, T. G. Roberts, *Nat. Rev. Cancer* 2005, **5**, 65.
- 5 D. J. Irvine, *Nat. Mater.* 2011, **10**, 342.
- 6 J. A. Hubbell, R. Langer, *Nat. Mater.* 2013, **12**, 963.
- 7 S. Mura, J. Nicolas, P. Couvreur, *Nat. Mater.* 2013, **12**, 991.
- 8 G. Cafo, G. Carbotti, A. Cuzzola, M. Fabbri, S. Ferrini, F. H. Kohnke, G. Papanikolaou, M. R. Plutino, C. Rosano, A. J. P. White, *J. Am. Chem. Soc.* 2013, **135**, 2544.
- 9 X. Wu, X. Sun, Z. Guo, J. Tang, Y. Shen, T. D. James, H. Tian, W. Zhu, *J. Am. Chem. Soc.* 2014, **136**, 3579.
- 10 Y. Zhou, W. Huang, J. Liu, X. Zhu, D. Yan, *Adv. Mater.* 2010, **22**, 4567.
- 11 M. N. Holme, I. A. Fedotenko, D. Abegg, J. Althaus, L. Babel, F. Favarger, R. Reiter, R. Tanasescu, P. L. Zaffalon, A. Ziegler, B. Muller, T. Saxer, A. Zumbuehl, *Nat. Nanotechnol.* 2012, **7**, 536.
- 12 M. H. Lee, J. Y. Kim, J. H. Han, S. Bhuniya, J. L. Sessler, C. Kang, J. S. Kim, *J. Am. Chem. Soc.* 2012, **134**, 12668.
- 13 F. Peng, Y. Su, X. Wei, Y. Lu, Y. Zhou, Y. Zhong, S. T. Lee, Y. He, *Angew. Chem. Int. Ed.* 2013, **52**, 1457.

- 14 S. Maiti, N. Park, J. H. Han, H. M. Jeon, J. H. Lee, S. Bhuniya, C. Kang, J. S. Kim, *J. Am. Chem. Soc.* 2013, **135**, 4567.
- 15 Q. Xing, N. Li, D. Chen, W. Sha, Y. Jiao, X. Qi, Q. Xu, J. Lu, *J. Mater. Chem. B* 2014, **2**, 1182.
- 16 P. Zhang, F. Cheng, R. Zhou, J. Cao, J. Li, C. Burda, Q. Min, J. Zhu, *Angew. Chem. Int. Ed.* 2014, **53**, 2371.
- 17 C. A. Poland, R. Duffin, I. Kinloch, A. Maynard, W. A. H. Wallace, A. Seaton, V. Stone, S. Brown, W. MacNee, K. Donaldson, *Nat. Nanotechnol.* 2008, **3**, 423.
- 18 Y. Shen, E. Jin, B. Zhang, C. J. Murphy, M. Sui, J. Zhao, J. Wang, J. Tang, M. Fan, E. V. Kirk, W. J. Murdoch, *J. Am. Chem. Soc.* 2010, **132**, 4259.
- 19 A. M. Alkilany, A. Shatanawi, T. Kurtz, R. B. Caldwell, R. W. Caldwell, *Small* 2012, **8**, 1270.
- 20 P. Huang, D. Wang, Y. Su, W. Huang, Y. Zhou, D. Cui, X. Zhu, D. Yan, *J. Am. Chem. Soc.* 2014, **136**, 11748.
- 21 K. Baba, H. E. Pudavar, I. Roy, T. Y. Ohulchanskyy, Y. Chen, R. K. Pandey, P. N. Prasad, *Mol. Pharm.* 2007, **4**, 289.
- 22 H. Kasai, T. Murakami, Y. Ikuta, Y. Koseki, K. Baba, H. Oikawa, H. Nakanishi, M. Okada, M. Shoji, M. Ueda, H. Imahori, M. Hashida, *Angew. Chem. Int. Ed.* 2012, **51**, 10315.
- 23 W. Li, Y. Yang, C. Wang, Z. Liu, X. Zhang, F. An, X. Diao, X. Hao, X. Zhang, *Chem. Commun.* 2012, **48**, 8120.
- 24 W. Li, X. Zhang, X. Hao, J. Jie, B. Tian, X. Zhang, *Chem. Commun.* 2013, **49**, 10989.
- 25 P. Huang, D. Wang, Y. Su, W. Huang, Y. Zhou, D. Cui, X. Zhu, D. Yan, *J. Am. Chem. Soc.* 2014, **136**, 11748.
- 26 J. Zhang, Y. Li, F. F. An, X. Zhang, X. Chen, C. S. Lee, *Nano Lett.* 2015, **15**, 313.
- 27 S. Santra, C. Kaitanis, O. J. Santiesteban, J. M. Perez, *J. Am. Chem. Soc.* 2011, **133**, 16680.
- 28 G. Lee, K. Eom, J. Park, J. Yang, S. Haam, Y. Huh, J. K. Ryu, N. H. Kim, J. I. Yook, S. W. Lee, D. S. Yoon, T. Kwon, *Angew. Chem. Int. Ed.* 2012, **51**, 5939.
- 29 J. Lai, B. P. Shah, E. Garfunkel, K. Lee, *ACS Nano* 2013, **7**, 2741.
- 30 Q. Wang, Y. Bao, J. Ahire, Y. Chao, *Adv. Healthcare Mater.* 2013, **2**, 459.
- 31 J. Tang, B. Kong, H. Wu, M. Xu, Y. Wang, Y. Wang, D. Zhao, G. Zheng, *Adv. Mater.* 2013, **25**, 6569.
- 32 Y. Yuan, Y. Chen, B. Z. Tang, B. Liu, *Chem. Commun.* 2014, **50**, 3868.
- 33 Q. Xing, N. Li, D. Chen, W. Sha, Y. Jiao, X. Qi, Q. Xua, J. Lu, *J. Mater. Chem. B* 2014, **2**, 1182.
- 34 M. Zheng, S. Liu, J. Li, D. Qu, H. Zhao, X. Guan, X. Hu, Z. Xie, X. Jing, Z. Sun, *Adv. Mater.* 2014, **26**, 3554.
- 35 Y. Yang, X. Zhang, C. Yu, X. Hao, J. Jie, M. Zhou, X. Zhang, *Adv. Healthcare Mater.* 2014, **3**, 906.
- 36 H. Tang, C. J. Murphy, B. Zhang, Y. Shen, E. A. V. Kirk, W. J. Murdoch, M. Radosz, *Biomaterials* 2010, **31**, 7139.
- 37 S. Barui, S. Saha, G. Mondal, S. Haseena, A. Chaudhuri, *Biomaterials* 2014, **35**, 1643.
- 38 D. Jin, K. W. Park, J. H. Lee, K. Song, J. G. Kim, M. L. Seo, J. H. Jung, *J. Mater. Chem.* 2011, **21**, 3641.
- 39 C. Xu, Y. Niu, A. Popat, S. Jambhrunkar, S. Karmakar, C. Yu, *J. Mater. Chem. B* 2014, **2**, 253.
- 40 S. Dey, K. Sreenivasan, *J. Mater. Chem. B* 2015, **3**, 824.

ARTICLE

- 41 H. Wang, S. Zhao, P. Agarwal, J. Dumbleton, J. Yu, X. Lu, X. He, *Chem. Commun.* 2015, **51**, 7733.
- 42 C. Stigliano, J. Key, M. Ramirez, S. Aryal, P. Decuzzi, *Adv. Funct. Mater.* 2015, **25**, 3371.
- 43 J. Zhang, F. An, Y. Li, C. Zheng, Y. Yang, X. Zhang and X. Zhang, *Chem. Commun.* 2013, **49**, 8072.
- 44 C. Yu, M. Zhou, X. Zhang, W. Wei, X. Chen and X. Zhang, *Nanoscale* 2015, **7**, 5683.
- 45 K. Pu, A. J. Shuhendler, J. V. Jokerst, J. Mei, S. S. Gambhir, Z. Bao, J. Rao, *Nat. Nanotechnol.* 2014, **9**, 233.
- 46 A. J. Shuhendler, K. Pu, L. Cui, J. P. Uetrecht, J. Rao, *Nat. Biotech.* 2014, **32**, 373.
- 47 I. C. Wu, J. Yu, F. Ye, Y. Rong, M. E. Gallina, B. S. Fujimoto, Y. Zhang, Y. H. Chan, W. Sun, X. H. Zhou, C. Wu, D. T. Chiu, *J. Am. Chem. Soc.* 2015, **137**, 173.
- 48 G. Prencipe, S. M. Tabakman, K. Welscher, Z. Liu, A. P. Goodwin, L. Zhang, J. Henry, H. Dai, *J. Am. Chem. Soc.* 2009, **131**, 4783.
- 49 K. Fuhrmann, J. D. Schulz, M. A. Gauthier, J. Leroux, *ACS Nano* 2012, **6**, 1667.
- 50 J. Logie, S. C. Owen, C. K. McLaughlin, M. S. Shoichet, *Chem. Mater.* 2014, **26**, 2847.
- 51 H. S. S. Qhattal, T. Hye, A. Alali, X. Liu, *ACS Nano* 2014, **8**, 5423.
- 52 C. Wang, L. Cheng, Z. Liu, *Biomaterials* 2011, **32**, 1110.
- 53 C. Wang, X. X. Ma, S. Q. Ye, L. Cheng, K. Yang, L. Guo, C. H. Li, Y. G. Li, Z. Liu, *Adv. Funct. Mater.* 2012, **22**, 2363.

Supporting Information

Self-carried Curcumin Nanoparticles for In vitro and In vivo Cancer Therapy with Real-time Monitoring of Drug Release

Jinfeng Zhang^{a,d†}, Shengliang Li^{b†}, Fei-Fei An^a, Juan Liu^b, Shubin Jin^b, Jin-Chao Zhang^c, Paul C. Wang^f, Xiaohong Zhang^{a,c*}, Chun-Sing Lee^{d*}, and Xing-Jie Liang^{b*}

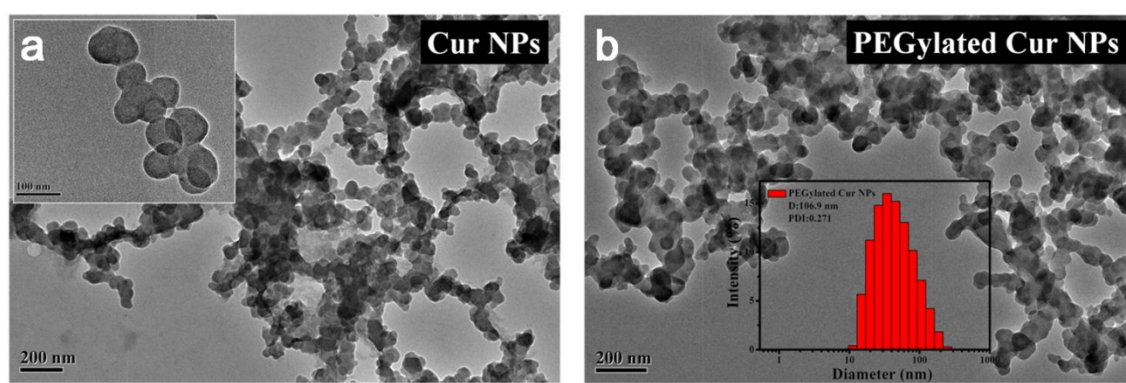


Fig. S1. TEM images of Cur NPs and PEGylated Cur NPs, inset in b is the DLS data of PEGylated Cur NPs (Diameter: 106.9 nm, PDI: 0.271).

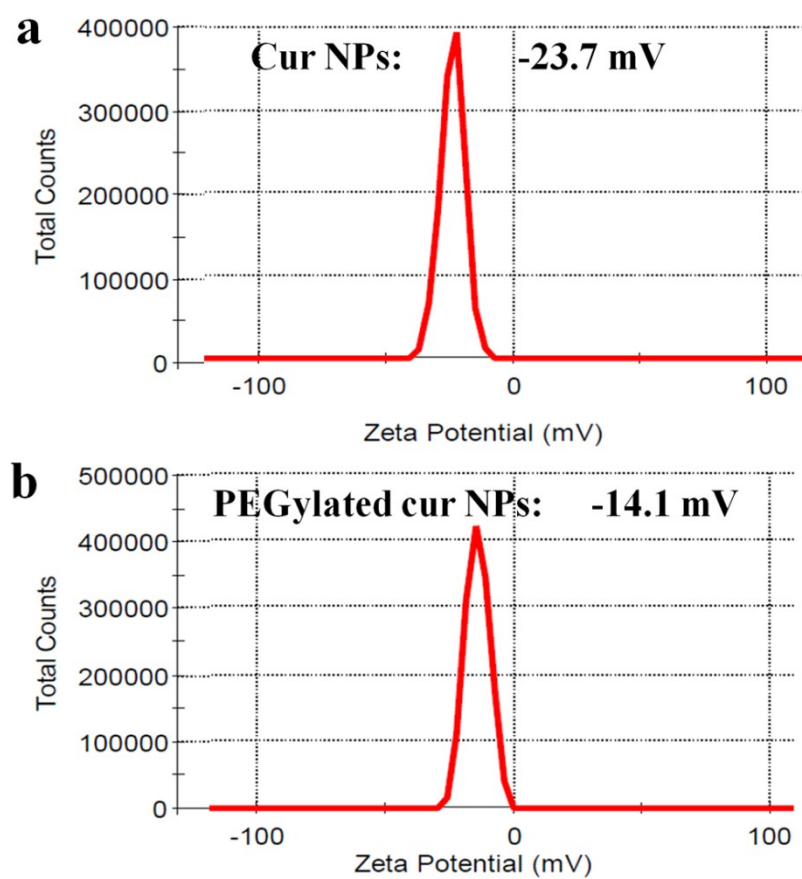


Fig. S2. Zeta potentials of (a) as-prepare Cur NPs and (b) PEGylated Cur NPs dispersed in deionized water both displaying negative charge.

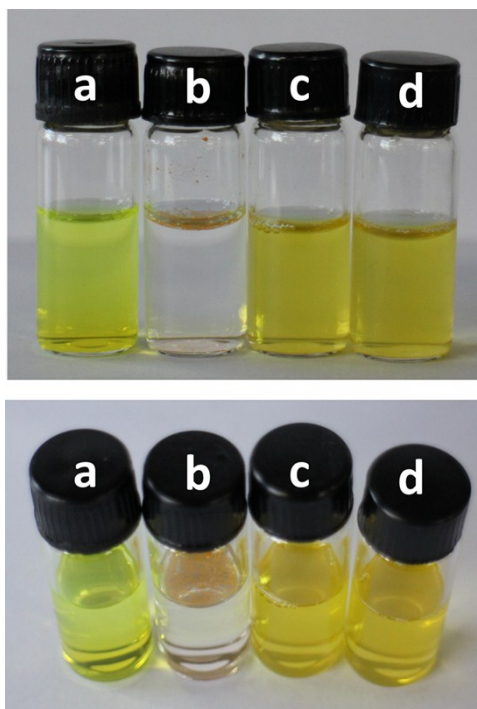


Fig. S3. Digital photographs of different samples including free Cur in THF (a), free Cur (b), Cur NPs (c) and PEGylated Cur NPs (d) dispersed in water respectively, which show a good dispersibility and better stability of NP than that of free drug in water.

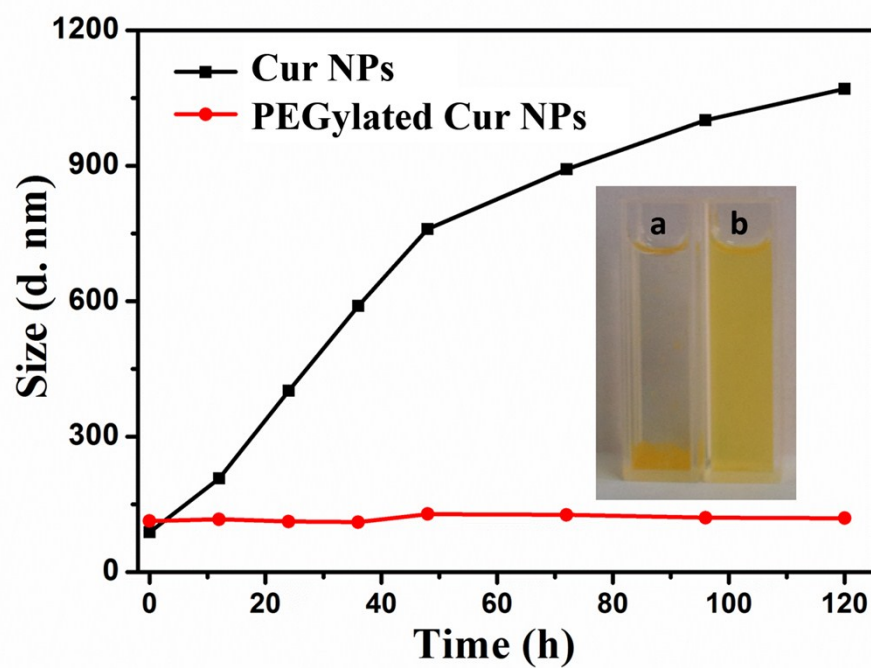


Fig. S4. Average particle sizes of the as-prepared Cur NPs and the PEGylated NPs dispersed in deionized water measured by DLS. Inset is digital image of the as-prepared Cur NPs (a) and the PEGylated Cur NPs (b) in water dispersions.

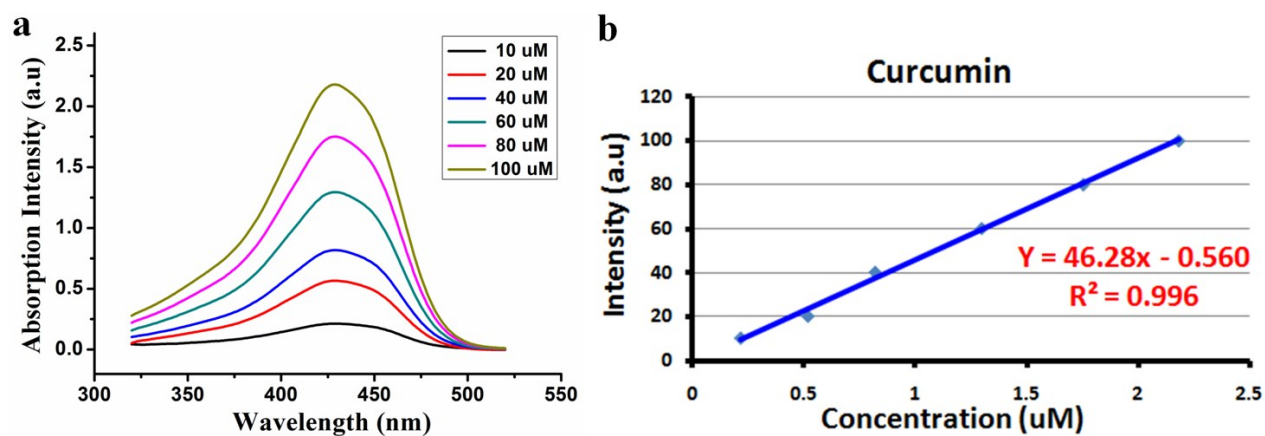


Fig. S5. The absorption spectra of Cur of different concentrations; b. The absorbance of Cur molecules at 428 nm (from a mixture of THF and water (v/v = 1:1)) as a function of Cur concentration.

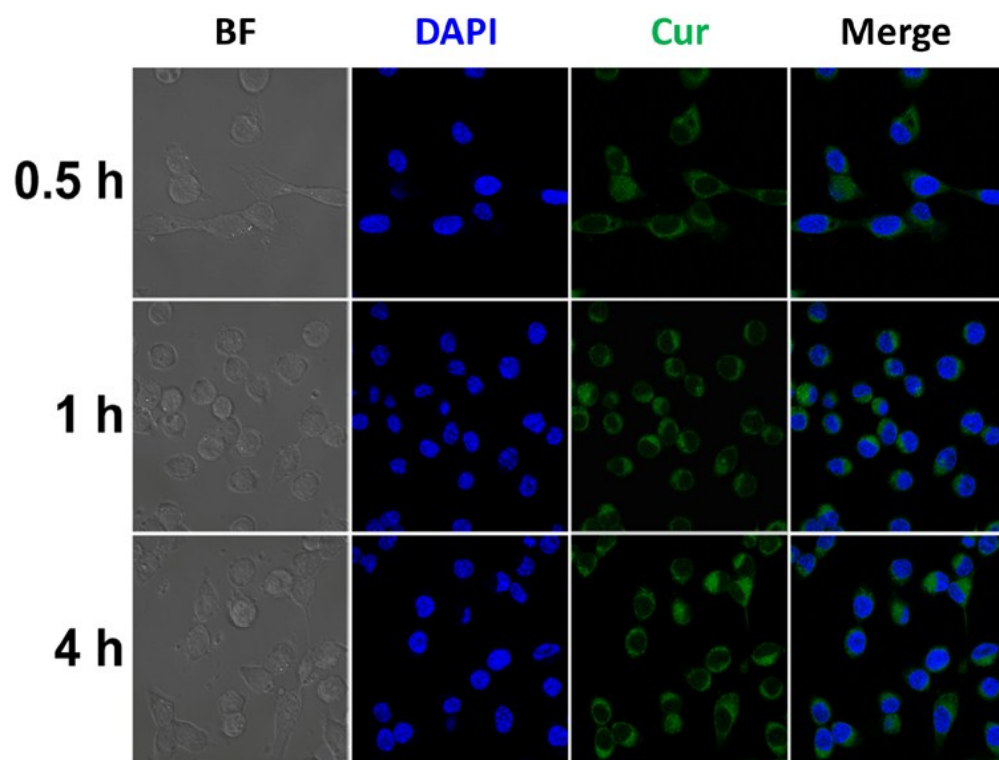


Fig. S6. Confocal microscopy images of CT-26 cells treated with PEGylated Cur NPs. The cells were incubated with PBS containing NPs (5 μ M), and then the images were obtained at each time point (0, 1, and 4 h). Cell images were obtained using excitation at 405 nm and 488nm respectively

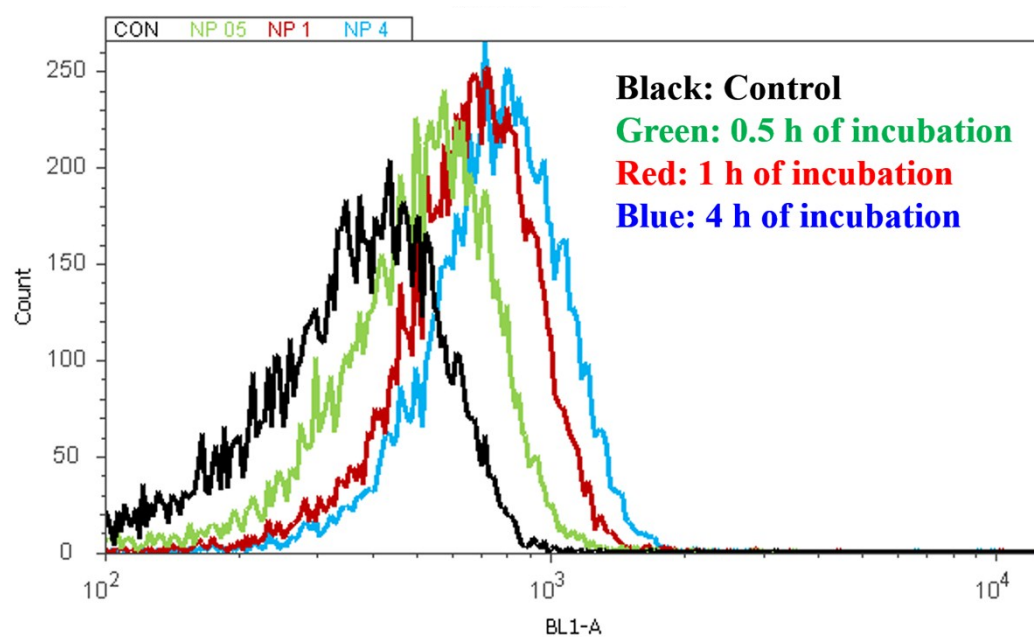


Fig. S7. Flow cytometric analyses of CT-26 cells after incubation with PEGylated Cur NPs for different durations.

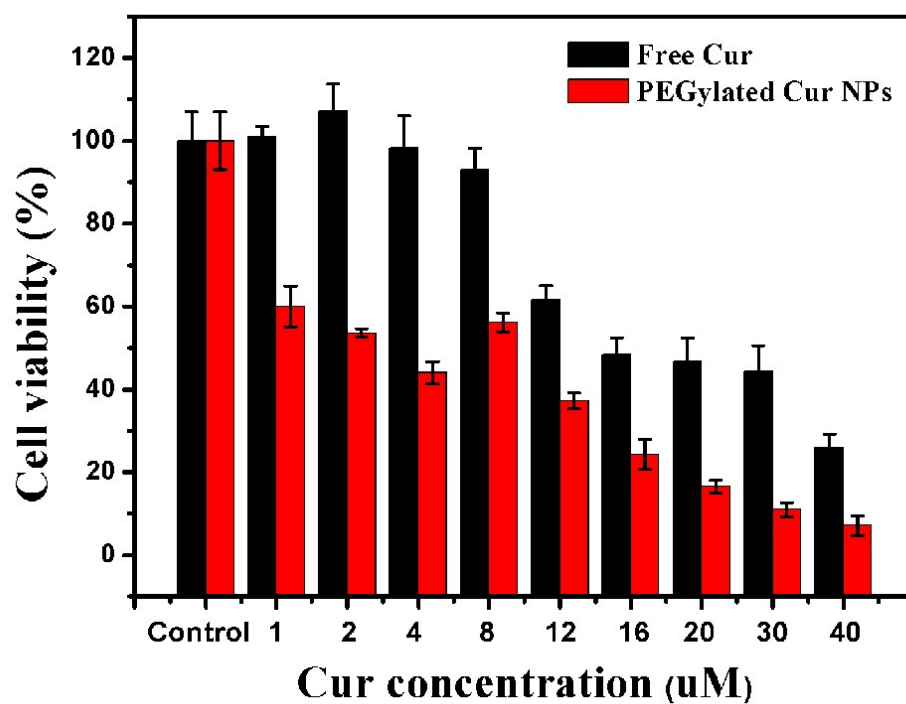


Fig. S8. Cell viability of free Cur and PEGylated Cur NPs in CT-26 cell line after 48 hours of incubation. Data represent mean values \pm standard deviation, $n=5$.

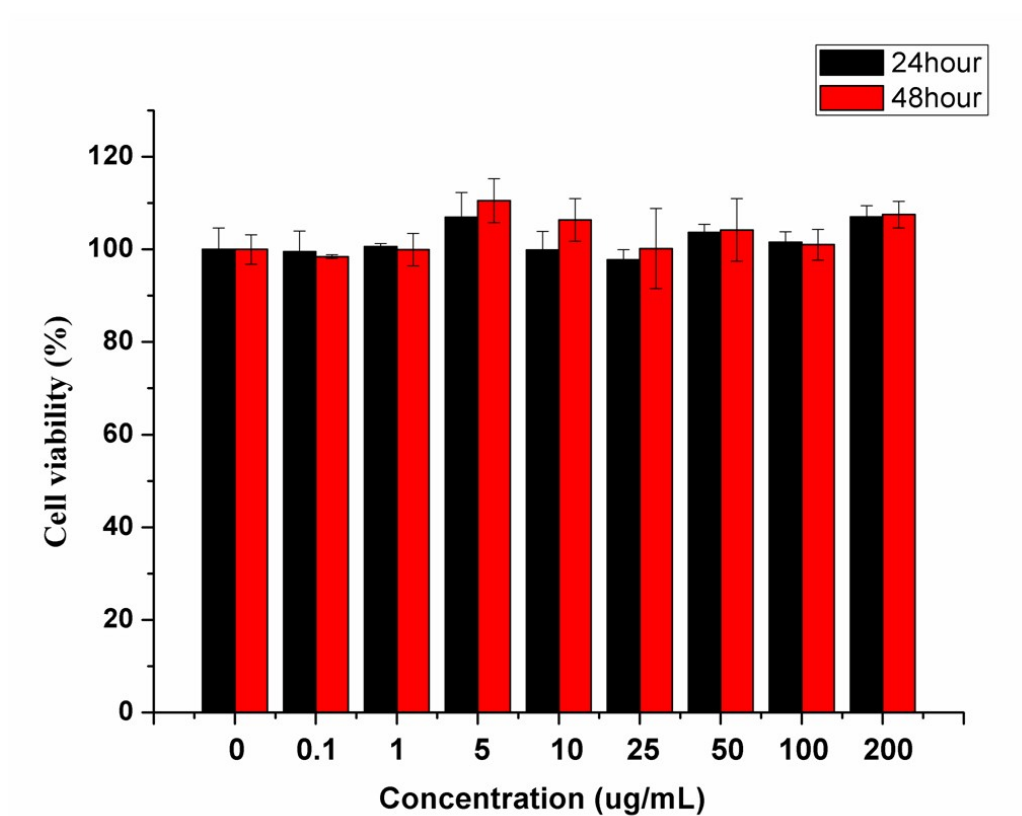


Fig. S9. Cell viability of C₁₈PMH-PEG in CT-26 cell line after 24 and 48 hours of incubation. Data represent mean values \pm standard deviation, n =5.

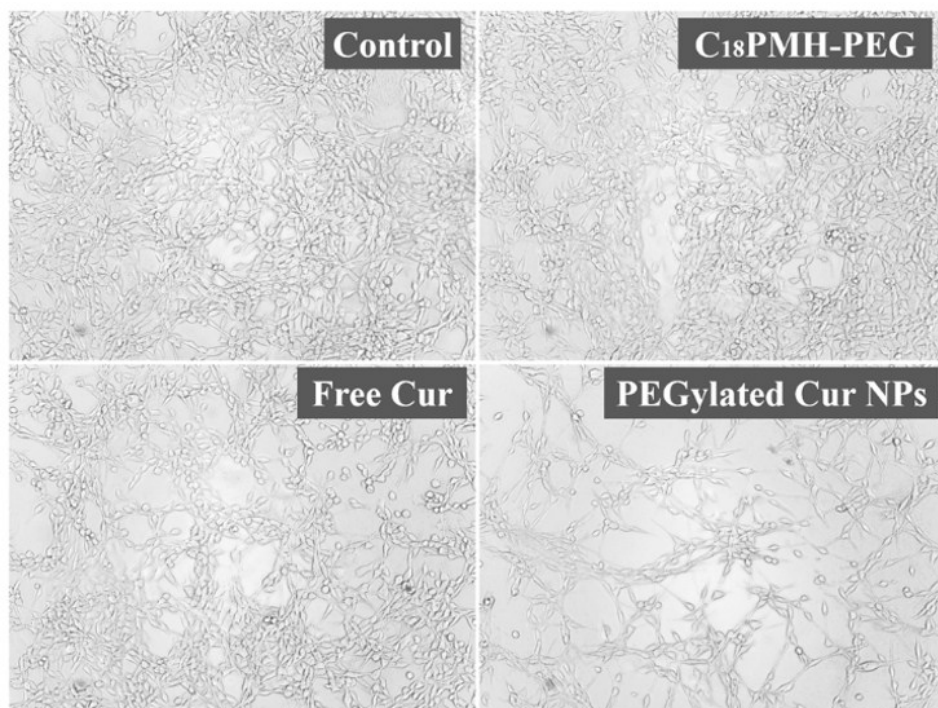


Fig. S10. Bright field of CT-26 cells after incubated with C₁₈PMH-PEG, Free Cur and PEGylated Cur NPs comparing to the control group.

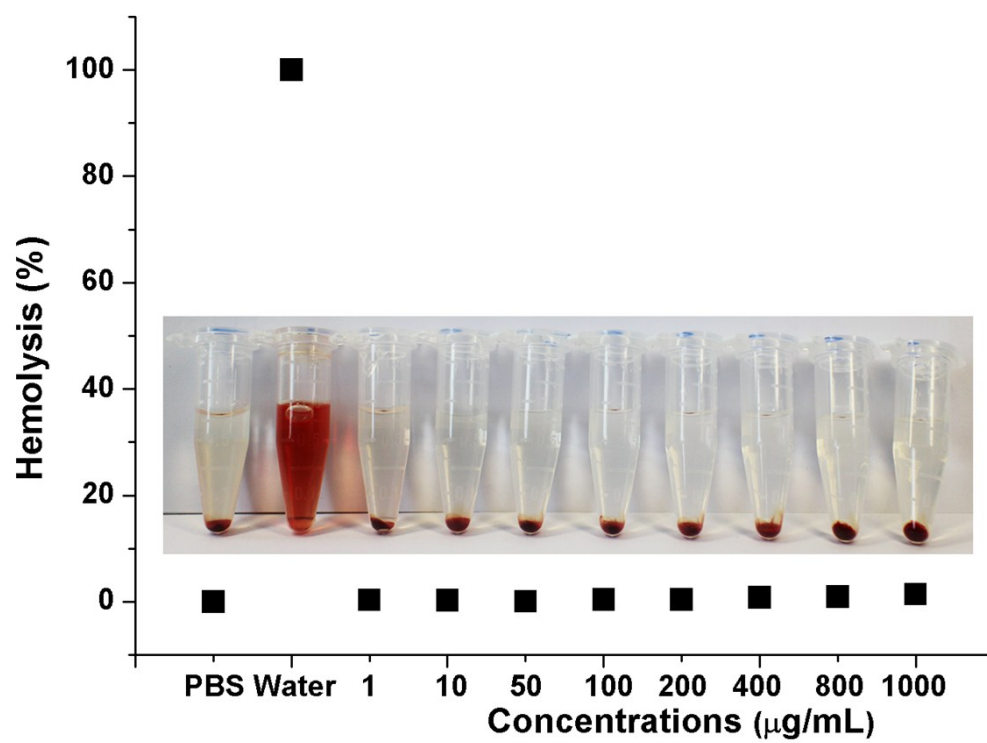


Fig. S11. Hemolysis assay of the PEGylated Cur NPs

Year	Journal	Cur loading capacity (%)	Carrier	Ref.
2015	Our work	78.5	Self-carried NPs	Our work
2009	<i>Chem. Eur. J.</i>	30	Porous silica matrix	1
2011	<i>Carbohydrate Polymers</i>	4.4	Dextran sulphate-chitosan NPs	2
2011	<i>Nanoscale</i>	12.95 ± 0.15	Polymeric micelles	3
2011	<i>Biomaterials</i>	11.2	Hybrid nanogels	4
2011	<i>J. Mater. Chem.</i>	35	Mesoporous hollow silica particles	5
2012	<i>Acta Pharmacologica Sinica</i>	0.7	PLGA nanoparticles	6
2012	<i>Carbohydrate Polymers</i>	4.1 ± 0.3	Chitosan/PCL nanoparticle	7
2012	<i>Mol. Pharmaceutics</i>	10	Solid Lipid NPs	8
2013	<i>Mol. Pharmaceutics</i>	0.93 ± 0.02	Polymeric NPs	9
2013	<i>Journal of Controlled Release</i>	7.2 ± 0.2	Polypeptide-curcumin conjugates	10
2013	<i>Biomacromolecules</i>	8	PLGA nanoparticles	11
2013	<i>J. Mater. Chem. B</i>	8	Polymeric micelles	12
2013	<i>Biomaterials</i>	14.85 ± 0.14	Polymeric micelles	13
2013	<i>Adv. Healthcare Mater.</i>	25 -60	Albumin NPs	14
2014	<i>J. Mater. Chem. B</i>	25.7 \ 29	Mesoporous silica NPs	15
2014	<i>Biomaterials</i>	16.1	MPEG-PLA-PAE copolymers	16
2014	<i>J. Mater. Chem. B</i>	0.31	SeNPs	17
2014	<i>ACS Nano</i>	5	N-palmitoyl chitosan NPs	18
2015	<i>J. Mater. Chem. B</i>	0.675	Gold nanoparticles	19
2015	<i>Chem. Commun.</i>	5.7 ± 1.4	Polymeric nanoparticles	20
2015	<i>Adv. Funct. Mater.</i>	2.8	Spherical polymeric nanoconstructs	21

Table S1. Comparison of drug loading content (wt. %) between our self-carried Cur NPs and other carrier-based drug delivery system for Cur-based cancer therapy

References

- [1] S. F. Chin, K. S. Iyer, M. Saunders, T. G. S. Pierre, C. Buckley, M. Paskevicius, C. L. Raston, *Chem. Eur. J.* **2009**, *15*, 5661.
- [2] A. Anitha, V. G. Deepagan, V. V. D. Rani, D. Menon, S. V. Nair, R. Jayakumar, *Carbohydrate Polymers* **2011**, *84*, 1158.
- [3] M. Gou, K. Men, H. Shi, M. Xiang, J. Zhang, J. Song, J. Long, Y. Wan, F. Luo, X. Zhao, Z. Qian. *Nanoscale* **2011**, *3*, 1558.

- [4] W. Wu, J. Shen, P. Banerjee, S. Zhou, *Biomaterials* **2011**, 32, 598.
- [5] D. Jin, K. W. Park, J. H. Lee, K. Song, J. G. Kim, M. L. Seo, J. H. Jung, *J. Mater. Chem.* **2011**, 21, 3641.
- [6] W. Punfa, S. Yodkeeree, P. Pitchakarn, C. Ampasavate, P. Limtrakul, *Acta Pharmacol. Sin.* **2012**, 33, 823.
- [7] J. Liu, L. Xu, C. Liu, D. Zhang, S. Wang, Z. Deng, W. Lou, H. Xu, Q. Bai, J. Ma, *Carbohydrate Polymers* **2012**, 90, 16.
- [8] K. Vandita, B. Shashi, K. G. Santosh, K. I. Pal, *Mol. Pharmaceutics* **2012**, 9, 3411.
- [9] P. Zou, L. Helson, A. Maitra, S. T. Stern, S. E. McNeil, *Mol. Pharmaceutics* **2013**, 10, 1977.
- [10] S. M. Sinclair, J. Bhattacharyya, J. R. McDaniel, D. M. Gooden, R. Gopalaswamy, A. Chilkoti, L. A. Setton, *J. Control. Release* **2013**, 171, 38.
- [11] P. Verderio, P. Bonetti, M. Colombo, L. Pandolfi, D. Prosperi, *Biomacromolecules* **2013**, 14, 672.
- [12] X. Gao, F. Zheng, G. Guo, X. Liu, R. Fan, Z. Qian, N. Huang, Y. Wei, *J. Mater. Chem. B* **2013**, 1, 5778.
- [13] C. Gong, S. Deng, Q. Wu, M. Xiang, X. Wei, L. Li, X. Gao, B. Wang, L. Sun, Y. Chen, Y. Li, L. Liu, Z. Qian, Y. Wei, *Biomaterials* **2013**, 34, 1413.
- [14] M. Cui, D. J. Naczynski, M. Zevon, C. K. Griffith, L. Sheihet, I. P. Fuentes, S. Chen, C. M. Roth, P. V. Moghe, *Adv. Healthcare Mater.* **2013**, 2, 1236.
- [15] C. Xu, Y. Niu, A. Popat, S. Jambhrunkar, S. Karmakar, C. Yu, *J. Mater. Chem. B*, **2014**, 2, 253.
- [16] Y. Yu, X. Zhang, L. Qiu, *Biomaterials* **2014**, 35, 3467.
- [17] B. Yu, X. Li, W. Zheng, Y. Feng, Y. S. Wong, T. Chen, *J. Mater. Chem. B* **2014**, 2, 5409.
- [18] H. L. Pu, W. L. Chiang, B. Maiti, Z. X. Liao, Y. C. Ho, M. S. Shim, E. Y. Chuang, Y. Xia, H. W. Sung, *ACS nano* **2014**, 8, 1213.
- [19] S. Dey, K. Sreenivasan, *J. Mater. Chem. B* **2015**, 3, 824.
- [20] H. Wang, S. Zhao, P. Agarwal, J. Dumbleton, J. Yu, X. Lu, X. He, *Chem. Commun.* **2015**, 51, 7733.
- [21] C. Stigliano, J. Key, M. Ramirez, S. Aryal, P. Decuzzi, *Adv. Funct. Mater.* **2015**, 25, 3371.

Title:

A Bivalent Recombinant Immunotoxin with High Potency against Tumors with EGFR and EGFRvIII Expression

Running Title: An EGFR and EGFRvIII-targeted immunotoxin

Jie Meng^{1*}, Yuanyi Liu², Shuying Gao², Stephen Lin¹, Xinbin Gu³, Martin G. Pomper⁴, Paul C Wang^{1,5}, Liang Shan¹

¹Molecular Imaging Laboratory, Department of Radiology and ³College of Dentistry, Howard University, Washington DC; ²Angimmune LLC, Rockville, MD; ⁴Department of Radiology, Johns Hopkins University, Baltimore, MD; and ⁵Department of Physics, Fu Jen Catholic University, New Taipei City, Taiwan

Keywords: Recombinant immunotoxin, EGFR, EGFRvIII, targeted therapy, cancer

Correspondence: Liang Shan, M.D., Ph.D.

Molecular Imaging Laboratory, Department of Radiology, Howard University

2041 Georgia Ave, NW, Washington DC 20060

Telephone: 202-865-3760, Email: liang.shan@howard.edu

***Footnote:** Dr. Jie Meng was a visiting scientist in the Molecular Imaging Laboratory at Howard University and her present address is the Institute of Basic Medical Sciences, Chinese Academy of Medical Sciences and Peking Union Medical College, Beijing, China

A list of abbreviations and acronyms

EGFR: epidermal growth factor receptor

EGFRvIII: epidermal growth factor receptor variant III

GBM: glioblastoma multiforme

mAbs: monoclonal antibodies

TKIs: tyrosine kinase inhibitors

RIT: recombinant immunotoxin

biscFv: bivalent single-chain variable fragment

DT: diphtheria toxin

DT390: an engineered diphtheria toxin fragment

P. pastoris: *Pichia pastoris*

V_L: light chain variable domain

V_H: heavy chain variable domains

scFv : single-chain variable fragment

SDS-PAGE: sodium dodecyl sulfate polyacrylamide gel electrophoresis

HPLC: high-performance liquid chromatography

IC₅₀: half maximal inhibition concentration

RTV: individual relative tumor volume

%TGI: percentage tumor growth inhibition

Abstract

EGFR and EGFRvIII are overexpressed in various types of cancer, serving as optimal targets for cancer therapy. Capitalizing on the high specificity of humanized antibody 806 (mAb806) to the EGFR and EGFRvIII overexpressed in cancer, we designed and generated a bivalent recombinant immunotoxin (RIT) by fusing the mAb806-derived bivalent single-chain variable fragment with a diphtheria toxin fragment, DT390. *In vitro*, DT390-BiscFv806 efficiently internalized into the cells and exhibited high cytotoxicity against the U87 glioblastoma cells and the EGFRvIII-transfected U87 (U87-EGFRvIII) cells with a half maximal inhibition concentration (IC_{50}) of 1.47 nM and 2.26×10^{-4} nM, respectively. Notably, DT390-BiscFv806 was four orders of magnitude more potent against the U87-EGFRvIII cells than against the parent U87 cells. The cytotoxicity against a group of six head and neck squamous cell carcinoma cell lines were further analyzed, showing an IC_{50} ranging from 0.24 nM to 156 nM, depending on the expression level of EGFR/EGFRvIII. In animals, the U87-EGFRvIII tumor xenografts grew extremely faster than the parental U87, and systemic administration of DT390-BiscFv806 significantly inhibited the growth of established U87-EGFRvIII and U87 tumor xenografts, showing a growth inhibition rate of 76.3% (59.82-96.2%) and 59.4% (31.5-76.0%), respectively. In pathology, the RIT-treated tumors exhibited a low mitotic activity and a large number of degenerative tumor cells, compared with the control tumors. The results indicate that DT390-BiscFv806 is promising for treatment of various types of cancer, especially for those with high EGFR expression or with EGFR and EGFRvIII co-expression.

Introduction

Epidermal growth factor receptor (EGFR) is a transmembrane tyrosine kinase belonging to the HER/erbB family. Activation of EGFR by its ligands results in homo- or heterodimerization of EGFR and autophosphorylation of tyrosine residues in its C-terminal domain, leading to cell proliferation and migration.¹ Various types of human cancer have been shown to overexpress the EGFR and possess the cancer-specific EGFR variant III (EGFRvIII).² One example is the glioblastoma multiforme (GBM), which shows EGFR overexpression in approximately 60-90% and amplification in 40-50% of tumors, and of the EGFR-amplified GBM, up to 60-70% possess EGFRvIII.^{3,4} Another example is the head and neck squamous cell carcinoma (HNSCC), which shows EGFR overexpression in up to 90% and gene amplification in 10-58%.^{5,6} A subset of HNSCC also possesses the EGFRvIII, although the EGFRvIII frequency varies from 0 to 42% in literature.^{7,8} Other types of cancer overexpressing EGFR/EGFRvIII include non-small cell lung carcinoma, breast cancer, colorectal carcinoma, and ovarian cancer. The high prevalence of EGFR overexpression and EGFRvIII-type mutation in various types of cancer has sparked the development of anti-EGFR monoclonal antibodies (mAbs) and tyrosine kinase inhibitors (TKIs).⁹⁻¹¹ Indeed, a large group of mAbs and TKIs have been generated and tested for their anti-tumor efficacy and benefits in treatment of patients.^{12,13} However, only mAbs have to date demonstrated a certain degree of survival improvement for a small subset of patients with GBM, head and neck squamous cell carcinoma, and other types of cancer.⁹⁻¹¹ Results with reversible and irreversible TKIs are generally disappointing.¹² Continued development of mAbs is facing formidable challenges, especially with the dose-limiting side effects induced by their binding with the EGFR expressed in normal tissues, and with the innate and acquired resistance associated with up-regulation of ligands to compete with mAbs for receptor binding, persistent activation of downstream signaling through multiple interacting pathways, and EGFR mutations.¹³

Recombinant immunotoxins (RITs) are a group of protein-based therapeutics comprising two functional moieties: one is the antibody fragment that allows the RITs to bind specifically to target cells and another is the bacterial toxin fragment that kills the cells upon cellular internalization.^{14,15} Compared to mAbs and antibody conjugates, RITs have an improved penetration capability and a greater anti-tumor efficacy. Because of the unique features of RITs such as high specificity, extraordinary potency and lack of drug resistance, EGFR-targeted RITs have been designed and constructed with different mAbs as the template such as the scFv(225)-ETA, scFv(14E1)-ETA, 425(scFv)-ETA', D2C7-IT, MR1scFvPE38KDEL, and scFv/rGel (E/rG).¹⁶⁻²⁰ RITs have also been generated by using epidermal growth factor (EGF) or transforming growth factor- α peptide as a template such as TP-38.²¹ Several RITs have been advanced from laboratory to the stage of Phase I and Phase II clinical trials. In general, several disadvantages of the current RITs limit their overall anti-tumor efficacy in clinical applications. Majority of these RITs have a relatively low binding affinity with EGFR due to their monovalency and most react with the EGFR expressed in cancer as well as in normal tissues, resulting in some dose-limiting side effects. Furthermore, only the RIT, D2C7-IT, has been reported to recognize both the wild-type EGFR and the EGFRvIII.¹⁷⁻¹⁹

The high specificity of mAb806 to the overexpressed EGFR and EGFRvIII in cancer, but not to the EGFR in normal tissue highlights its advantage over other mAbs for generation of RITs.²²⁻²⁴ The mAb806 was raised against mouse fibroblast cells expressing the EGFRvIII, and its unique specificity contributes to the fact that mAb806 binds to an epitope exposed only in the transitional untethered form of EGFR when it is overexpressed in cancer.²⁵ Preclinical and Phase I first-in-man clinical studies have confirmed the specificity as well as the high therapeutic index of mAb806, showing lack of normal tissue uptake in cancer patients.²⁶ Taking advantage of the unique specificity and humanization-derived benefits of the mAb806, we generated a bivalent RIT, designated as DT390-BiscFv806, by fusing an

engineered diphtheria toxin (DT) fragment (DT390) with the humanized mAb806-derived bivalent single-chain variable fragment (biscFv) *via* amino acid linkers. DT390 is an engineered fragment consisting of the catalytic and translocation domains of DT with a size of 390 amino acids. This bivalent RIT was expressed in a DT-resistant *Pichia pastoris* (*P. pastoris*) system (Patent No.: US7892786) and exhibited extraordinary potency against cancer cells with overexpressed EGFR only and those with co-expressed EGFR and EGFRvIII. Herein, we report the design and generation of the DT390-BiscFv806, and its cytotoxicity and anti-tumor efficacy.

Results

1. Generation and characterization of DT390-BiscFv806

DT390-BiscFv806 was constructed by cloning and integrating the light (V_L) and heavy (V_H) variable domain sequences into plasmid vectors and linked with the peptide $(G_4S)_3$ sequentially.²⁷⁻³⁰ The full linear sequence of DT390-BiscFv806 was DT390- V_L -(G_4S)₃- V_H -(G_4S)₃- V_L -(G_4S)₃- V_H , which was confirmed by DNA sequencing. The cartoon structure of DT390-BiscFv806 was shown in Fig. 1A, presenting a bivalent tandem scFv format. The product was expressed with the DT-resistant *P. pastoris* system. Purification of the product was achieved with a four-step scheme as described in the Materials and Methods. The raw and purified yields of DT390-BiscFv806 were ~15 mg/L and ~12 mg/L, respectively. The final product was adjusted to 0.1 mg/ml, filter-sterilized and stored at -80 °C in the buffer containing 10 mM Tris (pH, 7.2), 1 mM EDTA, 150 mM NaCl, and 5% glycerol.

The purity of the final product was >95% as estimated under non-reducing condition, presenting a single band in the 4-12% sodium dodecyl sulfate polyacrylamide gel electrophoresis (SDS-PAGE) gel (Fig. 1B). The product shown in lane 1 of Fig. 1B was used for the present studies. High-performance liquid chromatography (HPLC) with superdex 200 size-exclusion column analysis showed a major and a minor peak at the elution times of 28.323 min and 25.041 min, respectively (Fig. 1C). The major peak at 28.323 min represented the purified and the minor peak at 25.041 min might be the aggregated product. The third peak appeared in the HPLC profile was used as a reference, which was confirmed to be due to the EDTA added in the sample buffer in our previous studies. These results indicate that the final product of DT390-BiscFv806 was in a high purity with little aggregation.

2. Enhanced proliferation of U87 cells and growth of tumor xenografts by EGFRvIII expression

U87 cells are known to express EGFR, but do not possess EGFRvIII. The U87-EGFRvIII subline was established by stable transfection of EGFRvIII. High expression of EGFRvIII in the U87-EGFRvIII cells was confirmed with Western blotting (Fig. 2). To better understand the therapeutic efficacy of DT390-BiscFv806, we analyzed the effect of enforced expression of EGFRvIII on the growth of U87 cells as well as U87 tumor xenografts.

Cell availability assay showed that the proliferation of U87-EGFRvIII cells was significantly faster than that of the parental U87 cells with the cell doubling time of 11.18 h and 15.20 h, respectively. Interestingly, the stationary phase in the growth curve of U87-EGFRvIII cells delayed significantly. When 5×10^3 of U87 cells were seeded in the wells of 96-well plates, the stationary phase in the cell growth curve reached along with 100% confluence after 48 h. On the contrary, the stationary phase for U87-EGFRvIII cells became prominent only on day 6 after seeding of the cells, showing persistent proliferation.

In animals, enforced expression of EGFRvIII in U87-EGFRvIII cells resulted in the formation and growth of tumors significantly earlier than that of the parental U87 cells. The tumor nodules of U87-EGFRvIII were palpable as early as 10 days, while the tumor nodules of U87 were palpable at 20-30 days after 1×10^6 cell inoculation. The mean volume reached $117.1 \pm 30.9 \text{ mm}^3$ and 2341.1 ± 523.5

mm³ on day 13 and day 30, respectively for U87-EGFRvIII tumors, while the mean volume of U87 tumor xenografts was 18.8 ± 2.5 mm³ and 1048.7 ± 111.2 mm³ on day 30 and day 51, respectively, after cell inoculation (mean \pm SEM, $n = 5$ mice/group). The latent phase of U87-EGFRvIII tumor formation was 10-20 days shorter than that of the U87 tumor formation. However, no significant difference in the tumor volume doubling time was observed between the U87-EGFRvIII and U87 tumor xenografts (3.32 vs. 3.38 days, $P > 0.05$) as calculated based on the log phase of tumor growth curve.

3. High cytotoxicity of DT390-BiscFv806 against GBM and HNSCC cells

The cytotoxicity of DT390-BiscFv806 against the cultured cancer cells was determined after the cells were exposed to graded concentrations of DT390-BiscFv806. Fig. 3 shows the survival curves of different cancer cells plotted by the cell viability vs. the drug concentration, and the cell morphology under different concentrations of DT390-BiscFv806. The half maximal inhibitory concentration (IC₅₀) of DT390-BiscFv806 was measured to be 1.47 nM and 2.26×10^{-4} nM for U87 and U87-EGFRvIII cells, respectively (Table 1). Notably, DT390-BiscFv806 had more than four orders of magnitude more potency against the U87-EGFRvIII cells than against the parental U87 cells. In morphology, cell death was obvious after exposure to DT390-BiscFv806 (Fig. 3).

We further analyzed the cytotoxicity of DT390-BiscFv806 against a group of six HNSCC cell lines (Table 1). The cytotoxicity (IC₅₀) of DT390-BiscFv806 varied among the HNSCC cell lines with the highest against the JHU-13 (0.24 nM) and JHU-19 cells (0.89 nM), followed by JHU-29 (1.33 nM), JHU-6 (14.6 nM) and JHU-11 (21.7 nM), and the lowest against the JHU-22 cells (156 nM). To understand the EGFR expression status in the six HNSCC cell lines, we analyzed the presence of EGFRvIII using reverse transcription PCR (RT-PCR), the copy numbers of EGFR gene using real-time PCR, and the EGFR protein expression levels using Western blotting.^{31,32} In the analysis, U87-EGFRvIII cells were used as a positive control for the presence of EGFRvIII. Neither presence of EGFRvIII nor amplification of EGFR gene was detected in all of the six HNSCC cell lines (data not shown).³¹ The protein expression level of EGFR varied among the six cell lines with the highest in JHU-13 and the lowest in JHU-22 (Fig. 2).³² Comparison between the cytotoxicity and EGFR protein level showed a positive relationship between them in the HNSCC cell lines.

To understand the potential non-specific toxicity from DT390-BiscFv806, we treated the four most sensitive cell lines including U87-EGFRvIII, U87, JHU-13 and JHU-29 with a prostate-specific membrane antigen (PSMA)-targeted bivalent RIT, A-dmDT390-scFvDb(PSMA). The results showed that no significant cytotoxicity of A-dmDT390-scFvDb(PSMA) to either of the four cell lines were observed at the concentration of >100 nM. A-dmDT390-scFvDb(PSMA) was constructed by fusing a bisFv from antibody J591 with DT390, similar to the procedures to construct the DT390-BiscFv806. In our previous studies, A-dmDT390-scFvDb(PSMA) was confirmed to be highly cytotoxic to PSMA-expressing LNCaP prostate cancer cells (IC₅₀, 0.57 nM), but not to PSMA-negative PC-3 cells (IC₅₀, >100 nM).²⁹

4. High anti-tumor efficacy of DT390-BiscFv806 against established tumor xenografts

The efficacy of DT390-BiscFv806 was evaluated against the growth of established U87-EGFRvIII and U87 tumor xenografts. Because of the effect of enforced EGFRvIII expression, the growth patterns of U87 and U87-EGFRvIII tumor xenografts were significantly different. Therefore, different treatment regimens were designed to test the anti-tumor efficacy of DT390-BiscFv806 against the established U87 and U87-EGFRvIII tumor xenografts. Irrespective of the regimens, DT390-BiscFv806 significantly inhibited the growth of both U87-EGFRvIII and U87 tumor xenografts (Fig. 4).

Fig. 4A and 4B show the changes of mean individual relative tumor volume (RTV) and percentage tumor growth inhibition (%TGI) for U87-EGFRvIII tumors after DT390-BiscFv806 administration. The RTV changes over the time were significantly different between the treatment and control groups ($n = 6$ mice/group). At the end point of experiment (day 18 after beginning of treatment), the RTV was 5.5 ± 3.0 vs. 23.1 ± 9.2 ; the tumor weight was 0.9 ± 0.6 g vs. 2.2 ± 0.9 g; and the tumor volume was 836.7 ± 555.7 mm³ vs. 2523.7 ± 1136.2 mm³ for the treatment vs. control groups (mean \pm SD, all $P < 0.05$) (Fig. 5A). DT390-BiscFv806 led to a %TGI of 76.3% (ranging from 59.8%-96.2%) on the day 18, the last day after beginning of treatment. The cumulative %TGI increased over time, showing $34.7\% \pm 11.7$, $61.5\% \pm 15.9$, $71.3\% \pm 16.3$, and $76.3\% \pm 13.1$ on days 4, 10, 14, and 18, respectively (Fig. 4B).

Fig. 4C and 4D show the changes of mean RTV and %TGI over time for U87 tumors following DT390-BiscFv806 administration. Similarly, the RTV at each defined time point was also significantly different between the treatment and control groups ($n = 5$ mice/group). At the end point of experiment (day 21 after beginning of treatment), the RTV was 23.5 ± 11.8 vs. 57.9 ± 13.2 ($P < 0.05$) for the treatment vs. control groups and a %TGI of 59.4% (ranging from 31.5%-76.0%) was obtained. As shown in Fig. 4D, the cumulative %TGI was relatively stable from day 11 to day 21 after an initially rapid increase of tumor growth inhibition (day 4 to day 11) following treatment, showing $57.6\% \pm 17.1$, $56.7\% \pm 19.8$, $58.0\% \pm 13.9$, $50.6\% \pm 18.4$, and $59.4\% \pm 20.4$ on days 11, 14, 16, 18 and 21, respectively, which was different from that of the inhibitory growth of U87-EGFRvIII tumors; the latter showed an increased cumulative %TGI over time (Fig. 4B).

With the present dosage regimen, DT390-BiscFv806 was in general well tolerated by mice. However, a body weight loss of $>10\%$ was observed in three of the 12 mice bearing U87-EGFRvIII tumor xenografts (one control and two RIT-treated mice) and three of the ten mice bearing U87 tumor xenografts (one control and two RIT-treated mice). The mouse body weight loss in the control group might be associated with the rapid tumor growth, while in the treatment group it might be associated with the tumor growth as well as the DT390-BiscFv806 toxicity. There was a significant difference for the body weight loss/gain between the control and RIT-treated mice bearing the U87-EGFRvIII tumor xenografts ($P = 0.021$), but there was no significant difference for mice bearing U87 tumor xenografts ($P = 0.524$). During the experiments, no significant clinical signs of toxicity were observed such as sickness, diarrhea and lethargy.

5. Pathologic findings

We comparatively analyzed the pathology between the RIT-treated and the control tumor xenografts. Under microscopy, both of the RIT-treated and control tumors were composed of densely arranged tumor cells with heteromorphic and large nuclei. One striking change was the lower mitotic activity in the RIT-treated tumors than in the control tumors (Fig. 5B-5F). The mitotic figures were 5.23 ± 0.66 per high-powered fields (HPF, 400x) in the control group vs. 2.67 ± 0.86 per HPF in the RIT-treated group (two-tailed t -test, $P = 0.0002$) (Fig. 5B). Another striking change that was observed in all RIT-treated tumors was the presence of a large number of degenerative tumor cells. As shown in Fig. 5C and 5D, these degenerative cells had an empty cytoplasm and the outer boundary of nucleus with loss of the nuclear details. These cells distributed throughout the entire tumors with more in the central region than in the peripheral region of tumors. These degenerative cells were rarely seen in the tumors of control group (Fig. 5E and 5F). The mechanism and significance for the presence of a large number of degenerative cells in the RIT-treated tumors remain to be studied.

Necrosis was observed in tumors from both groups, showing more necrosis in larger tumors, but there was no obvious difference in the extent of necrosis among the tumors with similar size from the

two groups. Inflammatory cell infiltration was not obvious in the stroma of both RIT-treated and control tumors.

Discussion

The DT390-BiscFv806 we generated possesses some desirable properties as an EGFR- and EGFRvIII-targeted therapeutic agent. This RIT was constructed with a humanized biscFv that was derived from the mAb806 and its toxin component was DT390, different from other RITs that are *Pseudomonas* exotoxin A (PE) fragment-based. DT390 is a truncated form of DT, which retains its enzyme activity and membrane translocation function, while deleting the binding domain to prevent its binding with normal cells, thereby diminishing its systemic toxicity. Engineered DT and PE fragments have their own advantages and disadvantages.³³⁻³⁵ In general, PE fragments are more resistant to genetic manipulation, but induce more side effects (especially liver toxicity) and stronger immunogenicity than DT fragments. However, previous immunization of patients with DT vaccine could be of concern when DT fragment is used. Fortunately, no significant neutralizing effect by the existing circulating anti-DT antibodies has been observed in clinical trials with DT390-based RITs.^{35,36} This may be explained by the assumption that the epitopes targeted by the DT vaccine-induced neutralizing antibodies are mostly located in the deleted binding domain of DT. A DT390-based anti-CD3 monospecific RIT, OntakTM, was approved in 1999 by the U.S. FDA for treatment of cutaneous T-cell lymphoma and other diseases.³⁷ Because immunogenicity of RITs that is induced by the toxin component as well as the murine antibody fragments is a major issue for their clinical application, use of the humanized antibody fragment and DT390 in construction of DT390-BiscFv806 is expected to reduce its immunogenicity and side effects, making it more suitable for clinical use.

A challenge in RIT development is the difficulty in generating highly functional, multi-domain RITs, requiring an efficient expression system that should not only be resistant to the toxin component, but also able to properly fold proteins with multiple domains.³³ Bacteria are the most frequently used expression systems because of their resistance to toxins, but they lack the ability to efficiently fold complex proteins. Following expression in bacteria, multi-domain RITs must be re-folded chemically to recover their binding capability and bioactivity, thus the function of multi-domain RITs cannot be fully recovered in most situations. The majority, if not all of the current EGFR-targeted RITs, were monovalent and generated with bacterial expression systems. Toxin-resistant cell lines such as CHO and HEK293T are also used to produce RITs, but the production yield in most cases is very limited. To efficiently express DT-based RITs, Dr. Liu et al. the coauthor of this manuscript, have invented a DT-resistant *P. pastoris* expression system (Patent No.: US7892786). *P. pastoris* is a methylotrophic yeast with two alcohol oxidase genes. Its strong inducible promoter AOX1 allows *P. pastoris* to express a high level of proteins in a simple, inexpensive medium with a high growth rate in either a shake flask or a fermenter, making it suitable for both small and large scale production. Importantly, *P. pastoris* is capable of folding multi-domain RITs properly by forming disulfide bonds.²⁷⁻³⁰ The expression and purification parameters of this system have been further optimized for production scale up of RITs according to the U.S. FDA GMP guidelines. An example is the anti-CD3 RIT, Resimmune (A-dmDT390-bisFv(UCHT1)), which is under Phase II clinical trials and has been produced at a raw yield of ~207 mg/L and a purified yield of ~144.2 mg/L after a 163-hour induction period in a single batch of 120 L bioreactor culture.³⁸ For the DT390-BiscFv806 in the present study, its expression level was ~15 mg/L in shake-flasks, higher than that obtained for Resimmune under the same expression conditions.

Valency, molecular size, and circulation time are three key factors affecting the anti-tumor efficacy of a RIT.^{29,39,40} Use of biscFv to construct RIT can significantly improve its functional affinity. Under most conditions for bivalent binding, two measurable K_D exist, one for monovalent and the other

for bivalent. The overall binding affinity is determined by the fraction of bivalent binding. Increasing the bivalent binding fraction is one approach to enhance the binding affinity. Our previous studies on different formats of RITs have confirmed the higher binding affinity of bivalent RITs than that of monovalent RITs.^{28,29,40} The studies with RITs targeting PSMA (A-dmDT390-scFvDb(PSMA)) or CD3 (A-dmDT390-bisFv(UCHT1)) have shown that the binding affinity and cytotoxicity of the bivalent format are >2.5-fold and >10-fold higher, respectively, than that of a monovalent format.^{28,29,40} We expected that the bivalent DT390-BiscFv806 would have a high binding affinity and cytotoxicity to the targeted cells. Indeed, our data demonstrated that the cytotoxicity (IC₅₀) of T390-BiscFv806 was comparable to that of A-dmDT390-bisFv(UCHT1) (1.7×10^{-14} on Jurkat T cells) and A-dmDT390-scFvDb(PSMA) (5.7×10^{-12} on LNCaP prostate cancer cells).^{29,38} Regarding the molecular size, RITs with a small molecular size usually have a better tumor-penetrating capability than those with larger molecular size. DT390-BiscFv806 has a moderate molecular size of ~97 kDa, much smaller than full antibodies (~150 kDa), suggesting a better penetration capability than mAbs and a longer circulation time than monovalent RITs, increasing the chance to accumulate in tumors. Increasing the penetration capability and binding affinity while maintaining a proper circulating time by optimizing the primary and secondary structure of a RIT is critical to achieve an optimal anti-tumor efficacy.

To better understand the anti-tumor efficacy of our newly generated RITs, we first established a subline U87-EGFRvIII with stable co-expression of EGFR and EGFRvIII. Enforced expression of EGFRvIII led to significant changes of the U87 cell behaviors. Under the experimental conditions presented in the Materials and Methods, the U87 cells reached the stationary phase of growth after 100% confluence at ~48 h from seeding of the cells. On the contrary, U87-EGFRvIII cells kept proliferating up to day 6 when we completed the studies. This phenomenon was also reflected in the tumor formation in animals. The latent phase of U87-EGFRvIII tumor formation was much shorter than that of U87 tumor formation, although the doubling times of their tumor volumes were similar once the tumor growth entered the log growth phase. A possible explanation for this phenomenon is that enforced expression of EGFRvIII makes the U87-EGFRvIII cells resistant to apoptosis induced after 100% confluence, and when they are inoculated in mice, most cells stay alive and grow to a tumor mass with a shorter latent phase than the U87 cells. The results are consistent with other reports, although further detailed studies are necessary to elucidate the mechanisms underlying this phenomenon.⁴¹⁻⁴³

We first tested the cytotoxicity of DT390-BiscFv806 against the U87 and U87-EGFRvIII cells. The results showed that DT390-BiscFv806 was highly toxic against both U87 and U87-EGFRvIII cells. Interestingly, DT390-BiscFv806 had more than four orders of magnitude more potency against the U87-EGFRvIII cells than against the parental U87 cells. This result could be explained by the targeting effect of DT390-BiscFv806 on both EGFR and EGFRvIII, and indicates that DT390-BiscFv806 recognizes both EGFR and EGFRvIII. We further analyzed a group of six HNSCC cell lines to confirm the cytotoxic effect of DT390-BiscFv806. Although these HNSCC cell lines were not detected to possess either EGFRvIII, they also showed a high sensitivity to DT390-BiscFv806, which was associated with the protein expression levels of EGFR.

We tested the specificity of DT390-BiscFv806 against EGFR/EGFRvIII by treating the four most sensitive cell lines (U87-EGFRvIII, U87, JHU-13 and JHU-29) with a prostate-specific membrane antigen (PSMA)-targeted bivalent RIT, A-dmDT390-scFvDb(PSMA). We did not detect significant cytotoxicity of A-dmDT390-scFvDb(PSMA) to either of the four cell lines at the concentration of >200 nM. A-dmDT390-scFvDb(PSMA) was constructed by fusing a bisFv from the PSMA-specific antibody J591 with DT390 using similar procedures in constructing the DT390-BiscFv806. We have confirmed that A-dmDT390-scFvDb(PSMA) is highly cytotoxic and exhibited a high potency to PSMA-expressing

LNCaP cultured cells and tumor xenografts, but not to PSMA-negative PC-3 cultured cells and tumor xenografts in our previous studies.²⁹

We then tested the efficacy of DT390-BiscFv806 against the established U87-EGFRvIII and U87 tumor xenografts. Keeping the different growth features of U87-EGFRvIII and U87 cells in mind, we designed different protocols showing that the tumor growth was inhibited significantly by systemic administration of DT390-BiscFv806 with a mean %TGI of 76.3% (ranging from 59.8%-96.2%) and 59.4% (ranging from 31.5%-76.0%), respectively. These results indicate that DT390-BiscFv806 is efficacious to tumors with EGFR expression alone or with EGFR and EGFRvIII co-expression; and more efficacious against the latter. It is worth noting that most existing RITs react not only with the EGFR overexpressed in cancer, but also react with the EGFR expressed in normal tissue, resulting in unwanted toxicity to key organs, and to date, only the monovalent RIT, D2C7-IT, has been reported to recognize both the wild type EGFR and EGFRvIII.¹⁷⁻¹⁹ Because EGFRvIII is specifically expressed in cancer and plays a significant role in tumor progression and treatment failure, a RIT that recognizes the EGFRvIII is expected to enhance its anti-tumor benefits.

To better understand the anti-tumor mechanisms of DT390-BiscFv806, we comparatively analyzed the pathological differences between RIT-treated tumors and control tumors. Except for the decreased mitotic activity, a significant finding in the treated tumors is the appearance of a large number of degenerative tumor cells, but such cells were rarely observed in the control tumors. Interestingly, there was no obvious difference in the extent of necrosis among the tumors with similar size from the two groups. We hypothesized that the tumor cell death induced by RITs may be a slow process following the inhibition of protein synthesis by RITs and the appearance of degenerative tumor cells may be a representing phenomenon of this slow process, although further studies are necessary.

In summary, we generated a humanized bivalent scFv-derived, DT390-based RIT, DT390-BiscFv806, by capitalizing upon the unique specificity of mAb806 against EGFR and EGFRvIII overexpressed in cancer but not the EGFR in normal tissue, and taking the mAb806 humanization-derived benefits. This novel RIT was expressed with a DT-resistant *Pichia* expression system in a high yield and purity. DT390-BiscFv806 exhibited high cytotoxicity and anti-tumor efficacy against the cancer cells either with EGFR expression alone or with EGFR and EGFRvIII co-expression. It is notable that DT390-BiscFv806 was four orders of magnitude more potent against EGFR and EGFRvIII co-expressing U87-EGFRvIII cells than against the parental U87 cells with EGFR expression alone. The high anti-tumor efficacy and the unique properties of DT390-BiscFv806 make it promising for treatment of cancers such as GBM, HNSCC, and cancers of lung, breast, prostate, and ovary.

Materials and Methods

1. Design and generation of the bivalent RIT, DT390-BiscFv806

1) Design and cloning of DT390-BiscFv806

DT390-BiscFv806 was designed to have a linear sequence arrangement of DT390-V_L-(G₄S)₃-V_H-(G₄S)₃-V_L-(G₄S)₃-V_H, where (G₄S)₃ is the peptide linker, and V_L/V_H are the V_L and V_H variable domain sequences derived from the humanized mAb806 (Fig. 1A). DT390-BiscFv806 was constructed following the strategy we used to construct other RITs.²⁷⁻³⁰ Briefly, a set of primers were designed based on the sequences of V_L and V_H variable domains of the humanized mAb806, and the V_L and V_H domains were amplified with PCR. The amplified products were analyzed by electrophoresis in 1% agarose gels and purified using QIAquick Gel Extraction Kit (Qiagen, Valencia, CA). The *Bam*HI digested V_L PCR fragment was ligated to *Bgl* II digested V_H fragment using T4 ligase to generate the scFv. After confirming the scFv sequence with DNA sequencing, the first and second scFv fragments were subcloned into the *Xho*I and *Eco*RI sites of the plasmid vector pwPICZα-DT390, which contains the

DT390 fragment. The (G₄S)₃ was used as the linker to connect the two scFv to obtain the biscFv fragment.

2) DT390-BiscFv806 expression and purification

The linearized DT390-BiscFv806 construct in pwPICZ α -DT390 vector was transformed into the DT-resistant *P. pastoris* strain (Patent No.: US7892786). The transformants were selected on YPD (1% yeast extract, 2% peptone and 2% dextrose) plates containing zeocin (100 μ g/ml). Six colonies were randomly picked and cultivated in test tubes containing 5 mL YPD at 30 °C at 250 rpm for 24 h as growth phase I, then in YPG (1% yeast extract, 2% peptone, 1% glycerol) for another 24 h as growth phase II. The cultures were induced with methanol for 48 h at 25 °C at 225 rpm. Antifoam (0.02%) was added in all of the growth and induction medium, and phenylmethanesulfonyl fluoride (1 mM) was added with methanol to inhibit the protein degradation during the induction phase. The culture supernatants were analyzed under non-reducing condition with SDS-PAGE (Life Technologies, Grand Island, NY). The optimal clone was selected based on the gel electrophoresis and cultivated in 1000 mL shake-flasks for 48 h for growth and induction phase, respectively. The supernatant containing the desired product of DT390-BiscFv806 was purified following a four-step scheme: diafiltration, capture by hydrophobic chromatography, borate anion exchange chromatography, and anion exchange chromatography according to our established protocols.²⁷⁻³⁰

3) SDS-PAGE and HPLC analysis

The product of DT390-BiscFv806 was characterized with 4-12% SDS-PAGE and HPLC. Proteins fractionated by running the precast SDS-PAGE gels were stained with Coomassie blue staining reagent (Life Technologies) after washing the gels with distilled water. HPLC analysis was performed with a Shimadzu HPLC system using Superdex 200 size-exclusion column, 10/300 GL (GE healthcare, Pittsburgh, PA). The sample volume was 90 μ l using 100 μ l loop. The flow rate was 0.5 ml/min. The running time was 120 min and the running buffer was composed of 50 mM Phosphate buffer (pH, 7.0) and 150 mM NaCl.

2. *In vitro* experimental design

1) Cell lines and cell culture

The human glioblastoma cell line U87 and its subline U87-EGFRvIII and six HNSCC cell lines were used in the present studies. The U87 cell line was purchased from the American Type Culture Collection (ATCC, Rockville, MD) and classified as grade IV glioblastoma by the ATCC. U87-EGFRvIII subline was established by stable transfection of EGFRvIII to U87 cells. EGFR expression in U87 cells and EGFR/EGFRvIII co-expression in U87-EGFRvIII cells were confirmed using RT-PCR and Western blotting with the antibody Ab-5 (Thermo Scientific, Cambridge, MA). The antibody Ab-5 reacts with the extracellular domains of both EGFR and EGFRvIII. The effect of EGFRvIII expression on the U87 cell proliferation *in vitro* and in animals was also characterized (see Results section). The six HNSCC cell lines including JHU-6, JHU-11, JHU-13, JHU-19, JHU-22, and JHU-29, were originally established at Johns Hopkins University. JHU-6, JHU-19 and JHU-29 were from HNSCC arising from the base of tongue; JHU-11 and JHU-22 were from the larynx; and JHU-13 was from the neck node metastasis. Cells were routinely cultured in Dulbecco's Modified Eagle Medium/Nutrient Mixture F-12 (DMEM/F12) supplemented with 10% fetal bovine serum and 50 mg/mL penicillin/streptomycin (Life Technologies). All cultures were conducted at 37 °C in a humidified atmosphere containing 5% CO₂ in air.

2) Western blot analysis of EGFR and EGFRvIII expression

Cultured cells at the confluence of 70-80% were washed twice with phosphate buffered saline (PBS) and collected in RIPA lysis buffer (Santa Cruz Biotechnology, Santa Cruz, CA). The protein

concentration was quantified with the Bio-Rad protein assay (Bio-Rad, Hercules, CA). Whole-cell proteins (30 µg) were separated on 8% SDS-PAGE gels and transferred to polyvinylidene difluoride membranes (Amersham Corp., Arlington Heights, IL). The membranes were blocked with 5% nonfat dry milk for 1 h and then hybridized overnight at 4 °C with the primary antibody Ab-5. After washing with TBS-T buffer (20 mM Tris (pH 8.0), 150 mM NaCl, and 0.1% Tween 20), the membrane was rehybridized with horseradish peroxidase-conjugated anti-mouse antibody (Santa Cruz Biotechnology) for 1 h. Specific protein signals were detected with the chemiluminescence detection system (Bio-Rad). Same membrane was also probed with the antibody against β-actin (Thermo Scientific).

3) Determination of the DT390-BiscFv806 cytotoxicity

We first determined the cell proliferation of U87-EGFRvIII cells following stable transfection of EGFRvIII. U87-EGFRvIII and U87 cells (5×10^3) were seeded, respectively, in 96-well plates and the cell growth was determined at different time points from 3 h to 6 days with PrestoBlue cell viability reagent according to manufacturer's instruction (Life Technologies). The absorbance values at 570 nm and 600 nm (reference wavelength for normalization) were measured, respectively, with an OPTImaxTM Tunable Microplate Reader (Molecular Devices, Sunnyvale, CA). The normalized absorbance values were converted to the cell numbers based on the standard cell number-absorbance curve. Cell doubling time was used as the indicator of cell growth, which was calculated with the formula of $T \ln 2 / \ln(X_e/X_i)$, where T is the cell incubation time in the unit of h; and X_i and X_e are the cell numbers at the beginning and end of exponential phase, respectively, in the cell growth curve.

To determine the cytotoxicity of DT390-BiscFv806 against U87, U87-EGFRvIII, and HNSCC cells, 5×10^3 to 5×10^4 cells were seeded in wells of 96-well plates and allowed to grow overnight. Cells were then exposed to DT390-BiscFv806 at graded concentrations from 0 to 1×10^{-7} M for 48 h. The medium was replaced with fresh medium without DT390-BiscFv806 and the cells were allowed to grow for further 24 h. The cell viability was measured with the PrestoBlue cell viability reagent. The IC₅₀ of DT390-BiscFv806 against the cells was calculated with the Microsoft Excel software. The cell morphology was recorded with an inverted microscope connected to an image processing computer.

To test the potential non-specific cytotoxicity from DT390-BiscFv806, a PSMA-targeted bivalent RIT, A-dmDT390-scFvDb(PSMA), was used as a control. A-dmDT390-scFvDb(PSMA) was confirmed to be highly cytotoxic to PSMA-expressing LNCaP prostate cancer cells (IC₅₀, 0.57 nM), but not to PSMA-negative PC-3 cells (IC₅₀, >100 nM).²⁹ The GBM and HNSCC cell lines are absent of PSMA expression.

3. *In vivo* experimental design

1) Evaluation of the effect of enforced EGFRvIII expression on tumor xenograft growth

To evaluate the effect of enforced expression of EGFRvIII on the growth of U87 tumor xenografts, 1×10^7 subconfluent U87-EGFRvIII and U87 cells in 50 µl medium were inoculated, respectively, into the lower back of female athymic nude mice (ages ~6 weeks, Harlan, Indianapolis, IN). The mice were maintained in a ventilated rack system, and food and water were provided ad libitum. Animals were observed closely and the tumor size was measured with a caliper. The tumor volume was calculated with the formula of $V_t = (L \times W^2)/2$, where V_t is the volume in mm³ at the defined time point, and L and W are the length (large diameter) and width (small diameter) of a tumor, respectively.

The mouse body weight was also weighed at each time point. The mouse body weight loss was calculated with the formula of $\% = [(W_e - W_i)/W_i] \times 100\%$, where W_i is the mouse body weight in gram at the beginning of treatment and W_e is the body weight at the end time point of experiment. The W_i was adjusted to remove the tumor weight, while the tumor weight at the beginning of treatment was calculated based on the tumor volume and tumor density (1.05 g/mL).

2) Evaluation of anti-tumor efficacy against established tumor xenografts

The U87-EGFRvIII and U87 tumor xenografts were established by inoculating 1×10^7 subconfluent cells in the lower back of female athymic nude mice. When the tumor volume reached $>50 \text{ mm}^3$, the mice were divided into treatment and control groups with similar size and size distribution between the two groups. The treatment groups were given DT390-BiscFv806 and the control groups were given PBS. The anti-tumor efficacy was evaluated with the following parameters: tumor volume, tumor weight, RTV, and %TGI. The tumor weight was obtained at the end point of the experiment. The RTV was calculated as V_t/V_i , where V_i is the volume in mm^3 at the beginning of treatment and V_t is the volume at a defined time point. The %TGI was calculated with the equation of $\%TGI=100-(T/C \times 100)$, where T is the individual or mean RTV in the treatment group and C is the mean RTV in the control group at a defined time point.

3) Therapeutic protocols

Protocol 1: Therapeutic regimen for U87-EGFRvIII tumor xenografts: Two intense short courses of treatment were designed considering the extremely rapid growth of U87-EGFRvIII tumor xenografts. DT390-BiscFv806 was administered intravenously *via* tail vein injection. Each course included one dose of $50 \mu\text{g/kg}$ body weight ($\sim 1 \mu\text{g}$ per mouse) per day for 5 consecutive days, with an interval of two days in between the two courses. The activity of mice was monitored closely and their body weights were measured.

Protocol 2: Therapeutic regimen for U87 tumor xenografts: Because of the relatively slow growth of U87 tumor xenografts compared with that of the U87-EGFRvIII tumor xenografts, a different therapeutic regimen was designed including one intense short course (one dose per day for 5 consecutive days), followed by one dose every other day for an additional six doses. Each dose was $50 \mu\text{g/kg}$ body weight. DT390-BiscFv806 was administered intravenously *via* tail vein injection.

All animal studies were carried out in accordance with the guidelines of the Howard University Institutional Animal Care and Use Committees.

4. Pathological Analysis

At the completion of experiments, mice were sacrificed with overdose of isoflurane followed by neck dislocation. Tumors were sectioned in the maximum diameter, fixed in 10% neutral buffered formalin, and embedded in paraffin. Hematoxylin-eosin stained sections with $5 \mu\text{m}$ thickness were used for pathological analysis. The mitotic activity was assessed by counting the mitotic figures in 10 HPF (400x) from the most proliferative areas of tumor.

5. Statistical analysis

Statistical analyses were conducted with the statistical software OriginPro 7.0 (OriginLab, Northampton, MA). The treatment and control groups were compared using Student's *t*-test. Statistical significance was defined as $P < 0.05$.

Disclosure of Potential Conflicts of Interest:

No potential conflicts of interest were disclosed.

Acknowledgement:

This work was supported in part by the NIH/NCRR/RCMI/4, G12 RR003048 at Howard University, the US Army Medical Research and Materiel Command (W81XWH-10-1-0767), and Howard University College of Medicine Bridge Fund (U400067).

References

1. Hatanpaa KJ, Burma S, Zhao D, Habib AA. Epidermal growth factor receptor in glioma: signal transduction, neuropathology, imaging, and radioresistance. *Neoplasia* 2010; 9:675-84.
2. Wikstrand CJ, John H Sampson JH, Darell D Bigner DD. EGFRvIII: an oncogene deletion mutant cell surface receptor target expressed by multiple tumour types. *Expert Opin Ther Targets* 2000; 4:497-514.
3. Kuan CT, Wikstrand CJ, Bigner DD. EGFRvIII as a promising target for antibody-based brain tumor therapy. *Brain Tumor Pathol* 2000; 17:71-8.
4. Lo HW. EGFR-targeted therapy in malignant glioma: novel aspects and mechanisms of drug resistance. *Curr Mol Pharmacol* 2010; 3:37-52.
5. Chung CH, Ely K, McGavran L, Varella-Garcia M, Parker J, Parker N, Jarrett C, Carter J, Murphy BA, Netterville J et al. Increased epidermal growth factor receptor gene copy number is associated with poor prognosis in head and neck squamous cell carcinomas. *J Clin Oncol* 2006; 24:4170-6.
6. Temam S, Kawaguchi H, El-Naggar AK, Jelinek J, Tang H, Liu DD, Lang W, Issa JP, Lee JJ, Mao L. Epidermal growth factor receptor copy number alterations correlate with poor clinical outcome in patients with head and neck squamous cancer. *J Clin Oncol* 2007; 25:2164-70.
7. Sok JC, Coppelli FM, Thomas SM, Lango MN, Xi S, Hunt JL, Freilino ML, Graner MW, Wikstrand CJ, Bigner DD, et al. Mutant epidermal growth factor receptor (EGFRvIII) contributes to head and neck cancer growth and resistance to EGFR targeting. *Clin Cancer Res* 2006; 12:5064-73.
8. Keller J, Shroyer KR, Batajoo SK, Zhao HL, Dong LM, Hayman MJ, Chan EL. Combination of phosphorylated and truncated EGFR correlates with higher tumor and nodal stage in head and neck cancer. *Cancer Invest* 2010; 28:1054-62.
9. Chen LF, Cohen EEW, Grandis JR. New Strategies in Head and Neck Cancer: epidermal growth factor receptor inhibition in head and neck cancer. *Clin Cancer Res* 2010; 16:2489-95.
10. Cohen RB. Current challenges and clinical investigations of epidermal growth factor receptor (EGFR)- and ErbB family-targeted agents in the treatment of head and neck squamous cell carcinoma (HNSCC). *Cancer Treat Rev* 2014; 40:567-77.
11. Taylor TE, Furnari FB, Cavenee WK. Targeting EGFR for treatment of glioblastoma: molecular basis to overcome resistance. *Curr Cancer Drug Targets* 2012; 12:197-209.
12. De Witt Hamer PC. Small molecule kinase inhibitors in glioblastoma: a systematic review of clinical studies. *Neuro Oncol* 2010; 12:304-16.
13. Chong CR1, Jänne PA. The quest to overcome resistance to EGFR-targeted therapies in cancer. *Nat Med* 2013; 19:1389-400.
14. Pastan I, Hassan R, FitzGerald DJ, Kreitman RJ. Immunotoxin treatment of cancer. *Annu Rev Med* 2007; 58:221-37.
15. Shan L, Wang PC. Recombinant immunotoxin therapy of solid tumors: challenges and strategies. *J Basic Clin Med* 2013; 2:1-6.
16. Schmidt M, Vakalopoulou E, Schneider DW, Wels W. Construction and functional characterization of scFv(14E1)-ETA - a novel, highly potent antibody-toxin specific for the EGF receptor. *Br J Cancer* 1997; 75:1575-84.
17. Ochiai H, Archer GE, Herndon JE 2nd, Kuan CT, Mitchell DA, Bigner DD, Pastan IH, Sampson JH. EGFRvIII-targeted immunotoxin induces antitumor immunity that is inhibited in the absence of CD4+ and CD8+ T cells. *Cancer Immunol Immunother* 2008; 57:115-21.
18. Chandramohan V, Bigner DD. A novel recombinant immunotoxin-based therapy targeting wild-type and mutant EGFR improves survival in murine models of glioblastoma. *Oncoimmunol* 2013; 2:e26852.

19. Chandramohan V, Bao X, Keir ST, Pegram CN, Szafranski SE, Piao H, Wikstrand CJ, McLendon RE, Kuan CT, Pastan IH, et al. Construction of an immunotoxin, D2C7-(scdsFv)-PE38KDEL, targeting EGFRwt and EGFRvIII for brain tumor therapy. *Clin Cancer Res* 2013; 19:4717-27.
20. Azemar M, Schmidt M, Arlt F, Kennel P, Brandt B, Papadimitriou A, Groner B, Wels W. Recombinant antibody toxins specific for ErbB2 and EGF receptor inhibit the in vitro growth of human head and neck cancer cells and cause rapid tumor regression in vivo. *Int J Cancer* 2000; 86:269-75.
21. Sampson JH, Akabani G, Archer GE, Bigner DD, Berger MS, Friedman AH, Friedman HS, Herndon JE 2nd, Kunwar S, Marcus S, et al. Progress report of a Phase I study of the intracerebral microinfusion of a recombinant chimeric protein composed of transforming growth factor (TGF)-alpha and a mutated form of the Pseudomonas exotoxin termed PE-38 (TP-38) for the treatment of malignant brain tumors. *J Neurooncol* 2003; 65:27-35.
22. Panousis C, Rayzman VM, Johns TG, Renner C, Liu Z, Cartwright G, Lee FT, Wang D, Gan H, Cao D, et al. Engineering and characterisation of chimeric monoclonal antibody 806 (ch806) for targeted immunotherapy of tumours expressing de2-7 EGFR or amplified EGFR. *Br J Cancer* 2005; 92:1069-77.
23. Luwor RB, Johns TG, Murone C, Huang HJ, Cavenee WK, Ritter G, Old LJ, Burgess AW, Scott AM. Monoclonal antibody 806 inhibits the growth of tumor xenografts expressing either the de2-7 or amplified epidermal growth factor receptor (EGFR) but not wild-type EGFR. *Cancer Res* 2001; 61:5355-61.
24. Johns TG, Mellman I, Cartwright GA, Ritter G, Old LJ, Burgess AW, Scott AM. The antitumor monoclonal antibody 806 recognizes a high-mannose form of the EGF receptor that reaches the cell surface when cells over-express the receptor. *FASEB J* 2005; 19:780-2.
25. Johns TG, Adams TE, Cochran JR, Hall NE, Hoyne PA, Olsen MJ, Kim YS, Rothacker J, Nice EC, Walker F, et al. Identification of the epitope for the epidermal growth factor receptor-specific monoclonal antibody 806 reveals that it preferentially recognizes an untethered form of the receptor. *J Biol Chem* 2004; 279:30375-84.
26. Scott AM, Lee FT, Tebbutt N, Herbertson R, Gill SS, Liu Z, Skrinos E, Murone C, Saunderson TH, Chappell B, et al. A phase I clinical trial with monoclonal antibody ch806 targeting transitional state and mutant epidermal growth factor receptors. *Proc Natl Acad Sci USA* 2007; 104:4071-6.
27. Woo JH, Liu YY, Stavrou S, Neville DM. Increasing secretion of bivalent anti-T-cell immunotoxin by *Pichia pastoris*. *Appl Environ Microbiol* 2004; 70:3370-6.
28. Kim GB, Wang Z, Liu YY, Stavrou S, Mathias A, Goodwin KJ, Thomas JM, Neville DM. A fold-back single-chain diabody format enhances the bioactivity of an anti-monkey CD3 recombinant diphtheria toxin-based immunotoxin. *Protein Eng Des Sel* 2007; 20:425-32.
29. Zhang F, Shan L, Liu Y, Neville D, Woo JH, Chen Y, Korotcov A, Lin S, Huang S, Sridhar R, et al. An anti-PSMA bivalent immunotoxin exhibits specificity and efficacy for prostate cancer imaging and therapy. *Adv Healthc Mater* 2013; 2:736-44.
30. Liu YY, Woo JH, Neville DM. Overexpression of an anti-CD3 immunotoxin increases expression and secretion of molecular chaperone BiP/Kar2p by *Pichia pastoris*. *Appl Environ Microbiol* 2005; 71:5332-40.
31. Hauser BR, Zhu X, Califano J, Gu X. Detection of gene copy number of epidermal growth factor receptor in head and neck squamous cell carcinomas cell lines. *Cancer Res* 2008; 68: 3413.
32. Hauser BR. Epidermal growth factor receptor (EGFR) gene expression and its related biomarkers in head and neck squamous cell carcinoma [master's thesis]. [Washington DC]: Howard University; 2008. 58 p.

33. Liu YY, Woo JH, Neville DM. Targeted introduction of a diphtheria toxin resistant mutation into the chromosomal EF-2 locus of *Pichia pastoris* and expression of immunotoxin in the EF-2 mutants. *Protein Expr Purif* 2003; 30:262-74.
34. Li YM, Vallera DA, Hall WA. Diphtheria toxin-based targeted toxin therapy for brain tumors. *J Neurooncol* 2013; 114:155-64.
35. Adkins I, Holubova J, Kosova M, Sadilkova L. Bacteria and their toxins tamed for immunotherapy. *Curr Pharm Biotechnol*. 2012; 13:1446-73.
36. Matar AJ, Pathiraja V, Wang Z, Duran-Struuck R, Guscha A, Crepeau R, Tasaki M, Sachs DH, Huang CA. Effect of pre-existing anti-diphtheria toxin antibodies on T cell depletion levels following diphtheria toxin-based recombinant anti-monkey CD3 immunotoxin treatment. *Transpl Immunol* 2012; 27:52-4.
37. Manoukian G, Hagemeister F. Denileukin diftitox: a novel immunotoxin. *Expert Opin Biol Ther* 2009; 9:1445-51.
38. Woo JH, Liu JS, Kang SH, Singh R, Park SK, Su Y, Ortiz J, Neville DM, Willingham MC, Frankel AE. GMP production and characterization of the bivalent anti-human T cell immunotoxin, A-dmDT390-bisFv(UCHT1), for phase I/II clinical trials. *Protein Expr Purif* 2008; 58:1-11.
39. Bühler P, Wetterauer D, Gierschner D, Wetterauer U, Beile UE, Wolf P. Influence of structural variations on biological activity of anti-PSMA scFv and immunotoxins targeting prostate cancer. *Anticancer Res* 2010; 30:3373-9.
40. Thompson J, Stavrou S, Weetall M, Hexham JM, Digan ME, Wang Z, Woo JH, Yu Y, Mathias A, Liu YY, et al. Improved binding of a bivalent single-chain immunotoxin results in increased efficacy for in vivo T-cell depletion. *Protein Eng* 2001; 14:1035-41.
41. Nagane M, Coufal F, Lin H, Böglér O, Cavenee WK, Huang HJ. A common mutant epidermal growth factor receptor confers enhanced tumorigenicity on human glioblastoma cells by increasing proliferation and reducing apoptosis. *Cancer Res* 1996; 56:5079-86.
42. Nishikawa R, Ji XD, Harmon RC, Lazar CS, Gill GN, Cavenee WK, Huang HJ. A mutant epidermal growth factor receptor common in human glioma confers enhanced tumorigenicity. *Proc Natl Acad Sci USA* 1994; 91:7727-31.
43. Inda MM, Bonavia R, Mukasa A, Narita Y, Sah DW, Vandenberg S, Brennan C, Johns TG, Bachoo R, Hadwiger P, et al. Tumor heterogeneity is an active process maintained by a mutant EGFR-induced cytokine circuit in glioblastoma. *Genes Dev* 2010; 24:1731-45.

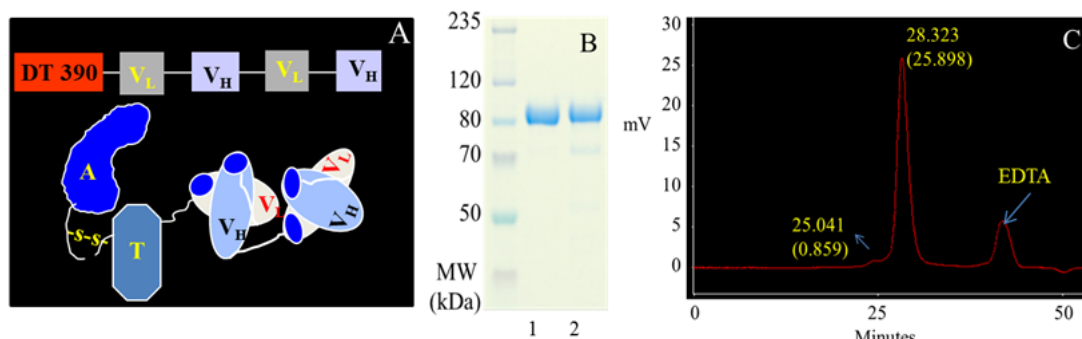


Figure 1: Schematic description and characterization of the EGFR- and EGFRvIII-specific bivalent recombinant immunotoxin, DT390-BiscFv806. 1A shows the linear sequence (upper panel) and cartoon structure (lower panel) of DT390-BiscFv806. 1B and 1C show the SDS-PAGE gel electrophoresis and HPLC analysis of DT390-BiscFv806, respectively. The loading volume of DT390-BiscFv806 was 6 μ l (0.768 μ g) and 90 μ l (11.52 μ g) for gel electrophoresis and HPLC analysis, respectively. Lanes 1 and 2 on the SDS-PAGE gel in 1B are DT390-BiscFv806 with different preparations and having different purity. The product in lane 1 was used in the present studies. Superdex 200 size-exclusion column analysis showed a major and a minor peak at the elution times of 28.323 min and 25.041 min, representing the purified and the aggregated product, respectively (1C). The third peak appeared in the HPLC profile was used as a reference, which was confirmed to be due to the EDTA added in the sample buffer in our previous studies. Both SDS-PAGE electrophoresis and HPLC analysis indicate a high purity of the final product.

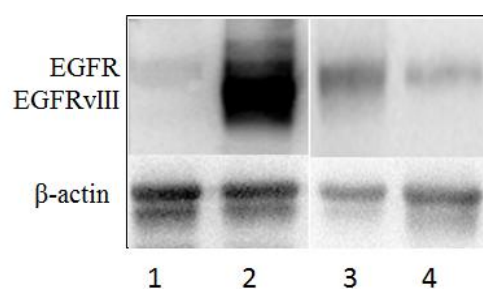


Figure 2: Western blot analysis of EGFR and EGFRvIII protein expression in cultured cells. Lanes 1 and 2 show the U87 and the U87-EGFRvIII cells without and with high expression of EGFRvIII, respectively. Lanes 3 and 4 are JHU-13 and JHU-22 cells as a representative of EGFR expression in head and neck squamous cell carcinoma (HNSCC) cell lines. No EGFRvIII expression was detected in the six HNSCC cell lines analyzed.

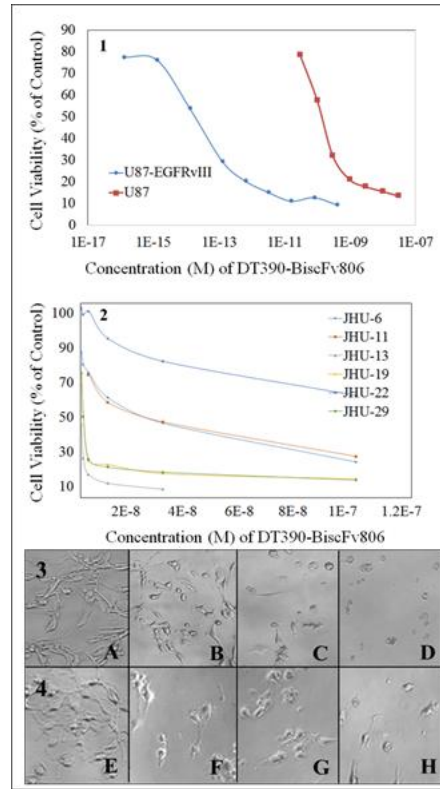


Figure 3: The high cytotoxicity of DT390-BiscFv806 against cancer cells. The panels 1 and 2 show the cell viability curves of glioblastoma cells and head and neck squamous cell carcinoma cells after exposure to graded concentrations of DT390-BiscFv806. The panels 3 and 4 show the representative morphology of the U87 (A to D) and U87-EGFRvIII (E to H) cells, respectively, following exposure of DT390-BiscFv806. The concentrations of DT390-BiscFv806 in the panels 3 and 4 were 0, 3×10^{-11} , 1×10^{-10} , and 1×10^{-8} M for A to D, and 0, 1×10^{-15} , 1×10^{-13} , and 1×10^{-11} for E to H, respectively.

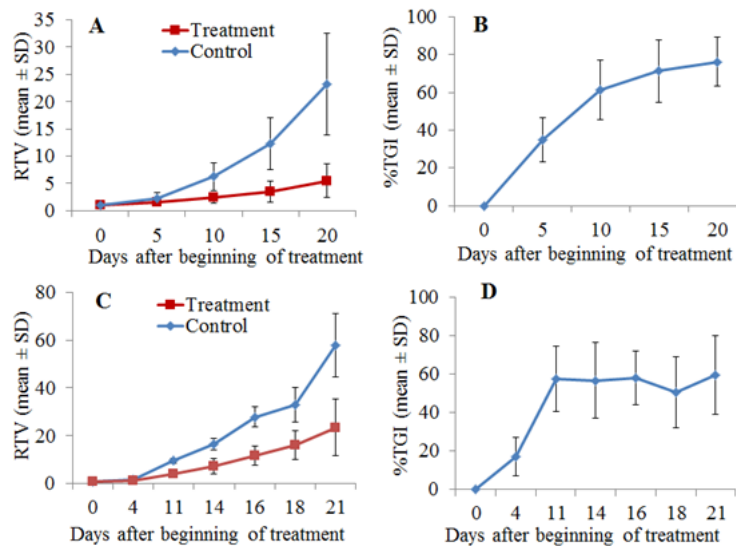


Figure 4: Growth inhibition of established tumor xenografts by DT390-BiscFv806. 4A and 4C represent the changes of the relative tumor volume (RTV) of U87-EGFRvIII and U87 tumor xenografts,

respectively, at different times after beginning of treatment. 4B and 4D show the changes of the percentage tumor growth inhibition (%TGI) of U87-EGFRvIII and U87 xenografts, respectively, at different times after beginning of treatment. The data were expressed as mean \pm SD of six mice per group. RTV and %TGI were calculated as indicated in the Section of Materials and Methods.

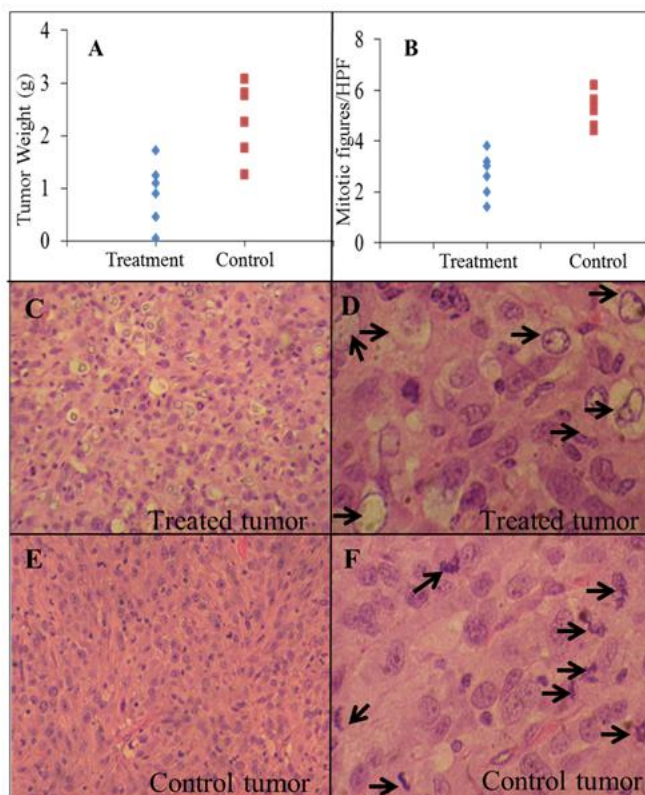


Figure 5: Comparative analysis between DT390-BiscFv806-treated U87-EGFRvIII tumors and control tumors. Compared with the control tumors, the treated tumors had a much lower tumor weight (2.2 ± 0.9 vs. 0.9 ± 0.6 g, $P < 0.05$), a lower number of mitosis (5.23 ± 0.66 vs. 2.67 ± 0.86 per high power field, $P < 0.05$), and many degenerative tumor cells throughout the entire tumors. These degenerative tumors cells were rarely seen in the control tumors. Arrows indicate degenerative tumor cells in 5D and mitosis in 5F. The original magnification was 100x for 5C and 5E, and 400x for 5D and 5F. Tumors were dissected on day 18 after beginning with or without DT390-BiscFv806 treatment.

Assessment of chemical exchange in tryptophan–albumin solution through ^{19}F multicomponent transverse relaxation dispersion analysis

Ping-Chang Lin¹

Received: 2 October 2014 / Accepted: 10 April 2015
© Springer Science+Business Media Dordrecht 2015

Abstract A number of NMR methods possess the capability of probing chemical exchange dynamics in solution. However, certain drawbacks limit the applications of these NMR approaches, particularly, to a complex system. Here, we propose a procedure that integrates the regularized nonnegative least squares (NNLS) analysis of multiexponential T_2 relaxation into Carr–Purcell–Meiboom–Gill (CPMG) relaxation dispersion experiments to probe chemical exchange in a multicompartimental system. The proposed procedure was validated through analysis of ^{19}F T_2 relaxation data of 6-fluoro-DL-tryptophan in a two-compartment solution with and without bovine serum albumin. Given the regularized NNLS analysis of a T_2 relaxation curve acquired, for example, at the CPMG frequency $\nu_{\text{CPMG}} = 125$, the nature of two distinct peaks in the associated T_2 distribution spectrum indicated 6-fluoro-DL-tryptophan either retaining the free state, with geometric mean $\ast/\text{multiplicative standard deviation (MSD)} = 1851.2 \text{ ms} \ast/1.51$, or undergoing free/albumin-bound interconversion, with geometric mean $\ast/\text{MSD} = 236.8 \text{ ms} \ast/1.54$, in the two-compartment system. Quantities of the individual tryptophan species were accurately reflected by the associated T_2 peak areas, with an interconversion state-to-free state ratio of 0.45 ± 0.11 . Furthermore, the CPMG relaxation dispersion analysis estimated the exchange rate

between the free and albumin-bound states in this fluorinated tryptophan analog and the corresponding dissociation constant of the fluorinated tryptophan–albumin complex in the chemical-exchanging, two-compartment system.

Keywords Kinetics · Multiexponential · Nonnegative least squares analysis · Protein–ligand interaction · Complex system

Protein dynamics, referring to temporal and spatial changes in protein properties from the biophysical perspective, plays an essential role in determining protein functions (Baldwin and Kay 2009; Kleckner and Foster 2011). Thus, it is of importance to gain insight into the dynamic process to understand, predict or manipulate the biological function and behavior of a particular protein (Kleckner and Foster 2011). Chemical exchange, one of the particular dynamic processes, indicates coexistence of two or more distinct chemical environments or states for the molecule(s) investigated, of which the properties can be assessed by an array of NMR-based modalities (Kleckner and Foster 2011). Although a number of existing NMR methods possess the capability of probing the chemical exchange properties on defined timescales (Kleckner and Foster 2011), these methods are barely applied to samples not prepared in solution due to their lack of notable differences in specified parameters between the exchange states, such as degeneracy in chemical shift and peak overlap caused by broad linewidths.

It has been increasingly applied to several disciplines that the nonnegative least squares (NNLS) algorithm accompanied by a regularization term is used to analyze the multiexponential ^1H transverse relaxation data of H_2O , from which identified T_2 components were attributed to

Electronic supplementary material The online version of this article (doi:10.1007/s10858-015-9929-4) contains supplementary material, which is available to authorized users.

✉ Ping-Chang Lin
pingchang.lin@howard.edu

¹ Department of Radiology, College of Medicine, Howard University, 2041 Georgia Ave, N.W., Washington, DC 20060, USA

different H₂O compartments, such as (1) cerebrospinal fluid, intra/extracellular water and water trapped between myelin bilayers in healthy human brain, (2) mobile water and proteoglycan-bound water in bovine patellar cartilage, and (3) intracellular and extracellular water compartments in hypertonic saline-injected masseter muscle (Gambarota et al. 2001; Laule et al. 2007; Reiter et al. 2011). Furthermore, the Carr–Purcell–Meiboom–Gill (CPMG) relaxation dispersion experiment has been widely used to quantitate the features of kinetics, thermodynamics and structures of proteins or nucleic acids in exchange processes. Examples include studies of the multi-site folding/unfolding exchange process in the ¹⁵N-labeled deuterated Gly48Met Fyn SH3 domain by measuring T₂ relaxations of backbone amide ¹H and ¹⁵N nuclei, the conformational exchange of ribose backbone groups in the GCAA RNA tetraloop by detecting ¹³C relaxation dispersion on the C2' and C4' resonances, and the kinetic, thermodynamic and structural properties of basic pancreatic trypsin inhibitor by analyzing transverse relaxation dispersions of the associated backbone ¹⁵N spins (Grey et al. 2003; Johnson and Hoogstraten 2008; Korzhnev et al. 2004, 2005). In the present work, we propose an affordable procedure that incorporates the regularized NNLS analysis of multiexponential T₂ relaxation curves into the CPMG relaxation dispersion experiment to study chemical exchange in a two-compartment system. By gathering a set of the regularized NNLS fits of T₂ relaxation curves at various CPMG frequencies in a tryptophan–albumin model to generate transverse relaxation dispersion curves, this approach demonstrated the potential for not only distinguishing T₂ components associated with the effective compartments separated by a semi-permeable membrane but also characterizing chemical exchange occurring in the millisecond time frame in a specified compartment.

A simple model of tryptophan binding serum albumin was selected to validate the NMR procedure of detecting the interconversion in a two-site exchange system. Serum albumin is the most abundant protein in blood plasma and is frequently used to investigate the strength of protein–ligand interaction due to owning a principal binding site for drugs, while tryptophan is one of a few endogenous substances bound to serum albumin (Cao et al. 2003; Fielding et al. 2005). Given the favorable NMR properties of ¹⁹F nuclei that provide a convenient label for NMR studies, we employed 6-fluoro-DL-tryptophan (6F-Trp), a fluorine-labeled tryptophan analog, to monitor its kinetic interaction with bovine serum albumin (BSA) (Jenkins and Lauffer 1990). In contrast to ¹³C or ¹⁵N CPMG relaxation dispersion experiments that may require a relaxation compensation element to equate evolution between in-phase and anti-phase transverse magnetizations, ¹⁹F–¹H couplings do not evolve significantly during the echo-spacing interval, $2\tau_{\text{CPMG}}$, if a restriction of $\tau_{\text{CPMG}} < 1/4J_{\text{FH}}$ is imposed

(Loria et al. 1999). Thus, without concerning in-phase/anti-phase evolution, the relaxation compensation was simply neglected and the CPMG echo train was implemented to acquire the ¹⁹F transverse relaxation data of 6F-Trp with a concentration of 45 mM at 20 ± 1 °C. All the individual points collected at the tops of the respective echoes were assembled to form a decay curve for estimating the T₂ relaxation times (detailed in the Supporting Information). Through varying $2\tau_{\text{CPMG}}$, the interval between successive 180° pulses, a set of CPMG experiments with the interleaved value of ν_{CPMG} , i.e. the reciprocal of $4\tau_{\text{CPMG}}$, ranging from 10 to 1250 Hz were recorded for the ¹⁹F transverse relaxation dispersion analysis. The same manner was respectively performed on the transverse relaxation data collected in the solution of BSA–6F-Trp complex and in the two-compartment system constituting sole 6F-Trp and BSA–6F-Trp complex solutions (abbreviated to two-compartmental 6F-Trp system), of which the sole 6F-Trp and the BSA–6F-Trp complex were separated into the respective layers by a semi-permeable dialysis membrane (Fig. 1). More details can be found in the Supporting Information.

The acquired ¹⁹F transverse decay curves were introduced into the multiexponential T₂ relaxation analysis by using the NNLS algorithm equipped with the Tikhonov regularization (Graham et al. 1996; Reiter et al. 2009):

$$\sum_{n=1}^N \left| \sum_{m=1}^M A_{nm} S_m - y_n \right|^2 + \mu \left| \sum_{m=1}^M S_m \right|^2 \quad (1)$$

in which y_n contains N echo amplitudes on a transverse relaxation curve (N is 192 at echo-spacing $\tau_{\text{CPMG}} = 25$ ms up to 20,480 at echo-spacing $\tau_{\text{CPMG}} = 0.2$ ms), A_{nm} denotes a matrix composed of $N \times (M - 1)$ kernels exhibiting exponential relaxations and $N \times 1$ entries of value 1, and S_m consists of $M - 1$ unknown amplitudes associated with the $M - 1$ transverse relaxation times and one unknown amplitude responding to baseline offset adjustment (detailed in the Supporting Information) (Reiter et al. 2009). In addition, μ is referred to as an NNLS regularizer that endures a certain degree of misfit to balance overfitting and underfitting of experimental data (Graham et al. 1996; Whittall and MacKay 1989). In this study, a set of 80 ($=M - 1$) possible T₂ relaxation values were equally spaced over the logarithmical scale between 0.1 and 5000 ms. The number of estimated T₂ values, $M - 1$, is much less than the number of data points, N , referring to large degrees of freedom for the regularized NNLS analysis of each decay curve. The outcome of the regularized NNLS analysis of a transverse relaxation curve was typically presented as a distribution of the continuous spectrum constructed by a subset of the 80 possible T₂ values. In fact, the regularized NNLS analysis bypasses a classical

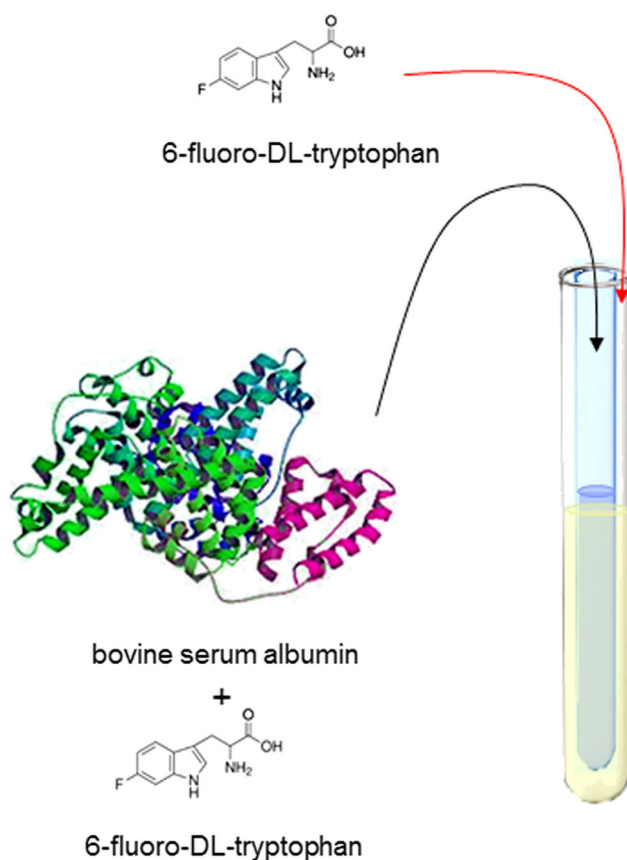


Fig. 1 Schematic of the two-compartmental 6F-Trp system. A 3-mm inner diameter tube made of semi-permeable dialysis membrane was inserted into a 5-mm NMR tube to separate the BSA–6F-Trp complex solution from the sole 6F-Trp solution for the ^{19}F transverse relaxation experiments

paradigm for exponentially ill-posed problems that render no unique solution to, for example, exponential analysis of a multicomponent transverse relaxation curve (Istratov and Vyvenko 1999). Figure 2 exhibits an example of T_2 distribution results attributed to the regularized NNLS analysis of ^{19}F transverse relaxation data acquired at $\nu_{\text{CPMG}} = 125$ Hz in the 6F-Trp solution, the BSA–6F-Trp complex solution, and the two-compartmental 6F-Trp system, respectively. The fits of the corresponding T_2 relaxation curves performed by the regularized NNLS analysis were evaluated by the χ^2 goodness-of-fit test, with the corresponding p values reported. The test indicated that high correlations were performed between the T_2 relaxation data and the fits resulting from the regularized NNLS approach, as shown in Fig. S1 and Table S2 in the Supporting Information.

The T_2 distribution results consisting of either one or two T_2 peaks were further fitted by a 4- or 7-parametric lognormal model (detailed in the Supporting Information). The statistic of each individual fit was reported as the geometric means and multiplicative standard deviations

(MSD) of the lognormal distributions accordingly. While a T_2 distribution consisted of two distinct peaks, the weight fractions of the 6F-Trp compartments associated with the peaks were determined by integrating the peak areas under the corresponding histogram bins, the amplitudes of which were estimated by the lognormal function. In Fig. 2a, the fit exhibited a single T_2 component of 1912.0 ms $\ast/1.31$ in geometric mean \ast/MSD , referring to free 6F-Trp in the 6F-Trp solution. Figure 2b shows a T_2 peak with reduction in its average of 149.6 ms $\ast/1.52$, indicating an indiscernible state made up of free and BSA-bound 6F-Trp in the BSA–6F-Trp complex solution. The indistinct pattern of the free and bound states, presented by a sole peak in the T_2 distribution, was due to occurrence of chemical exchange during acquisition of transverse relaxation data (Baldwin and Kay 2009). In contrast, the regularized NNLS analysis of relaxation data obtained from the two-compartmental 6F-Trp system revealed a T_2 distribution composed of two distinct peaks of 1851.2 ms $\ast/1.51$ and 236.8 ms $\ast/1.54$ in average, respectively (Fig. 2c). Through peak identification by reference to Fig. 2a, b, the outcome evidenced coexistence of the free 6F-Trp state and the interconversion of free and BSA-bound 6F-Trp in the two-compartmental 6F-Trp system. This result shows that the regularized NNLS algorithm is capable of conducting the multiple T_2 component analysis in different types of nuclei but not limited to ^1H transverse relaxations acquired mostly for water compartment analysis.

As noted, two distinct/resolvable peaks shown in the T_2 distributions in the two-compartmental 6F-Trp system refer to a free 6F-Trp state and an interconversion between free and BSA-bound 6F-Trp, respectively. This two-peak feature was observed as the corresponding transverse decay curves acquired at ν_{CPMG} ranging from 10 to 200 Hz (Table 1). The averaged T_2 values in interconversional 6F-Trp exhibited an increasing trend when ν_{CPMG} elevating. Such ν_{CPMG} -dependent T_2 relaxations indicated the presence of chemical exchange, and further analysis through implementing the CPMG relaxation dispersion was required. A minute relaxation dispersion was observed in T_2 distributions obtained from free 6F-Trp (Fig. 3), which was mainly due to underestimation of the relaxation times while using the NNLS algorithm to analyze the transverse decay curves with low single-to-noise ratios (Reiter et al. 2009). In addition, Table 1 shows the ratios of the fractional weight associated with the exchanging 6F-Trp to that associated with the free 6F-Trp in the two-compartment system, with an arithmetic average of 0.45 ± 0.11 at ν_{CPMG} varying between 10 and 200 Hz. The ratios reflected the quantities of 6F-Trp inside the semi-permeable dialysis membrane (i.e. 6F-Trp in the exchange state) and outside the membrane (i.e. free 6F-Trp), respectively. Briefly, by fitting the T_2 distributions with lognormal distributions the

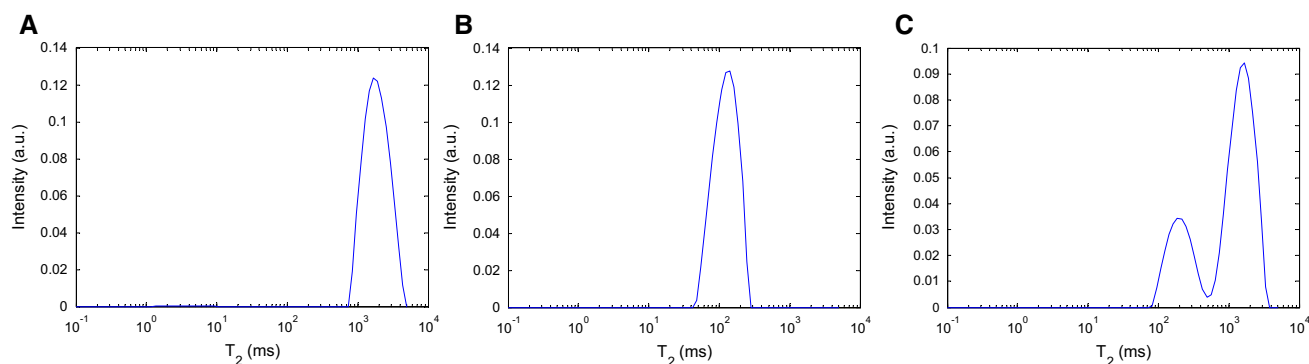


Fig. 2 T_2 distributions resulting from the regularized NNLS analysis of ^{19}F T_2 relaxation curves. The echo time present in the CPMG pulse sequence was $\tau_{\text{CPMG}} = 2$ ms. A single T_2 component was depicted in (a) the 6F-Trp solution and (b) the BSA-6F-Trp complex solution, respectively, while (c) two T_2 components were observed in the two-compartmental 6F-Trp system. The χ^2 statistics for goodness-of-fit

tests of the regularized NNLS-derived fits of T_2 relaxation curves exhibited $\chi^2 = 2317$, $p = 0.41$ for the 6F-Trp solution (Figure S1A), $\chi^2 = 2370$, $p = 0.16$ for the BSA-6F-Trp complex solution (Figure S1B), and $\chi^2 = 2206$, $p = 0.92$ for the two-compartmental 6F-Trp system (Figure S1C), all with degrees of freedom = 2303

estimated 6F-Trp quantitation provides a sensible outcome, compared to the quantity of 6F-Trp determined in the sample preparation with a BSA-6F-Trp complex-to-sole 6F-Trp ratio of 0.45.

Chemical exchange in slow ($k_{\text{ex}} \ll \delta\omega$; $\delta\omega$: chemical shift difference of the associated peaks between the exchanging states), intermediate ($k_{\text{ex}} \approx \delta\omega$), or fast regime ($k_{\text{ex}} \gg \delta\omega$) is detectable via a CPMG-based NMR experiment in which the spin-echo pulse train serves to refocus transverse magnetization dephasing and to lessen non-chemical-shift-derived relaxations including exchange broadening (Ishima and Torchia 1999; Kleckner and Foster 2011; Klobner et al. 2011; Palmer et al. 2001). Through alternating the echo-spacing, $2\tau_{\text{CPMG}}$, between successive 180° pulses, the effective transverse relaxation rate constant, R_2^{eff} , i.e. the reciprocal of effective T_2 , was conducted to estimate the exchange parameters, such as exchange rate k_{ex} , fractional spin population p_i on site A or B, and chemical shift difference $\delta\omega_{AB}$ between sites A and B (Kovrigin et al. 2006). Quantitative estimation of the parameters in the exchanging system can be achieved by analyzing the change in the R_2^{eff} relaxation rates, which were derived from the regularized NNLS fits of the associated T_2 decay curves, responding to varying ν_{CPMG} frequency (Fig. 3). As shown in Fig. 3a, the R_2^{eff} of free 6F-Trp in the 6F-Trp solution slightly fluctuated between 0.33 and 0.75 s^{-1} at the ν_{CPMG} measured. A similar R_2^{eff} profile of free 6F-Trp in the outer layer of the two-compartmental 6F-Trp system was observed, with the value alternating from 0.35 to 0.83 s^{-1} . In contrast, the observed R_2^{eff} of the 6F-Trp under exchange process varied from 1.79 s^{-1} at $\nu_{\text{CPMG}} = 750$ Hz up to 8.42 s^{-1} at $\nu_{\text{CPMG}} = 10$ Hz in the BSA-6F-Trp complex solution as well as from 0.80 ($\nu_{\text{CPMG}} = 500$ Hz) to 6.67 s^{-1} ($\nu_{\text{CPMG}} = 10$ Hz) in the inner layer of the

two-compartmental 6F-Trp system. This indicates that the sense of chemical exchange process was predominated by the binding and unbinding behavior of 6F-Trp on the BSA binding site. Thus, investigation of exchange process focuses primarily on the interconversion of free and BSA-bound 6F-Trp.

To examine a two-site exchange process in the slow exchange regime, the CPMG-based relaxation dispersion curves characterizing interconversional 6F-Trp were fitted into an analytical function of R_2^{eff} expressed on the more populated site A (Tollinger et al. 2001):

$$R_{2A}^{\text{eff}} = R_{2A} + k_A - k_A \frac{\sin(\delta\omega\tau_{\text{CPMG}})}{\delta\omega\tau_{\text{CPMG}}} \quad (2)$$

where R_{2A} , k_A and $\delta\omega$ denote the transverse relaxation rate without exchange on site A, the first-order forward rate constant and the chemical shift difference between two sites A and B, respectively. By considering the free state of 6F-Trp the more populated site A based on preparation of the BSA-6F-Trp complex solution, the relaxation dispersion fitting for interconversional 6F-Trp between the free and BSA-bound states can project the exchange parameters R_{2A} , k_A and $\delta\omega$. The estimated $\delta\omega$ was 1231 ± 155 Hz (or 3.27 ± 0.41 ppm) in the solution of BSA-6F-Trp complex, compared with the observation of a 3.45-ppm drift from the free peak to the BSA-bound peak for 6F-Trp in the ^{19}F spectra (Cao et al. 2003). In addition, a dispersion curve described in the slow exchange regime retained a particular damped oscillation feature near the low-frequency end of ν_{CPMG} (Fig. 3a), from which $\delta\omega$ can be estimated by identifying the frequency leading to the local extremum in the second term of Eq. 2, i.e. $\delta\omega = \tan(\delta\omega\tau_{\text{CPMG}})/\tau_{\text{CPMG}}$

Table 1 Regularized NNLS-derived T_2 distributions in the two-compartmental 6F-Trp system

ν_{CPMG} (Hz)	200	175	150	125	100	75	50	37.5	25	18.75	12.5	10
T_2 , long (ms)	1944.6	2140.5	1920.4	1851.2	1773.5	1737.0	1630.4	1558.5	1528.9	1528.2	1308.6	1211.7
σ_{long}	(1.47)	(1.67)	(1.43)	(1.51)	(1.42)	(1.43)	(1.54)	(1.40)	(1.52)	(1.45)	(1.42)	(1.32)
$[T_2]_{\text{long}}/\sigma_{\text{long}}$, T_2	[1321.8,	[1285.3,	[1345.1,	[1222.6,	[1251.4,	[1212.6,	[1057.3,	[1112.3,	[1004.1,	[1050.6,	[920.5,	[919.4,
$\text{long} \times \sigma_{\text{long}}$	2860.9]	3564.7]	2741.8]	2802.9]	2513.4]	2488.2]	2514.0]	2183.6]	2328.1]	2222.8]	1860.2]	1597.0]
T_2 , short (ms)	268.6	315.2	325.2	236.8	250.1	232.7	160.8	154.2	168.7	176.6	160.7	164.4
σ_{short}	(1.42)	(1.80)	(1.70)	(1.54)	(1.44)	(1.38)	(1.86)	(1.58)	(1.49)	(1.46)	(1.39)	(1.52)
$[T_2]_{\text{short}}/\sigma_{\text{short}}$, T_2 , short	[189.0,	[174.8,	[191.4,	[153.7,	[174.1,	[157.5,	[86.3,	[97.6,	[113.0,	[121.3,	[115.7,	[108.1,
$\times \sigma_{\text{short}}$	381.7]	568.6]	552.7]	364.7]	359.3]	343.6]	299.4]	243.5]	251.9]	257.0]	223.4]	250.0]
Area ratio (w_2 , short/ w_2 , long)	0.45	0.46	0.51	0.38	0.38	0.42	0.50	0.54	0.21	0.50	0.43	0.67

T_2 , long (or T_2 , short) and σ_{long} (or σ_{short}) are the geometric mean and the multiplicative standard deviation for long (or short) T_2 component, respectively. Data acquired at $\nu_{\text{CPMG}} = 250$ –1250 Hz are not shown due to the T_2 , long and T_2 , short components are indistinct

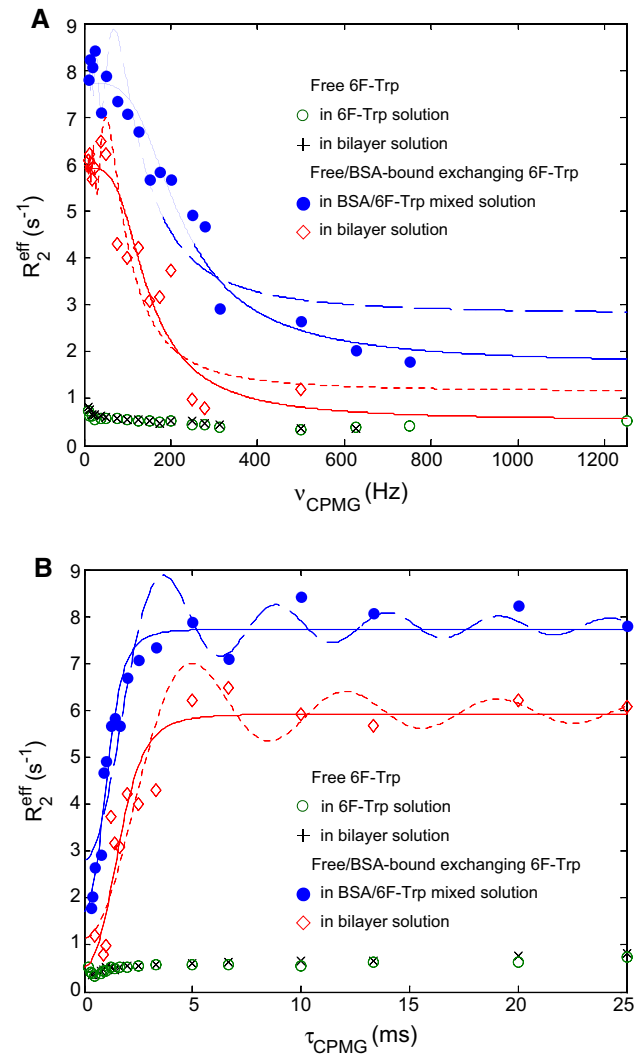


Fig. 3 ^{19}F effective transverse relaxation rates as a function of CPMG field strength for 6F-Trp compartments. Relaxation dispersion data collected in free/bound exchanging 6F-Trp are presented with the associated fitting curves. The fitting curves to relaxation dispersion data using Eq. 2 (slow exchange expression) are displayed in *dash lines*, while those using Eq. 3 (skewed population $P_A > P_B$ approximation) are in *solid lines*. The relaxation dispersions are plotted in (a) R_2^{eff} versus CPMG frequency and (b) R_2^{eff} versus half of echo-spacing τ_{CPMG}

(Tollinger et al. 2001). Accordingly, $\delta\omega$ was calculated by locating the first local maximum observed from the high-frequency end of the dispersion curve ($\delta\omega\tau_{\text{CPMG}} \approx 3\pi/2$); however, the estimated $\delta\omega$ of 2.51 ppm did not match the direct measure on the ^{19}F NMR spectra. This is likely due to the designed ν_{CPMG} frequencies not close enough to the loci of actual extrema on the dispersion curve (Fig. 3b).

In addition to profiling the damped oscillation on the relaxation dispersion curve, the curve fitting using Eq. 2 obtained the estimated R_{2A} and k_A of $2.80 \pm 0.77 \text{ s}^{-1}$ and $4.94 \pm 1.01 \text{ s}^{-1}$, respectively, for 6F-Trp undergoing chemical exchange in the BSA–6F-Trp complex solution. Still,

this fitting analysis untangles neither an exchange rate nor fractional populations in an exchange system (Kloiber et al. 2011). Alternatively, a simpler approximation of the Carver–Richards analysis that tackles prediction of the exchange rate and the spin populations is applicable to the condition of skewed populations $P_A > P_B$ from slow to fast exchange regimes (Ishima and Torchia 1999; Palmer et al. 2001):

$$R_2^{eff} = R_2 + \frac{P_A P_B \delta\omega^2 k_{ex}}{k_{ex}^2 + \left(P_A^2 \delta\omega^4 + \frac{144}{16\tau_{CPMG}^4}\right)^{1/2}} \quad (3)$$

in which R_2 and k_{ex} are the exchange-free transverse relaxation rate and the exchange rate constant, respectively. Through implementing Eq. 3 to fit the relaxation dispersion curve collected in the BSA–6F-Trp complex solution, the estimates of $k_{ex} = 249.8 \text{ s}^{-1}$, $P_A = 97.54 \%$ of 6F-Trp (or 43.98 mM) in the free state and $P_B = 2.46 \%$ of 6F-Trp (or 1.11 mM) in the bound state, which are expected because of the molar ratio of BSA to 6F-Trp being 2.51 % as the sample prepared. The populations P_A and P_B estimated, referring to the dissociation constant $K_D = 912 \text{ }\mu\text{M}$, are comparable to $P_A = 97.49\text{--}97.65 \%$ ($P_B = 2.51\text{--}2.35 \%$) calculated from the dissociation constant $K_D = \sim 10\text{--}3000 \text{ }\mu\text{M}$ reported in literature and the sample concentrations used in this study (Cao et al. 2003; Chanut et al. 1992; Fielding et al. 2005). Further, the estimates of R_2 and $\delta\omega$ were obtained from the same analysis, with the values of 1.72 s^{-1} and 1205 Hz (3.20 ppm), respectively. Here we simply demonstrated that the fits of the multiexponential- T_2 -analysis-derived CPMG relaxation dispersions were sensibly comparable to the results obtained from different approaches (Cao et al. 2003; Chanut et al. 1992; Fielding et al. 2005), although it is well known that the absolute values of the derived parameters including the dissociation constant in an exchange process are usually inaccurate and require multi-field relaxation dispersion data for faithful estimation (Cao et al. 2003; Kovrigin et al. 2006; Palmer et al. 2001).

In the two-compartmental 6F-Trp system, the same manner of fitting analyses using Eqs. 2 and 3 were also applied to the ^{19}F transverse relaxation dispersion curve associated with 6F-Trp undergoing exchange process. The fit via Eq. 2 estimated R_{2A} of $1.15 \pm 0.96 \text{ s}^{-1}$, k_A of $4.81 \pm 1.20 \text{ s}^{-1}$ and $\delta\omega$ of $904 \pm 142 \text{ Hz}$ ($2.40 \pm 0.38 \text{ ppm}$), while k_{ex} of 249.5 s^{-1} , P_A of 97.61 %, R_2 of 0.82 s^{-1} and $\delta\omega$ of 693 Hz were obtained by the simpler approximation with a prerequisite of $P_A \gg P_B$ (Eq. 3). The results indicate that the regularized NNLS analysis permits valid characterization of transverse relaxation dispersion of a given compartment in the presence of an uninteresting, “contaminating” compartment. Moreover, the regularized NNLS-integrated CPMG relaxation dispersion analysis provides a potential approach to investigation of exchanging kinetics, for example, in the nature of a

monomer–oligomer equilibrium with overlapping MR resonances, which precludes conventional NMR analyses.

In summary, investigation of chemical exchange process in a complex system, such as a two-compartment system, can be achieved through using a procedure that integrates the regularized NNLS analysis of multiexponential T_2 decay curves into the CPMG relaxation dispersion analysis. By exploiting the fluorinated amino acid as a ^{19}F NMR label, the procedure exhibited the capabilities of distinguishing two 6F-Trp species, quantitating these two species in the two-compartmental 6F-Trp system and rationally estimating the chemical exchange parameters for the interconversional 6F-Trp.

Acknowledgments This project was supported in part by Georgetown University Subgrant RX-4004-043-HU under National Center for Advancing Translational Sciences/NIH (8 UL1 TR000101-03), National Institute on Minority Health and Health Disparities/NIH (G12 MD007597), and US Army Medical Research and Materiel Command (W81XWH-10-1-0767).

Conflicts of interest The author declares that there is no conflict of interest.

Human and Animal Rights This research does not involve human participants or animals.

Informed consent None.

References

- Baldwin AJ, Kay LE (2009) NMR spectroscopy brings invisible protein states into focus. *Nat Chem Biol* 5:808–814. doi:10.1038/nchembio.238
- Cao B, Endsley S, Andersen NH (2003) ^{19}F NMR studies of tryptophan/serum albumin binding. *Bioorg Med Chem* 11:69–75. doi:10.1016/s0968-0896(02)00324-3
- Chanut E, Zini R, Trouvin JH, Riant P, Tillement JP, Jacquot C (1992) Albumin binding and brain uptake of 6-fluoro-DL-tryptophan: competition with L-tryptophan. *Biochem Pharmacol* 44:2082–2085. doi:10.1016/0006-2952(92)90112-v
- Fielding L, Rutherford S, Fletcher D (2005) Determination of protein-ligand binding affinity by NMR: observations from serum albumin model systems. *Magn Reson Chem* 43:463–470. doi:10.1002/mrc.1574
- Gambarota G, Cairns BE, Berde CB, Mulkern RV (2001) Osmotic effects on the T_2 relaxation decay of in vivo muscle. *Magn Reson Med* 46:592–599. doi:10.1002/mrm.1232
- Graham SJ, Stanchev PL, Bronskill MJ (1996) Criteria for analysis of multicomponent tissue T_2 relaxation data. *Magn Reson Med* 35:370–378. doi:10.1002/mrm.1910350315
- Grey MJ, Wang C, Palmer AG 3rd (2003) Disulfide bond isomerization in basic pancreatic trypsin inhibitor: multisite chemical exchange quantified by CPMG relaxation dispersion and chemical shift modeling. *J Am Chem Soc* 125:14324–14335. doi:10.1021/ja0367389
- Ishima R, Torchia DA (1999) Estimating the time scale of chemical exchange of proteins from measurements of transverse relaxation rates in solution. *J Biomol NMR* 14:369–372. doi:10.1023/A:1008324025406

- Istratov AA, Vyvenko OF (1999) Exponential analysis in physical phenomena. *Rev Sci Instrum* 70:1233–1257. doi:[10.1063/1.1149581](https://doi.org/10.1063/1.1149581)
- Jenkins BG, Lauffer RB (1990) Detection of site-specific binding and co-binding of ligands to human serum albumin using ^{19}F NMR. *Mol Pharmacol* 37:111–118
- Johnson JE Jr, Hoogstraten CG (2008) Extensive backbone dynamics in the GCAA RNA tetraloop analyzed using ^{13}C NMR spin relaxation and specific isotope labeling. *J Am Chem Soc* 130:16757–16769. doi:[10.1021/ja805759z](https://doi.org/10.1021/ja805759z)
- Kleckner IR, Foster MP (2011) An introduction to NMR-based approaches for measuring protein dynamics. *Biochim Biophys Acta Proteins Proteomics* 1814:942–968. doi:[10.1016/j.bbapap.2010.10.012](https://doi.org/10.1016/j.bbapap.2010.10.012)
- Kloiber K, Spitzer R, Tollinger M, Konrat R, Kreutz C (2011) Probing RNA dynamics via longitudinal exchange and CPMG relaxation dispersion NMR spectroscopy using a sensitive ^{13}C -methyl label. *Nucleic Acids Res* 39:4340–4351. doi:[10.1093/nar/gkq1361](https://doi.org/10.1093/nar/gkq1361)
- Korzhnev DM, Salvatella X, Vendruscolo M, Di Nardo AA, Davidson AR, Dobson CM, Kay LE (2004) Low-populated folding intermediates of Fyn SH3 characterized by relaxation dispersion NMR. *Nature* 430:586–590. doi:[10.1038/nature02655](https://doi.org/10.1038/nature02655)
- Korzhnev DM, Neudecker P, Mittermaier A, Orekhov VY, Kay LE (2005) Multiple-site exchange in proteins studied with a suite of six NMR relaxation dispersion experiments: an application to the folding of a Fyn SH3 domain mutant. *J Am Chem Soc* 127:15602–15611. doi:[10.1021/ja054550e](https://doi.org/10.1021/ja054550e)
- Kovrigin EL, Kempf JG, Grey MJ, Loria JP (2006) Faithful estimation of dynamics parameters from CPMG relaxation dispersion measurements. *J Magn Reson* 180:93–104. doi:[10.1016/j.jmr.2006.01.010](https://doi.org/10.1016/j.jmr.2006.01.010)
- Laule C, Vavasour IM, Kolind SH, Traboulsee AL, Moore GRW, Li DKB, MacKay AL (2007) Long T2 water in multiple sclerosis: what else can we learn from multi-echo T2 relaxation? *J Neurol* 254:1579–1587. doi:[10.1007/s00415-007-0595-7](https://doi.org/10.1007/s00415-007-0595-7)
- Loria JP, Rance M, Palmer AG 3rd (1999) Transverse-relaxation-optimized (TROSY) gradient-enhanced triple-resonance NMR spectroscopy. *J Magn Reson* 141:180–184. doi:[10.1006/jmre.1999.1891](https://doi.org/10.1006/jmre.1999.1891)
- Palmer AG III, Kroenke CD, Loria JP (2001) Nuclear magnetic resonance methods for quantifying microsecond-to-millisecond motions in biological macromolecules. *Methods Enzymol* 339:204–238. doi:[10.1016/s0076-6879\(01\)39315-1](https://doi.org/10.1016/s0076-6879(01)39315-1)
- Reiter DA, Lin PC, Fishbein KW, Spencer RG (2009) Multicomponent T-2 relaxation analysis in cartilage. *Magn Reson Med* 61:803–809. doi:[10.1002/mrm.21926](https://doi.org/10.1002/mrm.21926)
- Reiter DA, Roque RA, Lin PC, Doty SB, Pleshko N, Spencer RG (2011) Improved specificity of cartilage matrix evaluation using multiexponential transverse relaxation analysis applied to pathomimetically degraded cartilage Nmr. *Biomedicine* 24:1286–1294. doi:[10.1002/Nbm.1690](https://doi.org/10.1002/Nbm.1690)
- Tollinger M, Skrynnikov NR, Mulder FA, Forman-Kay JD, Kay LE (2001) Slow dynamics in folded and unfolded states of an SH3 domain. *J Am Chem Soc* 123:11341–11352. doi:[10.1021/ja011300z](https://doi.org/10.1021/ja011300z)
- Whittall KP, MacKay AL (1989) Quantitative interpretation of NMR relaxation data. *J Magn Reson* 84:134–152. doi:[10.1016/0022-2364\(89\)90011-5](https://doi.org/10.1016/0022-2364(89)90011-5)



Non-Invasive MRI and Spectroscopy of *mdx* Mice Reveal Temporal Changes in Dystrophic Muscle Imaging and in Energy Deficits

Christopher R. Heier¹, Alfredo D. Guerron¹, Alexandru Korotcov², Stephen Lin², Heather Gordish-Dressman^{1,3}, Stanley Fricke⁴, Raymond W. Sze⁵, Eric P. Hoffman^{1,3}, Paul Wang^{2,6}, Kanneboyina Nagaraju^{1,3*}

1 Center for Genetic Medicine Research, Children's National Medical Center, Washington, D.C., United States of America, **2** Department of Radiology, Howard University College of Medicine, Washington, D.C., United States of America, **3** Department of Integrative Systems Biology, George Washington University School of Medicine and Health Sciences, Washington, D.C., United States of America, **4** Department of Diagnostic Imaging and Radiology, Children's National Medical Center, Washington, D.C., United States of America, **5** Department of Radiology, Children's National Medical Center, Washington, D.C., United States of America, **6** Department of Electrical Engineering, Fu Jen Catholic University, Taipei, Taiwan

Abstract

In Duchenne muscular dystrophy (DMD), a genetic disruption of dystrophin protein expression results in repeated muscle injury and chronic inflammation. Magnetic resonance imaging shows promise as a surrogate outcome measure in both DMD and rehabilitation medicine that is capable of predicting clinical benefit years in advance of functional outcome measures. The *mdx* mouse reproduces the dystrophin deficiency that causes DMD and is routinely used for preclinical drug testing. There is a need to develop sensitive, non-invasive outcome measures in the *mdx* model that can be readily translatable to human clinical trials. Here we report the use of magnetic resonance imaging and spectroscopy techniques for the non-invasive monitoring of muscle damage in *mdx* mice. Using these techniques, we studied dystrophic *mdx* muscle in mice from 6 to 12 weeks of age, examining both the peak disease phase and natural recovery phase of the *mdx* disease course. T2 and fat-suppressed imaging revealed significant levels of tissue with elevated signal intensity in *mdx* hindlimb muscles at all ages; spectroscopy revealed a significant deficiency of energy metabolites in 6-week-old *mdx* mice. As the *mdx* mice progressed from the peak disease stage to the recovery stage of disease, each of these phenotypes was either eliminated or reduced, and the cross-sectional area of the *mdx* muscle was significantly increased when compared to that of wild-type mice. Histology indicates that hyper-intense MRI foci correspond to areas of dystrophic lesions containing inflammation as well as regenerating, degenerating and hypertrophied myofibers. Statistical sample size calculations provide several robust measures with the ability to detect intervention effects using small numbers of animals. These data establish a framework for further imaging or preclinical studies, and they support the development of MRI as a sensitive, non-invasive outcome measure for muscular dystrophy.

Citation: Heier CR, Guerron AD, Korotcov A, Lin S, Gordish-Dressman H, et al. (2014) Non-Invasive MRI and Spectroscopy of *mdx* Mice Reveal Temporal Changes in Dystrophic Muscle Imaging and in Energy Deficits. PLoS ONE 9(11): e112477. doi:10.1371/journal.pone.0112477

Editor: Diego Fraidenreich, Rutgers University -New Jersey Medical School, United States of America

Received: August 6, 2014; **Accepted:** October 4, 2014; **Published:** November 12, 2014

Copyright: © 2014 Heier et al. This is an open-access article distributed under the terms of the Creative Commons Attribution License, which permits unrestricted use, distribution, and reproduction in any medium, provided the original author and source are credited.

Data Availability: The authors confirm that all data underlying the findings are fully available without restriction. All relevant data are within the paper and its Supporting Information files.

Funding: CRH is supported by the National Institutes of Health's (http://www.nih.gov/) 5T32AR056993 and 5R24HD050846-02 grants. PW and this work were supported in part by the National Institutes of Health's G12MD007597 and United States Army Medical Research and Materiel Command (http://mrmc.amedd.army.mil/) W81XWH 10-1-0767 grants. KN is supported by National Institutes of Health's K26OD011171 and P50AR060836 grants, a Muscular Dystrophy Association (http://mda.org/) translational grant 30000783/4736, and the United States Department of Defense (http://www.defense.gov/) grants W81XWH-05-1-0659, W81XWH-11-1-0782, W81XWH-11-1-0330, and W81XWH-11-1-0782. The funders had no role in study design, data collection and analysis, decision to publish, or preparation of the manuscript.

Competing Interests: The authors have declared that no competing interests exist.

* Email: KNagaraju@childrensnational.org

Introduction

Duchenne muscular dystrophy (DMD) is the most common lethal genetic muscle disease diagnosed in children. Dystrophin-deficient *mdx* mice are a naturally occurring genetic model of DMD and are widely used for preclinical drug testing. Both DMD and *mdx* muscle undergo cycles of degeneration and regeneration, resulting in a chronic inflammatory state in skeletal muscle. Together, a clearly defined genetic cause and animal models establish a logical path for developing therapies for DMD through

translational medicine. Several such compounds have now begun to enter clinical trials, including drug classes that target either the skipping of problematic exons [1–3] or inflammation and membrane stability [4].

Two significant problems encountered thus far in the case of DMD and related translational areas are a lack of quantitative surrogate outcome measures [5] and a poor success rate in translating success in preclinical mouse trials into success in human clinical trials [6–8]. Currently, many outcome measures used in early DMD trials consist of measures that can be subjective, could

be susceptible to coaching effects or placebo effects, or show high variability [5,9]. In preclinical *mdx* studies, most outcome measures used are unique to mice or must be substantially altered or interpreted to account for species differences.

Magnetic resonance imaging (MRI) is the gold standard for imaging damage to soft-tissue such as muscle. MRI is a non-invasive technique that does not require anesthesia in humans. It provides advantages over microCT, X-ray, and ultrasound imaging techniques in that it does not use ionizing radiation, and provides high-resolution imaging with strong contrast in soft tissues [10,11]. Early MRI and nuclear magnetic resonance (NMR) spectroscopy studies have shown clear differences between DMD and healthy muscle. Adipose tissue replacement of muscle is prominent in standard T2-weighted MRI imaging of advanced-stage DMD patients [12,13]. Fat-suppression MRI techniques allow for enhanced imaging of edema and inflammation [12]. Nuclear magnetic resonance spectroscopy techniques show that DMD muscle is in a state of energy deficiency [14], and detect increased lipid content within muscle [15]. Given these studies establishing dystrophic muscle phenotypes, together with studies comparing clinical groups [16], changes over time [17], and correlation with clinical assessments [18,19], MRI is emerging as a potential key surrogate outcome measure for DMD clinical trials.

Here, we use MRI methodologies to study muscle damage and changes over time in *mdx* mice. One characteristic of the *mdx* disease is the period of peak necrosis and disease severity from 3 to 6 weeks of age; this severe disease is followed by a recovery period that produces mild phenotypes in the mice by 10–12 weeks of age [20–23]. We use a longitudinal strategy in which we image the same mice and muscles repeatedly from 6 to 12 weeks of age. This approach has several advantages: it examines two distinct disease phases, longitudinal measures increase statistical power, it facilitates design of non-invasive studies with technologies that are translatable to human muscle, and by assaying natural recovery periods it provides an idea of what therapeutic efficacy could look like. Here, we show clear MRI and NMR spectroscopy phenotypes in 6-week *mdx* mice in comparison to wild-type. These phenotypes include measures of muscle damage and a deficiency in energy metabolites. Interestingly, many of these differences are eliminated or reduced as *mdx* mice transition into the recovery phase of disease. Taken together, our results support the non-invasive use of MRI surrogate outcome measures for diagnosis, prognosis, and rehabilitation of muscle damage in muscular dystrophy.

Materials and Methods

Ethics Statement

All animal work was conducted according to relevant national and international guidelines. All studies were reviewed and approved by the Institutional Animal Care and Use Committee of Children's National Medical Center, the Washington DC Veterans Affairs Medical Center Institutional Animal Care and Use Committee, and by the Howard University Institutional Animal Care and Use Committee.

Animal care

All experiments were conducted according to protocols approved by the Institutional Animal Care and Use Committees of Children's National Medical Center, the Washington DC Veterans Affairs Medical Center, and Howard University. Animals were maintained in a controlled mouse facility with a 12 h light: 12 h dark photoperiod, fed *ad libitum*, and monitored daily for health. All *mdx* (C57BL/10ScSn-DMD<mdx>/J) and

wild-type (C57BL/10ScSnJ) female mice were obtained from the Jackson Laboratory (Bar Harbor, ME). Groups for the longitudinal study initially consisted of six wild-type and six *mdx* mice each. One wild-type mouse stopped breathing under anesthesia and was removed from the study. Mice were received at 4 weeks of age, allowed to acclimate for 2 weeks, and assayed beginning at 6 weeks of age. MRI and NMR spectroscopy were performed on each mouse every 2 weeks until the mice were 12 weeks of age. To immobilize the animals for MRI and NMR spectroscopy scans, they were anesthetized with 1.5% isoflurane, gently restrained in imaging position upon a plastic plate, and positioned in the center of the MRI scanner. For imaging, mice were placed in a holder that maintained their temperature at 37°C, with monitoring of their body temperature as well as respiratory and heart rates. Hindlimb muscles were examined in two sites per animal, including the leg and the thigh.

MRI and NMR spectroscopy

In vivo monitoring of mouse hindlimbs and muscle damage was performed using a 9.4 T, 89-mm vertical bore NMR spectrometer (Bruker Biospin MRI, Billerica, MA) with a 25-mm inner diameter dual nucleus ($^{31}\text{P}/^1\text{H}$) birdcage coil. For anatomical positioning, a pilot image set of three orthogonal imaging planes were used. MRI pulse sequences used for data acquisition used T2-weighted imaging (T2) and fat-suppressed T2-weighted imaging (FS) sequences optimized for imaging of muscle inflammation. The imaging sequence used was a rapid acquisition with relaxation enhancement (RARE) sequence: echo time (TE) = 7.4 ms; repetition time (TR) = 3,000 ms; RARE factor 16; flip angle $\alpha = 90^\circ$; field of view = 2.56 cm \times 2.56 cm; slice thickness = 1 mm with no gap between slices; matrix size = 256 \times 256; number of averages = 12.

Spectra were processed using TopSpin v1.5 software (Bruker Biospin MRI, Billerica, MA). For ^{31}P spectroscopy studies, unlocalized single-pulse spectroscopy was performed with 4k transients and a band width of 50 ppm. Integral areas of spectral peaks corresponding to inorganic phosphorous (Pi), phosphocreatine (PCr), and the three phosphate groups of adenosine triphosphate (α -ATP, β -ATP, and γ -ATP) were measured. Pi peaks were not detectable in several of the mice assayed (3 *mdx* and 5 wild-type); for these mice Pi values were uniformly omitted from the analyses. The presence of phosphomonoester (PME) or phosphodiester (PDE) peaks was also recorded; however, the signal-to-noise ratio of these peaks was not always adequate for accurate quantification. Levels of PCr and Pi were normalized by dividing by either the total ATP present in that spectrum or by the amount of β -ATP present in that spectrum. The results were consistent between both of these normalization methods; data are presented as the ratio of each parameter to total ATP.

For analysis of MRI images, two-dimensional sequential (2dseq) files were converted to digital imaging and communications in medicine (DICOM) files and analyzed using ImageJ v1.48 (NIH) software. To obtain volumetric data and account for possible variability between individual MRI slices, multiple consecutive MRI slices of each leg and thigh were assembled into image stacks encompassing 5- or 3-mm sections of the mouse hindlimb. Each stack was analyzed individually, and values for the two legs or thighs of each mouse were then averaged to obtain a single value for that mouse. For the leg, five consecutive slices along the long axis of the tibia were assayed, beginning 2 mm distal from the tibial plateau as a reference point to ensure mice were assayed at the same anatomical location. For the thigh, three consecutive slices along the long axis of the femur were assayed, beginning 6 mm proximal from the femoral condyles. Within each slice,

regions of interest were digitally traced in ImageJ for each leg such that they were defined as the total area internal to the leg or thigh. Within regions of interest in each individual MRI image, we measured the total cross-sectional area, as well as the volumetric area (in voxels, or volume pixels) of bone, of muscle (with bone subtracted), and of tissue exceeding threshold signal intensity. For cross-sectional area, the highest value for each leg or thigh was recorded as the maximal cross-sectional area (CSA_{max}). Bone was measured by digitally tracing the dark outline shape of the tibia or femur in MRI images, and measuring the area outlined. Muscle area was measured by subtracting bone from the combined muscle and bone area making up the full region of interest. Elevated signal intensity was measured using ImageJ software in a semi-automated manner by measuring the volumetric area in voxels that exceeded background threshold within the regions of interest. Percent of tissue with elevated signal intensity was calculated by dividing this measurement by the area in voxels measured for muscle.

Histology

Mice were assayed by T2 imaging of the leg as described above. Immediately after each imaging session, the imaged mouse was sacrificed and the whole leg fixed in formalin. This was performed with 3 *mdx* and 2 wild-type mice at 6 months of age. Paraffin cross-sections of the legs were made at locations of interest corresponding to MRI slices as specified in a sagittal positioning image (Histoserv, Inc.), and sections were stained with H&E. Images were obtained using an Olympus BX61TRF (Olympus, Center Valley, PA) microscope with an Olympus DP71 camera and Olympus DP Controller v3.2.1.276 software. Using ImageJ software, digital tracing and overlap of the tibia structure between H&E and MRI images was used to confirm anatomical location within a corresponding MRI slice. T2 images for specific slices were then compared to corresponding H&E images for qualitative analysis within regions of interest. Multiple images taken with a 4× objective were used to produce full cross-sectional H&E montage images of the leg, and an inset image within a representative area was taken with a 10× objective. Histopathology was assayed qualitatively as reported previously [24].

Statistical Analysis

All statistical analyses were performed by a dedicated biostatistician. Separate regression models were run for each measurement, method, and site. All models were mixed effects linear regression models with the mouse ID as the random coefficient. This approach allowed us to take into account the repeated measures taken at each time point. The main effects of strain and time were tested. All within-strain measurements were approximately normally distributed; therefore, no normalizing transformations were used. All single time-point strain comparisons were done using t-tests without adjustment for multiple testing to facilitate the powered design of trials with single time points. Sample size calculations were performed to determine the number of mice needed to detect a significant change with treatment, to facilitate future preclinical and proof-of-concept studies. Calculations were performed on *mdx* mice only, with the expectation that WT mice would not show the level of changes in inflammation and muscle changes expected in *mdx* mice. For PCr, the percent of voxels with elevated signal, maximum CSA, and volume of tissue with elevated intensity, we performed calculations to show a 20% change in mean value. Power analyses were one-sided in the direction of *mdx* value movement toward wild-type values and assumed a power of 80% and an $\alpha = 0.05$. Throughout the text, all data are presented as means \pm standard deviation unless otherwise noted.

Results

NMR spectroscopy shows *mdx* energetics deficit

To determine the state of energy metabolites in *mdx* versus healthy mice, we assayed the relative levels of phosphate metabolites in mice using un-localized ^{31}P spectroscopy. Here, the levels of phosphocreatine (PCr), inorganic phosphate (Pi), and adenosine triphosphate (ATP, with α -, β - and γ - peaks corresponding to its three phosphate groups) were assayed every 2 weeks beginning at 6 weeks of age (Figure 1A). At 6 weeks of age, PCr levels were significantly lower in *mdx* than in wild-type mice, with PCr:ATP ratios of 0.44 ± 0.05 and 0.58 ± 0.03 ($p \leq 0.001$), respectively (Figure 1B). The difference in PCr levels between *mdx* and wild-type mice was reduced by 8 weeks of age, as the *mdx* mice entered the recovery stage of their disease, with *mdx* levels resembling wild-type and no significant difference present from 8 weeks to 12 weeks of age. In contrast to PCr, the levels of Pi:ATP were significantly increased ($p < 0.05$) in *mdx* mice compared to wild-type at both 6 weeks and 8 weeks of age, after which they resembled wild-type (Figure 1C). These findings indicate that at 6 weeks of age, during the peak stage of *mdx* weakness and necrosis [20,22,23], the *mdx* mice experience an energy metabolism deficiency that subsequently improves during the recovery phase.

Longitudinal MRI of *mdx* muscle detects effects of *mdx* genotype and age

To image dystrophic muscle in live mice during the peak necrosis and recovery phases of the *mdx* condition, we performed T2-weighted imaging and fat-suppressed imaging of leg and thigh muscles every 2 weeks, from 6 to 12 weeks of age. Heterogeneous areas of elevated intensity were visible in all *mdx* mice and at all time points, in contrast to the more uniform and dark signal for healthy control muscle tissue (Figure 2A). Orientation and relevant anatomy are provided (Figure 2B). By aligning anatomically matched MRI slices using the tibial plateau as a reference point across successive time points, we observed qualitative changes in the sites and patterns of hyperintense foci within *mdx* leg muscles between two-week intervals.

Quantitatively, we detected significant effects of the *mdx* genotype on measures of muscle damage and size by both T2-weighted and fat-suppressed imaging, in both the leg and thigh muscles. No significant differences were observed in volumetric bone area between *mdx* and wild-type, for either the tibia or femur, for any of the imaging methods (Figure S1). In T2 imaging of *mdx* leg muscles, we found a significant increase in the percentage of tissue with elevated intensity ($p < 0.001$) that changed over time ($p < 0.01$), without a significant interaction effect being present. In T2 images of leg muscle, 6-week-old *mdx* mice had $21 \pm 3\%$ tissue with elevated signal, as compared to $4 \pm 2\%$ for wild-type mice ($p < 0.001$; Figure 2C). As the *mdx* mice entered the recovery phase of disease, they showed a 38% reduction in the levels of affected tissue, to a mean of $13 \pm 2\%$ of volume pixels (voxels) with elevated intensity at 8 weeks of age ($p < 0.001$). These values then remained fairly steady, with no significant decrease from 8 to 12 weeks of age. These data illustrate the ability of MRI to detect significant levels of affected tissue in dystrophic legs in 6- to 12-week old *mdx* mice.

We also wanted to gain insight into whether affected muscle in *mdx* is either being eliminated or being “diluted” as the muscle grows larger and enters the recovery phase. To do this, we assayed the absolute volume of tissue with elevated intensity in the legs as well as the cross-sectional area of the legs. We detected a significant effect of the *mdx* genotype ($p < 0.001$), with increased volume of elevated signal over wild-type at all ages (Figure 2D).

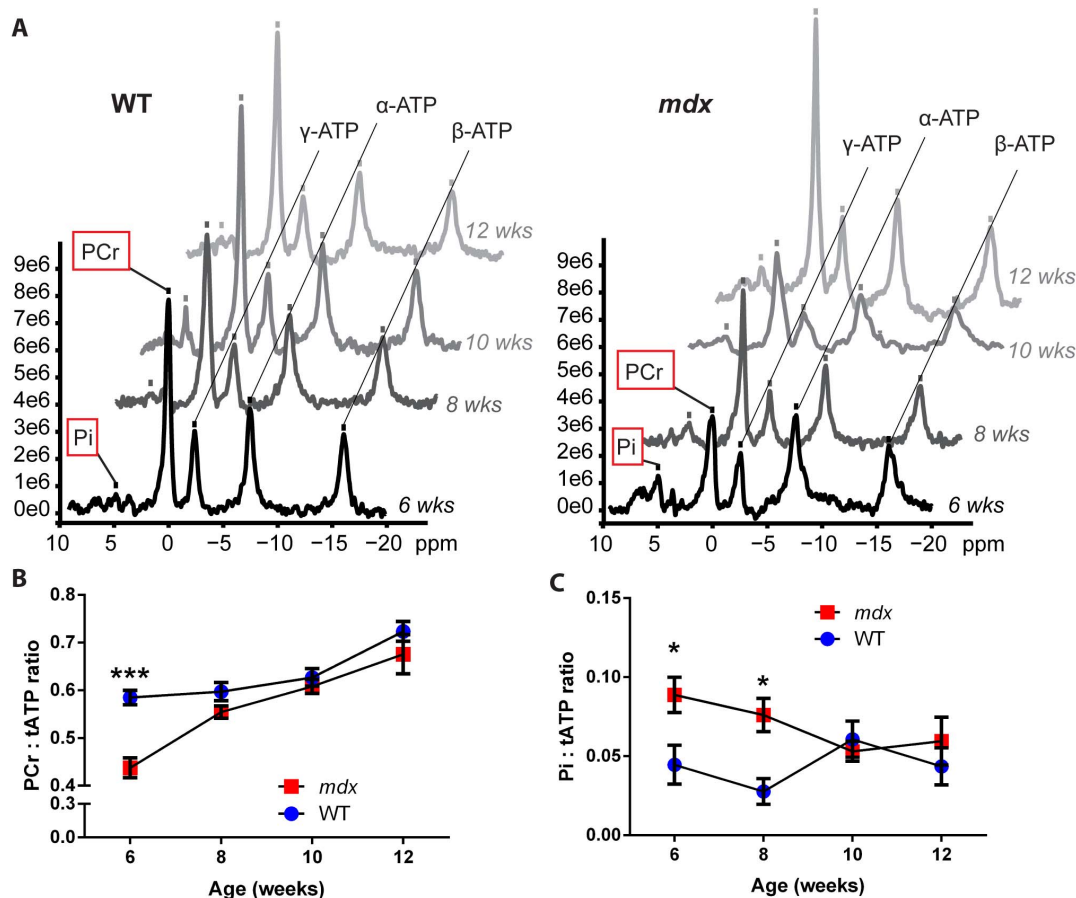


Figure 1. ³¹P NMR spectroscopy indicates an energy deficit in 6-week-old *mdx* mice. Beginning at 6 weeks of age, *mdx* and wild-type (WT) mice were assayed by ³¹P spectroscopy every 2 weeks. A) Representative ³¹P NMR spectra illustrating the peaks of several energy metabolites in one wild-type (left) and one *mdx* (right) mouse, from weeks 6 through 12. The inorganic phosphate, phosphocreatine, and three phosphate group peaks for ATP are labeled and marked by a tick mark. Graphs are aligned by parallel lines connecting the ATP peaks; phosphocreatine and inorganic phosphate showed differences between wild-type and *mdx* mice and are highlighted by a red box. B) Phosphocreatine levels are decreased in 6-week-old *mdx* mice, then change to near wild-type levels during the *mdx* recovery phase. C) Inorganic phosphate levels are elevated at 6 and 8 weeks in *mdx* mice compared to wild-type, then change to near wild-type levels by 10 weeks. Note, peaks for inorganic phosphate were not detectable in several mice of both genotypes (3 *mdx* and 5 wild-type); values for these mice were uniformly omitted from the Pi analysis (Pi, inorganic phosphate; PCr, phosphocreatine; ATP, adenosine triphosphate; tATP, total ATP; n = 3–6 mice per data point; data are means ± SEM; *p ≤ 0.05, ***p ≤ 0.001). doi:10.1371/journal.pone.0112477.g001

We detected no significant effects of time on the volume of elevated signal in *mdx* mice and no significant interaction effect. Examining the sizes of muscles throughout the 6- to 12-week period assayed, we detected significant effects of the *mdx* genotype ($p < 0.001$) and of time ($p < 0.001$) on CSA_{max} , without a significant interaction effect. Initially, the *mdx* mice showed a smaller but significant increase over wild-type in CSA_{max} ($p < 0.05$), with values of $27.7 \pm 1.3 \text{ mm}^2$ versus $24.7 \pm 2.6 \text{ mm}^2$, respectively (Figure 2E). In contrast to the results for elevated signal, as the *mdx* mice progressed into the recovery phase, differences in CSA_{max} between the *mdx* and wild-type mice became larger, with the difference increasing by 113% from week 6 to week 8. At 8 weeks, *mdx* calves had CSA_{max} values of $34.7 \pm 2.2 \text{ mm}^2$, versus $28.4 \pm 2.5 \text{ mm}^2$ for wild-type ($p < 0.01$), and this difference was maintained through 12 weeks of age, at which point the *mdx* mice had CSA_{max} values of $40.0 \pm 3.9 \text{ mm}^2$, versus $33.5 \pm 1.3 \text{ mm}^2$ for wild-type ($p < 0.01$). Together, these MRI data show that as *mdx* mice recover from the necrotic phase and assume a milder phenotype [20,22,23], they show a decrease in the percentage of affected tissue driven by an increase in muscle size, without a complete resolution of phenotype.

To enhance the visualization of signal from possible edema and inflammation, given the reduced signal likely from possible fatty infiltration of the muscle, we performed fat-suppressed imaging immediately following the standard T2-weighted imaging (Figure 3). Here again, we saw significant phenotypes in 6-week old *mdx* mice, with an average of $9 \pm 3\%$ tissue with elevated intensity present in *mdx* mice, versus $1 \pm 1\%$ for wild-type mice ($p < 0.001$). Following week 6, *mdx* mice again showed a 40% reduction in affected leg tissue as they entered the recovery phase of disease, to $5 \pm 4\%$ versus $0.6 \pm 0.3\%$ for wild-type ($p < 0.05$) at 8 weeks. Values for both genotypes were then maintained at similar levels through 12 weeks of age. These data are consistent with the T2 imaging results.

For the thigh muscles, results were qualitatively consistent with those found for the leg muscles; we again observed changes in the patterns of affected tissue over time within the same mouse in anatomically aligned MRI slices (Figure 4A). Orientation and relevant anatomy are provided (Figure 4B). In standard T2 images, 6-week old *mdx* mice showed a significant increase in the percentage of tissue with elevated signal, with values of $22 \pm 5\%$ versus $7 \pm 1\%$ for wild-type mice ($p < 0.001$; Figure 4C).

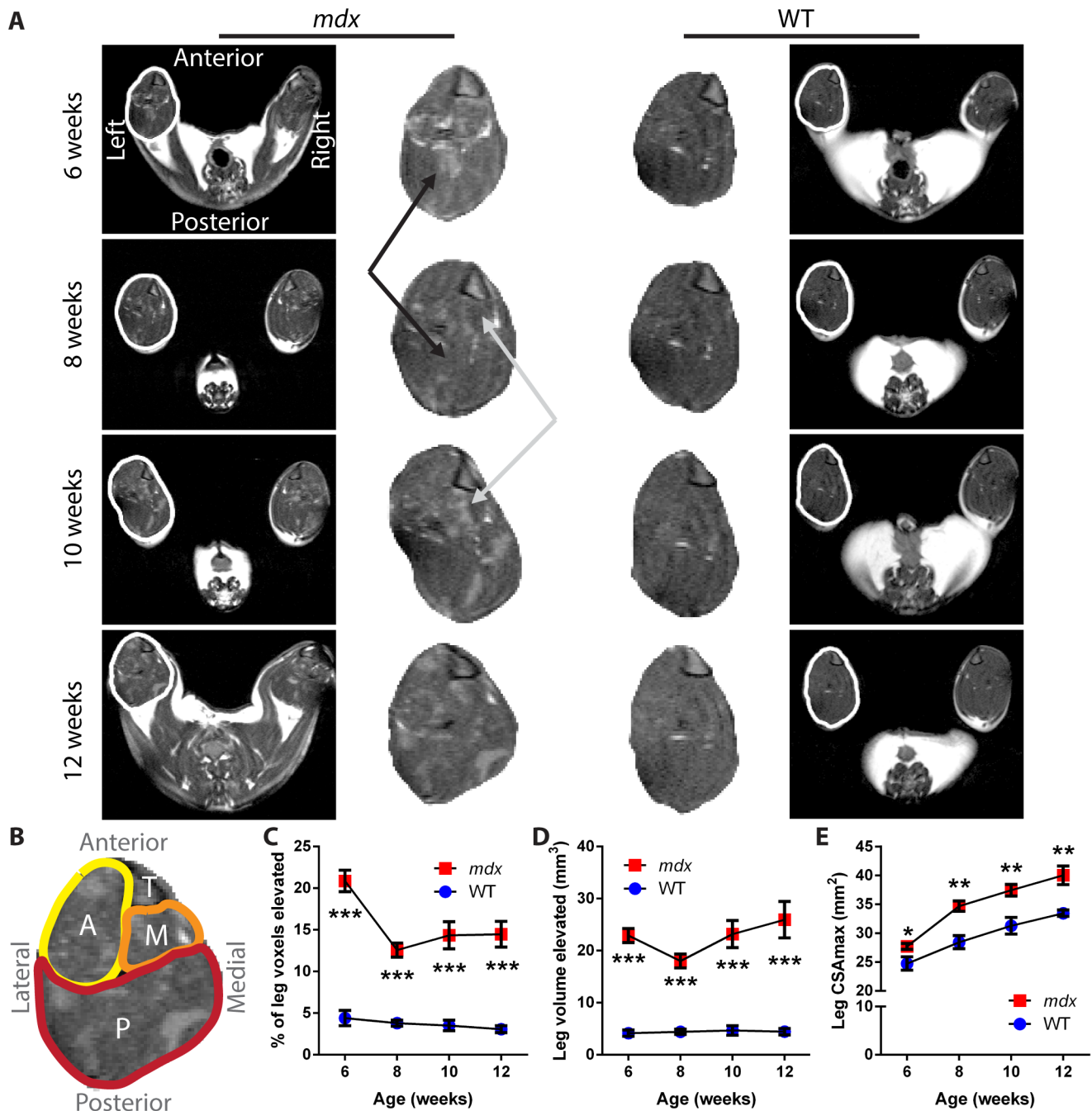


Figure 2. T2 of *mdx* leg shows changes in dystrophic muscle and cross-sectional area over time. A) Representative T2-weighted images from one *mdx* mouse (left) and one wild-type mouse (right) over time, each imaged from 6 to 12 weeks of age. The full MRI image of each mouse is provided on the outside column, with the leg of the left hindlimb for each mouse outlined in white and a magnified version of the leg muscles provided in the center columns. The black arrows mark a region of *mdx* muscle that showed a reduction in intensity between time points, while the gray arrows mark a region that showed an elevation of intensity between time points. The tibia, visible as a triangular structure in the upper right corner of each leg section, was used to orient the muscle slices. B) Orientation and anatomy of the leg cross sections. Anterior muscle groups (A, yellow) include tibialis anterior and extensor digitorum longus. Medial muscle groups (M, orange) include flexor hallucis and flexor digitorum. Posterior muscle groups (P, red) include gastrocnemius, soleus, and plantaris. The tibia bone is also marked (T). C) The percentage of tissue within the leg muscle that showed signal intensity elevated over the threshold that separates healthy muscle from affected tissue illustrates a change between the necrotic (6 week) and recovery phases of *mdx* disease. D) The absolute volume of tissue with elevated signal intensity detected within the leg of mice. E) The CSA_{max} values over time show the growth of muscle, and an increase for the *mdx* mice as compared to wild-type mice (n = 5 wild-type and 6 *mdx* mice; data are means \pm SEM; * p < 0.05, ** p < 0.01, *** p < 0.001).

doi:10.1371/journal.pone.0112477.g002

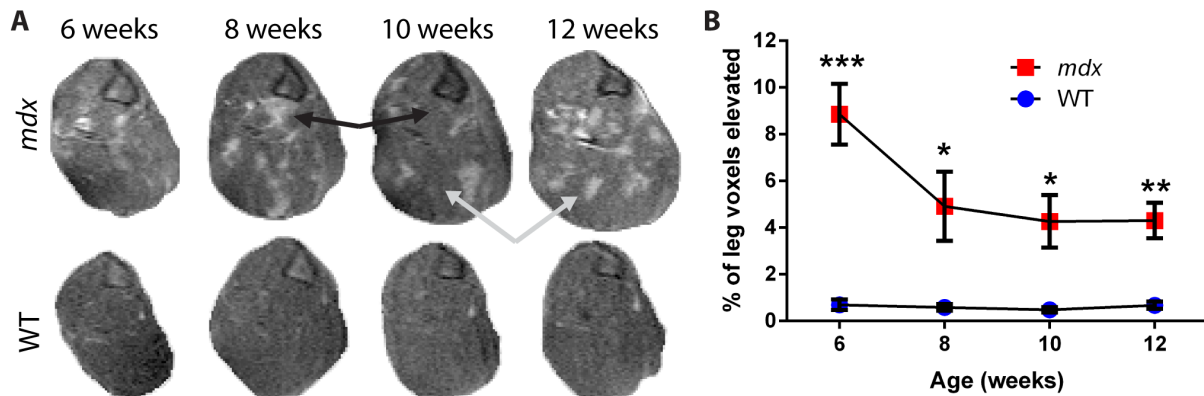


Figure 3. Longitudinal fat-suppressed imaging of dystrophic *mdx* leg muscles. A) Representative fat-suppressed images of leg muscle from the left hindlimb of one *mdx* (top) and one wild-type (bottom) mouse over time, each imaged from 6 to 12 weeks of age. Black arrows mark a region of muscle that showed a reduction in intensity between time points, while gray arrows mark a region that showed an increased intensity between time points. The tibia is present as a triangular structure in the upper right corner of the leg sections. B) The percentage of tissue within the leg that has an elevated signal intensity shows a difference between *mdx* and wild-type mice at all time points and illustrates a change between the peak disease (6 week) and recovery phases of *mdx* disease ($n=5$ wild-type and 6 *mdx* mice; data are means \pm SEM; * $p<0.05$, ** $p<0.01$, *** $p<0.001$). doi:10.1371/journal.pone.0112477.g003

This parameter decreased steadily over time for the *mdx* thigh, to $14\pm5\%$ for *mdx* and $5\pm1\%$ for wild-type mice at 12 weeks ($p<0.01$). Examining the absolute volume of tissue with increased signal independent of muscle size, we found a significant effect of the *mdx* genotype at all time points ($p<0.01$), but no significant effect of time over the ages assayed (Figure 4D). The size of the thigh muscle, as measured by CSA_{max}, was not significantly different between genotypes at 6 weeks of age (Figure 4E). However, as with the leg, CSA_{max} increased for the *mdx* thighs when compared to wild-type, beginning at 8 weeks of age with values of 57.9 ± 2.4 mm² for *mdx* versus 49.3 ± 6.4 mm² for wild-type ($p<0.05$). This size differential continued to increase through 12 weeks, to 73.0 ± 7.5 mm² for *mdx* versus 57.0 ± 3.2 mm² for wild-type mice ($p<0.01$).

In fat-suppressed imaging of the thigh, *mdx* mice again showed a significant increase in the percentage of tissue with elevated signal at 6 weeks, with $17\pm6\%$ as compared to $2\pm1\%$ for wild-type ($p<0.001$; Figure 5). By 10 weeks of age, this decreased to $9\pm1\%$ for *mdx* and $2\pm1\%$ for wild-type ($p<0.001$) as the mice progressed to the recovery stage of disease. Together, thigh data are in agreement with the leg. These data illustrate that *mdx* mice show a substantial decrease in the percentage of affected tissue and an increase in muscle area as they progress from the peak disease phases [20,22,23] to the recovery phase of the disease.

Histopathology present in affected areas of dystrophic *mdx* leg MRI

To determine pathology present within areas of elevated intensity in MRI of *mdx* hindlimb muscles, we performed an additional experiment comparing H&E histology to matched MRI slices (Figure 6). Here, T2 images of the leg were obtained in 6-month old *mdx* and wild-type mice, with legs collected for histology immediately following MRI. Consistent with younger mice, *mdx* mice but not wild-type mice displayed heterogeneous patterns with foci of elevated signal intensity in their leg muscles (Figure 6A–B). By comparing matched H&E stained sections to MRI slices, we found areas of increased MRI intensity in dystrophic muscle correspond to histology regions containing a mix of inflammation, degenerating fibers, regenerating fibers, and hypertrophic fibers (Figure 6C–D). Inflammation and myofiber degeneration or regeneration were not observed in either of the

wild-type controls. Results were consistent between individual mice with the same genotype. These data indicate areas of elevated intensity in dystrophic *mdx* muscle correspond to dystrophic lesions that include a combination of inflammation with degenerating and regenerating myofibers.

Statistical power calculations suggest assays to use for lowest sample size

To determine the methodology that may be of best utility in preclinical drug or intervention efficacy studies, we performed statistical sample size calculations on MRI and spectroscopy data. Here, we calculated the sample sizes of *mdx* mice needed to detect 20% changes in *mdx* metabolite or imaging measures; in previous studies, we detect up to 40% to 50% effects from drug treatment on measures of muscle pathology and inflammation in similar aged *mdx* mice [4]. Our statistical power analyses indicated that ³¹P NMR spectroscopy performed along with T2 imaging of leg muscles at 6 weeks of age requires the lowest number of *mdx* mice to detect drug efficacy. At 6 weeks of age significant phenotypes are presented, and 20% intervention effects can be detected with 4 *mdx* mice for ³¹P phosphocreatine levels, and with 7 or 8 mice for T2 quantification of affected tissue in leg muscle (Table 1). In contrast to the leg, T2 measurements in 6-week-old *mdx* thighs required 13 or more mice for detection of drug effects. Using fat suppression acquisition methods increased the number of 6-week old mice needed for detection of intervention effects to 39 or more mice for both muscle groups. As *mdx* mice grew older, the number of mice needed to detect intervention effects in T2 images also increased to 22 or more at week 12, while ³¹P phenotypes were absent (Table S1). Together, these data indicate that a protocol of leg T2 MRI combined with ³¹P spectroscopy in mice that are 6 weeks of age provides several sensitive outcome measures for *mdx* studies.

Discussion

MRI shows promise as a surrogate outcome measure for DMD that is capable of non-invasively detecting muscle damage in patients. Here we use magnetic resonance technologies to identify and longitudinally characterize phenotypes in the *mdx* model of DMD. Since *mdx* mice naturally show a peak of necrosis, weakness

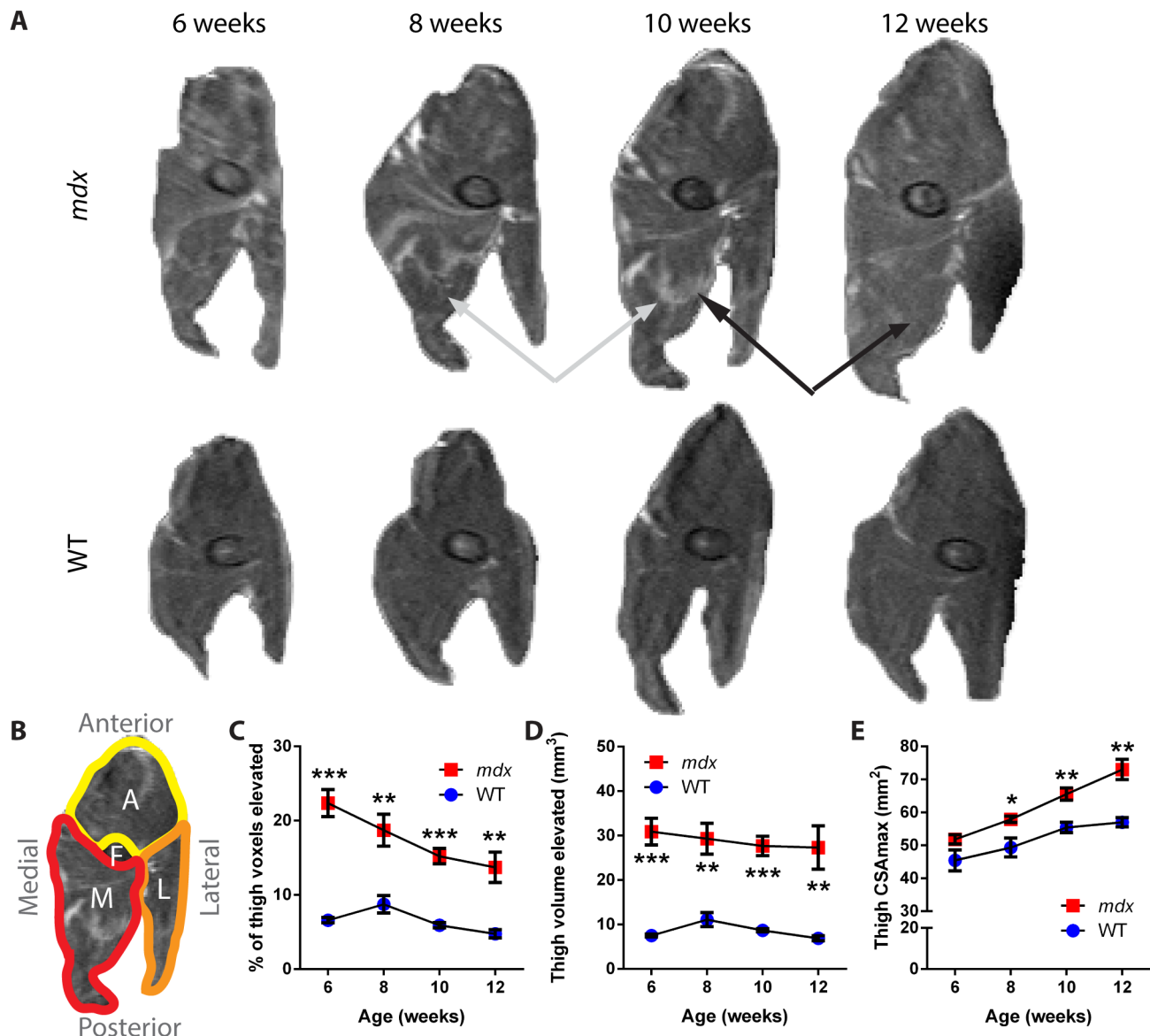


Figure 4. Changes in T2 imaging and cross-sectional area of dystrophic *mdx* thighs over time. A) Representative T2-weighted images of thigh muscle from the right hindlimb of one *mdx* and one wild-type mouse over the study period. The black arrows mark a region of muscle that showed a reduction in intensity over time, while the gray arrows mark a region that showed an increased intensity over time. The femur is visible as an elliptical structure towards the center of the thigh. B) Orientation and anatomy of thigh cross sections. Anterior muscle groups (A, yellow) include vastus intermedius, vastus lateralis, and rectus femoris. Lateral muscle groups (L, orange) include biceps, semitendinosus and semimembranosus muscles. Medial muscle groups (M, red) include gracilis and adductor muscles. The femur bone (F) is also marked. C) The percentage of tissue within the thigh muscle that showed a signal intensity elevated over the threshold that separates healthy muscle from affected tissue shows a difference between *mdx* and wild-type mice at all time points. D) The absolute volume of tissue with an elevated signal within the thigh of *mdx* and wild-type mice. E) CSA_{max} shows growth of the muscle size over time, and an increase in the cross-sectional area of the thigh muscle in *mdx* mice as compared to wild-type mice from 8 weeks onward (n = 5 wild-type and 6 *mdx* mice; data are means \pm SEM; * p < 0.05, ** p < 0.01, *** p < 0.001). doi:10.1371/journal.pone.0112477.g004

and disease at 3 to 6 weeks of age [20–23], followed by a natural recovery phase in which they show only mild skeletal muscle disease, the peak disease phase is commonly used to assess preclinical efficacy of therapeutics [4,25]. We find *mdx* mice show significant imaging and spectroscopic alterations during this peak disease phase. Furthermore, these changes decrease as mice progress to the recovery phase. Our findings indicate non-invasive MRI and NMR spectroscopy are sensitive outcome measures that can be used to study disease and evaluate potential therapies in the *mdx* model of muscular dystrophy.

Energy metabolites detected using ³¹P spectroscopy show a significant deficit of phosphocreatine in 6- to 8-week old *mdx* mice. Significant deficits in phosphocreatine and increased inorganic phosphate are also found in DMD patients [14]. Since energy for muscle contractions comes from phosphocreatine, which is used for generation of ATP through a reversible reaction with creatine phosphokinase, the PCr:ATP ratio is reflective of the energy state of muscle [26–28]. Thus, the decrease in PCr:ATP reflects a muscle bioenergetics deficit in both dystrophic 3- to 12-year-old DMD patients [14] and 6-week-old *mdx* mice. Similar results have

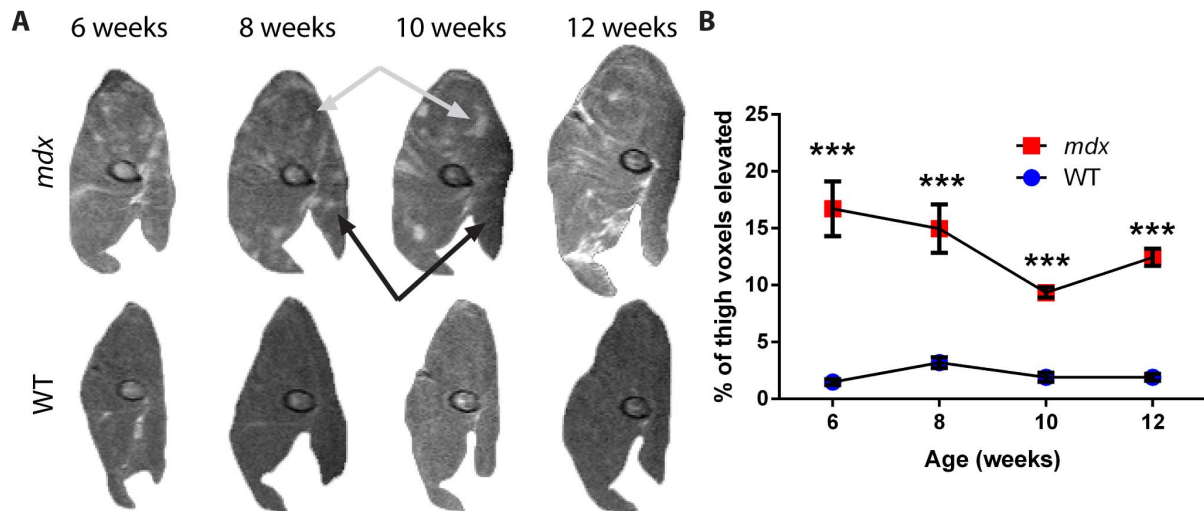


Figure 5. Longitudinal fat-suppressed MRI of dystrophic *mdx* thigh muscles. A) Representative fat-suppressed images of thigh muscle from the right hindlimb of one *mdx* and one wild-type mouse over the course of the study. Black arrows mark a region of muscle that showed a reduction in intensity over time, while gray arrows mark a region that showed an increase in intensity over time. The femur is visible as an elliptical structure in the central area of the thigh. B) The percentage of tissue with an elevated signal intensity within the thigh shows a difference between *mdx* and wild-type mice at all time points ($n=5$ wild-type and 6 *mdx* mice; data are means \pm SEM; *** $p<0.001$).
doi:10.1371/journal.pone.0112477.g005

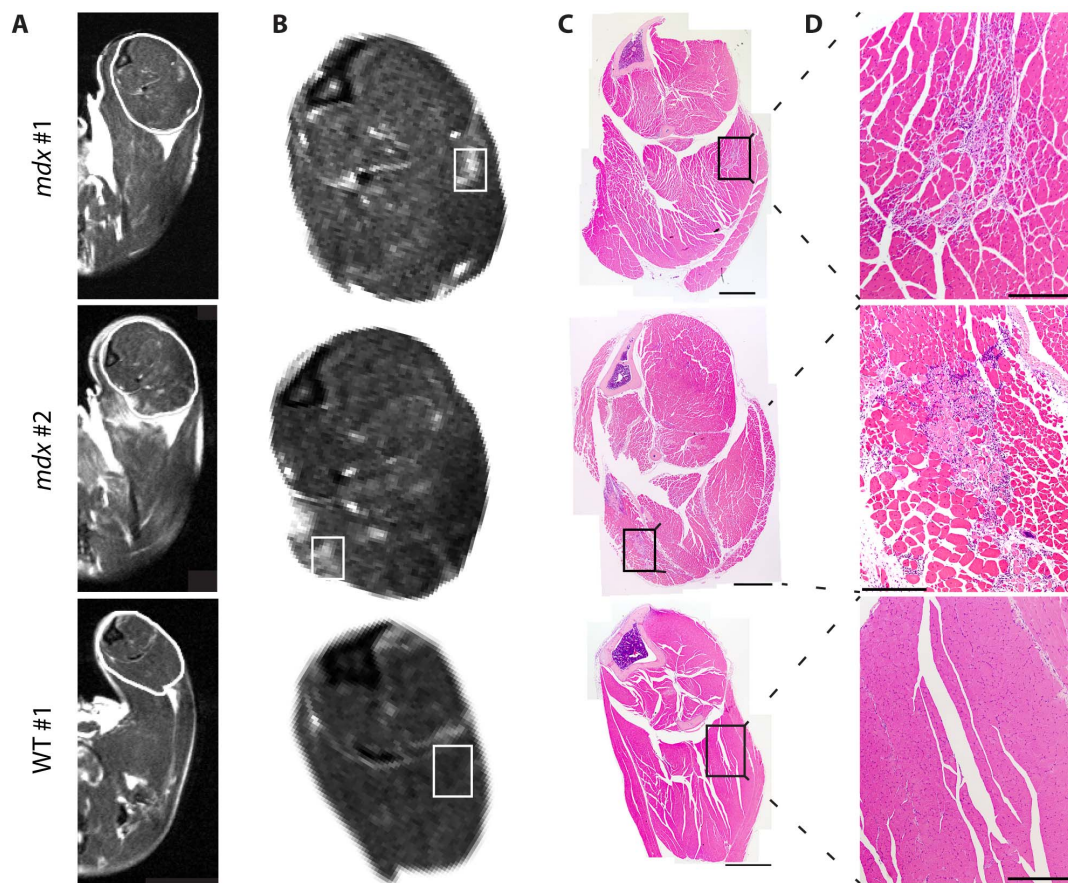


Figure 6. T2 imaging and histology of the *mdx* leg. Additional mice were assayed by T2 imaging at 6 months of age, followed by immediate collection of the whole leg for histology. A) Representative T2 images are provided of *mdx* (top two rows) and wild-type (bottom row) mice. The region of interest outlined in white is shown enlarged in (B). C) H&E stained cross section images corresponding to MRI slices in panels A and B. A montage image of the full leg is provided, with the inset area displayed in (D) at higher magnification (Rectangles in B and C represent the approximate areas presented in higher magnification images in D; Scale bars = 2 mm in C and 0.5 mm in D).
doi:10.1371/journal.pone.0112477.g006

Table 1. Statistical sample size calculations to detect intervention effects in *mdx* mice.

Method	Measure	Site	Values at 6 weeks of age		N per group to detect a 20% change in <i>mdx</i>
			WT mean \pm SD	<i>mdx</i> mean \pm SD	
³¹ P NMR Spec	PCr: tATP		0.585 \pm 0.030	0.438 \pm 0.047	4
T2	% elevated signal	Leg	4 \pm 2	21 \pm 3	8
	Vol. elevated (mm ³)	Leg	4.16 \pm 1.36	22.91 \pm 3.31	7
	% elevated signal	Thigh	7 \pm 1	22 \pm 5	13
	Vol. elevated (mm ³)	Thigh	7.52 \pm 0.75	30.89 \pm 7.33	18
Fat Suppression	% elevated signal	Leg	1 \pm 1	9 \pm 3	41
	Vol. elevated (mm ³)	Leg	0.70 \pm 0.49	10.00 \pm 3.55	39
	% elevated signal	Thigh	1 \pm 1	17 \pm 6	39
	Vol. elevated (mm ³)	Thigh	1.69 \pm 0.73	23.34 \pm 9.04	58

Abbreviations: NMR Spec, Nuclear Magnetic Resonance spectroscopy; PCr, phosphocreatine; tATP, total adenosine triphosphate; Vol., Volume; WT, wild-type.

been found in *ex vivo* cardiac studies of *mdx* mice, where a decrease in PCr is found in association with a decrease in mitochondrial content of heart tissue [29]. Consistent with heart muscle, we and others find significant mitochondrial deficits in *mdx* skeletal muscle [30]. Other muscle disorders such as mitochondrial myopathies and polio paralysis show a deficit in phosphocreatine levels as well [31,32]. Interestingly, we find the PCr:ATP ratio in *mdx* increases to a level not significantly different from wild-type by 8 to 10 weeks of age. This illustrates an improvement in energetics of dystrophic *mdx* skeletal muscle during the period associated with recovery.

MRI of *mdx* muscle provides significant phenotypes at all ages examined, characterized by hyper-intense foci and a more heterogeneous appearance. Histology shows these imaging phenotypes correspond to dystrophic lesions containing a mix of inflammation with degenerating, regenerating, and hypertrophic myofibers. This is consistent with Walter et al, who find hyperintense regions are consistent with dystrophic lesions and damaged myofibers enhanced by contrast agents, and who use ¹H spectroscopy in *mdx* to show minimal fatty infiltration in comparison to DMD [33]. We see foci of hyper-intense signal change over time, consistent with a dynamic disease process [20] and with time frames established for muscle repair following crush injury [34]. We find cross-sectional area of *mdx* muscle increases over time, while absolute volume of dystrophic lesions in imaging does not. Data in the literature indicate such increases in CSA_{max} are the result of hypertrophy and regeneration [23,35–37].

Comparing spectroscopy and imaging results, there is a discrepancy in *mdx* mice. Spectroscopy shows an initial energetics deficit that is eliminated by 8–10 weeks, while imaging phenotypes improve but persist at all ages examined (including 6 months). Established muscle histology and function data may provide insight into these differences. Through matched histology, we find *mdx* imaging phenotypes are consistent with sites containing inflammation along with myofiber degeneration and regeneration. Previous studies establish this histopathology peaks at 3–6 weeks, then improves but persists throughout the *mdx* lifespan [20–23]. In a longitudinal study we are unable to assay isolated muscles for function, but isometric force data in the literature establish muscle function at stages we examined. Throughout the lifespan of their disease, *mdx* muscles show deficits in normalized strength, where force is measured relative to mass (kN/kg) or cross-sectional area (kN/m²) [4,23,25,37,38]. However, raw absolute force measure-

ments (expressed in kN or mN) behave differently. During peak *mdx* disease (within ages 3–7 weeks), *mdx* muscles show deficits in absolute tetanic forces for extensor digitorum longus (EDL) [23], soleus [23], tibialis anterior (TA) [21], and diaphragm [39]. As *mdx* enter a recovery phase (approximately 2–8 months of age) strength deficits improve [20] and raw measures of isolated EDL [23,37], soleus [37], and TA [38] muscle forces are usually at or above wild-type levels. Comparing these observations and stages, it may be possible that energetics deficits play a role in decreased raw isometric forces during peak *mdx* disease. Consistent with this, creatine treatment targeting energetics deficits in DMD is found to both increase phosphocreatine and preserve muscle function over placebo in a short term study [14]. Alternatively, there may be a threshold of inflammation and muscle damage that manifests as metabolite or force deficits, and mice may cross this during recovery. More investigations will be needed to clarify the relationship of energetics, histopathology, and strength in *mdx* muscle.

Though some measures are consistent between *mdx* and DMD, their disease courses have clear differences. A main difference is that DMD is progressive. As children age they show increasing weakness, fibrosis, and infiltration of muscle with fatty tissue. MRI and NMR studies of DMD (summarized in Table 2) show striking differences from controls as fatty adipose tissue replaces muscle [13,15,40,41]. In DMD, edema is observed within damaged muscle [12]. At advanced ages, *mdx* disease does eventually progress, with injury phenotypes becoming more pronounced after 8 months [38], cardiac deficits around 9 months [42,43], and advanced histopathology with susceptibility to rhabdomyosarcoma around 2 years [44]. However, *mdx* typically do not progress to a point with the degree of muscle wasting and fatty infiltration apparent in DMD. The *mdx* stages we examine here may be most consistent with early DMD, where muscle shows weakness, pathology and inflammation, but patients do not yet exhibit extensive replacement of muscle with fibrotic and fatty tissue. Moving forward, many gene therapy, antisense oligos, and next-generation drug strategies will indeed want to target early DMD stages to prevent muscle loss and to target stages with more myofibers present.

Our power analyses and time course show the period of peak *mdx* disease provides a useful window with more severe phenotypes, ³¹P energetics phenotypes, and increased statistical power for detecting intervention effects. Here we calculate sample

Table 2. MR imaging and spectroscopy phenotypes in dystrophinopathies.

Reference	Study Description	Assay	Study population	Findings in dystrophy	Our findings in <i>mdx</i>
Banerjee [57]	DMD vs. controls; effects of creatine	³¹ P NMR Spectroscopy	DMD; 27 patients, 8 controls	PCr is lower & Pi is higher in DMD	PCr is lower and Pi higher in 6 week <i>mdx</i>
Forbes [58]	Ambulant DMD vs. controls	T2 MR Imaging	DMD; 30 patients, 10 controls	CSAmax higher in DMD (MG, Sol, ST)	CSAmax up for <i>mdx</i> in all weeks (leg & thigh)
Kinali [13]	Leg muscle of DMD	T2 MR Imaging	DMD; 34 patients	Non-muscle content and fat higher in DMD	Non-muscle higher in <i>mdx</i> muscle in all weeks
Newman [15]	Forearms of DMD vs. controls	¹ H NMR Spectroscopy	DMD; 6 patients aged 9–15 years	Fat content higher in DMD	No fatty infiltration visible in <i>mdx</i>
Kim [12]	T1 and FS imaging of DMD pelvic muscles	Fat-Suppressed T2 Imaging	DMD; 42 patients	DMD Edema; GMa, VL, GMe most frequent	Inflammation and muscle damage present in <i>mdx</i>
Dunn [53]	Quantitative MRI of <i>mdx</i> vs. WT	T2 Mapping	<i>mdx</i> ; 32–48 weeks	T2 decrease, ¹ H density & water increase	Inflammation and muscle damage present in <i>mdx</i>
Zhang [29]	Cardiac function and metabolism in <i>mdx</i>	MRI & <i>ex vivo</i> ³¹ P NMR Spec	<i>mdx</i> and WT; 32 weeks	Decreased PCr in heart ; RV & LV defects	Decreased PCr in skeletal muscle
McIntosh [34]	Crush injury and <i>mdx</i> vs. controls	T2 images	<i>mdx</i> ; 8–10 weeks	Dystrophic foci seen; muscle changes over 21 days post-injury	Changes in natural <i>mdx</i> lesions between 2 to 4 week intervals
Stuckey [45]	Cardiac morphology and function in <i>mdx</i> vs. controls	Longitudinal cardiac & Gd MRI	<i>mdx</i> ; 4–52 weeks	RV Dysfunction by 1 & LV by 12 months; fibrosis by 6 months	Heart fibrosis after 6 months; 8 weeks if dosed with prednisone[4]
Pratt [55]	Case study of a single <i>mdx</i> leg	MRI	One single <i>mdx</i> mouse; 5–80 weeks	Peak in MRI hetero-geneity, recovery after 13 weeks	Peak phenotypes in necrotic phase, damage persists at 8–12 weeks
Straub [46]	Agent-enhanced MRI of <i>mdx</i> and <i>Sgca</i> ^{-/-} mice	MS-325 agent MRI	<i>mdx</i> & <i>Sgca</i> ^{-/-} ; 8–10 weeks	Enhances dystrophic muscle contrast	
Amthor [47]	Albumin targeting of dystrophic muscle	Gd enhanced MRI	<i>mdx</i> ; 11–13 weeks	HSA targets to dystrophic muscle	
Odintsov [48]	MRI detection of transplanted stem cells	MRI of labeled stem cells	<i>mdx</i> and dKO; 5–30 weeks	MRI tracks Fe-labeled stem cells short-term	
Martins-Bach [51]	Metabolic profiling of <i>mdx</i> muscle	<i>In vitro</i> ¹ H NMR Spec	Lysates of <i>mdx</i> muscle; 12–24 weeks	Identified metabolites altered in <i>mdx</i> lysates	
Xu [52]	Metabolic changes in muscle after injury	¹ H NMR Spec	Injured WT & <i>mdx</i> TAs; 8 weeks	Intramuscular lipids increase post injury	Energetics deficit in necrotic phase
Mathur [54]	Effects of exercise on T2 values in muscle	T2 Mapping	<i>mdx</i> and WT; 20–60 weeks	T2, affected area up in <i>mdx</i> & after running	Affected area increased in necrotic phase
Walter [33]	Gene therapy effects on dystrophic muscle	T2 Mapping	<i>mdx</i> & <i>γsg</i> ^{-/-} mice; 1 year post-therapy	MRI tracks gene therapy efficacy in <i>mdx</i>	6 week <i>mdx</i> leg provides best stat power

Abbreviations: CSAmax, maximum cross-sectional area; FS, fat suppressed T2; Gd, gadolinium; GMa, gluteus maximus; GMed, gluteus medius; HSA, human serum albumin; MR, Magnetic Resonance; MG, medial gastrocnemius; PCr, phosphocreatine; RV, right ventricular; Sg, Sarcoglycan; Sgca, Sarcoglycan alpha; Sol, soleus; ST, semitendinosus; tATP, total adenosine triphosphate; VL, vastus lateralis; WT, wild-type.

doi:10.1371/journal.pone.0112477.t002

sizes needed to detect 20% intervention effects. In our experience with prednisone and with VBP15, we observe substantially larger than 20% intervention effects at these ages in *mdx* mice [4]. For example, fluorescent live-imaging shows a 52% decrease in markers of necrosis, and histology a 38% decrease in inflammatory foci with drug treatment [4]. Over the course of only a few weeks, we see elimination of ³¹P spectroscopy phenotypes and a dramatic reduction in the percentage of muscle affected. These findings will be valuable for design of imaging and pre-clinical therapeutic studies, by providing more phenotypes and larger differences from baseline health in controls.

Other imaging studies provide insight into *mdx* physiology (summarized in Table 2), but most avoid the critical necrotic phase of the *mdx* disease course. Cardiac MRI shows *mdx* mice can exhibit heart dysfunction by one month [45], and decreased cardiac phosphocreatine content at 8 months [29]. Agents can help visualize disrupted muscle integrity [46,47] or detect

transplanted stem cells [48–50]. Metabolic profiling shows alterations in injured muscle and lysates of 3- to 6-month old *mdx* mice [51,52]. T2 mapping has been performed in 20- to 60-week-old *mdx* [53,54]. One case study reports a single *mdx* leg assayed longitudinally to 80 weeks [55]. Dunn et al. initially showed dystrophic lesions can be detected via MRI and that crush injuries are repaired over approximately 3 weeks [53], consistent with our findings for naturally occurring *mdx* dystrophic lesions. Mathur and Vohra et al. characterized effects of exercise on *mdx*, finding effects of the *mdx* genotype and of running on muscle T2 and % affected area, with medial muscles particularly affected by running [54]. Gene correction in *mdx* and limb girdle muscular dystrophy mouse models show MRI can be used to detect therapeutic improvement in muscular dystrophy [33,56].

The *mdx* mouse provides researchers with a genetic model of the cause of DMD (dystrophin deficiency), and MRI is emerging as an important surrogate outcome measure for muscle damage.

In the present study we have found NMR phenotypes and provide new information on the dynamic disease process in *mdx* mice. Although *mdx* is typically regarded as a very mild disease model, we find ^{31}P spectroscopy and T2 imaging of the 6-week old *mdx* leg show significant differences from WT mice and could provide robust outcome measures, even with relatively few animals. These findings can improve preclinical trial design by reducing the number of animals required to detect effects, allowing for longitudinal non-invasive quantification of muscle disease, and using measures that are translatable to human clinical studies.

Supporting Information

Figure S1 Measurement of bone sizes within hindlimb sections assayed by MRI. Within the MRI slice stacks encompassing the 5-mm leg and 3-mm thigh regions analyzed, bone volume was assayed for each hindlimb. A) Tibia volume as measured in assayed T2 images of the leg. C) Tibial volume within the fat suppressed sections of leg that were analyzed. B) Femur

volume in assayed T2 sections of the thigh. D) Femur volume as measured within assayed fat suppressed images of the thigh. (TIF)

Table S1 Statistical sample sizes to detect 20% intervention effects in *mdx* mice. (DOC)

Acknowledgments

The authors would like to thank Debbie McClellan for assistance with this manuscript.

Author Contributions

Conceived and designed the experiments: CRH ADG AK SL HGD SF RS EPH PW KN. Performed the experiments: CRH ADG ALK SL HGD. Analyzed the data: CRH ADG AK SL HGD SF PW KN. Contributed reagents/materials/analysis tools: CRH ADG AK HGD SF RS EPH PW KN. Wrote the paper: CRH ADG SL HGD PW KN.

References

- Alter J, Lou F, Rabinowitz A, Yin H, Rosenfeld J, et al. (2006) Systemic delivery of morpholino oligonucleotide restores dystrophin expression bodywide and improves dystrophic pathology. *Nat Med* 12: 175–177.
- Yokota T, Lu QL, Partridge T, Kobayashi M, Nakamura A, et al. (2009) Efficacy of systemic morpholino exon-skipping in Duchenne dystrophy dogs. *Ann Neurol* 65: 667–676.
- Mendell JR, Rodino-Klapac LR, Sahenk Z, Roush K, Bird L, et al. (2013) Eteplirsen for the treatment of Duchenne muscular dystrophy. *Ann Neurol* 74: 637–647.
- Heier CR, Damsker JM, Yu Q, Dillingham BC, Huynh T, et al. (2013) VBP15, a novel anti-inflammatory and membrane-stabilizer, improves muscular dystrophy without side effects. *EMBO Mol Med* 5: 1569–1585.
- Hoffman EP, McNally EM (2014) Exon-skipping therapy: a roadblock, detour, or bump in the road? *Sci Transl Med* 6: 230fs214.
- Prinz F, Schlange T, Asadullah K (2011) Believe it or not: how much can we rely on published data on potential drug targets? *Nat Rev Drug Discov* 10: 712.
- Perrin S (2014) Preclinical research: Make mouse studies work. *Nature* 507: 423–425.
- Scott S, Kranz JE, Cole J, Lincecum JM, Thompson K, et al. (2008) Design, power, and interpretation of studies in the standard murine model of ALS. *Amyotroph Lateral Scler* 9: 4–15.
- Lu QL, Cirak S, Partridge T (2014) What Can We Learn From Clinical Trials of Exon Skipping for DMD? *Mol Ther Nucleic Acids* 3: e152.
- Huang Y, Majumdar S, Genant HK, Chan WP, Sharma KR, et al. (1994) Quantitative MR relaxometry study of muscle composition and function in Duchenne muscular dystrophy. *J Magn Reson Imaging* 4: 59–64.
- Mercuri E, Pichiechio A, Allsop J, Messina S, Pane M, et al. (2007) Muscle MRI in inherited neuromuscular disorders: past, present, and future. *J Magn Reson Imaging* 25: 433–440.
- Kim HK, Merrow AC, Shiraj S, Wong BL, Horn PS, et al. (2013) Analysis of fatty infiltration and inflammation of the pelvic and thigh muscles in boys with Duchenne muscular dystrophy (DMD): grading of disease involvement on MR imaging and correlation with clinical assessments. *Pediatr Radiol* 43: 1327–1335.
- Kinali M, Arechavala-Gomez V, Cirak S, Glover A, Guglieri M, et al. (2011) Muscle histology vs MRI in Duchenne muscular dystrophy. *Neurology* 76: 346–353.
- Banerjee B, Sharma U, Balasubramanian K, Kalaivani M, Kalra V, et al. (2010) Effect of creatine monohydrate in improving cellular energetics and muscle strength in ambulatory Duchenne muscular dystrophy patients: a randomized, placebo-controlled ^{31}P MRS study. *Magn Reson Imaging* 28: 698–707.
- Newman RJ, Bore PJ, Chan L, Gadian DG, Styles P, et al. (1982) Nuclear magnetic resonance studies of forearm muscle in Duchenne dystrophy. *Br Med J (Clin Res Ed)* 284: 1072–1074.
- Forbes SC, Walter GA, Rooney WD, Wang DJ, DeVos S, et al. (2013) Skeletal muscles of ambulant children with Duchenne muscular dystrophy: validation of multicenter study of evaluation with MR imaging and MR spectroscopy. *Radiology* 269: 198–207.
- Willcocks RJ, Arpan IA, Forbes SC, Lott DJ, Senesac CR, et al. (2014) Longitudinal measurements of MRI-T2 in boys with Duchenne muscular dystrophy: effects of age and disease progression. *Neuromuscul Disord* 24: 393–401.
- Kim HK, Laor T, Horn PS, Racadio JM, Wong B, et al. (2010) T2 mapping in Duchenne muscular dystrophy: distribution of disease activity and correlation with clinical assessments. *Radiology* 255: 899–908.
- Arpan I, Forbes SC, Lott DJ, Senesac CR, Daniels MJ, et al. (2013) T(2) mapping provides multiple approaches for the characterization of muscle involvement in neuromuscular diseases: a cross-sectional study of lower leg muscles in 5–15-year-old boys with Duchenne muscular dystrophy. *NMR Biomed* 26: 320–328.
- Muntoni F, Mateddu A, Marchei F, Clerck A, Serra G (1993) Muscular weakness in the *mdx* mouse. *J Neurol Sci* 120: 71–77.
- Dangain J, Vrbova G (1984) Muscle development in *mdx* mutant mice. *Muscle Nerve* 7: 700–704.
- Tanabe Y, Esaki K, Nomura T (1986) Skeletal muscle pathology in X chromosome-linked muscular dystrophy (*mdx*) mouse. *Acta Neuropathol* 69: 91–95.
- Anderson JE, Bressler BH, Ovalle WK (1988) Functional regeneration in the hindlimb skeletal muscle of the *mdx* mouse. *J Muscle Res Cell Motil* 9: 499–515.
- Spurney CF, Gordish-Dressman H, Guerrero AD, Sali A, Pandey GS, et al. (2009) Preclinical drug trials in the *mdx* mouse: assessment of reliable and sensitive outcome measures. *Muscle Nerve* 39: 591–602.
- Huynh T, Uaesoontrachoon K, Quinn JL, Tatem KS, Heier CR, et al. (2013) Selective modulation through the glucocorticoid receptor ameliorates muscle pathology in *mdx* mice. *J Pathol* 231: 223–235.
- Kushmerick MJ (1985) Patterns in mammalian muscle energetics. *J Exp Biol* 115: 165–177.
- Kushmerick MJ (1987) Energetics studies of muscles of different types. *Basic Res Cardiol* 82 Suppl 2: 17–30.
- Kushmerick MJ (1995) Skeletal muscle: a paradigm for testing principles of bioenergetics. *J Bioenerg Biomembr* 27: 555–569.
- Zhang W, ten Hove M, Schneider JE, Stuckey DJ, Sebag-Montefiore L, et al. (2008) Abnormal cardiac morphology, function and energy metabolism in the dystrophic *mdx* mouse: an MRI and MRS study. *J Mol Cell Cardiol* 45: 754–760.
- Jahnke VE, Van Der Meulen JH, Johnston HK, Ghimbovski S, Partridge T, et al. (2012) Metabolic remodeling agents show beneficial effects in the dystrophin-deficient *mdx* mouse model. *Skelet Muscle* 2: 16.
- Sharma U, Kumar V, Wadhwa S, Jagannathan NR (2007) In vivo ^{31}P MRS study of skeletal muscle metabolism in patients with postpolio residual paralysis. *Magn Reson Imaging* 25: 244–249.
- Taylor DJ, Kemp GJ, Radda GK (1994) Bioenergetics of skeletal muscle in mitochondrial myopathy. *J Neurol Sci* 127: 198–206.
- Walter G, Cordier L, Bloy D, Sweeney HL (2005) Noninvasive monitoring of gene correction in dystrophic muscle. *Magn Reson Med* 54: 1369–1376.
- McIntosh LM, Baker RE, Anderson JE (1998) Magnetic resonance imaging of regenerating and dystrophic mouse muscle. *Biochem Cell Biol* 76: 532–541.
- Coulton GR, Curtin NA, Morgan JE, Partridge TA (1988) The *mdx* mouse skeletal muscle myopathy: II. Contractile properties. *Neuropathol Appl Neurobiol* 14: 299–314.
- Coulton GR, Morgan JE, Partridge TA, Sloper JC (1988) The *mdx* mouse skeletal muscle myopathy: I. A histological, morphometric and biochemical investigation. *Neuropathol Appl Neurobiol* 14: 53–70.
- Lynch GS, Hinkle RT, Chamberlain JS, Brooks SV, Faulkner JA (2001) Force and power output of fast and slow skeletal muscles from *mdx* mice 6–28 months old. *J Physiol* 535: 591–600.
- Dellorusso C, Crawford RW, Chamberlain JS, Brooks SV (2001) Tibialis anterior muscles in *mdx* mice are highly susceptible to contraction-induced injury. *J Muscle Res Cell Motil* 22: 467–475.

39. Kumar A, Bhatnagar S, Kumar A (2010) Matrix metalloproteinase inhibitor batimastat alleviates pathology and improves skeletal muscle function in dystrophin-deficient *mdx* mice. *Am J Pathol* 177: 248–260.
40. Lamminen AE (1990) Magnetic resonance imaging of primary skeletal muscle diseases: patterns of distribution and severity of involvement. *Br J Radiol* 63: 946–950.
41. Phoenix J, Betal D, Roberts N, Helliwell TR, Edwards RH (1996) Objective quantification of muscle and fat in human dystrophic muscle by magnetic resonance image analysis. *Muscle Nerve* 19: 302–310.
42. Quinlan JG, Hahn HS, Wong BL, Lorenz JN, Wenisch AS, et al. (2004) Evolution of the *mdx* mouse cardiomyopathy: physiological and morphological findings. *Neuromuscul Disord* 14: 491–496.
43. Spurney CF, Knobloch S, Pistilli EE, Nagaraju K, Martin GR, et al. (2008) Dystrophin-deficient cardiomyopathy in mouse: expression of Nox4 and Lox are associated with fibrosis and altered functional parameters in the heart. *Neuromuscul Disord* 18: 371–381.
44. Chamberlain JS, Metzger J, Reyes M, Townsend D, Faulkner JA (2007) Dystrophin-deficient *mdx* mice display a reduced life span and are susceptible to spontaneous rhabdomyosarcoma. *FASEB J* 21: 2195–2204.
45. Stuckey DJ, Carr CA, Camelliti P, Tyler DJ, Davies KE, et al. (2012) In vivo MRI characterization of progressive cardiac dysfunction in the *mdx* mouse model of muscular dystrophy. *PLoS One* 7: e28569.
46. Straub V, Donahue KM, Allamand V, Davisson RL, Kim YR, et al. (2000) Contrast agent-enhanced magnetic resonance imaging of skeletal muscle damage in animal models of muscular dystrophy. *Magn Reson Med* 44: 655–659.
47. Amthor H, Egelhof T, McKinnell I, Ladd ME, Janssen I, et al. (2004) Albumin targeting of damaged muscle fibres in the *mdx* mouse can be monitored by MRI. *Neuromuscul Disord* 14: 791–796.
48. Odintsov B, Chun JL, Mulligan JA, Berry SE (2011) 14.1 T whole body MRI for detection of mesoangioblast stem cells in a murine model of Duchenne muscular dystrophy. *Magn Reson Med* 66: 1704–1714.
49. Cahill KS, Gaidosh G, Huard J, Silver X, Byrne BJ, et al. (2004) Noninvasive monitoring and tracking of muscle stem cell transplants. *Transplantation* 78: 1626–1633.
50. Walter GA, Cahill KS, Huard J, Feng H, Douglas T, et al. (2004) Noninvasive monitoring of stem cell transfer for muscle disorders. *Magn Reson Med* 51: 273–277.
51. Martins-Bach AB, Bloise AC, Vainzof M, Rahnamaye Rabbani S (2012) Metabolic profile of dystrophic *mdx* mouse muscles analyzed with in vitro magnetic resonance spectroscopy (MRS). *Magn Reson Imaging* 30: 1167–1176.
52. Xu S, Pratt SJ, Spangenburg EE, Lovering RM (2012) Early metabolic changes measured by ¹H MRS in healthy and dystrophic muscle after injury. *J Appl Physiol* (1985) 113: 808–816.
53. Dunn JF, Zaim-Wadghiri Y (1999) Quantitative magnetic resonance imaging of the *mdx* mouse model of Duchenne muscular dystrophy. *Muscle Nerve* 22: 1367–1371.
54. Mathur S, Vohra RS, Germain SA, Forbes S, Bryant ND, et al. (2011) Changes in muscle T2 and tissue damage after downhill running in *mdx* mice. *Muscle Nerve* 43: 878–886.
55. Pratt SJ, Xu S, Mullins RJ, Lovering RM (2013) Temporal changes in magnetic resonance imaging in the *mdx* mouse. *BMC Res Notes* 6: 262.
56. Pacak CA, Walter GA, Gaidosh G, Bryant N, Lewis MA, et al. (2007) Long-term skeletal muscle protection after gene transfer in a mouse model of LGMD-2D. *Mol Ther* 15: 1775–1781.
57. Bach JR (2007) Medical considerations of long-term survival of Werdnig-Hoffmann disease. *Am J Phys Med Rehabil* 86: 349–355.
58. Roos M, Sarkozy A, Chierchia GB, De Wilde P, Schmedding E, et al. (2009) Malignant ventricular arrhythmia in a case of adult onset of spinal muscular atrophy (Kugelberg-Welander disease). *J Cardiovasc Electrophysiol* 20: 342–344.

Appendix 6 Reprints of Abstract Presentations (2015/07—)

1. Shan L, Lin S, Wang PC. Engineered Antibody Fragments for PSMA-targeted Imaging and Therapy of Prostate Cancer. World Molecular Imaging Conference 2015, Honolulu, HI, September 2-5, 2015.
2. Lin S, Zhang ZJ, Wang PC. Fabrication of a Microfluidic Device for Generating Liposomal Nanoparticles as Drug Delivery Vehicle. ChinaNANO 2015, Beijing, China, September 3-5, 2015.
3. Wang PC. Fabrication Microfluidic Device for Generating Liposome, Recombinant Immunotoxins (RITs) for Cancer Therapy, paraCEST MRI Agent for In Vivo pH Imaging. National Center for Nanoscience and Technology, Beijing, China, September 16, 2015
4. Wang PC. Introduction of Howard University Molecular Imaging Lab – Applications of Nanotechnology in Medical Imaging and Targeted Drug Delivery. Catholic University of America, Washington, DC, October 28, 2015.

Abstract

Shan L, Lin S, Wang PC. Engineered Antibody Fragments for PSMA-targeted Imaging and Therapy of Prostate Cancer. World Molecular Imaging Conference 2015, Honolulu, HI, September 2-5, 2015.

Engineered Antibody Fragments for PSMA-targeted Imaging and Therapy of Prostate Cancer

Liang Shan, Stephen Lin, Paul C. Wang

Molecular Imaging Laboratory, Department of Radiology, Howard University

Monoclonal antibodies have long been attracted for molecular imaging of cancer because of their high specificity along with the potential of imparting molecular specificity into existing imaging modalities. However, several issues including long circulation time and poor tissue penetration form critical barriers for the imaging efficiency of antibodies. To improve the pharmacokinetics of antibodies, three different formats of small antibody fragments were generated including the single-chain variable fragment (scFv, 27 kDa), bivalent tandem scFv (biscFv, 54.6 kDa), and bivalent scFv fold-back diabody (scfbDb, 54.6 kDa). These fragments were designed by capitalizing upon the high specificity of J591 antibody against the extracellular domain of prostate-specific membrane antigen (PSMA). Competition assay showed that the binding affinity of scfbDb was 7-fold and 2.5-fold higher than that of biscFv and scFv formats, respectively. To further test the delivery efficiency of scfbDb, a recombinant immunotoxin was then generated by fusing the scfbDb with a mutated diphtheria toxin moiety (DT390). Fluorescent microscopy and flow cytometry demonstrated that scfbDb efficiently mediated the entry of DT390 into the PSMA-positive LNCaP cancer cells but not into the PSMA-negative PC-3 cells, inducing LNCaP cell apoptosis and growth arrest (IC_{50} , ~ 0.57 nM). In animal models of tumor xenografts, the PSMA-targeting specificity of scfbDb was confirmed with optical imaging, showing specific accumulation in LNCaP tumors. Intraperitoneal administration of the scfbDb-based immunotoxin significantly inhibited the growth of established LNCaP tumor xenografts, but not the growth of PC-3 xenografts (0.27 ± 0.09 vs. 0.67 ± 0.11 g; $P < 0.05$). These results indicate that the engineered antibody fragments, especially the scfbDb, could serve as a springboard to develop PSMA-targeted imaging and therapeutic agents with high sensitivity and specificity against prostate cancers.

Abstract Lin S, Zhang ZJ, Wang PC. Fabrication of a Microfluidic Device for Generating Liposomal Nanoparticles as Drug Delivery Vehicle. ChinaNANO 2015, Beijing, China, Sept 3-5, 2015

Fabrication of a Microfluidic Device for Generating Liposomal Nanoparticles as Drug Delivery Vehicle

Stephen Lin^{1,a}, Zhenjiang Zhang^{1,b}, Paul C Wang^{*1,2,c}

¹ Molecular Imaging Laboratory, Department of Radiology, Howard University, Washington DC, 20060

² Department of Physics, Fu Jen Catholic University, Taipei, Taiwan

^a stephen.lin@howard.edu, ^b zhengjiang.zhang@howard.edu, ³ pwang@howard.edu

Keywords: nanoparticle, liposome, microfluidics, cancer, MRI

Abstract

One of the major challenges in cancer diagnosis is detection of early tumors. Targeted nanoparticles are increasingly being investigated for use as a vehicles to deliver diagnostic agents to tumors [1]. In particular, liposomes are widely studied because of their high biocompatibility. It has been shown that the dynamic uptake of the nanoparticles depends on the nanoparticle size. In order to study this relationship, the nanoparticles used must have a narrow size distribution. Current methods of fabricating liposomes include sonication and extrusion techniques. A new method using a microfluidic device proposed to generate liposomes with a very narrow size distribution through hydrodynamic focusing [2,3].

A blank mold consisting of photoresist laminated on a glass slide was photopatterned using UV light through a laser-plotted photomask, creating a mold with microfluidic channels. The mold was cast in polydimethylsiloxane (PDMS), which was plasma bonded to a glass slide, resulting in a completed microfluidic device. Liposomes were generated by infusing the device with a lipid tincture and aqueous buffer solution. Liposome size and size distribution was measured with dynamic light scattering.

The device was tested with a lipid formulation consisting of DPPC, cholesterol and DSPE-PEG. A 1:10 infusion ratio resulted in a Z-average size of 139.9nm and a polydispersity index (PDI) of 0.128. With a 1:20 ratio, the Z-average size was 91.4nm with a PDI of 0.163.

A microfluidic device designed for the generation of liposomes was successfully fabricated. The device allows easy control of the liposome diameter, accomplished by modifying the infusion ratio, and the lipid formulation. Early tests show the PDI is comparable to established extrusion-based technique. Further refining of the technique is expected to significantly improve the size distribution. The liposomes can then be used as targeted delivery vehicles by encapsulating imaging agents and coating with targeting ligands.

References

- [1] A. Korotcov, L. Shan, H. Meng, T.X. Wang, R. Sridhar, Y.R. Zhao, X.J. Liang, P.C. Wang: *A Nanocomplex System as Targeted Contrast Agent Delivery Vehicle for MRI Dynamic Contrast Enhancement Study*. Journal of Nanotechnology. 10(11), 7113-7116. 2010.
- [2] A. Jahn, W.N. Vreeland, M. Gaitan, L.E. Locascio: *Controlled Vesicle Self-Assembly in Microfluidic Channels with Hydrodynamic Focusing*. Journal of the American Chemical Society, 126(9), 2674-2675. 2004.
- [3] R.R. Hood, D.L. Devoe, A. Andar, P.W. Swaan, D.M. Omiatek, W.N. Vreeland: *Microfluidic Synthesis of PEGylated Liposomes*. MAMNA 2012 Spring Symposium on Microsystems for Measurement and Instrumentation, Mar 27, 2012, Annapolis, MD, USA.

Abstract Wang PC. Fabrication Microfluidic Device for Generating Liposome, Recombinant Immunotoxins (RITs) for Cancer Therapy, paraCEST MRI Agent for In Vivo pH Imaging. National Center for Nanoscience and Technology, Beijing, China, September 16, 2015

Fabrication of a Microfluidic Device for Generating Liposomal Nanoparticles as Drug Delivery Vehicle

Stephen Lin^{1,a}, Zhenjiang Zhang^{1,b}, Paul C Wang^{*1,2,c}

¹ Molecular Imaging Laboratory, Department of Radiology, Howard University, Washington DC, 20060, USA

² Department of Physics, Fu Jen Catholic University, Taipei, Taiwan

^a stephen.lin@howard.edu, ^b zhengjiang.zhang@howard.edu, ³ pwang@howard.edu

*Corresponding Author

Keywords: nanoparticle, liposome, microfluidics, cancer, MRI

Abstract

One of the major challenges in cancer diagnosis is detection of early tumors. Targeted nanoparticles are increasingly being investigated for use as a vehicles to deliver diagnostic agents to tumors [1]. In particular, liposomes are widely studied because of their high biocompatibility. It has been shown that the dynamic uptake of the nanoparticles depends on the nanoparticle size. In order to study this relationship, the nanoparticles used must have a narrow size distribution. Current methods of fabricating liposomes include sonication and extrusion techniques. A new method using a microfluidic device proposed to generate liposomes with a very narrow size distribution through hydrodynamic focusing [2,3].

A blank mold consisting of photoresist laminated on a glass slide was photopatterned using UV light through a laser-plotted photomask, creating a mold with microfluidic channels. The mold was cast in polydimethylsiloxane (PDMS), which was plasma bonded to a glass slide, resulting in a completed microfluidic device. Liposomes were generated by infusing the device with a lipid tincture and aqueous buffer solution. Liposome size and size distribution was measured with dynamic light scattering. The device was tested with a lipid formulation consisting of DPPC, cholesterol and DSPE-PEG. A 1:10 infusion ratio resulted in a Z-average size of 139.9nm and a polydispersity index (PDI) of 0.128. With a 1:20 ratio, the Z-average size was 91.4nm with a PDI of 0.163.

A microfluidic device designed for the generation of liposomes was successfully fabricated. The device allows easy control of the liposome diameter, accomplished by modifying the infusion ratio, and the lipid formulation. Early tests show the PDI is comparable to established extrusion-based technique. Further refining of the technique is expected to significantly improve the size distribution. The liposomes can then be used as targeted delivery vehicles by encapsulating imaging agents and coating with targeting ligands.

Abstract Wang PC. Introduction of Howard University Molecular Imaging Lab – Applications of Nanotechnology in Medical Imaging and Targeted Drug Delivery. Catholic University of America, Washington, DC, October 28, 2015.

Introduction of Howard University Molecular Imaging Laboratory

Paul C. Wang, PhD
Professor
Department of Radiology/
Howard University

Abstract

The Howard Molecular Imaging Laboratory (MIL) is a university core facility to promote and support a sustainable long-term research using modern imaging technology to study the mechanism of disease processes and their response to therapy at the molecular, subcellular, cellular, and whole animal levels. The objectives of MIL are (1) to provide state-of-the-art instrumentation, technical expertise and essential services for molecular, cellular and in vivo imaging (2) to provide a broader training in biomedical imaging through methodology- centered seminars, workshops, mini-courses, and internships (3) to foster new multidisciplinary research collaborations using modern imaging techniques. The MIL has a 9.4T and a 7T NMR machines for small animal imaging and MR spectroscopy studies, a PerkinElmer Spectrum optical imaging machine, and will have a PET/CT machine in spring 2015. The MIL provides expertise in imaging experiment design, and offers high resolution and high sensitivity MRI, optical imaging, and multi-photon confocal microscopy imaging services. The MIL also provides expertise and services in: development of efficient organ and intracellular targeting and amplification strategies, as well as in developing strategies for identifying suitable biomarkers, or imaginable gene products. The MIL provides assistance to develop nanoparticles with ligands to transfect cells with bioluminescent or fluorescent markers, targeted to specific receptors, proteins or biochemical pathways for in vitro and in vivo studies.